TESIS DE LA UNIVERSIDAD
DE ZARAGOZA

2025

158

Jesús Ángel García Arnay

Geological-geomorphological mapping, landscape evolution and paleohydrology in NW Terra Cimmeria and SE Nepenthes Mensae, and analysis of closed depressions in SW Arabia Terra, Mars

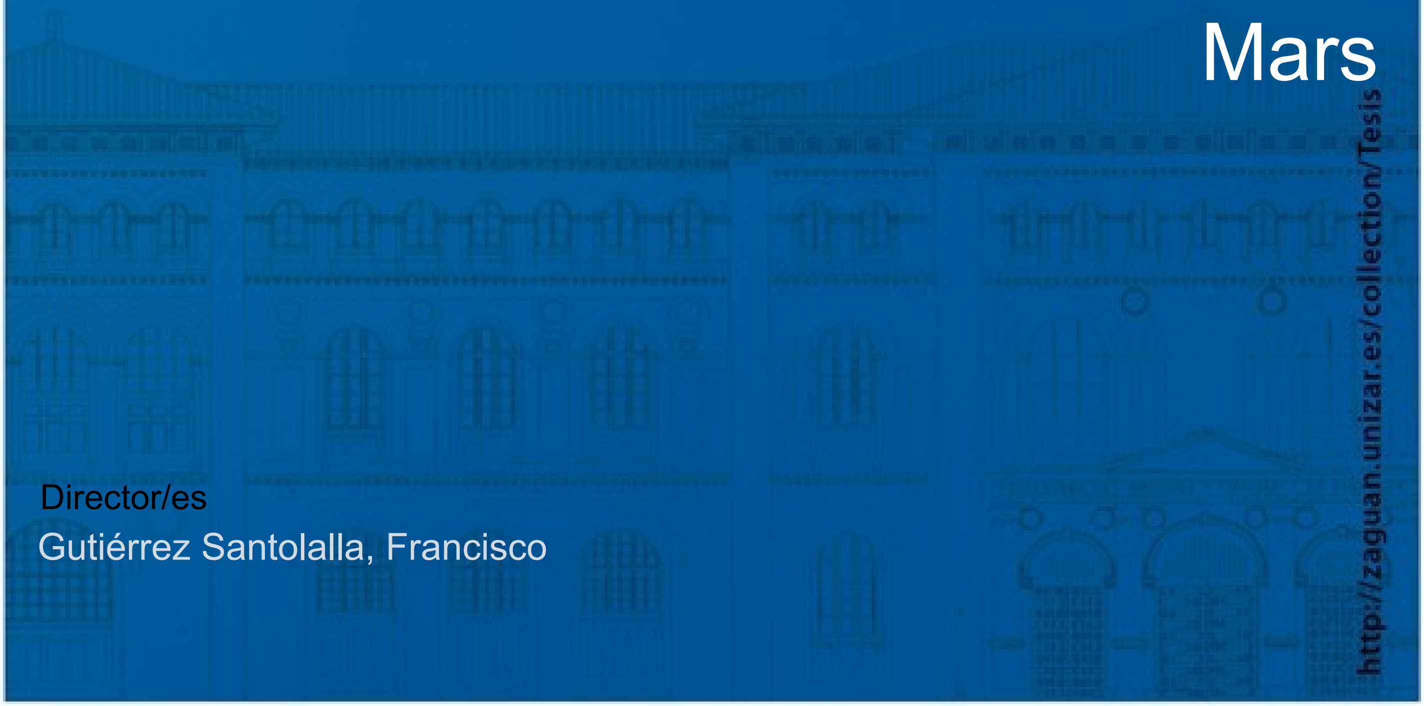

Director/es
Gutiérrez Santolalla, Francisco

ISSN 2254-7606

Prensas de la Universidad
Universidad Zaragoza

Universidad de Zaragoza
Servicio de Publicaciones

ISSN 2254-7606

Tesis Doctoral

GEOLOGICAL-GEOMORPHOLOGICAL MAPPING, LANDSCAPE EVOLUTION AND PALEOHYDROLOGY IN NW TERRA CIMMERIA AND SE NEPENTHES MENSAE, AND ANALYSIS OF CLOSED DEPRESSIONS IN SW ARABIA TERRA, MARS

Autor

Jesús Ángel García Arnay

Director/es

Gutiérrez Santolalla, Francisco

UNIVERSIDAD DE ZARAGOZA
Escuela de Doctorado

Programa de Doctorado en Geología

2023

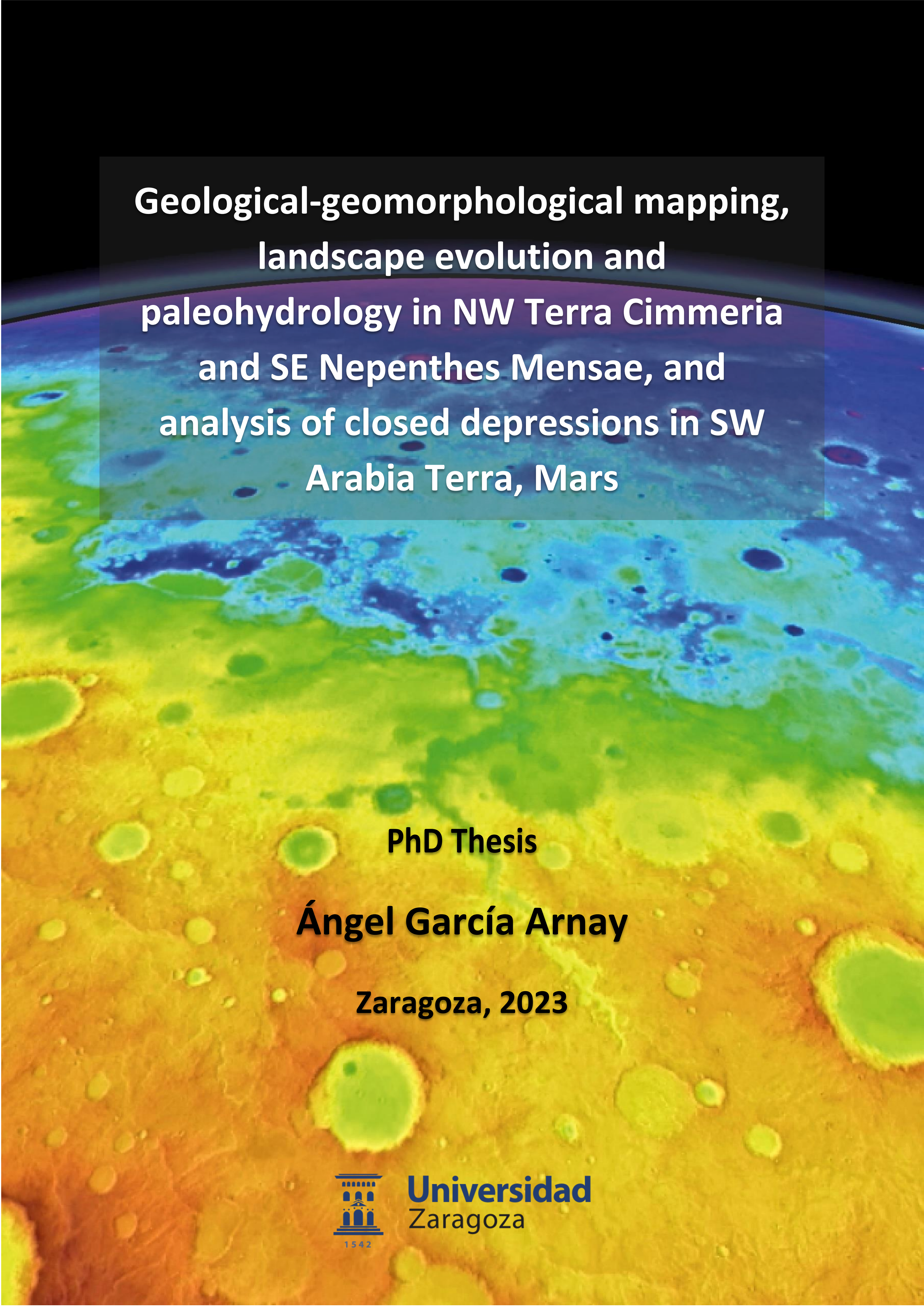

Geological-geomorphological mapping, landscape evolution and paleohydrology in NW Terra Cimmeria and SE Nepenthes Mensae, and analysis of closed depressions in SW Arabia Terra, Mars

PhD Thesis

Ángel García Arnay

Zaragoza, 2023

Universidad
Zaragoza

Departamento de
Ciencias de la Tierra
Universidad Zaragoza

Instituto Universitario de Investigación
en Ciencias Ambientales
de Aragón
Universidad Zaragoza

GEOLOGICAL-GEOMORPHOLOGICAL MAPPING, LANDSCAPE EVOLUTION AND PALEOHYDROLOGY IN NW TERRA CIMMERIA AND SE NEPENTHES MENSAE, AND ANALYSIS OF CLOSED DEPRESSIONS IN SW ARABIA TERRA, MARS

Author:

Ángel GARCÍA ARNAY

A Thesis developed at the University of Zaragoza for fulfilling the requirements to obtain the degree of Doctor in Geology

University of Zaragoza – 2023

Supervisor:

Dr. Francisco Gutiérrez Santolalla (Univ. Zaragoza)

LIST OF SCIENTIFIC CONTRIBUTIONS

This PhD Thesis compiles the results of the investigations presented in five scientific publications (two of them currently under review). Four of these papers have been published in or submitted to international journals included in the Scientific Citation Index (SCI): Icarus, Geomorphology, and the Journal of Maps. The remaining paper has been published in Geogaceta, a peer-reviewed journal of short papers from works presented at the biannual scientific meetings of the Geological Society of Spain.

Four of these publications focus on the geology, landscape evolution and paleohydrology of the northwest Terra Cimmeria and southeast Nepenthes Mensae, whereas the remaining paper of this Thesis analyzes the morphometry, spatial distribution and origin of the sinkhole-like depressions in Kotido Crater, southwest Arabia Terra.

The scientific publications that form part of this PhD Thesis are listed below in chronological order:

García-Arnay, Á., Fernández, S., de Pablo, M.Á., Gutiérrez, F., 2018. The dominant morphogenetic role of surface runoff in Licus Vallis, Mars: results from geomorphological and morphometric analyses. Geogaceta 63, 63–66. http://www.sociedadgeologica.es/archivos/geogacetas/geo63/geo63_16.pdf

Contribution: Main contributor and corresponding author, conducting the bulk of work, including data collection and analysis, as well as writing of the article.

Parenti, C., Gutiérrez, F., Baioni, D., **García-Arnay, Á.**, Sevil, J., Luzzi, E., 2020. Closed depressions in Kotido crater, Arabia Terra, Mars. Possible evidence of evaporite dissolution-induced subsidence. Icarus 341, 113680. https://doi.org/10.1016/j.icarus.2020.113680

Journal Impact Factor (2020): 3.508 (Q2: 26/68)

Contribution: Data collection, implementation together with the senior author (C. Parenti) of the GIS project, development of methodologies for the computation of some of the morphometric parameters of the depressions, and participation in the mapping tasks and writing of the article.

García-Arnay, Á., Gutiérrez, F., 2020. Reconstructing paleolakes in Nepenthes Mensae, Mars, using the distribution of putative deltas, coastal-like features, and terrestrial analogs. Geomorphology 359, 107129. https://doi.org/10.1016/j.geomorph.2020.107129

Journal Impact Factor (2020): 4.139 (Q1: 45/200)

Contribution: Main contributor and corresponding author, conducting the bulk of work, including data collection and analysis, as well as writing of the article.

García-Arnay, Á., Gutiérrez, F., 2022. Unravelling the geological and geomorphological evolution of the Terra Cimmeria-Nepenthes Mensae transitional zone, Mars. Geomorphology (*Under review*).

Contribution: Main contributor and corresponding author, conducting the bulk of work, including data collection and analysis, as well as writing of the article.

García-Arnay, Á., 2022. Geologic-geomorphic map of the Terra Cimmeria-Nepenthes Mensae transitional zone, Mars - 1:1.45Million. Journal of Maps (*Under review*).

Furthermore, some of the results of these scientific papers were presented in national and international conferences and meetings through print-only abstracts, as well as poster and oral communications, which are listed below in chronological order:

García-Arnay, Á., de Pablo, M.Á., Fernández-Menéndez, S. and Gutiérrez, F., 2017. Geomorphological mapping of the region of Nepenthes Mensae, Mars. Evidence of an ancient sea. 9th International Conference on Geomorphology (New Delhi, India). Poster presentation.

García-Arnay, Á., Fernández, S., de Pablo, M.Á., Gutiérrez, F., 2017. The dominant morphogenetic role of surface runoff in Licus Vallis, Mars: results from geomorphological and morphometric analyses. LXIII Sesión Científica de la Sociedad Geológica de España. (Elche, Spain). Oral presentation.

García-Arnay, Á., Gutiérrez, F., Fernández, S., 2018. Coastal-like features in Nepenthes Mensae, Mars, as paleowater-level indicators, and a terrestrial analog. 49th Lunar and Planetary Science Conference (The Woodlands, United States), Print-only abstract.

García-Arnay, Á., Gutiérrez, F., de Pablo, M.Á., Fernández, S., 2018. Characterization and interpretation of the fan-shaped and terrace-like features identified in Nepenthes Mensae, Mars. EGU General Assembly Conference (Vienna, Austria). Poster presentation.

Parenti, C., **García-Arnay, Á.**, Sevil, J., Gutiérrez, F., Baioni, D., Luzzi, E., Soldati, M., 2019. Closed depressions in Kotido Crater, Arabia Terra. Possible evidence of evaporite dissolution-induced sinkholes. VIII Italian Young Geomorphologists' Days (Milan and Veny Valley, Italy). Poster presentation.

Baioni, D., Gutiérrez, F., **García-Arnay, Á.**, Luzzi, E., Parenti, C., Sevil, J., Nesci, O., 2019. Two possible episodes of karstification in the Equatorial Layered Deposit within Kotido Crater, Arabia Terra, Mars. SGI-SIMP-SOGEI Conference (Parma, Italy). Oral presentation.

Parenti, C., Gutiérrez, F., Baioni, D., **García-Arnay, Á.**, Sevil, J., Luzzi, E., 2019. Collapse sinkholes attributable to evaporite dissolution in Kotido Crater, Arabia Terra. IAG Regional Conference on Geomorphology (Athens, Greece). Poster presentation.

ACKNOWLEDGEMENTS / AGRADECIMIENTOS

Me gustaría expresar mi más sentido agradecimiento a mi director y tutor de la Tesis, Francisco Gutiérrez Santolalla, Francho, por haber querido embarcarse conmigo en este apasionante viaje a Marte. Durante este tiempo, Francho ha sido para mí un referente tanto en lo científico, como en lo personal. Su entusiasmo, su esfuerzo incansable, su liderazgo, y su excelente talante y sentido del humor han sido para mí una fuente de inspiración. Contar con su apoyo permanente y refuerzo positivo ha sido fundamental para el buen desarrollo de esta Tesis, y para transmitirme confianza. Quiero también agradecerle que me haya integrado en el equipo, trabajando con los demás compañeros del grupo en las otras líneas de investigación, haciendo que pusiera, para variar, los pies en la Tierra. Me siento afortunado de que hayas sido mi director. ¡Mil gracias, Francho!

Manifestar también lo afortunado que me siento por haber formado parte de esta gran familia geomorfológica que ha sido mi grupo de investigación. Gloria y Jesús, quiero agradeceros el apoyo y confianza que siempre me habéis brindado, vuestra pasión por la enseñanza de la Geología, y por todos los momentos geniales que hemos vivido juntos. A mi compañero Jorge, por su compañerismo, su cercanía y por estar siempre dispuesto a ayudarme. A Domingo e Iván por su apoyo, orientación, y por todos los momentos que hemos compartido.

Quiero dedicarle un afectuoso agradecimiento a Susana del Carmen, por haber depositado su confianza en mí cuando llamé a su puerta para realizar mi TFG sobre un área de Marte. Susana, ¡ahí comenzó todo, en el lejano 2013! Muchísimas gracias por tu entusiasmo y apoyo permanentes, y por tu amistad. Deseo también expresar mi sincero agradecimiento a Miguel Ángel por haberme enseñado algunas de las principales técnicas en Geología Planetaria, por haber revisado algunas de las contribuciones científicas de esta Tesis, y por haberme dado a conocer la apasionante zona de Marte en la que llevo trabajando durante estos últimos 9 años.

Mi agradecimiento también a Olga Prieto-Ballesteros, mi supervisora durante la estancia de 3 meses en el Centro de Astrobiología (INTA-CSIC). Fue un placer y una gran oportunidad haber podido trabajar contigo en la región marciana de Coogoon Valles. Muchas gracias por haberme enseñado la apasionante técnica del análisis de datos espectrales de la superficie de Marte, que tan importante ha sido a la hora de caracterizar los posibles deltas en Nepenthes Mensae.

Mi piacerebbe anche ringraziare il Prof. Gian Gabriele Ori e il Dott. Andrea Pacifici per avermi accettato nell’International Research School of Planetary Sciences (Università degli Studi "G. D'Annunzio") a Pescara (Italia) per fare uno stage di ricerca di 3 mesi. È stata una gran esperienza e un piacere aver potuto condividere quel bel tempo con tutti voi e imparare tante cose nuove. Grazie mille anche ai miei colleghi Francesca Mancini e Adriano Tullo per il loro inestimabile aiuto per avermi mostrato come generare DEM partendo da immagini stereoscopiche della superficie di Marte, così come a Katherine, Gianluca, Davide, Mafalda e gli altri colleghi per il loro aiuto, stima e per i tanti momenti speciali trascorsi assieme.

Muchas gracias también a todos los revisores y editores que, con sus sugerencias y comentarios, han contribuido a mejorar la calidad científica del compendio de publicaciones que incluye esta Tesis Doctoral: Rogelio Linares y Rosana Menéndez, que revisaron el manuscrito enviado a la revista *Geogaceta*; Jim Head, Joel Davis, y un revisor anónimo, por su revisión del manuscrito presentado a la revista *Geomorphology*; y, finalmente, a los revisores anónimos que contribuyeron a la mejora del manuscrito enviado a la revista *Icarus*.

Expresar también mi alegría y agradecimiento a la Sociedad Española de Geomorfología (SEG) por el apoyo y reconocimiento a mi investigación al haberme concedido el 2º Premio a la "Mejor Publicación Científica de Socios Jóvenes de la SEG" por el artículo *Reconstructing paleolakes in Nepenthes Mensae, Mars, using the distribution of putative deltas, coastal-like features, and terrestrial analogs*.

Mi agradecimiento al Instituto Universitario de Ciencias Ambientales de Aragón (IUCA), del que he formado parte durante los últimos cinco años y, en especial, a Jacqueline Sambou, su responsable de comunicación, por su cercanía y profesionalidad, y por haber facilitado la difusión de algunos de los resultados de esta Tesis, de los que se hicieron eco después la prensa, radio y televisión. También quiero dar las gracias a Carmina Puyod, la coordinadora de la Unidad de Cultura Científica de la Universidad de Zaragoza, por haber pensado en mí como referente dentro de las Ciencias Planetarias en la Universidad.

Expresar mi gratitud y reconocimiento a todos aquellos profesores y profesoras que me han enseñado tantas cosas, e inculcado la pasión por la Geología a lo largo de estos años, tanto en el *Grado en Geología* de la Universidad de Oviedo, como durante el *Máster en Geología: Técnicas y Aplicaciones* en la Universidad de Zaragoza. Así como a los investigadores Juan Remondo, Ana Moreno, Mario Morellón y Blas Valero por su apoyo, afecto y acogida.

El Doctorado me ha brindado también la oportunidad de conocer a personas maravillosas como Alicia, Cristina y Úrbez, con quienes he tenido tantas conversaciones geniales durante nuestras míticas comidas en grupo, y vivido tantos momentos dentro y fuera del campus. Vuestro apoyo y amistad son el mejor regalo. Cómo no mencionar también a mis queridas Carlotta y Juliana, ¡nuestra amistad traspasa las fronteras de la distancia y el tiempo! Guardo también con cariño los momentos vividos con los compañeros que vinieron de estancia a nuestro grupo, en especial Sofia, Neri, Ergin, Esra y Xiao. Además, este viaje no hubiera sido igual sin la gran familia geológica que representan todos los amigos y compañeros del Departamento, en especial Ana, Fer, Elisa, Diego, Álvaro y Manu, entre otros muchos.

Mi profundo agradecimiento a mis "amigos-hermanos", Susana, Víctor y Juanjo, porque sois un faro de luz en mi vida, y un referente. A mis amigos Joel, Samu, Marina, Juanjo, Andrei y Jesús, de mi grupo cántabro, por tantos grandes momentos vividos durante nuestros viajes, y por vuestro apoyo. A mis queridas amigas asturianas Celia, compañera de batallas durante la carrera, y Ana. A mi querido sevillano, Antonio, por su cariño y por estar ahí siempre. A mis "mañicos" Dani, Carlos y Iulen, por haberme acogido tanto y tan bien durante estos años, ¡sois como mi segunda familia! A Ettore, por su amistad y por hacerme sentir como en casa en Italia.

A mi familia y, en particular, a mis padres, por su cariño y apoyo incondicionales, y por haber sembrado en mí, desde niño, la semilla de la curiosidad, y el gusto por la Ciencia, potenciando siempre mi gran afición: la Astronomía. Mamá, papá, sin vosotros nada de esto hubiera sido posible. Y, por supuesto, a mi chico, Alessandro, por su amor, paciencia y apoyo.

A todos vosotros, y a muchos otros más, mi más sincero agradecimiento.

Esta Tesis Doctoral ha sido financiada por un contrato de Personal Investigador Predoctoral en Formación (C237/2016) del Gobierno de Aragón y el Fondo Social Europeo, así como por el proyecto CGL2017-85045-P del Ministerio de Ciencia e Innovación del Gobierno de España. Agradecer también las ayudas recibidas (CB 5/18 y CB 2/21) por la Universidad de Zaragoza, la Fundación Bancaria Ibercaja y la Fundación CAI, en el marco de su programa “Ibercaja-CAI”, así como la beca concedida por la Comisión Europea, en el marco del programa “Erasmus+ KA 1”, para la realización de las estancias de investigación en el Centro de Astrobiología (INTA-CSIC, Madrid, 3 meses) y en la *International Research School of Planetary Sciences* (*Università degli Studi "G. D'Annunzio"*, Pescara, 3 meses).

«Somewhere, something incredible is waiting to be known».

Carl Sagan

Esta tesis se la dedico a mis padres.

INDEX

ABSTRACT

This PhD Thesis is focused on the mapping and characterization of the NW Terra Cimmeria and SE Nepenthes Mensae, as well as of the enclosed depressions within Kotido Crater (SW Arabia Terra). The main objectives are: (1) unravel the geological and geomorphological history of the complex and poorly explored NW Terra Cimmeria and SE Nepenthes Mensae, focusing on the different types of processes involved in their configuration, and (2) propose hypotheses regarding the origin and evolution of the closed depressions occurring within Kotido Crater.

The NW Terra Cimmeria and SE Nepenthes Mensae represent one of the most striking highland-lowland transitional zones on Mars, comprising two highly-contrasting geologic-geomorphic domains bounded by the 2-km-high dichotomy escarpment in the equatorial region of Mars. A comprehensive study largely based on cartographic work and complemented by multiple analyses (morphology, morphometry, crater densities, spectral data and radar profiles) has permitted us to produce, for the first time, a 1:1.45Million geologic-geomorphic map of this transitional zone (-5°31′–5°38′ N, 119°20′–129°55′ E), displaying nineteen geologic units and numerous geomorphic features. In addition, this study reveals that (1) the exposed geological record of this transitional zone formed over a long time span comprising from the Early Noachian to recent times, (2) the inferred compressional and extensional tectonic deformation shaped the landscape at least from the Late Noachian to Late Hesperian, and (3) extensional tectonics, which postdate the compressional deformation, has controlled the development and evolution of the dichotomy escarpment, the system of NW-SE-oriented basins that used to host paleolakes from the Late Noachian to Late Hesperian, and the fissure volcanism in their deepest areas. These findings provide insight into the fundamental morphogenetic role played by compressional and extensional tectonics on the configuration of the landscape in these regions, and represent a reference geologic-geomorphologic framework for future studies in this area and other sectors along the highland-lowland transitional zone of Mars.

The morphogenetic role played by liquid water on the configuration of this transitional zone has been examined in detail: A watershed analysis was carried out in the Licus Vallis watershed (NW Terra Cimmeria), the largest drainage basin in this study area, in order to characterize the morphometry of the stream network and assess the relative contribution of runoff and groundwater sapping erosion in valley formation. This work reveals that (1) this drainage basin exhibits the characteristics of a young watershed with a non-equilibrium profile, fourth-order streams, V-shaped valleys, very low drainage density, and a dendritic drainage pattern; and (2) erosion related to surface runoff appears to be the dominant erosional process involved in the formation of Licus Vallis. However, the presence of theatre-like valley heads seems to indicate that sapping erosion associated with springs may have played some role in the headward propagation of valleys. Moreover, a comprehensive study on 9 out of 24 fan-shaped deposits and 54 coastal-like benches identified in SE Nepenthes Mensae was carried out in order to determine the origin of these landforms and reconstruct the paleogeography of the inferred paleolakes. This analysis largely based on geomorphological mapping, morphological and morphometric analyses, spatial-altitudinal distribution relationships, crater counting, spectral analysis, and comparison with terrestrial analogs supports that (1) the fan-shaped and coastal-like benches are likely putative Gilbert-type deltas and paleoshore platforms, respectively, and (2) these features may be attributable to paleoshorelines developed along the margins of an

ancient inner sea or system of interconnected paleolakes indicating a mean water level at around −1,950 m, consistent with the mean elevation reported for the putative Arabia shoreline in the lowlands. These findings reveal the important morphogenetic role that the putative fluvio-lacustrine activity has played in the evolution of the Terra Cimmeria-Nepenthes Mensae transitional zone at least during Late Noachian to Late Hesperian times.

The identification of putative sinkholes on Mars may provide evidence of dissolution processes caused by underground circulation of liquid water and information on paleoclimatic and paleohydrological conditions. A detail study based on geomorphological mapping, morphometric analyses and spatial distribution relationships of 513 closed depressions developed on sulphate-bearing Equatorial Layered Deposits (ELDs) within Kotido Crater was performed in order to interpret the possible processes involved in their origin and the factors controlling the evolution of these depressions. This analysis reveals a number of features supporting that the depressions correspond to collapse sinkholes related to evaporite dissolution: (1) suitable topographic and litho-structural conditions for the development of a fracture-controlled epigene evaporite karst; (2) presence of open fissures at the foot of the scarped margins; (3) dimensions and frequency-size distributions comparable with those reported on Earth; and (4) spatial association with fractures. Some characteristics of the depressions indicate that they have been re-shaped and enlarged by wind erosion. The relatively fresh appearance of the depressions and the lack of impact craters suggest a poorly constrained Amazonian karstification phase in the region.

RESUMEN

Esta Tesis Doctoral se centra en la cartografía y caracterización del noroeste de Terra Cimmeria y sureste de Nepenthes Mensae, así como de las depresiones cerradas en el lecho del Cráter Kotido (suroeste de Arabia Terra). Los objetivos principales son: (1) desentrañar la historia geológica y geomorfológica del noroeste de Terra Cimmeria y sureste de Nepenthes Mensae, dos regiones complejas y poco exploradas, centrándonos en los diferentes tipos de procesos implicados en su configuración, y (2) proponer hipótesis sobre el origen y la evolución de las depresiones cerradas que se encuentran dentro del cráter Kotido.

El noroeste de Terra Cimmeria y el sureste de Nepenthes Mensae representan una de las zonas de transición entre las tierras altas y bajas más llamativas de Marte, comprendiendo dos dominios geológico-geomorfológicos muy diferentes, que están divididos por el escarpe de la dicotomía, de 2 km de altura, en la región ecuatorial del planeta. Un estudio exhaustivo basado, en gran medida, en trabajo cartográfico y complementado por múltiples análisis (morfología, morfometría, densidades de cráteres, datos espectrales y perfiles de radar) nos ha permitido elaborar, por primera vez, un mapa geológico-geomorfológico, en escala 1:1.450.000, de esta zona de transición (-5°31'-5°38' N, 119°20'-129°55' E), que muestra diecinueve unidades geológicas y numerosos rasgos geomorfológicos. Además, este estudio revela que (1) el registro geológico expuesto de esta zona de transición se formó a lo largo de un extenso período de tiempo, que abarca desde el Noéico temprano hasta tiempos recientes, (2) la deformación tectónica compresiva y extensiva dio forma al paisaje, al menos desde el Noéico tardío hasta el Hespérico tardío, y (3) la tectónica extensiva, que es posterior a la deformación compresiva, ha controlado el desarrollo y la evolución del escarpe de la dicotomía, el sistema de cuencas orientadas al noroeste-sureste, que albergaron paleolagos desde el Noéico tardío hasta el Hespérico tardío, y el vulcanismo de tipo fisural en sus zonas más profundas. Estos hallazgos dan cuenta del papel morfogenético fundamental que ha desempeñado la tectónica compresiva y extensiva en la configuración del paisaje en estas regiones, y representan un marco geológico y geomorfológico de referencia para futuros estudios en esta área y en otros sectores a lo largo de la zona de transición entre las tierras altas y bajas de Marte.

Se ha examinado en detalle el papel morfogenético que ha desempeñado el agua líquida en la configuración de esta zona de transición: Se ha llevado a cabo un análisis de la cuenca hidrográfica de Licus Vallis (noroeste de Terra Cimmeria), la mayor cuenca de drenaje en esta área de estudio, con el fin de caracterizar la morfometría de la red de valles y evaluar la contribución relativa de la escorrentía superficial y de la erosión por *sapping* en la formación de los valles. Este trabajo revela que (1) esta cuenca de drenaje presenta las características de una cuenca joven con un perfil en desequilibrio, canales de cuarto orden, valles en forma de V, una densidad de drenaje muy baja y un patrón de drenaje dendrítico; y (2) la escorrentía superficial parece haber sido el proceso erosivo dominante implicado en la formación de los valles de Licus Vallis. Sin embargo, la presencia de cabeceras de valle en forma de teatro parece indicar que la erosión por *sapping* puede haber desempeñado algún papel en la erosión remontante de los valles. Además, se ha realizado un exhaustivo análisis de 9 de los 24 depósitos en forma de abanico y 54 terrazas identificados en el sureste de Nepenthes Mensae con el fin de determinar el origen de estas morfologías y reconstruir la paleogeografía de los paleolagos inferidos. Este análisis, basado en gran medida en cartografía geomorfológica, análisis morfológicos y morfométricos, relaciones de distribución espacio-altitudinal, recuento

de cráteres, análisis espectral y la comparación con análogos terrestres, indica que (1) los depósitos en forma de abanico y las terrazas son, probablemente, posibles deltas de tipo Gilbert relictos y antiguas plataformas costeras, respectivamente, y (2) estas morfologías pueden ser atribuidas a paleocostas desarrolladas a lo largo de los márgenes de un antiguo mar interior o sistema de paleolagos interconectados que indican un nivel de agua medio en torno a los −1.950 m, consistente con la elevación media estimada para la posible línea de costa de Arabia en las tierras bajas. Estos hallazgos revelan el importante papel morfogenético que la actividad fluvio-lacustre ha desempeñado probablemente en la evolución de la zona transicional de Terra Cimmeria-Nepenthes Mensae, al menos desde el Noéico tardío al Hespérico tardío.

La identificación de posibles dolinas en Marte puede aportar pruebas sobre los procesos de disolución causados por la circulación subterránea de agua líquida, así como informar sobre las condiciones paleoclimáticas y paleohidrológicas presentes en el pasado. Se ha llevado a cabo un detallado estudio basado en cartografía geomorfológica, análisis morfométricos y relaciones de distribución espacial de 513 depresiones cerradas desarrolladas en los Depósitos Estratificados Ecuatoriales (ELDs, según sus siglas en inglés), ricos en sulfatos, en el lecho del Cráter Kotido con el fin de interpretar los posibles procesos implicados en su origen, así como los factores que han controlado la evolución de estas depresiones. Este análisis revela una serie de características que apuntan a que las depresiones corresponden a dolinas de colapso relacionadas con la disolución de evaporitas: (1) condiciones topográficas y litoestructurales adecuadas para el desarrollo de un karst evaporítico epigénico controlado por fracturas; (2) presencia de fisuras abiertas al pie de los márgenes escarpados; (3) dimensiones y distribuciones de tamaño-frecuencia comparables con las observadas en la Tierra; y (4) asociación espacial con fracturas. Algunas características de las depresiones indican que han sido remodeladas y ampliadas por la erosión eólica. El aspecto relativamente fresco de las depresiones y la ausencia de cráteres de impacto sugieren una fase de karstificación probablemente durante el período Amazónico.

CHAPTER

1. Background, objectives and outline of the Thesis

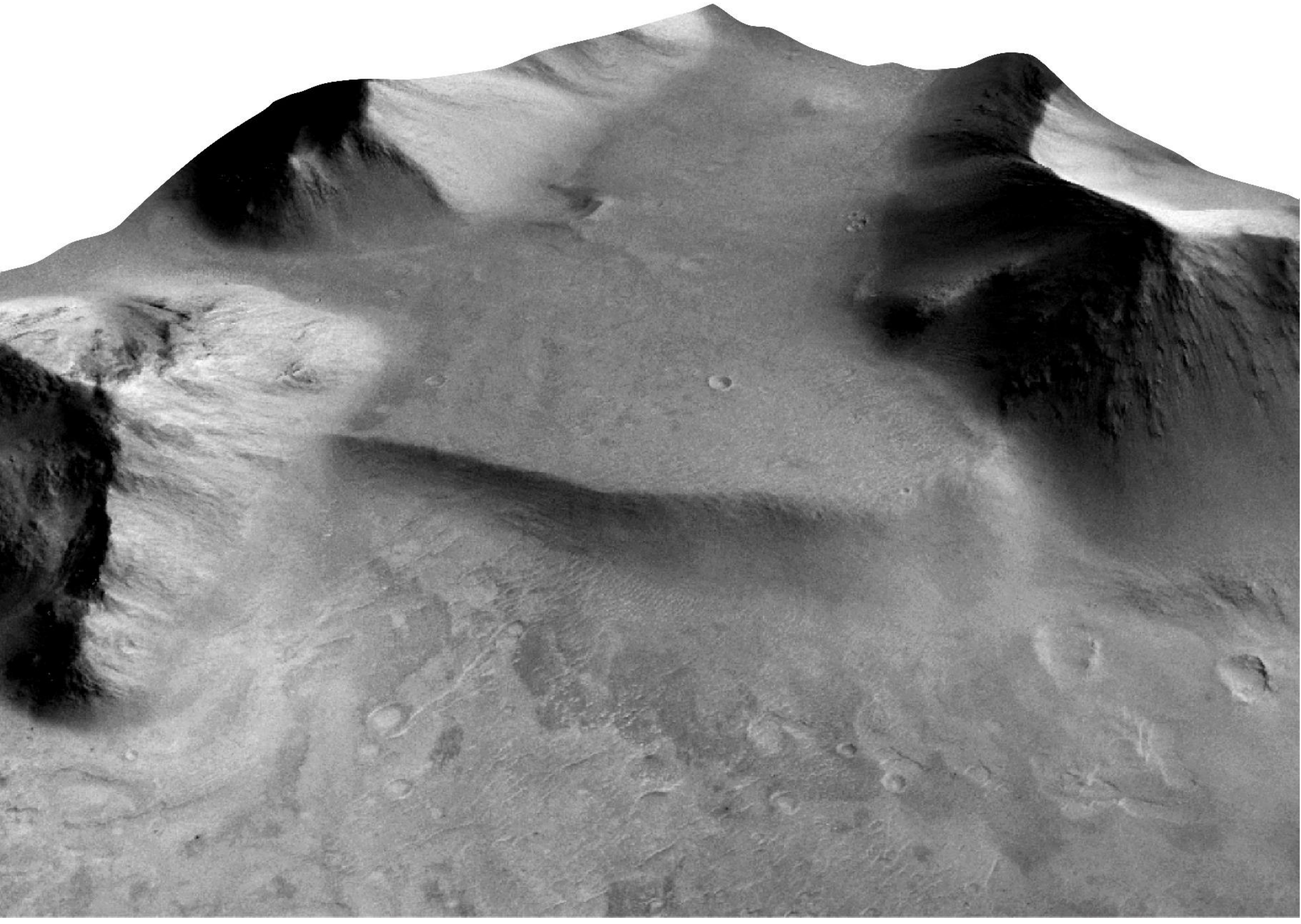

1.1 BACKGROUND

1.1.1 The highland-lowland transitional zone

The crustal dichotomy (McCauley et al., 1972) is one of the most prominent geomorphic features on the surface of Mars (Solomon et al., 2005). This megalandform, probably formed during the early Mars (Tanaka et al., 1992a), circumscribes the planet bounding two contrasting geologic and geomorphic domains: the ancient, densely cratered and rough highland plateaus in the south, and the younger, sparsely cratered and relatively smooth lowland plains in the north (Morgan et al., 2009).

Studies dealing with this boundary have proposed various endogenic and exogenic interpretations to explain the origin of the dichotomy (McGill and Squyres, 1991), while it remains as an unresolved problem (e.g., Andrews-Hanna et al., 2008; Golabek et al., 2011). The main endogenic hypotheses include: (1) long-wavelength mantle convection resulting in large-scale upwelling (Zhong and Zuber, 2001; Roberts and Zhong, 2006; Ke and Solomatov, 2006), (2) long-wavelength "cumulate overturn" of a stratified magma ocean resulting from the crystallization of an early magma ocean (Elkins-Tanton et al., 2005), and (3) an early plate tectonics phase involving the creation of a thin crust in the northern hemisphere from relict spreading centers, with the crustal dichotomy representing a passive margin (Sleep, 1994). Several exogenic (i.e., impact-related) hypotheses have also been proposed: (1) a single "mega-impact" event responsible for the creation of the "Borealis basin" (Wilhelms and Squyres, 1984), (2) the impact "megadome" hypothesis, according to which the melt generated by a giant impact overfilled the impact basin to form the highlands (Reese et al., 2011), and (3) multiple impact depressions merged into a large basin forming the lowlands in the northern hemisphere (Frey et al., 1986; Frey and Shultz, 1988). Although the origin of the dichotomy remains as an open issue, it seems probable that multiple processes may have operated in conjunction to form this major geomorphic feature (Reese et al., 2010), which may have been subsequently modified by tectonic, fluvial, glacial, eolian, and mass wasting processes (Watters and Robinson, 1999; Tanaka et al., 2005).

The topography of the highland-lowland boundary varies laterally, ranging from an escarpment up to 3 km in local relief (Irwin et al., 2004) in the region of Nilosyrtis Mensae (Levy et al., 2007), to gently-sloping surfaces with no obvious scarp in northern Arabia Terra (McGill, 2000). The geomorphic expression of the highland-lowland transition in Aeolis Mensae (e.g., Irwin et al., 2004; Irwin et al., 2005) is similar to that of the region of Nilosyrtis Mensae. Both regions are characterized by the occurrence of a remarkable dichotomy escarpment (~2 km in local relief) and closed depressions in the lowlands interrupted by mesas and knobs composed of materials of the highland plateau. According to Irwin et al. (2004), the latter landforms probably correspond to residual reliefs resulting from fracture-controlled differential erosion acting along the edge of the retreating escarpment. In these regions the highland residuals north of the escarpment show an increasing degree of degradation, grading northward from mesas to sparse knobs (Irwin et al., 2004). The approximate alignment of mesa margins, buttes and knobs in Nilosyrtis Mensae, as well as the straightness and orientation of valleys, mostly parallel to the dichotomy escarpment, have been ascribed to the occurrence of Noachian-aged grabens along the crustal dichotomy (Levy et al., 2007). These transitional provinces show various morpho-tectonic features such as fracture-controlled linear valleys known as fretted valleys, extensional troughs forming chains of closed depressions in the lowlands, and lobate scarps ascribable to thrust faults in the adjacent highlands (McGill and Dimitriou, 1990; Watters, 2003a, 2003b; Watters and McGovern, 2006).

As illustrates a number of previous works, studies on the upland-lowland transition zones of Mars offer the opportunity for gaining insight into the endogenic and exogenic processes involved in the origin and evolution of the dichotomy escarpment and nearby areas (e.g., Andrews-Hanna et al., 2008; Golabek et al., 2011), as well as improving our understanding of the early Mars (e.g., McGill and Dimitriou, 1990; Watters, 2003a, 2003b; Watters and McGovern, 2006; Levy et al., 2007). In this Thesis we present a comprehensive geologic-geomorphic study in one of the most highly contrasting transitional zones between the highlands and lowlands on Mars: the complex region comprising the NW Terra Cimmeria and SE Nepenthes Mensae, which remains as a poorly explored area (e.g., Skinner and Tanaka, 2018). Its geomorphic expression is similar to that displayed in Nilosyrtis Mensae and Aeolis Mensae, including two contrasting geological and geomorphological domains bounded by a remarkable 2-km-high escarpment. The analyzed area corresponding to the Terra Cimmeria-Nepenthes Mensae Transitional Zone (CNTZ) covers about 415,000 km^2 (equivalent to ~71% of the Iberian Peninsula).

This transitional zone has been covered by multiple global and regional geologic maps produced by the United States Geological Survey (USGS, U.S. Department of the Interior) (e.g., King, 1978; Scott and Carr, 1978; Hiller, 1979; Greeley and Guest, 1987; Tanaka et al., 1992b; Tanaka et al., 2005; Tanaka et al., 2014). Nevertheless, the scale of these maps precludes the representation of important features, and as a result there is a lack of detailed cartographic works providing a comprehensive geologic-geomorphic framework for this transitional zone. Therefore, the production of more detailed geological-geomorphological maps can be considered as a valuable and innovative contribution. Recently, Skinner and Tanaka (2018) produced the regional-scale geologic map of the transition zone between Terra Cimmeria and Utopia Planitia, which is located northwest of our study area. Due to its proximity, this map provides a geological framework with which to compare our study.

1.1.2 Evidence of fluvial and coastal activity on Mars

Numerous geomorphological (e.g., fluvial- and coastal-like landforms) and geochemical (e.g., phyllosilicate-bearing layered deposits) lines of evidence strongly suggest that liquid water was once abundant on the surface of Mars and played an important morphogenetic role during the early stages of its history (e.g., Baker, 2001; Bibring et al., 2006; Carr, 2012), as well as during relatively short periods in more recent times (e.g., Malin and Edgett, 2000), as supported by the large outflow channels developed during the Hesperian and Amazonian periods, attributable to the catastrophic release of large amounts of groundwater (Andrews-Hanna and Phillips, 2007). Well-developed valley networks carved into the Noachian highlands, such as those located in NW Terra Cimmeria, may be the result of past fluvial erosion (e.g., Irwin et al., 2005), and/or a combination of both runoff and groundwater sapping erosion (Malin and Carr, 1999; Harrison and Grimm, 2005).

The occurrence of fan-shaped deposits attributable to deltas and alluvial fans have been widely reported on Mars (e.g., Kleinhans, 2005; Di Achille and Hynek, 2010a; Rivera-

Hernández and Palucis, 2019; Morgan et al., 2022). These landforms are located at the mouth of stream networks where the flow becomes unconfined, such as at impact craters (e.g., Goudge et al., 2015), or along the highland-lowland dichotomy escarpment (e.g., Fassett and Head III, 2008). Some of the best-known delta-like features on Mars are probably the Jezero and the Eberswalde deltas, which show multiple lobes carved by clearly visible distributary channels with a meandering pattern (Wood, 2006; Pondrelli et al., 2008; Schon et al., 2012).

The identification of putative deltas supports the existence in the past of long-lived liquid water masses forming ancient lakes, or even a possible ocean developed in the Martian low-lying plains (e.g., Head III et al., 1999; Carr and Head III, 2003; Di Achille and Hynek, 2010b; Fawdon et al., 2018; Davis et al., 2022). Laterally continuous benches with nearly consistent elevation located along the margins of depressions and lowlands, and very probably associated with ancient masses of water, have been interpreted as erosional and/or aggradational coastal landforms attributable to paleoshorelines (e.g., Parker et al., 1993; Ghatan and Zimbelman, 2006).

In the last few years, studies carried out in this Thesis and by other authors have highlighted the instrumental role played by liquid water on the shaping of NW Terra Cimmeria and SE Nepenthes Mensae (e.g., Goudge and Fassett, 2018; Rivera-Hernández and Palucis, 2019; García-Arnay and Gutiérrez, 2020). In particular, fan-shaped aggradational landforms ascribed to Gilbert-type deltas and alluvial fans have been identified in SE Nepenthes Mensae (e.g., Irwin et al., 2005; de Pablo and Pacifici, 2008; García-Arnay, 2016; García-Arnay et al., 2018a, 2018b; Rivera-Hernández and Palucis, 2019; García-Arnay and Gutiérrez, 2020). Furthermore, benches interpreted as putative shore platforms were also described along the margins of the low-lying plains and residual reliefs associated with the belt of closed depressions distributed along the foot of the dichotomy escarpment in SE Nepenthes Mensae, supporting the past occurrence of lakes in this region (García-Arnay and Gutiérrez, 2020).

1.1.3 Karst-like processes on Mars

The occurrence of karst landforms has been hypothesized in many regions of Mars since the first images of the Viking Orbiter became available (Schaeffer, 1990; Kargel et al., 2004; Preuschmann et al., 2006; Wyrick et al., 2004). The Martian surface contains soluble evaporite-bearing formations in numerous regions, as indicated by the detection of sulphate minerals on the surface from spectral data collected by several spectroscopic instruments onboard different missions (e.g., Bibring et al., 2006; Murchie et al., 2007).

According to Johnson (2008), four basic conditions are required for the development of evaporite karst: (1) the presence of soluble evaporitic sediments; (2) a supply of liquid water unsaturated with respect to the evaporitic minerals; (3) an outlet whereby the solution (or brine) can scape; and (4) a gradient driving water to flow through the system. All these conditions can be found on Mars. Smith et al. (2006) indicated that Mars hosts environments with evaporite sediments favorable for karst development and has a weaker gravitational field that should allow the formation of subsurface cavities larger than those occurring on Earth before their collapse. The presence of liquid water at the surface and in the subsurface has been widely demonstrated (e.g., Carr, 2012; Schon et al., 2012; García-Arnay and Gutiérrez, 2020). Suitable subsurface flow conditions can be assured by the presence of permeability features (e.g., fractures) and hydraulic gradients largely governed by the topography.

Unravelling the origin of closed depressions on the surface of Mars is often a challenging geomorphological problem. Their formation may be related to several genetic mechanisms acting individually or in combination (e.g., Waltham, 1989), among which are (1) the lowering of the ground by preferential surface dissolution at specific locations (e.g., solution sinkholes), and (2) the subsidence due to mass and/or volume depletion in the subsurface (e.g., subsidence sinkholes, thermokarst depressions, collapse calderas, sinkholes related to the collapse of lava tubes, compaction/consolidation-related depressions). Karst sinkholes are postulated as useful lithological indicators and valuable markers of past paleoclimatic and paleohydrological conditions, since dissolution requires the presence of liquid water.

Schaeffer (1990), using low-resolution images, distinguished three major localities in the northern plains of Mars (Arcadia Planitia, western Utopia Planitia, and eastern Acidalia Planitia) with "thumbprint" terrain riddled by depressions that could be related to differential solution of extensive carbonate deposits in low-lying areas. Studies based on high-resolution images provide strong evidence of the presence of sinkholes developed on Martian evaporite sediments (e.g. Baioni et al., 2009; Baioni and Wezel, 2010; Flahaut et al., 2015; Baioni and Sgavetti, 2013; Baioni and Tramontana, 2017), which are widely regarded as the main diagnostic surface landform in karst areas (Ford and Williams, 2007). Similar landforms have been documented in Meridiani Planum (Baioni, 2019), Tyrrhena Terra (Baioni and Tramontana, 2016), Coprates Chasma (Baioni et al., 2011), Tithonium Chasma (Baioni, 2013) and Juventae Chasma (Baioni and Tramontana, 2017). The origin and factors controlling the evolution of the sinkhole-like depressions developed on evaporite-bearing layered deposits on the floor of Kotido Crater (SW Arabia Terra) have been analyzed in this Thesis (Parenti et al., 2020).

1.2 OBJECTIVES

This PhD Thesis seeks to (1) unravel the geological and geomorphological history of the NW Terra Cimmeria and SE Nepenthes Mensae, focusing on the different types of processes involved in the configuration of these equatorial regions, and (2) propose hypotheses regarding the origin and evolution of the closed depressions occurring within Kotido Crater in SW Arabia Terra. More specifically, the main aims leading to the development of this PhD Thesis have been the following:

- Producing the first regional-scale geological-geomorphological map (1:1.45M) of the transitional zone between NW Terra Cimmeria and SE Nepenthes Mensae in order to (1) identify, describe, interpret and correlate the different geologic units and geomorphic features of this transitional zone, analyzing their geometrical relationships and estimating their age to reconstruct the geological and geomorphological history from the Noachian period to recent times, and (2) provide insight into the endogenic and exogenic processes involved in the configuration of the central sector of this transitional zone (representing about 35% of total mapped surface), focusing on the formation of the system of closed depressions (paleolake basins), the evolution of the dichotomy escarpment, and the reconstruction of its long-term history.

- ❖ Reconstructing the paleohydrology in NW Terra Cimmeria and SE Nepenthes Mensae, largely based on detailed geomorphological mapping, focusing on (1) the morphometric characteristics of the stream network in the catchment of Licus Vallis (NW Terra Cimmeria), which is the largest drainage basin in the study area, in order to gain insight into the morphogenetic role played by liquid water in the past, assessing the relative contribution of runoff and groundwater sapping erosion in valley formation, and (2) the morphometry, spatial distribution, surface composition, chronological ascription and origin of fan-shaped deposits and coastal-like benches in SE Nepenthes Mensae, reconstructing the paleogeography of the inferred paleolakes and proposing a selection of terrestrial analogs.

- ❖ Analyzing the morphometry and distribution patterns of the sinkhole-like depressions and fractures developed on sulphate-bearing layered deposits within the Kotido Crater, as well as their spatial relationships with other features, in order to interpret the possible morphogenetic processes involved in their origin and the factors controlling the evolution of these depressions.

1.3 OUTLINE OF THE THESIS

This PhD Thesis is composed of 8 chapters: the present chapter (Chapter 1) states the objectives of the Thesis and provides an overview based on publications related to (1) the different hypotheses concerning the origin of the crustal dichotomy boundary and spatially-related areas, (2) the catalogue of geological maps including the NW Terra Cimmeria and SE Nepenthes Mensae, (3) the occurrence of fluvial- and coastal-like landforms on the Martian surface, and (4) studies on the factors leading to the origin and evolution of sinkhole-like depressions on Mars. Chapter 2 presents the geographical and geological context of the two study areas. Chapter 3 describes the different data and methods used to carry out this research.

The main contributions of this Thesis are presented from Chapters 4 to 6, of which Chapter 4 includes two scientific papers currently under review submitted to SCI international journals, while Chapters 5 and 6 comprise the results published in three peer-reviewed scientific papers:

- ❖ Chapter 4 comprises the results presented in two scientific papers currently under review related to the geological and geomorphological mapping, and endogenic and exogenic processes involved in the formation and evolution of the transitional zone between NW Terra Cimmeria and SE Nepenthes Mensae on Mars.

- ❖ Chapter 5 presents the characterization of the drainage network in the Licus Vallis watershed, focusing on the contribution of runoff and groundwater sapping erosional processes in its configuration, and reconstruction of paleolakes in SE Nepenthes Mensae from the distribution of possible deltas and coastal-like landforms. These results are presented on García-Arnay et al. (2018a) and García-Arnay and Gutiérrez (2020).

- Chapter 6 assesses the controlling factors involved in the formation and development of the enclosed depressions in the floor of Kotido Crater (SW Arabia Terra). These results are presented on Parenti et al. (2020).

Chapter 7 summarizes and analyzes the main results achieved, and outlines the ongoing research and potential further investigations. Finally, the key results obtained in this Thesis are summarized in Chapter 8.

In addition, one Annex has been attached at the end of the manuscript, containing the geologic-geomorphic map of the Terra Cimmeria-Nepenthes Mensae transitional zone on Mars, displayed in a sheet at 1:1.45M in A1 format (594 x 841 mm).

CHAPTER

2. Study areas

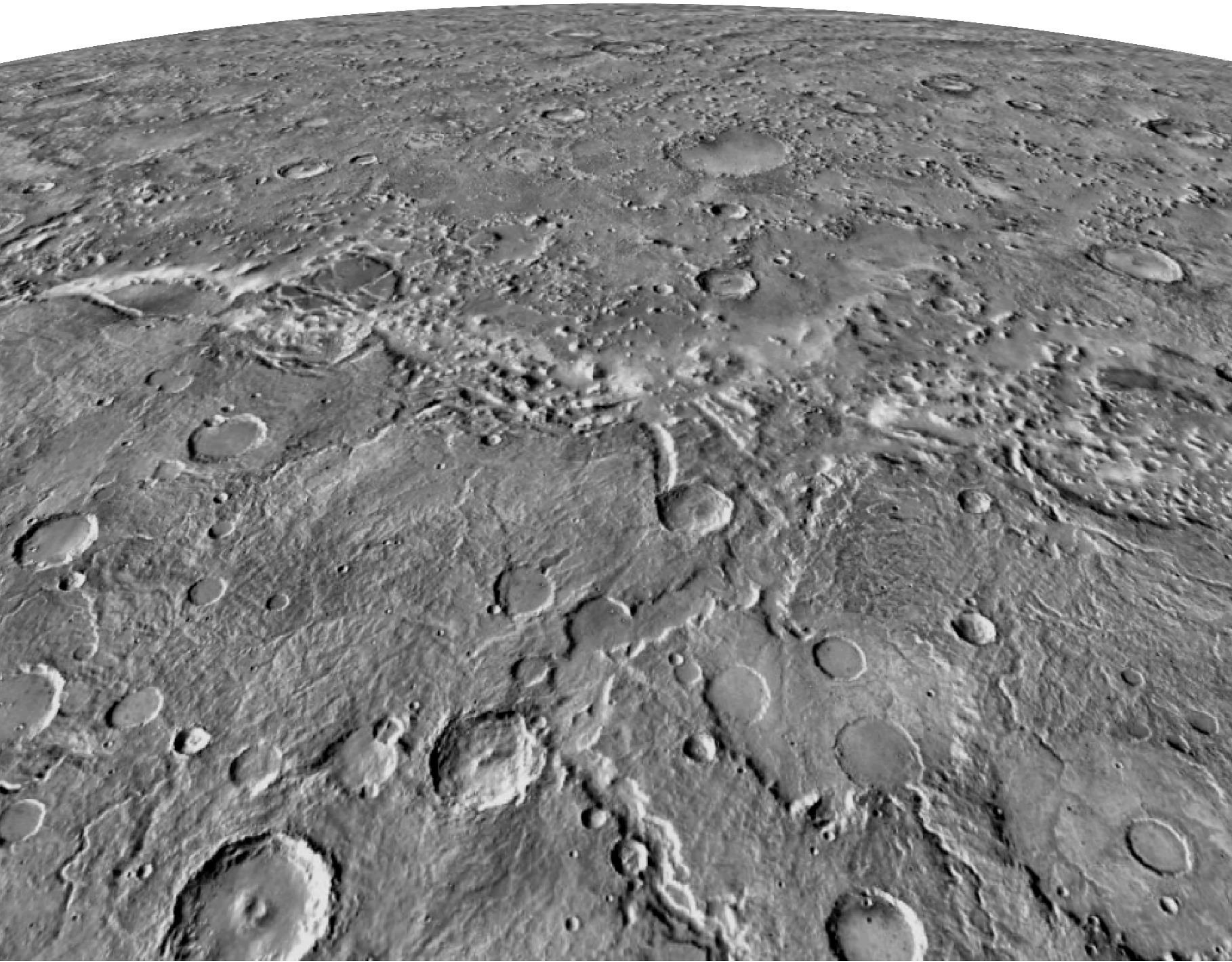

Two distinct equatorial areas located in opposite hemispheres of Mars were selected: (1) the NW Terra Cimmeria and SE Nepenthes Mensae, in the eastern hemisphere, and (2) the east-central sector of the floor of Kotido Crater situated in the SW Arabia Terra, in the western hemisphere.

2.1 TERRA CIMMERIA-NEPENTHES MENSAE TRANSITIONAL ZONE

The Terra Cimmeria-Nepenthes Mensae Transitional Zone (CNTZ) comprises two contrasting geological-geomorphological domains bounded by the dichotomy escarpment, in the equatorial region of Mars (Fig. 2.1). The sector of the CNTZ analyzed corresponds to the northwest part of Terra Cimmeria, and the southeast zone of Nepenthes Mensae (-5°31’–5°38’ N, 119°20’–129°55’ E).

Terra Cimmeria forms part of the highland province, south of the dichotomy boundary, and was mapped as a “Middle Noachian highland unit” (mNh) characterized by moderately to heavily degraded terrains formed by undifferentiated impact, volcanic, fluvial and basin-fill materials, according to the most recent global geological map of Mars (Tanaka et al., 2014). The southernmost sector of Terra Cimmeria within the study area displays the highest elevations, decreasing northward to form the plateau situated south of the dichotomy. This heavily cratered region has been tectonically contracted, as indicated by the presence of numerous lobate scarps, wrinkle ridges and ridge crests (e.g., Watters and Robinson, 1999). It is also dissected by ancient V-shaped fluvial valleys (e.g., Irwin and Howard, 2002), which mouths are located along the dichotomy escarpment, with a local relief of around 2 km. The valleys seem to be locally disrupted by compressional tectonic deformation, as suggests the occurrence of defeated and beheaded channels associated with lobate scarps. They also show a clear structural control in the vicinity of the dichotomy, following the orientation of morpho-structural troughs both subparallel and subperpendicular to the escarpment, probably generated by extensional tectonic deformation and/or lateral spreading along the dichotomy. Licus Vallis, which is the main ancient fluvial valley in the study area, shows an apparently poorly-evolved watershed, as suggested by its convex hypsometric curve and a very low drainage density (García-Arnay et al., 2018a). According to García-Arnay et al. (2018a), sapping erosion may also have contributed to the headward expansion of valleys, as supported by the existence of amphitheater-shaped valley heads. The paired terraces and knickpoints observed within this and other valleys seem to support base-level variations in the mouth area of the watersheds and/or rejuvenation by vertical tectonic movements (Goudge and Fassett, 2018). The majority of the valley networks, including Licus Vallis, show moderately preserved fan-shaped deposits at their mouths, most of them interpreted as Gilbert-type deltas and alluvial fans (e.g., Irwin et al., 2005; de Pablo and Pacifici, 2008; García-Arnay et al., 2018a, 2018b; Rivera-Hernández and Palucis, 2019; García-Arnay and Gutiérrez, 2020).

The terrains north of Terra Cimmeria correspond to the region of Nepenthes Mensae, which is part of the transitional province north of the dichotomy. It was mapped as the “Hesperian and Noachian transition unit” (HNt) and described as Noachian impact breccias, volcanic rocks, and aprons formed by mass-wasted deposits during the Hesperian period (Tanaka et al., 2014). This region displays two distinct areas: (1) tectonically-contracted plateaus with frequent eolian erosional landforms, and (2) a chain of interconnected NW-SE-trending closed depressions at the foot of the dichotomy escarpment in the knobby terrain (Irwin et al., 2004). These closed depressions together with the dichotomy escarpment are probably related to extensional deformation (Watters, 2003a; Watters and McGovern, 2006). Both areas display numerous residual reliefs (knobs and mesas) formed by highland materials. The presence of morpho-structural elements along the dichotomy may have also controlled the erosion pattern of the highlands, as suggested by fracture-controlled erosional troughs displayed by residual reliefs such as mesas. The fan-shaped deposits and coastal-like benches associated with the closed depressions, interpreted as putative Gilbert-type deltas and paleoshore platforms, respectively (García-Arnay and Gutiérrez, 2020), may be attributable to landforms developed along the shores of interconnected paleolakes, probably formed from the Late Noachian to Late Hesperian.

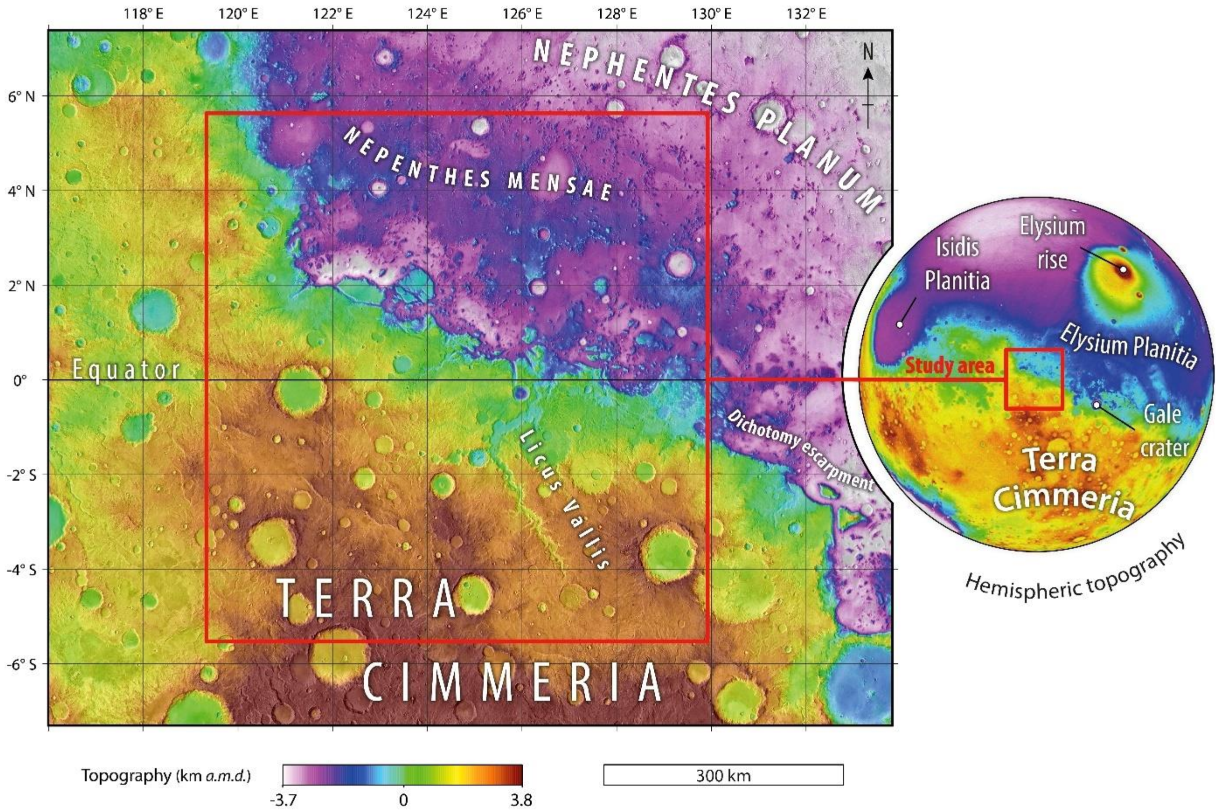

Fig. 2.1. (Left) Colorized elevation model (km above Martian datum, a.m.d.) derived from HRSC-MOLA blended data over a mosaic of THEMIS-IR day images, with the CNTZ framed by the red rectangle. (Right) Location of the CNTZ in the eastern hemisphere of Mars.

2.2 KOTIDO CRATER

The analyzed area is located in the east-central sector of Kotido Crater (centered at 9.1°W, 1°N), situated in the SW Arabia Terra (Fig. 2.2). This equatorial region, characterized by a gently sloping topography, represents a gradual transition between the highlands and lowlands of Mars, in contrast with the sharp dichotomy observed in the CNTZ. The Kotido Crater is one of the many impact craters that hosts Equatorial Layered Deposits (ELDs). This is the informal term used to collectively designate the light-toned layered deposits found in a wide range of geomorphic settings within the equatorial regions of Mars (e.g., Okubo et al., 2009; Pondrelli et al., 2019). The stratigraphic distribution of the ELDs ranges from the Noachian-Hesperian transition to the Early Hesperian (e.g., Pondrelli et al., 2005), and according to spectral data they include monohydrated and/or polyhydrated sulphates (e.g., Gendrin et al., 2005; Bibring et al., 2006; Mangold et al., 2008). These sulphate-bearing sediments postdate Noachian argillaceous units and are thought to record a major environmental change in the history of Mars (Bibring et al., 2006).

The Kotido Crater is an impact crater 40 km across and around 1 km deep, from the rim to the floor (see Fig. 2.2). The substratum in which the Kotido Crater was formed and that underlies the ELDs is formed by rocks of the "Middle Noachian highland unit" (mNh) (Tanaka et al., 2014). The ELDs correspond to the "Undivided etched unit" (HnMeu) mapped by Hynek and Di Achille (2017) within the crater and in the nearby inter-crater plains. These authors indicate that the surfaces of unit HnMeu are "tabular to rugged and intensely affected by eolian erosion". Pondrelli et al. (2019), using the equations of Garvin et al. (2003) and Robbins and Hynek (2013), reconstructed the original geometry of the crater, inferring a rough thickness estimate for its sedimentary fill of 1 km. Pondrelli et al. (2019) mapped the ELDs of Kotido Crater at 1:20,000 scale, where they show significant variability and good exposure conditions with limited dust cover. They analyzed their characteristics (i.e., morphology, texture, composition) and architectural features in order to infer the depositional environment and processes.

The ELDs exposed in Kotido Crater consist of interbedded light- and dark-toned deposits, locally with interspersed intermediate-tone mounds (Pondrelli et al., 2019). The light-toned sediments are composed of well-stratified layers or packages of meter-scale thickness forming undulated surfaces. The dark-toned layers are made of more erodible material with smoother topographic texture that tend to occur in topographically lower areas. The attitude of the ELDs of Kotido Crater show spatial variations. In the central sector of the crater they mainly lie horizontally or show gentle dips, whereas in the marginal areas are affected by gentle folds.

Pondrelli et al. (2019) reported and illustrated the following morphological features in the layered deposits of Kotido Crater: (1) Mounds in lateral continuity with the layered deposits, displaying a rounded depositional geometry, occasionally with an apical pit, and commonly forming alignments. (2) Straight to sinuous scarps, mesas, buttes and cuestas controlled by the more resistant horizontal or dipping light-toned beds, acting as caprocks. (3) Elongated yardangs with a prevalent NE trend generated by eolian erosion. (4) Kilometer-scale linear layered ridges made up of resistant material and locally in spatial association with the mounds. These structurally controlled features are interpreted as fissure ridges formed by the upwelling of material through fractures or faults. According to Pondrelli et al. (2019), these lineaments show a roughly radial or circular distribution, suggesting that they are influenced by fracturing associated with the formation of the impact crater. (5) Numerous closed depressions that riddle the ELDs, which are the focus of this investigation. Regarding these depressions, Pondrelli et al. (2019) indicate that their "characteristics are comparable both in shape and size with dissolution-related morphologies typical, although not exclusive, of evaporite rocks". They also point that "eolian erosion has been invoked to explain similar morphologies in the etched terrains of Arabia Terra". Pondrelli et al. (2019) interpret that the ELDs of Kotido Crater were deposited in a playa-lake environment with spring mounds and fissure ridges fed by salt-rich pressurized groundwater. Sedimentation was characterized by alternating periods of evaporitic (light-toned layers) and fine-grained detrital sedimentation (dark-toned layers). They propose that the gentle dips and antiforms observed in the strata could be related to deposition over an inherited topography (i.e., sediments draping a paleorelief) or postsedimentary deformation. A similar interpretation was proposed by Pondrelli et al. (2015) for the ELDs occurring inside and around the nearby Firsoff Crater. Other authors relate ELDs occurring all over the region to deposition in groundwater discharge areas (Ori and Baliva, 1999; Malin and Edgett, 2000; Rossi et al., 2008; Oehler and Allen, 2008; Pondrelli et al., 2011; Franchi et al., 2014; Luzzi et al., 2018). Andrews-Hanna et al. (2010) proposed that oscillations of the regional groundwater table may have played an important role in the deposition of ELDs.

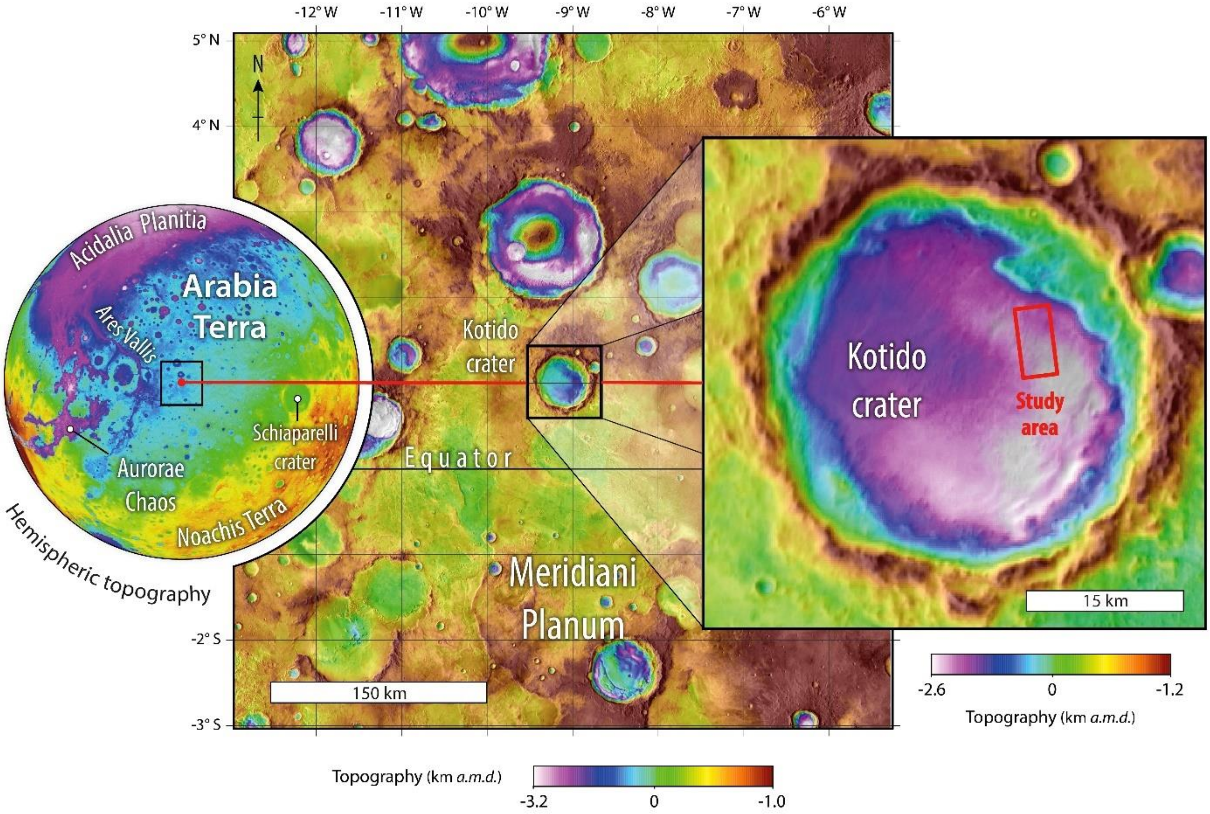

Fig. 2.2. (Left) Location of Kotido Crater in the western hemisphere of Mars indicated by the red point. The black box marks the position of the regional topography shown in the center of the figure. (Center) Colorized elevation model (km above Martian datum, a.m.d.) derived from HRSC-MOLA blended data over a mosaic of THEMIS-IR day images, with Kotido Crater indicated by the black box. (Right) Wide view of the topography of Kotido Crater with the situation of the study area within the crater floor framed by a red rectangle.

The ELDs in the study area of Kotido Crater are unconformably overlain by dark-toned dune fields, mainly concentrated in topographic lows, and slope deposits with distinctive rockfalls. The latter are typically associated with steep-slopes controlled by resistant light-toned deposits (caprock), including the scarped margins of the closed depressions and residual reliefs.

CHAPTER

3. Data and Methods

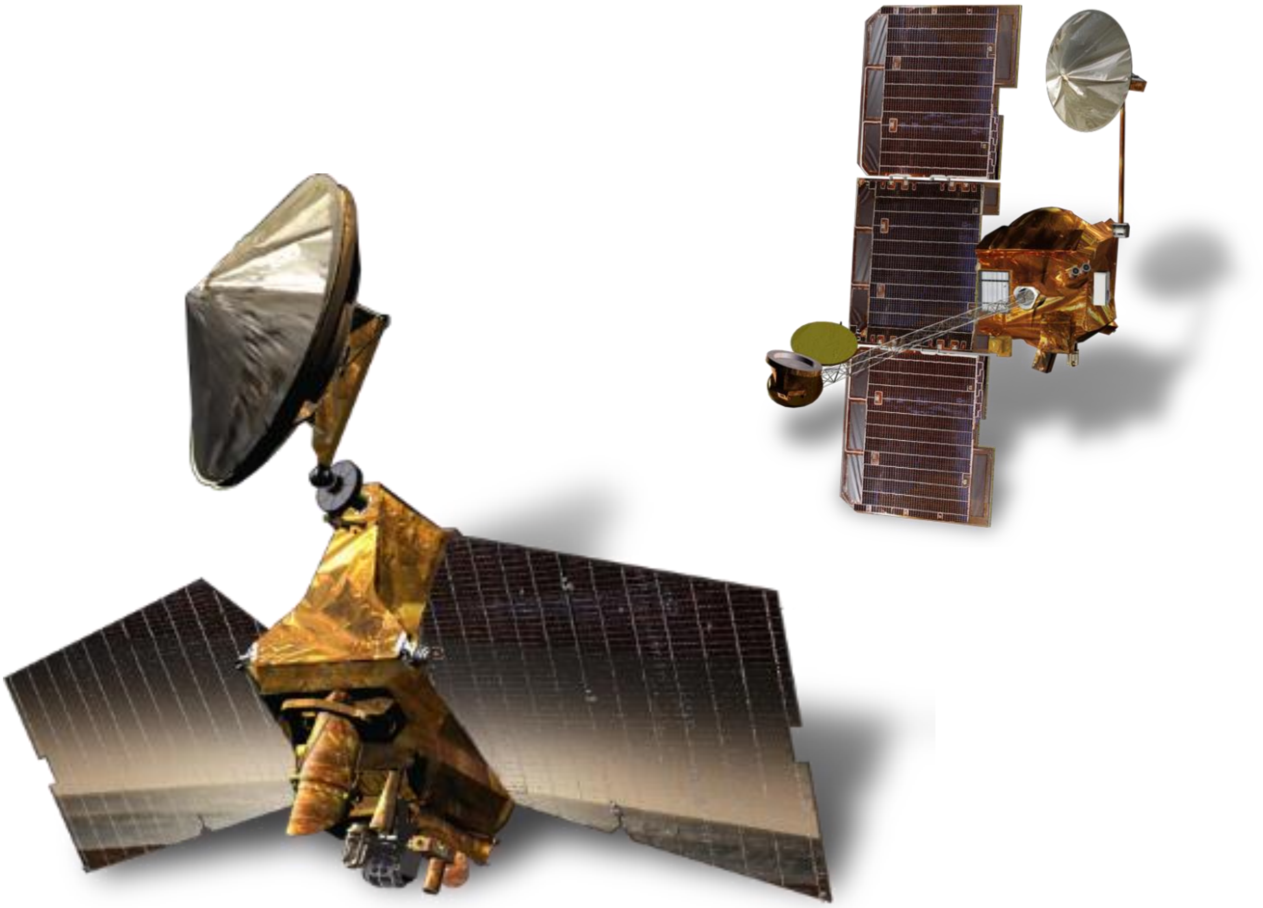

Image credits: NASA/JPL

3.1 DATA COLLECTION

3.1.1 Imagery

Visible imagery included panchromatic images acquired by: (1) the High Resolution Stereo Camera (HRSC, 12.5 m/pixel) (Neukum et al., 2004) on board the ESA's Mars Express, and (2) the Context Camera (CTX, 5-6 m/pixel) (Malin et al., 2007), as well as additional images from the High Resolution Imaging Science Experiment (HiRISE, ~25-50 cm/pixel) (McEwen et al., 2007), both instruments on board NASA's Mars Reconnaissance Orbiter. The global CTX image mosaic (Dickson et al., 2018) covers the totality of the two study areas, whereas HiRISE images cover specific zones of the CNTZ and the totality of the study area in Kotido Crater. Infrared imagery comprised the daytime infrared image mosaic obtained by the Thermal Emission Imaging System (THEMIS, 100 m/pixel) (Christensen et al., 2004, 2013), on board NASA's Mars Odyssey. In order to differentiate surface materials on the basis of their thermophysical properties, we used the THEMIS-based thermal inertia (TI) (Fergason et al., 2006), which is derived from the nighttime infrared image mosaic captured by THEMIS.

3.1.2 Topographic data

Topographic data were extracted from Digital Elevation Models (DEMs) acquired by instruments with different spatial resolution and coverage: laser altimeter point shots from the Mars Orbiter Laser Altimeter (MOLA, 463 m/pixel) (Zuber et al, 1992), on board NASA's Mars Global Surveyor, as well as stereo-pair images from the High Resolution Stereo Camera (HRSC, 50-75 m/pixel), on board ESA's Mars Express. The characterization and morphometric analysis of the landforms in the CNTZ were carried out, where possible, using the HRSC-derived topographic data that displays the best spatial resolution publicly available in this study area. In order to cover areas where HRSC data are not available, we used a HRSC and MOLA blended DEM (Fergason et al., 2018, ~200 m/pixel). The imagery and topographic data were integrated into a Geographic Information System (ESRI's ArcGIS 10.5.1) to map and carry out multiple analyses. Spatial data were projected into the geographic coordinate system "GCS_Mars_2000_Sphere", with an equidistant cylindrical projection and a central meridian of 125°E, that is approximately located in the center of the CNTZ.

In addition, in order to properly characterize the enclosed depressions in Kotido Crater, a DEM was produced from the stereo-pair images ESP_016776_1810 and ESP_016921_1810 (0.5 m/pixel) from HiRISE instrument. This HiRISE-derived DEM (~0.58 m/pixel) was generated by means of ASP (Ames Stereo Pipeline, NASA). It was bundle adjusted to the global topography provided by the MOLA dataset and aligned to HRSC. Spatial data were projected on the coordinate system Mars2000 Equidistant Cylindrical. DEMs generated using the NASA ASP may include non-consistent elevation data along shadowed areas (e.g., inner part of the depression rims) because the stereo correlation in these zones does not capture clear distinctive boundaries that can be easily matched between the stereo-pair images (Watters et al., 2017; Beyer et al., 2018). As a result, the DEM used in the cartographic analysis includes some noticeable no-data gaps in these areas. Elevation data corresponding to these areas were interpolated in order to minimize their effect in the calculation of volume parameters.

3.1.3 CRISM spectral data

The mineral composition of the surficial material in geologic units of special interest was inferred from hyperspectral data obtained by the Compact Reconnaissance Imaging Spectrometer for Mars (CRISM, ~18-36 m/pixel) (Murchie et al., 2007), onboard NASA's Mars Reconnaissance Orbiter. The CRISM instrument is a visible-infrared imaging spectrometer with a wavelength range from 0.362 to 3.92 µm. We selected CRISM data with corrected I/F (radiance/solar irradiance) from the Targeted Empirical Record (TER) and the Map-projected Targeted Reduced Data Record (MTRDR). We analyzed three CRISM scenes: FRT000064CE (~18 m/pixel, and ~10 km across), FRT00017610 (~18 m/pixel, ~10x10 km) and HRL000134F5 (~36 m/pixel, ~10x20 km) to determine the composition of surface material in three different areas with paleoenvironmental interest. These CRISM scenes include (1) fan-shaped deposits previously interpreted as deltas, and (2) spatially associated fluvial and volcanic deposits.

3.1.4 SHARAD radar profiles

The analysis of radargrams contributed to the interpretation of the subsurface structure of the CNTZ. We selected 8 radargrams located across the CNTZ (from West to East: S_01966502, S_02617902, S_01832001, S_02674602, S_02596802, S_01981001, S_01846503, S_02569101) that were obtained by the Mars Shallow Radar Sounder (SHARAD) (Seu et al., 2007), on board NASA's Mars Reconnaissance Orbiter.

3.2 MAPPING METHODS

3.2.1 Surface units

The geologic-geomorphic map (see Chapter 4 and Annex) was produced applying methodologies and techniques used in planetary geological mapping (e.g., Greeley and Batson, 1990; Wilhelms, 1990), as well as in geological mapping of Mars (e.g., Skinner and Tanaka, 2003; Tanaka et al., 2014; Skinner and Tanaka, 2018). We mainly used a combination of imagery (visible and infrared) and topographic data that permitted the identification of the surface units essentially on the basis of their more representative surface features (Skinner and Tanaka, 2003). This approach was also used for the characterization of the units, the analysis of their geometrical relationships, and their correlation. We used the THEMIS daytime infrared image mosaic as a primary base map to identify the lateral extent of the units and their general characteristics. CTX and HiRISE images, as well as the TI mosaic, were used as supplementary datasets for refining the mapping of the boundaries of the units and interpreting their origin. The spectral data provided information on the mineral composition of some units of special interest (e.g., delta deposits and volcanic materials). The mapped units were named on the basis of their geographic location, where applicable, dominant landforms and/or genesis, as well as stratigraphic relationships (Hansen, 2000; Tanaka et al., 2005; Skinner and Tanaka, 2018). The units were also labeled and grouped following an analogous methodology to that applied by Skinner and Tanaka (2018) for the geological map of Nepenthes Planum.

3.2.2 Drainage networks and watersheds

The stream network and watershed boundaries were initially mapped using the toolset “Hydrology” in ArcGIS. The “Flow accumulation” tool permitted to preliminarily delineate the stream network by applying a threshold value of 14,000 cells (equivalent to an area of 35 km^2) to select cells with high accumulated flow. The drainage network mapped automatically, which included numerous artifacts, was improved manually using imagery and TI data. The frequent occurrence of unconsolidated sediments (e.g., eolian deposits) in the valley floors, characterized by a lower apparent TI, helped to improve the delineation of the drainage network. Watershed boundaries were delineated considering the base levels defined by each putative delta at the mouth of drainage basins.

3.2.3 Putative deltas and alluvial fans

The mapping of the putative deltas and alluvial fans was challenging due to their moderate preservation conditions and relatively limited size. We decided to delineate the proximal edges of the putative deltas and alluvial fans where the flows debouching from the fluvial valleys used to become unconfined (García-Arnay and Gutiérrez, 2020). Several morphological features were also described such as layering, the occurrence of lobes and stepped profiles, or the type of watershed. In Table 1 of Chapter 4 we summarize the identified putative deltas and alluvial fans in the CNTZ, as well as those previously reported by other authors located within the study area.

3.2.4 Impact craters

All crater rims >5 km in diameter have been mapped in the CNTZ. Well-preserved and pervasive crater materials with rim diameter ranging between 5 and 13 km were mapped as “Crater unit – undivided”. This unit does not distinguish among different crater-related components due to their relatively small size in comparison with the map scale. In contrast, the different preserved components (i.e., rim, wall, floor, peak, and ejecta) of craters ≥13 km in rim diameter were depicted in the map.

3.2.5 Sinkhole-like depressions

The mapping of the enclosed depressions was carried out in the basis of the HiRISE images. Automatic mapping using the DEM was discarded since these procedures tend to generate a high proportion of false positives and overlook numerous sinkholes (e.g., Doctor and Young, 2013; De Carvalho-Junior et al., 2014). Eventually, topographic profiles constructed with the DEM aided in the identification and precise mapping of the depression margins. The cartographic inventory includes simple depressions and compound basins resulting from the coalescence of several adjoining depressions. It excludes potential former closed depressions opened by erosion, which mapping would be highly subjective.

3.3 MORPHOMETRIC ANALYSES

3.3.1 Drainage networks and watersheds

In order to analyze the drainage basin morphometry of Licus Vallis, we ranked the stream network using Strahler's classification (Strahler, 1952), and calculated morphometric parameters based on Horton's Laws (Horton, 1945). This analysis includes the consideration of linear, areal and relief aspects of the drainage basin. The following linear parameters were obtained for the drainage network: stream order, number of streams, stream length, bifurcation ratio, mean length, cumulative mean length and length ratio. Table I of Chapter 5 includes the definition of these parameters and the procedure used for their measurement. Drainage density (D_d) is a fundamental areal parameter that appraises the degree of fluvial dissection in a drainage basin, which in planet Earth is related to several factors such as climate, relief, substrate, runoff coefficient or vegetation cover. According to Horton (1945), drainage density (D_d) is defined as the total length of streams of all orders in a drainage basin (L_T), divided by the total basin area (A). It is expressed by the formula $D_d = L_T/A$.

Provided all other factors remain equal, higher drainage density values commonly indicate low permeability and highly erodible substrate, while low drainage density occurs in areas of highly resistant and/or permeable substrate. The relief aspects include, among others, the mean stream slope as a function of order, which is the average gradient expressed in degrees measured along all the stream segments of each order. Another relief parameter is the hypsometric curve. Hypsometric analyses relate the normalized elevation versus the normalized area of a drainage basin. This curve is used to estimate the geomorphic maturity of catchments.

3.3.2 Putative deltas and coastal-like benches

In order to identify equipotential surfaces corresponding to paleolevels of possible long-standing liquid-water bodies, we extracted the elevation values (expressed in meters above Martian datum, a.m.d.) from the mapped putative deltaic and coastal-like landforms (e.g., Irwin and Zimbelman, 2012). In the case of putative deltas, we considered the slope break between the delta plain and the delta front, which was interpreted as the mean highstand level (e.g., Di Achille, and Hynek, 2010b). In spite of the difficulties to infer the water level from the elevation of shore platforms on Earth (e.g., Trenhaile, 1987; Sunamura, 1992), we decided to consider the inner edge, also called the "shoreline angle" (e.g., Figueiredo et al., 2014; Zazo et al., 2013; Hearty et al., 2007). The spatial-altitudinal distribution of the putative deltas and benches permitted us to constrain their elevation range, and reconstruct the distribution of ancient liquid-water bodies.

The approximate volume of the largest mass of liquid water was calculated using the ArcGIS tool "Polygon volume". It calculates the volume resulting from the intersection between the lake bottom derived from a TIN model and a horizontal surface defined by the mean elevation estimated for the water level. The maximum depth was estimated by the difference between the mean elevation of the water level and the elevation of the deepest point, which was calculated using the ArcGIS tool "Zonal Statistics as Table", while the mean depth is given by the difference between the mean water level elevation and the average elevation of the depression surface. In this investigation, we assumed that: (1) the present regional topography is similar to the one that existed during the development of the analyzed landforms, and (2) the landforms formed when the Martian hydrosphere was persistent and a long-standing body of liquid water was present in the region (e.g., Di Achille and Hynek, 2010b).

The areas estimated for some deltas should be considered as minimum values due to surface reduction related to erosional processes (e.g., landsliding). The delta-shape index, or elongation of the delta, is a dimensionless morphometric parameter defined by the expression $S_d = W_d/2L_d$, where L_d is the delta length given by the maximum distance parallel to the paleoflow direction, and W_d is the delta width, defined as the maximum distance across the foot of the delta front and perpendicular to W_d. S_d values of 1 correspond to semicircular deltas, while $S_d > 1$ and $S_d < 1$ indicate oblate and prolate deltas with long axes perpendicular or parallel to the paleoflow direction, respectively. These definitions were adapted for this work from Caldwell and Edmonds (2014). We also estimated the mean slope for the deltaic plains and fronts, as well as several morphological attributes related to both the deltas and their associated watersheds as defined by Di Achille and Hynek (2010a) in order to characterize qualitatively: (1) the type of drainage network, distinguishing between poorly-developed stream networks (Lw) and steep canyons (C); (2) the morphology of the delta front, differentiating between steep simple fronts (M1) and stepped fronts with benches or slope breaks (M2); (3) evidence of avulsion (multi-lobate deltas); and (4) visible layering (see Table 1 in Chapter 5).

3.3.3 Sinkhole-like depressions

The map produced, together with the DEM, were used to extract morphometric parameters, analyze frequency-size relationships and perform spatial analyses. The following morphometric parameters were obtained for the depressions: major axis, orientation of major axis, area, elongation ratio, perimeter, circularity ratio, mean elevation of the perimeter, volume, elevation of deepest point and depth. Table 1 of Chapter 6 includes the definition of these parameters and the procedure used for their measurement. The volume estimation of the depressions was calculated with the polygon volume tool of ArcGIS following the procedure explained in Table 1 of Chapter 6. However, a null volume was obtained for 29 depressions (<6% of the inventory) of limited area (<550 m^2), probably related to artefacts in the DEM and a small offset between the images used for mapping and the DEM. The volume of these depressions has been indirectly estimated using an exponential regression with a reasonable goodness of fit ($y = 0.0012\ x^{1.8598}$; $R^2 = 0.689$) that relates the area of the sinkholes smaller than 5,000 m^2 and their volume. Table 2 of Chapter 6 includes maximum, minimum and average values of some of the parameters, as well as the standard deviation. The frequency-size relationships of the depressions have been analyzed considering their major axis, area and volume and generating best-fit regression functions.

The spatial distribution analysis includes, in addition to qualitative observations, the production of density maps of depressions and fractures, the calculation of the Nearest Neighbour Index (NNI) for the depressions, and the comparison of rose diagrams generated with the orientation of the depressions, fractures and wind direction. Two types of sinkhole density models were generated computing the number of depressions and the proportion of the area occupied by depressions within a search radius. The density model by number was generated with the centroids of the depressions and applying a uniform Kernel function (ArcGIS tools “Feature to Point” and “Kernel Density”, respectively). The areal density map was generated transforming the depression polygons into raster and then into points (Polygon to Raster and Raster to Point tools) and applying a uniform Kernel function (“Kernel Density” tool). In both cases, the default search radius was used, calculated specifically to the input dataset using a spatial variant of Silverman’s Rule of Thumb that is robust to spatial outliers (i.e., points far away from the rest) (Silverman, 1986). The NNI of the depressions was calculated with their centroids with the ArcGIS tool “Average Nearest Neighbour” to quantify their dispersion versus clustering.

3.3.4 Orientation of landforms

Azimuth data from mapped landforms of interest were extracted automatically with the “Minimum Bounding Geometry” tool available on “Data Management” toolbox of ArcGIS, and plotted on rose diagrams with GeoRose 0.5.1 software (Yong Technology Inc.).

3.4 CHRONOLOGY OF SURFACE UNITS

Numerical dating of surface units was carried out following the procedure proposed by Warner et al. (2015). Crater-counting areas for each unit of interest and their associated crater populations were mapped and computed using the “CraterTools” toolset for ESRI’s ArcGIS (Kneissl et al., 2011). Primary craters with geometric centers within the count area were mapped manually based on three points selected along the crater rim. In general, we decided to exclude from our count areas the surfaces occupied by well-preserved ejecta blankets and their superposed crater populations because they represent the age of the impact event and postdate the target surface (Warner et al., 2015). However, crater populations on ejecta blankets were included when it was necessary to estimate the age of the associated impact event. In order to minimize the potential bias derived from the variable cratering pattern, we selected, where possible, crater-counting areas larger than 1,000 km^2 (Warner et al., 2015). Crater size-frequency diagrams (CSFD) for each counting area were generated using CraterStats2 software (Michael and Neukum, 2010) and the absolute age models were derived from crater production and chronology functions defined by Hartmann (2005). The numerical age of the units (i.e., the age range estimated for the end of their formation), as well as the final age of the resurfacing events were estimated from simple and corrected cumulative data-dependent fits, respectively. The assignation of the chronologic period(s) and epoch of Mars (Michael, 2013) to each mapped unit, which is indicated in the unit codes in capital letters (see map legend in Annex), was based on both the numerical age estimates obtained by crater counting and their relative chronology inferred from geometrical relationships.

3.5 SPECTRAL ANALYSIS

The spectral analysis was carried out using the CRISM Analysis Toolkit (CAT, version 7.3.1), an IDL/ENVI-based software system developed by the CRISM Science Team (Morgan et al., 2014). Spectral curves and spectral parameter maps were obtained, respectively, from the corrected I/F, and the refined spectral summary parameters (Viviano-Beck et al., 2014). The occurrence of clay-bearing surfaces was identified on spectral parameter maps obtained by the PHY product (D2300 -red-, D2200 -green-, BD1900r2 -blue-) for the three analyzed projected CRISM scenes following the procedure described by Viviano-Beck et al. (2014). Surfaces with olivine-bearing deposits were detected from the spectral parameter map derived from the MAF product (OLINDEX3 -red-, LCPINDEX2 -green-, HCPINDEX2 -blue-) for the projected CRISM scene HRL000134F5. In order to highlight these compositional units (i.e., clay- and olivine-bearing units), we adjusted the values displayed for each RGB channel applying stretch limits. I/F spectra were extracted from the unprojected CRISM scenes FRT000064CE and

FRT00017610 and averaged from a Region of Interest (ROI) selected for each compositional unit to obtain average spectra (s1). In order to minimize atmospheric contributions and instrument artifacts, these average spectra (s1) were ratioed to an average spectrum from a ROI of relatively spectrally featureless materials (s2) extracted from each CRISM scene. The ratioed I/F spectra (s1/s2) were compared with the CRISM and ENVI spectral libraries (Viviano-Beck et al., 2015) in order to identify the minerals that best match to CRISM spectra.

3.6 SUBSURFACE ANALYSIS

The NE-SW-oriented SHARAD radargrams were analyzed with the JMARS 5 software (ASU's Mars Space Flight Facility), which permitted us, in combination with geomorphic data, to identify possible tectonic features and layering. Geologic cross-sections shown in Chapter 4 summarize our interpretation of the subsurface stratigraphic relationships among the units, as well as the possible tectonic structures that occur along the profiles. They were constructed on the basis of the information provided by radargrams, topographic data, the geologic units, as well as the spectral analysis and formation ages of the units.

CHAPTER

---

4. Geology and landscape evolution of the Terra Cimmeria-Nepenthes Mensae Transitional Zone

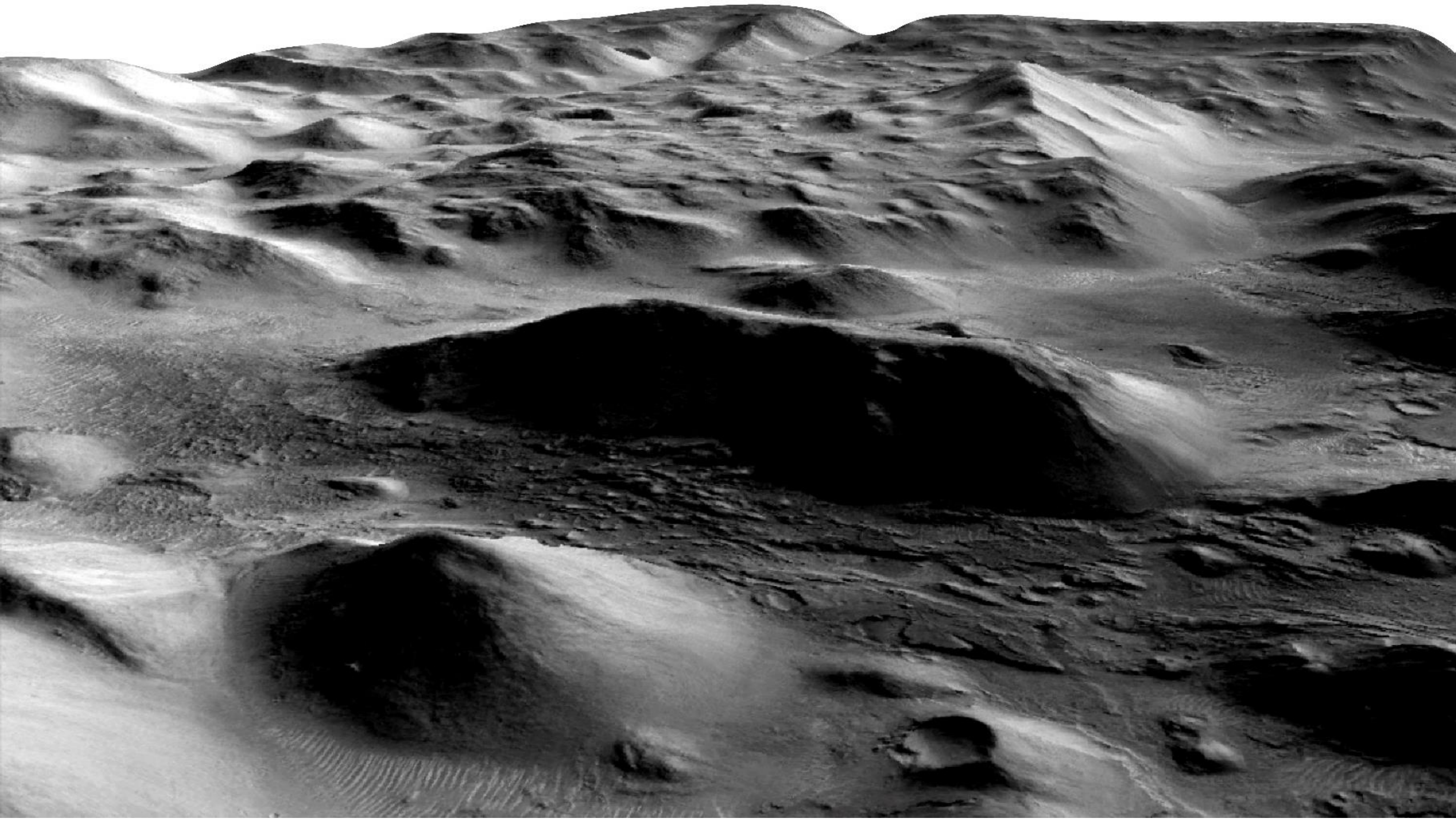

INTRODUCTION AND GOALS

The region comprising NW Terra Cimmeria and SE Nepenthes Mensae is one of the most striking transitional zones between the highlands and lowlands on Mars, including two contrasting geological and geomorphological domains bounded by a remarkable 2-km-high escarpment. Despite its importance there is a lack of detailed cartographic works providing a reference geologic-geomorphic framework for this transitional zone, remaining as a complex and poorly studied area (e.g., Skinner and Tanaka, 2018). Investigations focused on the upland-lowland transition zones of Mars offer the opportunity for gaining insight into the geologic-geomorphic processes involved in the origin and evolution of the dichotomy escarpment, which remains as an unresolved problem (e.g., Andrews-Hanna et al., 2008; Golabek et al., 2011), as well as improving our understanding of the early Mars (e.g., McGill and Dimitriou, 1990; Watters, 2003a, 2003b; Watters and McGovern, 2006; Levy et al., 2007).

The analyzed area in the Terra Cimmeria-Nepenthes Mensae Transitional Zone (CNTZ), which covers about 415,000 km^2 (equivalent to ~71% of the Iberian Peninsula), has been included in multiple global and regional geologic maps produced by the United States Geological Survey (USGS, U.S. Department of the Interior) (e.g., King, 1978; Scott and Carr, 1978; Hiller, 1979; Greeley and Guest, 1987; Tanaka et al., 1992b; Tanaka et al., 2005; Tanaka et al., 2014). Nevertheless, the scale of these maps precludes the representation of important features. Therefore, the production of more detailed geological-geomorphological maps can be considered as a valuable and innovative contribution.

The results recorded in this Chapter are presented in two scientific papers currently under review related to the geology, geomorphology and evolution of the CNTZ from the Noachian period to recent times: (1) The regional-scale mapping (1:1.45Million) of the different geologic units and geomorphic features of the CNTZ, focusing on the analysis of their geometrical relationships, as well as their description, interpretation, correlation and chronological ascription. (2) A comprehensive local- and regional-scale geological study carried out at the central sector of the CNTZ (representing about 35% of total mapped surface), largely based on cartographic work, and complemented by crater counting, as well as spectral and subsurface analyses. The objective of this latter work is to provide insight into the endogenic and exogenic processes involved in the configuration of this transitional zone, focusing on the formation of the system of closed depressions that used to host paleolakes, the evolution of the present-day dichotomy escarpment, and the reconstruction of the long-term geological-geomorphological history of the region.

GEOLOGIC-GEOMORPHIC MAP OF THE TERRA CIMMERIA-NEPENTHES MENSAE TRANSITIONAL ZONE, MARS - 1:1.45MILLION

Ángel García-Arnay(a)*

[a] Grupo Procesos Geoambientales y Cambio Global, IUCA, Departamento de Ciencias de la Tierra, Universidad de Zaragoza, 50009 Zaragoza, Spain

* Corresponding author e-mail address: arnay@unizar.es

Abstract

A 1:1.45Million geologic-geomorphic map of NW Terra Cimmeria and SE Nepenthes Mensae (-5°31′–5°38′ N, 119°20′–129°55′ E) is presented here for the first time, displaying one of the highland-lowland transitional zones of Mars with greatest contrast and diversity. The Terra Cimmeria-Nepenthes Mensae Transitional Zone comprises two complex and poorly studied geologic-geomorphic domains bounded by the dichotomy escarpment. Despite its significance, there is a lack of detailed cartographic works focused on this area. The map produced in this work displays nineteen geologic units and numerous geomorphic features. Detailed mapping, morphologic and morphometric analyses and crater counting has permitted us to constrain the stratigraphy of this transitional zone and reconstruct its geological history from the Early Noachian to recent times. The map provides insight into the processes involved in the origin and development of this transitional zone and offers a reference geologic-geomorphic framework for future studies in the region.

Keywords: Planetary mapping; Dichotomy boundary; Paleolakes; Deltas; Tectonic geomorphology; Landslides

1. Introduction

Studies carried out in the highland-lowland transitional zone of Mars permit us to shed light into the geologic-geomorphic processes involved in the origin and evolution of the dichotomy boundary and its nearby areas, as well as to improve our understanding of the early history of Mars (e.g., McGill and Dimitriou, 1990; Watters, 2003a, 2003b; Watters and McGovern, 2006; Levy et al., 2007). This work focuses on one of the most contrasting highland-lowland transitional zones: the ancient and densely-cratered highland plateaus of the northwestern part of Terra Cimmeria, south of the dichotomy boundary, and the relatively young and poorly-cratered lowland plains of the southeastern area of Nepenthes Mensae, north of Terra Cimmeria, mapped as Middle Noachian highland unit (mNh) and Hesperian and Noachian transition unit (HNt), respectively (Tanaka et al., 2014) (Fig. 1). These geologic-geomorphic domains in the equatorial region of Mars are bounded by the dichotomy escarpment with a local relief of ~2 km. The Terra Cimmeria-Nepenthes Mensae Transitional Zone (CNTZ), which remains as a complex and poorly studied area (e.g., Skinner and Tanaka, 2018), is characterized by: (1) tectonically-contracted areas as inferred by the occurrence of lobate scarps, ridge crests and wrinkle ridges in the Terra Cimmeria (e.g., Watters and Robinson, 1999; Watters, 2003b) and Nepenthes Mensae regions; (2) fracture-controlled linear troughs in the vicinity of the dichotomy escarpment, probably generated by extensional tectonic deformation and/or lateral spreading along the escarpment (e.g., Irwin et al., 2004); (3) interconnected NW-SE-trending

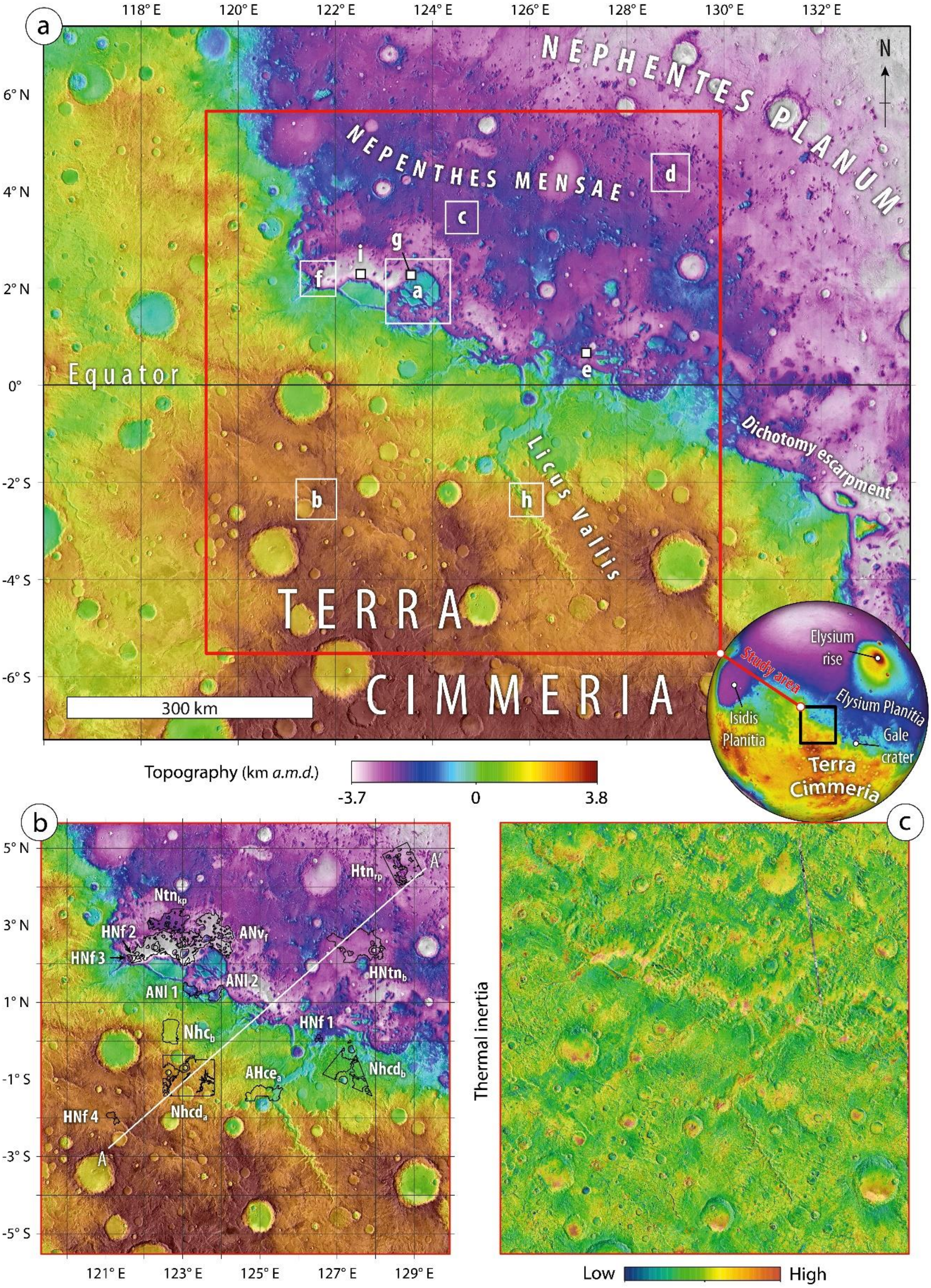

Fig. 1: (a) Colorized elevation model (km above Martian datum, a.m.d.) derived from HRSC-MOLA blended data over a mosaic of THEMIS-IR day images, with the study area framed by a red rectangle. White polygons and squares indicate the location of the images of Fig. 2. (b) Study area with black polygons indicating the crater-counting areas selected for dating the main surface units (Fig. 4a). The white line indicates the trace of the geological cross-section (A-A') (Fig. 5). (c) Qualitative THEMIS-derived TI mosaic of the study area over THEMIS-IR day images.

closed depressions at the foot of the dichotomy, probably related to extensional tectonics (Watters, 2003a; Watters and McGovern, 2006); and (4) pervasive residual reliefs probably related to mass-wasting processes and "basal sapping of volatiles" in Nepenthes Mensae (Tanaka et al., 2005). Fluvio-lacustrine activity seems to have played a fundamental role in the configuration of the CNTZ, as indicated by the presence of ancient V-shaped fluvial valleys in the Cimmeria region (e.g., Irwin and Howard, 2002; Goudge and Fassett, 2018; García-Arnay et al., 2018b), as well as moderately preserved Gilbert-type deltas and alluvial fans at their mouths (e.g., Irwin et al., 2005; de Pablo and Pacifici, 2008; García-Arnay et al., 2018a, 2018b; Rivera-Hernández and Palucis, 2019; García-Arnay and Gutiérrez, 2020). Furthermore, the occurrence of putative deltas and paleoshore platforms spatially associated with closed depressions in Nepenthes Mensae suggest the presence of paleolakes (García-Arnay and Gutiérrez, 2020). Although these findings show the relevance of the CNTZ, there is a lack of detailed cartographic works providing a reference geologic-geomorphic framework of this transitional zone. The study area has been included over time in multiple geologic maps produced by the United States Geological Survey (USGS, U.S. Department of the Interior) (e.g., King, 1978; Scott and Carr, 1978; Hiller, 1979; Greeley and Guest, 1987; Tanaka et al., 1992; Tanaka et al., 2005; Tanaka et al., 2014). However, the scale of these maps precludes the representation of important features. Recently, Skinner and Tanaka (2018) produced the regional-scale geologic map of the transitional zone between Terra Cimmeria and Utopia Planitia, northwest of the study area, providing a reference framework to compare with the CNTZ.

This work presents, for the first time, a detailed regional-scale geological-geomorphological map of NW Terra Cimmeria and SE Nepenthes Mensae providing insight into the processes involved in the configuration of this transitional zone, focusing on (1) the identification, description and interpretation of the different geologic units and geomorphic features; (2) the estimation of the chronology of the main surface units; and (3) the reconstruction of the protracted geological-geomorphological history.

2. Data and methods

2.1 Imagery and topographic data

The utilized visible imagery comprised the global CTX image mosaic acquired by the Context Camera (CTX, 5-6 m/pixel) (Malin et al., 2007; *Dickson et al., 2018*), and additional images from the High Resolution Imaging Science Experiment (HiRISE, ~25-50 cm/pixel) (McEwen et al., 2007), both instruments on board NASA's Mars Reconnaissance Orbiter. Infrared imagery included the daytime infrared image mosaic obtained by the Thermal Emission Imaging System (THEMIS, 100 m/pixel) (Christensen et al., 2004, 2013), on board NASA's Mars Odyssey. The THEMIS-based thermal inertia (TI) (Fergason et al., 2006), which is derived from THEMIS nighttime infrared images, was used to differentiate surface materials (Fig. 1c).

Topographic data were extracted from Digital Elevation Models (DEMs) derived from the Mars Orbiter Laser Altimeter (MOLA, 463 m/pixel) (Zuber et al, 1992), on board NASA's Mars Global Surveyor, as well as from the High Resolution Stereo Camera (HRSC, 50-75 m/pixel), on board ESA's Mars Express. A HRSC and MOLA blended DEM (Fergason et al., 2018, ~200 m/pixel) was used to cover areas where HRSC data are not available. In order to map the geologic units and landforms, establish their geometrical relationships, and carry out morphological and morphometric analyses, data were integrated into a Geographic Information System (ESRI's ArcGIS 10.5.1) and projected into the geographic coordinate system "GCS_Mars_2000_Sphere", with an equidistant cylindrical projection and a central meridian of 125°E.

2.2 Mapping methods

The geologic-geomorphic map was produced applying methodologies and techniques widely used in planetary geological mapping (e.g., Greeley and Batson, 1990; Wilhelms, 1990), and in geological mapping of Mars (e.g., Skinner and Tanaka, 2003; Tanaka et al., 2014; Skinner and Tanaka, 2018). Visible and infrared imagery together with topographic data were used to identify, interpret and correlate the surface units, largely on the basis of their primary surface features (Skinner and Tanaka, 2003). The THEMIS daytime infrared images were used as a primary base map, whereas CTX and HiRISE images, as well as the TI mosaic, were used as supplementary datasets. The name of the mapped units was based on their geographic location, where applicable, prevalent features and/or origin, as well as stratigraphic relationships (Hansen, 2000; Tanaka et al., 2005; Skinner and Tanaka, 2018). The drainage network was drawn automatically applying the toolset "Hydrology" in ArcGIS, and later improved by removing manually artifacts using visible imagery and TI data. The proximal edges of fan-shaped features were delineated where the paleoflows debouching from the valleys used to become unconfined (García-Arnay and Gutiérrez, 2020). All crater rims >5 km in diameter have been mapped. The different preserved components of craters ≥13 km in rim diameter were depicted in the map. However, the "Crater unit – undivided", which comprises well-preserved crater materials with rim diameters between 5 and 13 km, does not distinguish among crater-related components due to their relatively small size compared to the map scale. Azimuth data from selected mapped landforms were plotted on rose diagrams with the GeoRose 0.5.1 software (Yong Technology Inc.) (Fig. 3).

2.3 Chronology of surface units

The correlation of map units was carried out on the basis of the numerical formation age estimates derived from crater size-frequency distributions and their relative chronology inferred from geometrical relationships (see Fig. 4). Crater populations for each unit of interest were mapped and computed using the "CraterTools" toolset for ESRI's ArcGIS (Kneissl et al., 2011). All primary craters larger than 50 or 100 m in rim diameter with centroids within the count area were mapped. Crater-counting areas larger than 1,000 km^2 were selected, where possible, to minimize the potential bias related to the variable cratering pattern (Warner et al., 2015). Surfaces occupied by well-preserved ejecta blankets were excluded from the count areas, except when it was necessary to estimate the formation age of the associated impact event. Cumulative crater size-frequency diagrams for each sampling area were generated using the CraterStats2 software (Michael and Neukum, 2010), and the absolute age models were derived from chronology and crater production functions defined by Hartmann (2005).

3. Geologic units of the CNTZ

The map differentiates 19 units that have been grouped according to their geographic distribution (see the map in "Supplementary material"). Three units have been identified in the

Cimmeria region of the highland province: The Cimmeria dissected units include two well-differentiated members with rugged and heavily cratered surfaces dissected by V-shaped valleys (e.g., Tanaka et al., 2005, 2014; Skinner and Tanaka, 2018). Member a ($Nhcd_a$) occurs in the topographically higher sector, whereas member b ($Nhcd_b$) crops out in the plateau situated south of the dichotomy, at lower elevation than member a, forming residual reliefs (knobs and mesas) in the transitional province (Fig. 2a). Member a ($Nhcd_a$) shows a higher crater density than member b, NW-SE-striking lobate scarps, and less commonly ridge crests (Fig. 2b). Member b ($Nhcd_b$) with a gradational boundary with the older member $Nhcd_a$ is characterized by localized NE-SW-oriented ridge crests, and scarce occurrence of lobate scarps with NW-SE orientation. It shows deeper valleys with a dominant NE-SW orientation, and a secondary NW-SE trend near the dichotomy escarpment. The Cimmeria basin unit (Nhc_b) is a moderately cratered unit that occurs in depressions inset into member $Nhcd_a$, exhibiting smooth surfaces, wrinkle ridges, and absence of channels (Fig. 2b).

Three units have been recognized in the Nepenthes Mensae region of the transitional province: The Nepenthes knobby plateau unit (Ntn_{kp}) is a moderately cratered unit that occurs in the inter-crater plateaus of Nepenthes Mensae, characterized by knobby terrains with residual hills made up of materials of the unit $Nhcd_b$ and mass-wasted materials (e.g., Tanaka et al., 2005) (Fig. 2c). This unit, with a gradational boundary with the older unit $Nhcd_b$ and the younger unit $HNtn_b$, shows NW-SE-trending lobate scarps and yardangs with pervasive NW-SE orientation. The Nepenthes basin unit ($HNtn_b$) crops out in the NW-SE-trending closed depressions at the foot of the dichotomy escarpment, which used to host paleolakes (Rivera-Hernández and Palucis, 2019; García-Arnay and Gutiérrez, 2020), as well as on floors of poorly-preserved impact basins. The Nepenthes basin unit, which overlies unit $Nhcd_b$, is characterized by a lower crater density than unit Ntn_{kp}, and relatively smooth terrains locally interrupted by residual reliefs, wrinkle ridges, pitted cones and small tholi. The Nepenthes ridged plain unit (Htn_{rp}) that occurs in the northeast sector of the map exhibits undulating, low-lying plains with pervasive NW-SE-oriented wrinkle ridges and scattered knobs of unit $Nhcd_b$ (Fig. 2d). This unit, which is less-cratered than units Ntn_{kp} and $HNtn_b$, overlies unit $Nhcd_b$ and grades into the older unit Ntn_{kp}.

Seven impact crater units have been distinguished. Well-preserved craters with rim diameter between 5 and 13 km were mapped as the crater unit–undivided (AHc_u). This unit is frequently characterized by hummocky crater floors with rare occurrence of central peak or pit, and lobate ejecta deposits. The preserved morpho-structural components of moderately to well-preserved impact craters with rim diameter ≥13 km were mapped: The crater floor unit (AHc_f) is characterized by smooth, near-planar surfaces, frequently displaying a central peak and/or pit in the center of the crater (Fig. 2b). The crater peak unit (AHc_p) shows hills with irregular and grooved surfaces, and frequent occurrence of central pits. The crater wall unit (AHc_w) comprises scarps, discontinuous terraces, blocks, and rockfalls with locally rugged surfaces. The rim crater unit (AHc_r) is formed by inward-facing scarps frequently dissected by gullies. The crater ejecta units include two morpho-facies: (1) the crater ejecta unit–facies a ($AHce_a$), which represents the inner unit characterized by rugged lobes with flowbands, and (2) the crater ejecta unit–facies b ($AHce_b$) corresponds to the distal deposits that are formed by smooth flow-oriented lobes.

Six spatially-dispersed units have been mapped: The volcanic flow unit (ANv_f), which crops

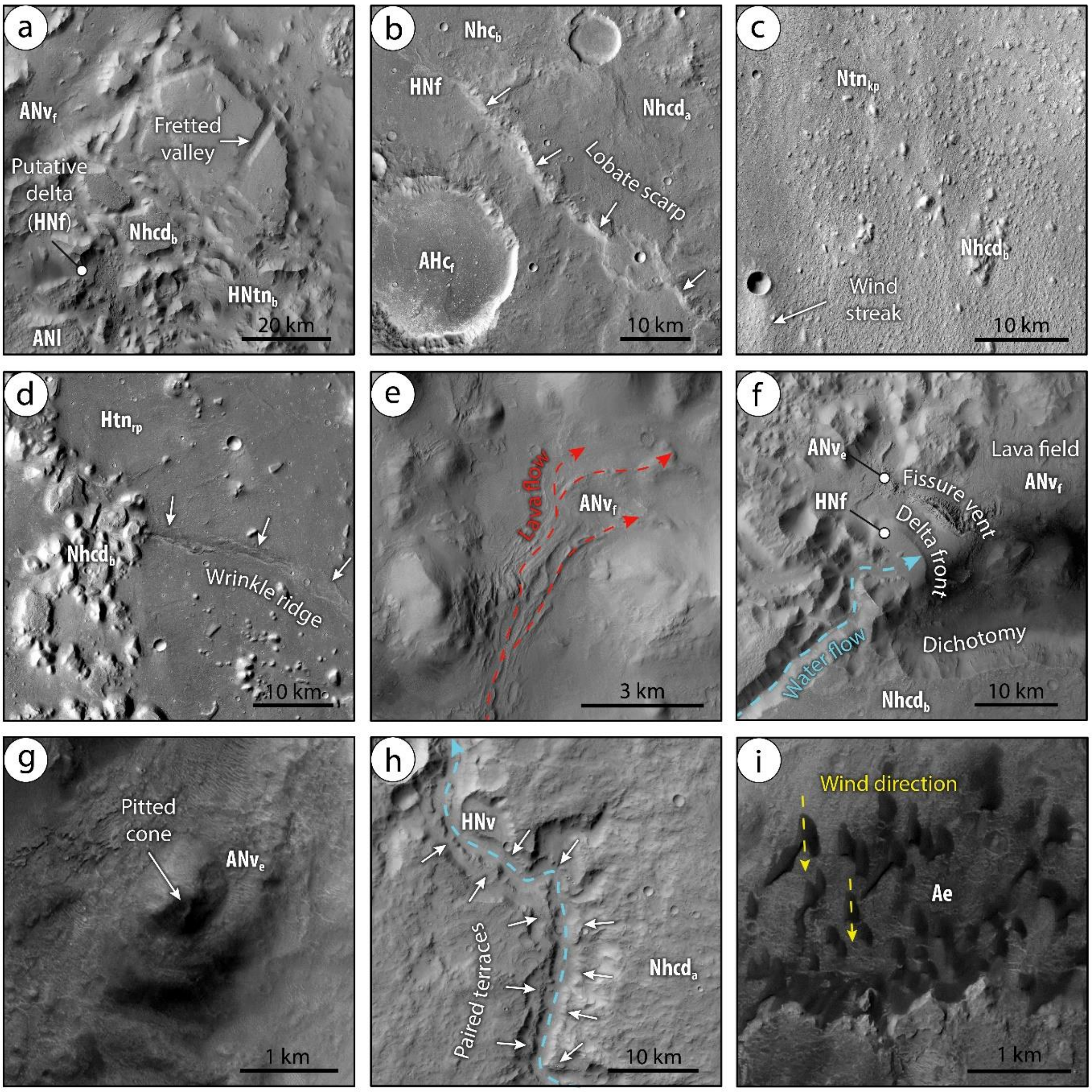

***Fig. 2**: CTX images showing remarkable landforms in the CNTZ (locations indicated in Fig. 1a). (a) Mesa-like landform in a megalandslide dissected by troughs related to fracture-controlled gravitational extension. (b) SW-facing lobate scarp attributable to a surface-rupturing thrust fault occurring in unit Nhcd$_a$. (c) Knobby terrain of unit Ntn$_{kp}$ displaying wind streaks. (d) Tectonically-contracted plains of unit Htn$_{rp}$ exhibiting wrinkle ridges and knobs. (e) Moderately-preserved putative lava flows of unit ANv$_f$. (f) Putative Gilbert-type delta and volcanic features such as fissure vents and lava fields. (g) Volcano-like pitted cone of unit ANv$_e$. (h) Paired terraces in Licus Vallis. (i) Dark-tone barchan dune fields of unit Ae. North is up in all images.*

out in the deeper areas of the depressions of Nepenthes Mensae, and locally in the highlands near the dichotomy. It exhibits smooth to rugged, poorly-cratered surfaces, often with channels, overlapping lobes, and NE-SW-striking wrinkle ridges (Fig. 2e). This unit locally grades into the coeval unit ANv$_e$, locally overlies units HNtn$_b$ and Nhcd$_b$, and underlies unit HNf. The volcanic edifice unit (ANv$_e$), which is laterally associated with unit ANv$_f$, is characterized by isolated and coalesced raised fissures with sloping, and rugged to smooth surfaces, as well as small cone- and mound-shaped features (Fig. 2f, g). The valley unit (HNv) that is carved in units

Nhcd$_{a}$ and Nhcd$_{b}$, and rarely in unit Ntn$_{kp}$ displays smooth deposits underlying the low-TI valley floors (Fig. 2h). The fan unit (HNf), which is laterally associated with unit HNv, is related to fan-shaped deposits with smooth to corrugated surfaces due to differential erosion (Fig. 2f). The landslide unit (ANl) mostly occurs associated with the dichotomy escarpment locally overlying units Nhcd$_{b}$ and HNtn$_{b}$. It is characterized by rugged, rolling, and hummocky terrains. The eolian unit (Ae) consists of dark-tone, barchan and longitudinal dune fields occurring near the foot of the dichotomy, and locally overlying units ANv$_{f}$, AHc$_{f}$, HNv, HNtn$_{b}$ and Nhcd$_{b}$ (Fig. 2i).

4. Geomorphic features

The main landforms that occur within the geological units have also been mapped. Two types of scarps were differentiated: (1) Lobate scarps are linear to sinuous, NW-SE-oriented ridge-like landforms (Fig. 3a) showing asymmetric transverse profiles with convex and SW-facing scarps (e.g., Watters and Robinson, 1999) (Fig. 2b). These landforms mostly occur in units Nhcd$_{a}$, Nhcd$_{b}$ and Ntn$_{kp}$. Lobate scarps often disrupt valleys and pre-existing crater floors. (2) The linear to sinuous dichotomy escarpment ca. 2 km high, which is dissected by numerous valleys in unit Nhcd$_{b}$ (Fig. 2f). The escarpment shows a dominant NW-SE orientation that turns into a N-S trend in the western sector of the map.

Four types of ridges have been recognized: (1) Wrinkle ridges are linear to curvilinear ridges with crenulated crests, and asymmetric cross profiles (e.g., Watters, 1988) (Fig. 2d). These landforms show a NW-SE orientation within units Nhc$_{b}$ and HNtn$_{b}$, and a NE-SW trend in the unit ANv$_{f}$ (Fig. 3b). (2) Ridge crests are ridges that display a near-symmetric transverse profile (e.g., Watters et al., 2009). They frequently occur in units Nhcd$_{a}$ and Nhcd$_{b}$ with a dominant NE-SW orientation, and a secondary NW-SE trend (Fig. 3c). (3) Volcanic ridges are linear to curvilinear ridges related to fissure vents in unit ANv$_{e}$ that display smooth to rugged slopes, and weak NE-SW and NW-SE prevalent orientations. (4) Channel ridges, often known as “inverted channels”, related to relief inversion by differential erosion are characterized by a sinuous pattern and scarcely occur in valley floors (e.g., Burr et al., 2010).

Four types of negative relief morphologies were distinguished: (1) Troughs are linear to curvilinear steep-walled depressions (Fig. 2a). These landforms, which form a distinctive polygonal pattern with a dominant NW-SE orientation and a secondary NE-SW trend (Fig. 3d), occur in the vicinity of the dichotomy cutting into unit Nhcd$_{b}$. (2) Valleys are networks of V-shaped, steep-walled depressions with linear to sinuous trace and dendritic to trellis pattern (Fig. 2h). Their path seems to be locally controlled by lobate scarps, ridge crests and troughs, with evidence of deflections. (3) Channels are linear to sinuous, shallow and narrow depressions occurring in the valley floors, locally with positive relief sections. The channel networks mostly occur in units Nhcd$_{a}$ and Nhcd$_{b}$ and scarcely in unit Ntn$_{kp}$. They exhibit an orthogonal pattern with a dominant NE-SW orientation, and a secondary NW-SE trend, probably controlled by fractures. It is common the occurrence of knickpoints, as well as defeated and beheaded channels. (4) Sinkhole-like depressions are elongated, closed depressions with scarped boundaries (e.g., Parenti et al., 2020). The major axis of these features that locally occur in unit ANv$_{f}$ display a predominant NW-SE orientation.

Two types of mound- and cone-shaped landforms associated with unit ANv$_{e}$ were mapped: (1) Pitted cones are conical hills with smooth slopes and central pits (e.g., Skinner and Tanaka,

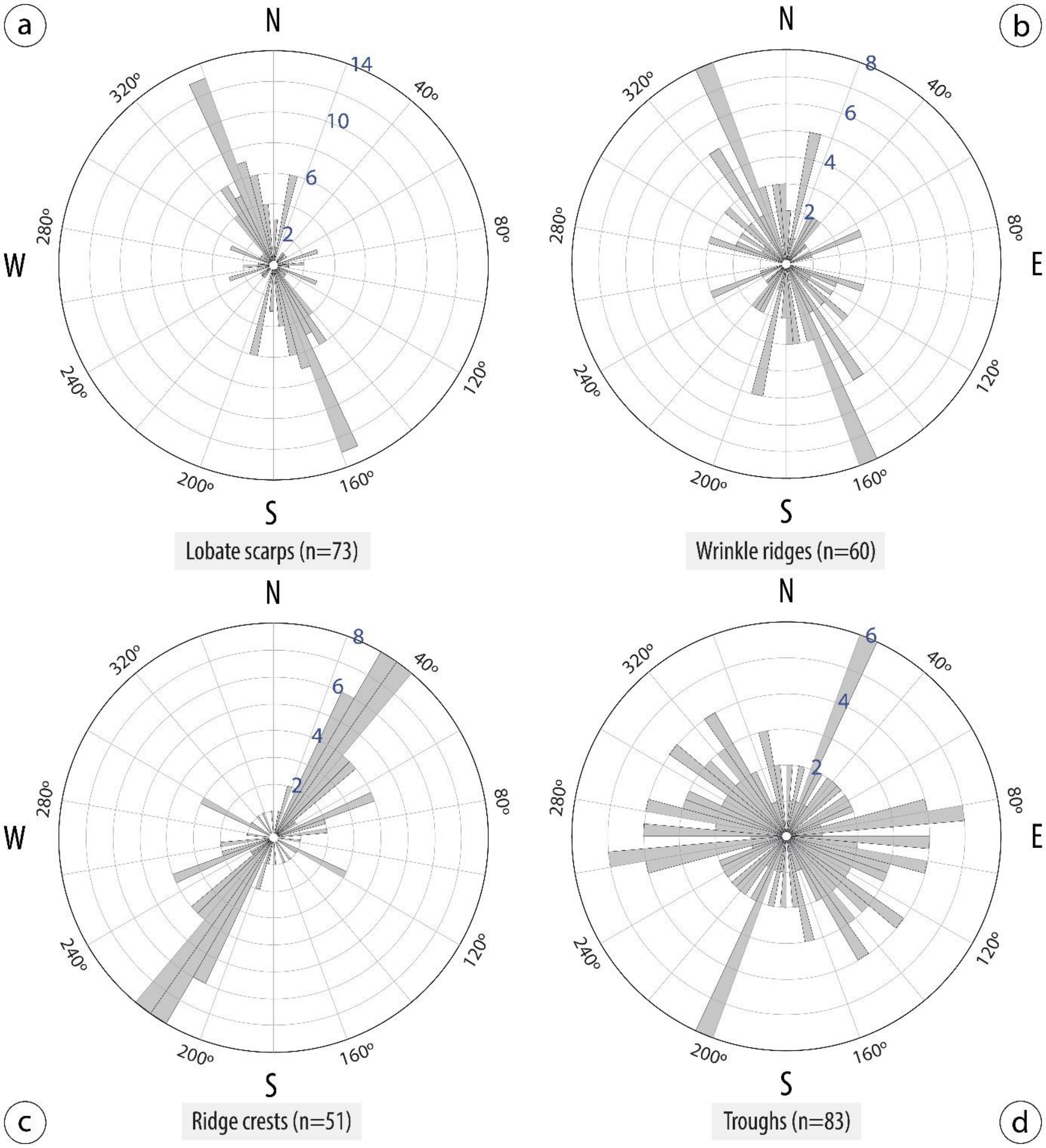

***Fig. 3**: Rose diagrams displaying the distribution of the orientation of lobate scarps (a), wrinkle ridges (b), ridge crests (c), and troughs (d). n: number of features.*

2018) (Fig. 2g). These landforms occur in unit ANv_f, and less frequently in units Ntn_{kp} and $HNtn_b$. (2) Small tholi, which generally occur in unit ANv_f and rarely in unit $HNtn_b$, are mounds often exhibiting central peaks and subtle outward-facing slopes bounded by marginal scarps (e.g., Skinner and Tanaka, 2018).

5. Numerical age estimations

In order to obtain estimations of the numerical surface age of the main map units, the crater size-frequency distribution was analyzed in 14 counting areas (see Fig. 4a and Appendix - Fig. A1). In the highland province, average formation age estimates of 4.00 ± 0.04/0.06 Ga (Early to

Middle Noachian) and 3.89 ± 0.03/0.04 Ga (Middle Noachian) were obtained for units $\mathrm{Nhcd_a}$ and $\mathrm{Nhcd_b}$, respectively, and 3.62 ± 0.02/0.02 Ga (Late Noachian) for unit $\mathrm{Nhc_b}$, considering crater-counting areas of ~4,600, ~1,800 and ~790 $\mathrm{km^2}$, respectively. In the transitional province, units $\mathrm{Ntn_{kp}}$, $\mathrm{HNtn_b}$ and $\mathrm{Htn_{rp}}$ yielded average formation ages of 3.76 ± 0.03/0.04 Ga (Late Noachian), 3.63 ± 0.05/0.08 Ga (Late Noachian to Early Hesperian), and 3.37 ± 0.07/0.13 (Early Hesperian to Late Hesperian), using counting areas of ~1,200, ~2,400 and ~1,800 $\mathrm{km^2}$, respectively. Among the spatially-dispersed units, the unit $\mathrm{ANv_f}$ yielded an average formation age of 1.83 ± 0.17/0.17 Ga (Early Amazonian) using the fit to the D >450 m crater population and considering a counting area of ~9,000 $\mathrm{km^2}$. Four counting areas were selected for unit HNf, located in the largest putative deltas and alluvial fans in the CNTZ (deltas referred to as "D2" (see Fig. 2f) and "D7" by García-Arnay and Gutiérrez (2020)). Putative deltas "D7" and "D2" (lower and upper surfaces) yielded, respectively, average formation age estimates of 3.64 ± 0.04/0.07 Ga (Late Noachian), 3.63 ± 0.10/0.31 Ga (Late Noachian to Late Hesperian; lower delta "D2") and 1.99 ± 0.36/0.36 Ga (Early Amazonian; upper delta "D2"), with corresponding counting areas of ~85.4, ~53, and ~41.1 $\mathrm{km^2}$ (areas HNf 1, HNf 2 and HNf 3, respectively). In the case of the largest alluvial fan, the fit to the D >225 m crater population provided an average formation age estimate of 3.29 ± 0.10/0.20 Ga (Early Hesperian to Early Amazonian), with a counting area of ~166.2 $\mathrm{km^2}$ (area HNf 4). Two counting areas of ~318 and ~314 $\mathrm{km^2}$ (areas ANl 1 and ANl 2, respectively) were considered for unit ANl, with average formation age estimates of 1.01 ± 0.33/0.33 Ga (Early to Middle Amazonian) and 0.80 ± 0.17/0.17 Ga (Middle Amazonian), respectively. A minimum age estimate for the cessation of fluvial activity in the main valley of Licus Vallis was obtained analyzing the crater size-frequency distribution of the crater population developed on the ejecta deposits of unit $\mathrm{AHce_a}$ that overlap the middle course of the valley. These deposits do not exhibit any evidence of reworking by fluvial activity. Considering a counting area of ~860 $\mathrm{km^2}$, the fit with the D >300 m crater population provided a minimum age estimate for the cessation of fluvial activity of 3.39 ± 0.05/0.07 Ga (Early to Late Hesperian).

6. Interpretation and correlation of map units

The interpretation of the geologic units and landforms and their surface chronology, based on geometrical relationships and crater counts, is summarized here (see Figs. 4 and 5). The documented stratigraphic record of the CNTZ began in the Early to Middle Noachian, with the emplacement of units $\mathrm{Nhcd_a}$ and $\mathrm{Nhcd_b}$ in the Cimmeria region, interpreted as moderately to heavily degraded undifferentiated highland materials related to impact, volcanic, basin-fill, and fluvial processes. Both units form part of the unit mNh (Middle Noachian) defined by Tanaka et al. (2014). The unit $\mathrm{Nhcd_b}$ possibly also correlates with unit $\mathrm{Nhc_1}$ (Early to Middle Noachian) mapped by Skinner and Tanaka (2018). The widespread occurrence of lobate scarps related to thrust faults (e.g., Watters and Robinson, 1999) suggests that these units were affected by NE-SW-oriented tectonic shortening. In the Late Noachian, uncertain-origin depressions inset into unit $\mathrm{Nhcd_a}$ were filled by sediments to form unit $\mathrm{Nhc_b}$, consisting of slightly to moderately degraded undifferentiated deposits probably related to fluvial, basin-fill and impact processes. This tectonically contracted unit, as inferred by wrinkle ridges attributed to thrust faults (e.g., Andrews-Hanna, 2020), likely correlates with unit lNh (Late Noachian) defined by Tanaka et al. (2014). From the Late Noachian, fluvial activity started to carve units $\mathrm{Nhcd_a}$ and $\mathrm{Nhcd_b}$ to form the valley networks and associated putative deltas and alluvial fans corresponding to units HNv

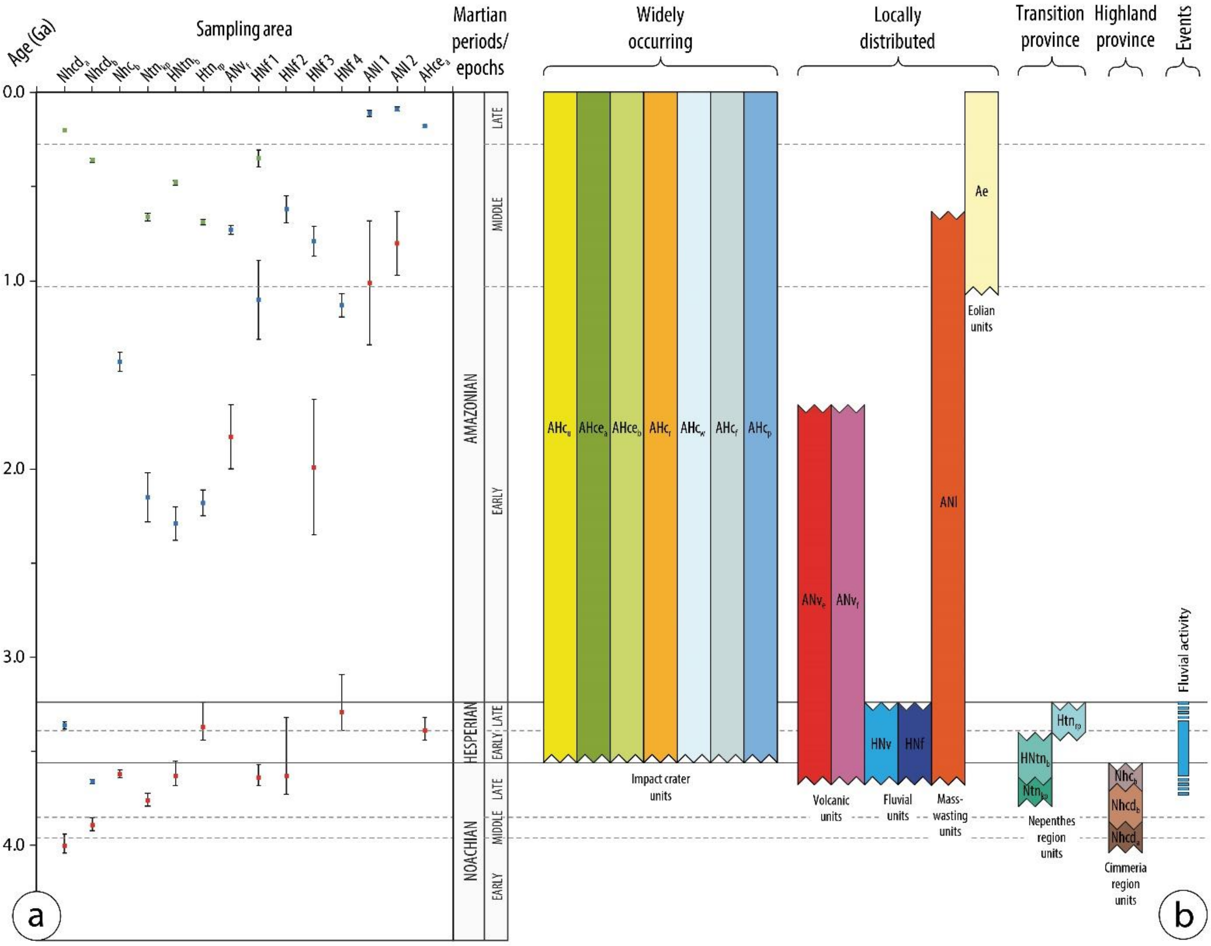

Fig. 4: (a) Diagram showing age estimations (red and blue/green boxes for formation and resurfacing ages, respectively), and their error bars (vertical black lines) from the crater size-frequency diagrams for the main mapped units (see Fig. A1). (b) Correlation of map units based on ages estimated by crater counting and geometrical relationships between units. Hachured polygon borders indicate possible, extended durations. Horizontal continuous and dashed lines indicate the boundaries between the Martian geological periods and epochs, respectively (Michael, 2013).

and HNf, respectively, most probably lasting up to Late Hesperian times. Fluvial valleys are locally disrupted by thrust faults and transformed into beheaded drainages. The Nepenthes Mensae region is characterized by knobby terrains, probably generated by basal sapping and mass-wasting processes (Tanaka et al., 2005), as well as a belt of large extensional depressions and troughs (e.g., Watters, 2003a). The unit Ntn$_{kp}$ is probably formed by undifferentiated materials attributed to volcanic and impact products, and mass-wasted deposits forming aprons around knobs and mesas of the unit Nhcd$_b$. This tectonically contracted unit, with morphotectonic features indicating a NE-SW shortening trend, was formed during the Late Noachian. The locally contracted unit HNtn$_b$, that is probably underlain by lacustrine, fluvial, and mass-wasted materials ascribed to the Late Noachian and Early Hesperian, is related to the paleolake basins (e.g., García-Arnay and Gutiérrez, 2020). The units Ntn$_{kp}$ and HNtn$_b$ are integrated into unit HNt (Noachian and Hesperian) by Tanaka et al. (2014). The units Nhc$_2$ (Middle to Late Noachian) and HNhc$_3$ (Late Noachian to Early Hesperian) defined by Skinner and Tanaka (2018) may correlate with the mapped units Ntn$_{kp}$ and HNtn$_b$, respectively. The unit Htn$_{rp}$, formed during Early to Late Hesperian times, consists of tectonically contracted materials related to impact, mass-wasting, fluvio-lacustrine and volcanic processes. It likely correlates with the unit eHt (Early Hesperian) defined by Tanaka et al. (2014). The units ANv$_e$ and ANv$_f$ are ascribable to different types of volcanic edifices and high-TI lava fields, respectively. These genetically-linked units were coevally emplaced from Late Noachian to Early Amazonian times, and are integrated into unit HNt of Tanaka et al. (2014). The unit ANl consists of deposits related to large landslides (e.g., rock spreads, slumps and falls) that were probably accumulated from the Late Noachian to the Middle Amazonian. Through the Amazonian period, eolian activity formed the dune fields of unit Ae, as well as erosional landforms like yardangs and wind streaks, indicating a persistent S-directed wind.

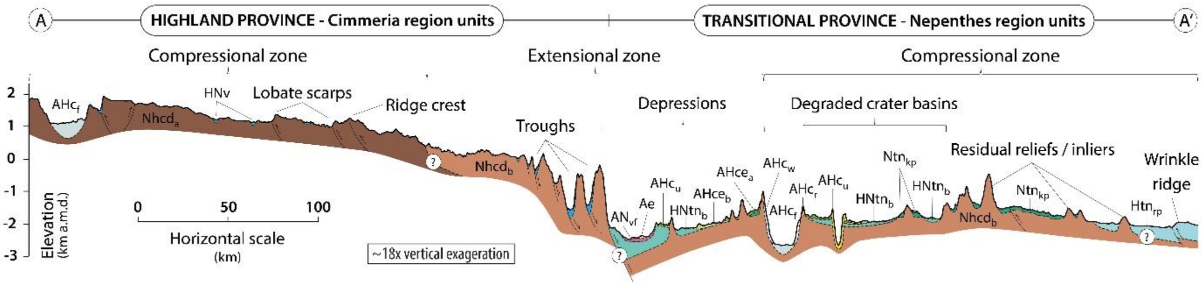

Fig. 5: Geological cross-section A-A′ (see location in Fig. 1b) constructed on the basis of cartographic relationships and crater-counting-based ages (Fig. 4).

7. Conclusions

The production of the 1:1.45M geologic-geomorphic map of the NW Terra Cimmeria and SE Nepenthes Mensae has permitted us to (1) constrain the stratigraphy of this poorly explored highland-lowland transitional zone of Mars, differentiating nineteen geologic units that include a wide variety of geomorphic features; and (2) reconstruct its long-term geological history that ranges from the Early Noachian to recent times. The mapping has also shed light on the role played by the inferred compressional and extensional tectonics, as well as the fluvio-lacustrine activity on the configuration of the landscape in the CNTZ during the Noachian and Hesperian times. This work provides a detailed geologic-geomorphic framework for future studies within this transitional zone, of special interest from the paleohydrological perspective and for understanding the evolution of early Mars.

Software

ESRI's ArcGIS 10.5.1 was used for mapping, performing multiple analyses and generate the layout of the map. The final editing of the map was carried out using Adobe Illustrator CS6 and Adobe Photoshop CS4. Azimuth data were plotted with the GeoRose 0.5.1 software (Yong Technology Inc.). "CraterTools" toolset for ESRI's ArcGIS (Kneissl et al., 2011) and "CraterStats2" software (Michael and Neukum, 2010) were used to map and compute the crater populations, and generate the crater size-frequency diagrams, respectively.

Acknowledgments

I am very grateful to Prof. Francisco Gutiérrez (Universidad de Zaragoza, Spain) for his supervision and endless scientific support to carry out this work, as well as for the review of the manuscript. This work has been sponsored by the Instituto de Investigación en Ciencias Ambientales de Aragón (IUCA).

Disclosure statement

No potential conflict of interest was reported by the author.

Funding

This research was supported by a PhD scholarship granted to ÁG-A (ref. C237/2016) by the Gobierno de Aragón (Spain) and the European Social Fund, as well as by grants awarded by the Ibercaja-CAI mobility programme (ref. CB 2/21; Universidad de Zaragoza, Fundación Bancaria Ibercaja and Fundación CAI) and the Erasmus+ Traineeship programme (ref. 53971; European Commission) to fund a research stay of ÁG-A at the International Research School of Planetary Sciences (Università degli Studi "G. D'Annunzio", Italy).

Data availability statement

The input data that support this work are freely available from these resources: (1) The PDS Geosciences Node Mars Orbital Data Explorer at [https://ode.rsl.wustl.edu/mars/index.aspx]; (2) The THEMIS-IR Day Global Mosaic of Mars at [https://astrogeology.usgs.gov/search/map/Mars/Odyssey/THEMIS-IR-Mosaic-ASU/Mars_MO_THEMIS-IR-Day_mosaic_global_100m_v12]; (3) The Mars THEMIS-Derived Global Thermal Inertia Mosaic at [https://astrogeology.usgs.gov/maps/mars-themis-derived-global-thermal-inertia-mosaic]; (4) The CTX Global Mosaic of Mars at [http://murray-lab.caltech.edu/CTX/]; and (5) The Mars HRSC and MOLA Blended Digital Elevation Model at [http://bit.ly/HRSC_MOLA_Blend_v0].

References

Andrews-Hanna, J.C., 2020. The tectonic architecture of wrinkle ridges on Mars. Icarus 351, 113937. https://doi.org/10.1016/j.icarus.2020.113937.

Burr, D.M., Williams, R.M., Wendell, K.D., Chojnacki, M., Emery, J.P., 2010. Inverted fluvial features in the Aeolis/Zephyria Plana region, Mars: Formation mechanism and initial paleodischarge estimates. J. Geophys. Res. Planets 115(E7). https://doi.org/10.1029/2009JE003496.

Christensen, P.R., Jakosky, B.M., Kieffer, H.H., Malin, M.C., McSween, H.Y., Nealson, K., Mehall, G.L., Silverman, S.H., Ferry, S., Caplinger, M., Ravine, M., 2004. The thermal emission imaging system (THEMIS) for the Mars 2001 Odyssey Mission. Space Sci. Rev. 110 (1–2), 85–130. https://doi.org/10.1023/B:SPAC.0000021008.16305.94.

Christensen, P.R., Fergason, R.L., Edwards, C.S., Hill, J., 2013. THEMIS-derived thermal inertia mosaic of Mars: product description and science results. Lunar and Planetary Science Conference Abstracts vol. 44 (p. #2822).

de Pablo, M.Á., Pacifici, A., 2008. Geomorphological evidence of water level changes in Nepenthes Mensae, Mars. Icarus 196 (2), 667–671. https://doi.org/10.1016/j.icarus.2008.04.005.

Dickson, J.L., Kerber, L.A., Fassett, C.I., Ehlmann, B.L., 2018. A global, blended CTX mosaic of Mars with vectorized seam mapping: a new mosaicking pipeline using principles of non-destructive image editing. Lunar and Planetary Science Conference Abstracts vol. 49 (p. #2480).

Fergason, R.L., Christensen, P.R., Kieffer, H.H., 2006. High-resolution thermal inertia derived from the Thermal Emission Imaging System (THEMIS): Thermal model and applications. J. Geophys. Res. Planets 111(E12). https://doi.org/10.1029/2006JE002735.

Fergason, R.L., Hare, T.M., Laura, J., 2018. HRSC and MOLA Blended Digital Elevation Model at 200m v2, Astrogeology PDS Annex. U.S. Geological Survey http://bit.ly/HRSC_MOLA_Blend_v0.

García-Arnay, Á., Gutiérrez, F., de Pablo, M.Á., Fernández, S., 2018a. Characterization and interpretation of the fan-shaped and terrace-like features identified in Nepenthes Mensae, Mars. EGU General Assembly Conference Abstracts vol. 20 (p. # 808). Retrieved from https://figshare.com/articles/Characterization_and_interpretation_of_the_fanshaped_and_terrace-like_features_identified_in_Nepenthes_Mensae_Mars/9824609.

García-Arnay, Á., Fernández, S., de Pablo, M.Á., Gutiérrez, F., 2018b. The dominant morphogenetic role of surface runoff in Licus Vallis, Mars: results from geomorphological and morphometric analyses. Geogaceta 63, 63–66 Retrieved from. http://www.sociedadgeologica.es/archivos/geogacetas/geo63/geo63_16.pdf.

García-Arnay, Á., Gutiérrez, F., 2020. Reconstructing paleolakes in Nepenthes Mensae, Mars, using the distribution of putative deltas, coastal-like features, and terrestrial analogs. Geomorphology 359, 107129. https://doi.org/10.1016/j.geomorph.2020.107129.

Goudge, T.A., Fassett, C.I., 2018. Incision of Licus Vallis, Mars, from multiple lake overflow floods. J. Geophys. Res. Planets 123 (2), 405–420. https://doi.org/10.1002/2017JE005438.

Greeley, R., Guest, J., 1987. Geologic map of the eastern equatorial region of Mars. U.S. Geological Survey, IMAP 1802, Scale 1:5,000,000. https://doi.org/10.3133/i1802B.

Greeley, R., Batson, R.M., 1990. Planetary Mapping. Cambridge Univ. Press p. 296.

Hansen, V.L., 2000. Geologic mapping of tectonic planets. Earth Planet. Sc. Lett. 176(3–4), 527–542. https://doi.org/10.1016/S0012-821X(00)00017-0.

Hartmann, W.K., 2005. Martian cratering 8: isochron refinement and the chronology of Mars. Icarus 174 (2), 294–320. https://doi.org/10.1016/j.icarus.2004.11.023.

Hiller, K.H., 1979. Geologic map of the Amenthes Quadrangle of Mars. U.S. Geological Survey, IMAP 1110, Scale 1:5,000,000. https://doi.org/10.3133/i1110.

Irwin, R.P., Howard, A.D., 2002. Drainage basin evolution in Noachian Terra Cimmeria, Mars. J. Geophys. Res. Planets 107 (E7). https://doi.org/10.1029/2001JE001818.

Irwin III, R.P., Watters, T.R., Howard, A.D., Zimbelman, J.R., 2004. Sedimentary resurfacing and fretted terrain development along the crustal dichotomy boundary, Aeolis Mensae, Mars. J. Geophys. Res. Planets 109(E9). https://doi.org/10.1029/2004JE002248.

Irwin, R.P., Howard, A.D., Craddock, R.A., Moore, J.M., 2005. An intense terminal epoch of widespread fluvial activity on early Mars: 2. Increased runoff and paleolake development. J. Geophys. Res. Planets 110 (E12). https://doi.org/10.1029/2005JE002460.

King, E.A., 1978. Geologic map of the Mare Tyrrhenum Quadrangle of Mars. US Geological Survey Report, IMAP 1073. https://doi.org/10.3133/i1073.

Kneissl, T., van Gasselt, S., Neukum, G., 2011. Map-projection-independent crater size-frequency determination in GIS environments—new software tool for ArcGIS. Planet. Space Sci. 59 (11), 1243–1254. https://doi.org/10.1016/j.pss.2010.03.015.

Levy, J.S., Head, J.W., Marchant, D.R., 2007. Lineated valley fill and lobate debris apron stratigraphy in Nilosyrtis Mensae, Mars: Evidence for phases of glacial modification of the dichotomy boundary. J. Geophys. Res. Planets 112(E8). https://doi.org/10.1029/2006JE002852.

Malin, M.C., Bell, J.F., Cantor, B.A., Caplinger, M.A., Calvin, W.M., Clancy, R.T., Lee, S.W., 2007. Context camera investigation on board the Mars Reconnaissance Orbiter. J. Geophys. Res. Planets 112 (E5). https://doi.org/10.1029/2006JE002808.

McEwen, A.S., Eliason, E.M., Bergstrom, J.W., Bridges, N.T., Hansen, C.J., Delamere, W.A., Grant, J.A., Gulick, V.C., Herkenhoff, K.E., Keszthelyi, L., Kirk, R.L., Mellon, M.T., Squyres, S.W., Thomas, N., Weitz, C.M., 2007. Mars reconnaissance orbiter's high resolution imaging science experiment (HiRISE). J. Geophys. Res. Planets 112 (E5). https://doi.org/10.1029/2005JE002605.

McGill, G.E., Dimitriou, A.M., 1990. Origin of the Martian global dichotomy by crustal thinning in the late Noachian or early Hesperian, J. Geophys. Res. 95, 12,595–12,605. https://doi.org/10.1029/JB095iB08p12595.

Michael, G.G., 2013. Planetary surface dating from crater size–frequency distribution measurements: multiple resurfacing episodes and differential isochron fitting. Icarus 226 (1), 885–890. https://doi.org/10.1016/j.icarus.2013.07.004.

Michael, G.G., Neukum, G., 2010. Planetary surface dating from crater size–frequency distribution measurements: partial resurfacing events and statistical age uncertainty. Earth Planet. Sci. Lett. 294 (3), 223–229. https://doi.org/10.1016/j.epsl.2009.12.041.

Parenti, C., Gutiérrez, F., Baioni, D., García-Arnay, Á., Sevil, J., Luzzi, E., 2020. Closed depressions in Kotido crater, Arabia Terra, Mars. Possible evidence of evaporite dissolution-induced subsidence. Icarus 341, 113680. https://doi.org/10.1016/j.icarus.2020.113680

Rivera-Hernández, F., Palucis, M.C., 2019. Do deltas along the crustal dichotomy boundary of Mars in the Gale crater region record a northern ocean? Geophys. Res. Lett. 46, 8689–8699. https://doi.org/10.1029/2019GL083046.

Scott, D.H., Carr, M.H., 1978. Geologic Map of Mars: U.S. Geological Survey Investigations Series, I-1083, Scale 1:25,000,000. http://pubs.er.usgs.gov/publication/i1083.

Skinner Jr, J.A., Tanaka, K.L., 2003. How should planetary map units be defined? Lunar and Planetary Science Conference Abstracts vol. 34 (p. #2100). Retrieved from: https://www.lpi.usra.edu/meetings/lpsc2003/pdf/2100.pdf.

Skinner Jr, J.A., Tanaka, K.L., 2018. Geological Map of the Nepenthes Planum Region, Mars. US Geological Survey Scientific Investigations Map 3389, Scale 1:1,506,000. https://doi.org/10.3133/sim3389.

Tanaka, K.L., Chapman, M.G., Scott, D.H., 1992. Geologic map of the Elysium region of Mars. US Geological Survey Report, IMAP 2147. https://doi.org/10.3133/i2147.

Tanaka, K.L., Skinner, J.A., Hare, T.M., 2005. Geologic map of the northern plains of Mars. US Geological Survey Scientific Investigations Map 2888, Scale 1:15,000,000. https://doi.org/10.3133/sim2888.

Tanaka, K.L., Skinner Jr., J.A., Dohm, J.M., Irwin III, R.P., Kolb, E.J., Fortezzo, C.M., Platz, T., Michael, G.G., Hare, T.M., 2014. Geologic Map of Mars. US Geological Survey Scientific Investigations Map 3292, Scale 1:20,000,000. pamphlet 43 p. https://doi.org/10.3133/sim3292.

Warner, N.H., Gupta, S., Calef, F., Grindrod, P., Boll, N., Goddard, K., 2015. Minimum effective area for high resolution crater counting of Martian terrains. Icarus 245, 198–240. https://doi.org/10.1016/j.icarus.2014.09.024.

Watters, T.R., 1988. Wrinkle ridge assemblages on the terrestrial planets. J. Geophys. Res. Solid Earth 93(B9), 10236-10254. https://doi.org/10.1029/JB093iB09p10236.

Watters, T.R., 2003a. Lithospheric flexure and the origin of the dichotomy boundary on Mars, Geology 31, 271–274. https://doi.org/10.1130/0091-7613(2003)031%3C0271:LFATOO%3E2.0.CO;2.

Watters, T.R., 2003b. Thrust faults along the dichotomy boundary in the eastern hemisphere of Mars, J. Geophys. Res. Planets 108(E6), 5054. https://doi.org/10.1029/2002JE001934.

Watters, T.R., Robinson, M.S., 1999. Lobate scarps and the Martian crustal dichotomy. J. Geophys. Res. Planets 104(E8), 18981-18990. https://doi.org/10.1029/1998JE001007.

Watters, T.R., McGovern, P.J., 2006. Lithospheric flexure and the evolution of the dichotomy boundary on Mars. Geophys. Res. Lett. 33(8). https://doi.org/10.1029/2005GL024325.

Watters, T.R., Solomon, S.C., Robinson, M.S., Head, J.W., André, S.L., Hauck II, S.A., Murchie, S.L., 2009. The tectonics of Mercury: The view after MESSENGER's first flyby. Earth Planet. Sc. Lett. 285(3-4), 283-296. https://doi.org/10.1016/j.epsl.2009.01.025.

Wilhelms, D.E., 1990. Geologic mapping. In: Greeley, R., Batson, R.M. (Eds.), Planetary Mapping. Cambridge University Press, NY, pp. 208-260.

Zuber, M.T., Smith, D.E., Solomon, S.C., Muhleman, D.O., Head, J.W., Garvin, J.B., 1992. The Mars Observer laser altimeter investigation. J. Geophys. Res. Planets 97 (E5), 7781–7797. https://doi.org/10.1029/92JE00341.

Appendix

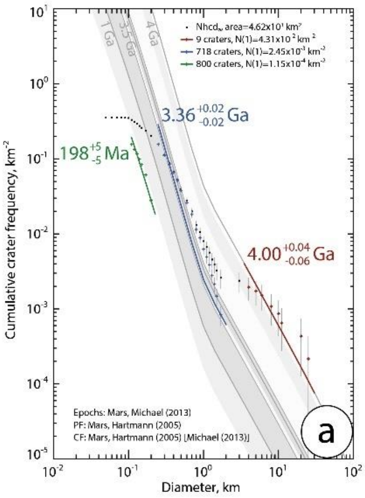
Nhcd_w, area=4.62x10¹ km²
9 craters, N(1)=4.31x10⁻² km⁻²
718 craters, N(1)=2.45x10⁻³ km⁻²
800 craters, N(1)=1.15x10⁻⁴ km⁻²
1 Ga
3.5 Ga
4 Ga
198 +5 -5 Ma
3.36 +0.02 -0.02 Ga
4.00 +0.04 -0.06 Ga
Epochs: Mars, Michael (2013)
PF: Mars, Hartmann (2005)
CF: Mars, Hartmann (2005) [Michael (2013)]
a
Cumulative crater frequency, km⁻²
Diameter, km

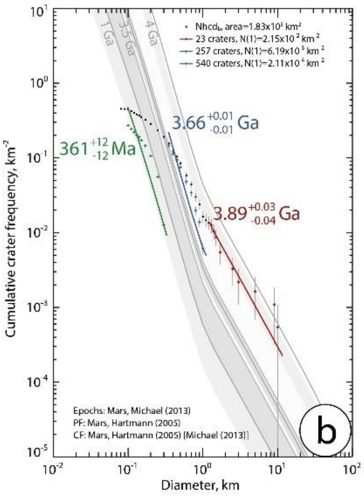
Nhcd_b, area=1.83x10³ km²
23 craters, N(1)=2.15x10⁻² km⁻²
257 craters, N(1)=6.19x10⁻³ km⁻²
540 craters, N(1)=2.11x10⁻⁴ km⁻²
1 Ga
3.5 Ga
4 Ga
361 +12 -12 Ma
3.66 +0.01 -0.01 Ga
3.89 +0.03 -0.04 Ga
Epochs: Mars, Michael (2013)
PF: Mars, Hartmann (2005)
CF: Mars, Hartmann (2005) [Michael (2013)]
b
Cumulative crater frequency, km⁻²
Diameter, km

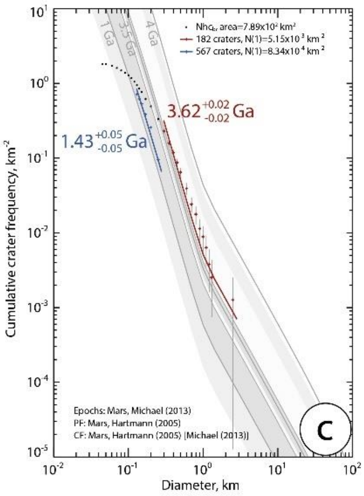
Nhc_b, area=7.89x10² km²
182 craters, N(1)=5.15x10⁻³ km⁻²
567 craters, N(1)=8.34x10⁻⁴ km⁻²
1 Ga
3.5 Ga
4 Ga
1.43 +0.05 -0.05 Ga
3.62 +0.02 -0.02 Ga
Epochs: Mars, Michael (2013)
PF: Mars, Hartmann (2005)
CF: Mars, Hartmann (2005) [Michael (2013)]
c
Cumulative crater frequency, km⁻²
Diameter, km

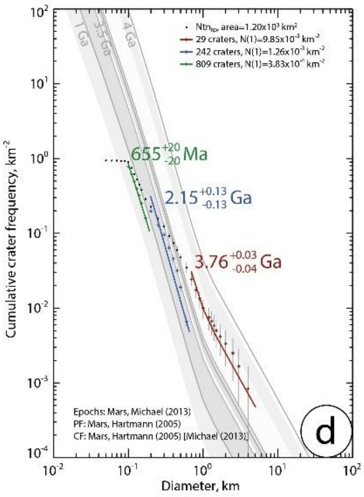
Ntn_lo, area=1.20x10³ km²
29 craters, N(1)=9.85x10⁻³ km⁻²
242 craters, N(1)=1.26x10⁻³ km⁻²
809 craters, N(1)=3.83x10⁻⁴ km⁻²
1 Ga
3.5 Ga
4 Ga
655 +20 -20 Ma
2.15 +0.13 -0.13 Ga
3.76 +0.03 -0.04 Ga
Epochs: Mars, Michael (2013)
PF: Mars, Hartmann (2005)
CF: Mars, Hartmann (2005) [Michael (2013)]
d
Cumulative crater frequency, km⁻²
Diameter, km

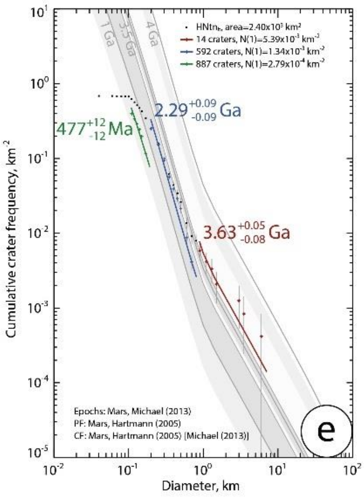
HNtn_s, area=2.40x10³ km²
14 craters, N(1)=5.39x10⁻³ km⁻²
592 craters, N(1)=1.34x10⁻³ km⁻²
887 craters, N(1)=2.79x10⁻⁴ km⁻²
1 Ga
3.5 Ga
4 Ga
477 +12 -12 Ma
2.29 +0.09 -0.09 Ga
3.63 +0.05 -0.08 Ga
Epochs: Mars, Michael (2013)
PF: Mars, Hartmann (2005)
CF: Mars, Hartmann (2005) [Michael (2013)]
e
Cumulative crater frequency, km⁻²
Diameter, km

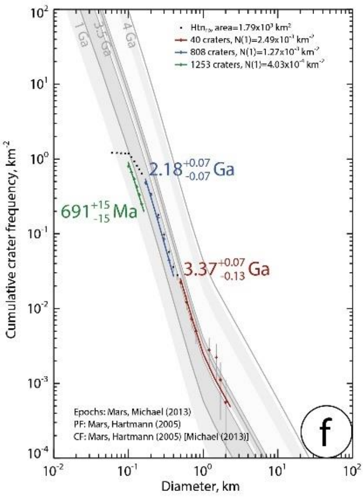
Htn_ro, area=1.79x10³ km²
40 craters, N(1)=2.49x10⁻³ km⁻²
808 craters, N(1)=1.27x10⁻³ km⁻²
1253 craters, N(1)=4.03x10⁻⁴ km⁻²
1 Ga
3.5 Ga
4 Ga
691 +15 -15 Ma
2.18 +0.07 -0.07 Ga
3.37 +0.07 -0.13 Ga
Epochs: Mars, Michael (2013)
PF: Mars, Hartmann (2005)
CF: Mars, Hartmann (2005) [Michael (2013)]
f
Cumulative crater frequency, km⁻²
Diameter, km

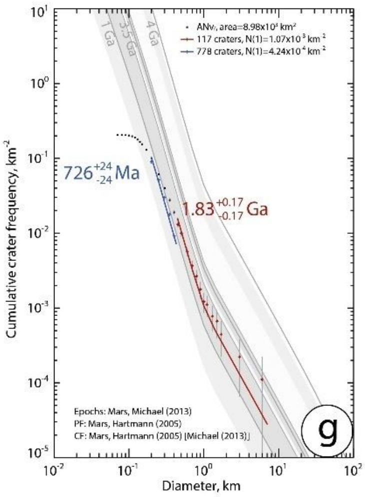
ANv_f, area=8.98x10³ km²
117 craters, N(1)=1.07x10⁻³ km⁻²
778 craters, N(1)=4.24x10⁻⁴ km⁻²
1 Ga
3.5 Ga
4 Ga
726 +24 -24 Ma
1.83 +0.17 -0.17 Ga
Epochs: Mars, Michael (2013)
PF: Mars, Hartmann (2005)
CF: Mars, Hartmann (2005) [Michael (2013)]
g
Cumulative crater frequency, km⁻²
Diameter, km

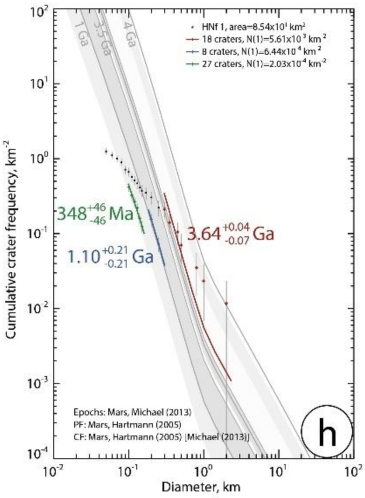
HNf 1, area=8.54x10¹ km²
18 craters, N(1)=5.61x10⁻³ km⁻²
8 craters, N(1)=6.44x10⁻⁴ km⁻²
27 craters, N(1)=2.03x10⁻⁴ km⁻²
1 Ga
3.5 Ga
4 Ga
348 +46 -46 Ma
1.10 +0.21 -0.21 Ga
3.64 +0.04 -0.07 Ga
Epochs: Mars, Michael (2013)
PF: Mars, Hartmann (2005)
CF: Mars, Hartmann (2005) [Michael (2013)]
h
Cumulative crater frequency, km⁻²
Diameter, km

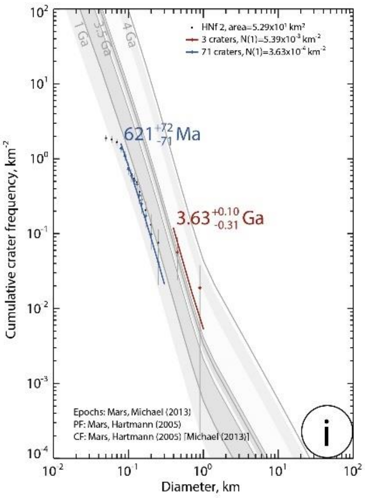
HNf 2, area=5.29x10¹ km²
3 craters, N(1)=5.39x10⁻³ km⁻²
71 craters, N(1)=3.63x10⁻⁴ km⁻²
1 Ga
3.5 Ga
4 Ga
621 +72 -71 Ma
3.63 +0.10 -0.31 Ga
Epochs: Mars, Michael (2013)
PF: Mars, Hartmann (2005)
CF: Mars, Hartmann (2005) [Michael (2013)]
i
Cumulative crater frequency, km⁻²
Diameter, km

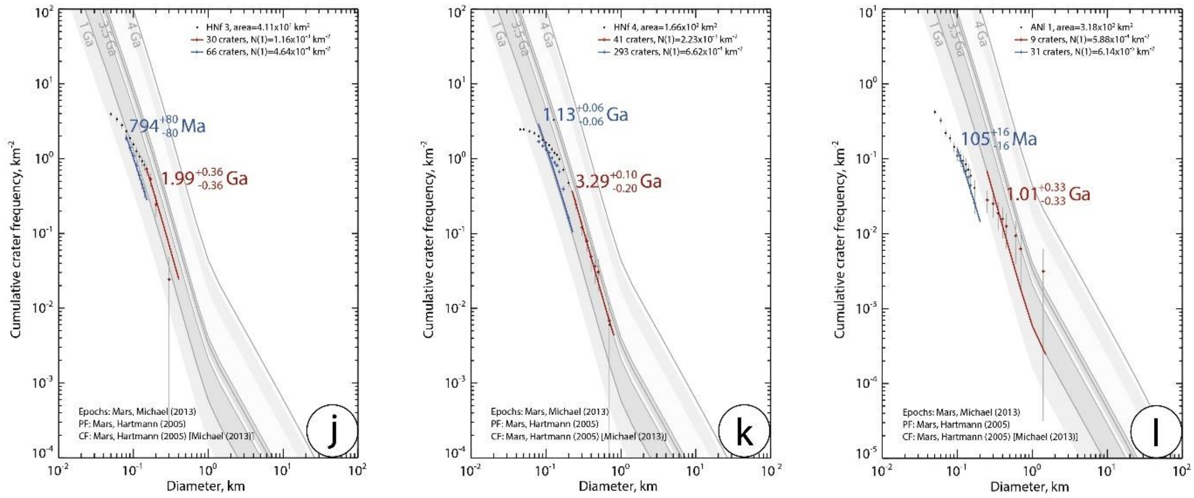

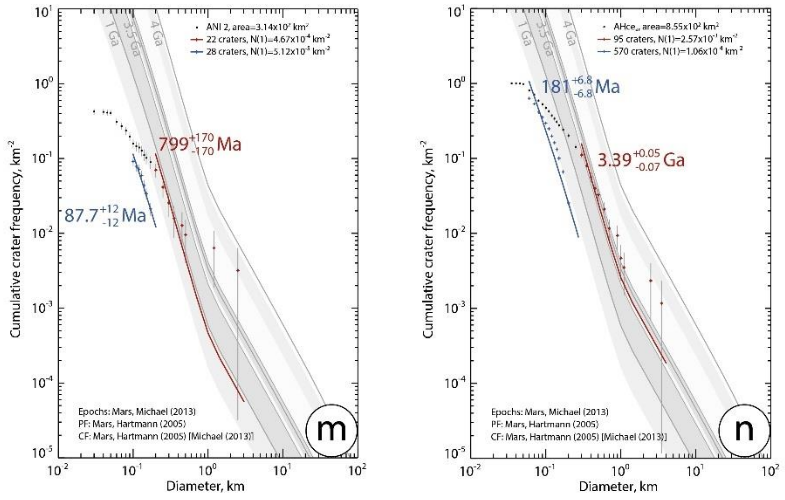

Count area	D$_{min}$ (m)	n
Nhcd$_{a}$	100	1,642
Nhcd$_{b}$	100	831
Nhc$_{b}$	50	1,428
Ntn$_{kp}$	100	1,128
HNt$_{nb}$	100	1,639
Htn$_{rp}$	100	2,159
ANv$_{f}$	100	1,836
HNf 1	50	107
HNf 2	50	100
HNf 3	50	162
HNf 4	50	411
ANl 1	50	135
ANl 2	50	133
AHce$_{a}$	50	859

***Fig. A1**: (a-n) Crater size-frequency diagrams for each counting area (see locations in Fig. 1b). Age models display simple cumulative fits for the formation ages (red fit lines), and corrected cumulative fits for the resurfacing events (blue and green fit lines). The grey shadow bands represent the time boundaries between the different Martian geological epochs (Michael, 2013). "D$_{min}$" and "n" refer to the minimum crater diameter and the number of counted craters for each counting area, respectively.*

UNRAVELLING THE GEOLOGICAL AND GEOMORPHOLOGICAL EVOLUTION OF THE TERRA CIMMERIA-NEPENTHES MENSAE TRANSITIONAL ZONE, MARS

Ángel García-Arnay(a)*, Francisco Gutiérrez(a)

[a] Departamento de Ciencias de la Tierra, Universidad de Zaragoza, 50009 Zaragoza, Spain

* Corresponding author e-mail address: arnay@unizar.es

Abstract

The Terra Cimmeria-Nepenthes Mensae Transitional Zone comprises two highly-contrasting geologic-geomorphic domains bounded by the dichotomy escarpment in the equatorial region of Mars. This research provides insight into the geological and geomorphological evolution of the poorly explored NW Terra Cimmeria and SE Nepenthes Mensae. A detailed study largely based on cartographic work and complemented by multiple analyses focused on crater densities, spectral data and radar profiles reveals that (1) the exposed geological record of this transitional zone formed over a long time-span comprising from the Early Noachian to recent times, (2) the inferred compressional and extensional tectonic stresses shaped the landscape at least from the Late Noachian to Late Hesperian, and (3) extensional tectonics, which postdated the compressional deformation, has controlled the development and evolution of the 2-km-high dichotomy escarpment, the system of NW-SE-oriented basins that used to host paleolakes from the Late Noachian to Late Hesperian, and the fissure volcanism in their deepest areas. These findings shed light into the fundamental morphogenetic role played by compressional and extensional tectonics, and fluvio-lacustrine activity on the configuration of the landscape in these regions. This work provides a reference geologic-geomorphologic framework for future studies in this area and other sectors along the highland-lowland transitional zone of Mars.

Keywords: Mars; Planetary mapping; Dichotomy boundary; Tectonic geomorphology

1. Introduction

The highland-lowland transition, often referred to as the crustal dichotomy (McCauley et al., 1972), represents one of the most prominent geomorphic features on the surface of Mars (Solomon et al., 2005), formed during the early Noachian (Tanaka et al., 1992a). This hemispheric feature that circumscribes the planet bounds two contrasting geologic and geomorphic domains comprised by the ancient, densely cratered and rough highland plateaus in the south, and the younger, sparsely cratered and relatively smooth lowland plains in the north (Morgan et al., 2009). The geomorphic expression of the Martian dichotomy varies laterally, ranging from an escarpment up to 3 km in local relief (Irwin et al., 2004), like the one with associated residual reliefs of highland materials in Nilosyrtis Mensae (Levy et al., 2007), to gently-sloping surfaces with no obvious scarp as occurs in northern Arabia Terra (McGill, 2000). Nonetheless, the highland-lowland boundary cannot be traced along the Tharsis region, where its geomorphic expression has probably been obliterated by more recent volcanic materials (Zuber et al., 2000). Studies carried out along the upland-lowland boundary have put forward various endogenic and exogenic interpretations for its formation (McGill and Squyres, 1991), which remains as an unresolved problem (e.g., Andrews-Hanna et al., 2008; Golabek et al., 2011). The main externally-driven (impact-related) hypotheses include: (1) a single “mega-impact” event responsible for the creation of the “Borealis basin” (Wilhelms and Squyres, 1984), (2) the impact “megadome” hypothesis, according to which the melt generated by a giant impact overfilled the impact basin to form the highlands (Reese et al., 2011), and (3) multiple impact depressions merged into a large basin forming the lowlands in the northern hemisphere (Frey et al., 1986; Frey and Shultz, 1988). Several endogenic hypotheses have also been proposed: (1) long-wavelength mantle convection resulting in large-scale upwelling (Zhong and Zuber, 2001; Roberts and Zhong, 2006; Ke and Solomatov, 2006), (2) long-wavelength “cumulate overturn” of a stratified magma ocean resulting from the crystallization of an early magma ocean (Elkins-Tanton et al., 2005), and (3) an early plate tectonics phase involving the creation of a thin crust in the northern hemisphere from relict spreading centers, with the crustal dichotomy representing a passive margin (Sleep, 1994). The models based on multiple impacts and plate tectonics to explain the origin of the dichotomy have not been sufficiently supported and remain as untested hypotheses (Roberts, 2015). Although the origin of the dichotomy remains as an open issue, it seems probable that multiple processes may have operated in conjunction to form this major geomorphic feature (Reese et al., 2010), which may have been subsequently modified by tectonic, fluvial, glacial, eolian, and mass wasting processes (Watters and Robinson, 1999; Tanaka et al., 2005).

The geomorphic expression of the highland-lowland boundary in Aeolis Mensae (e.g., Irwin et al., 2004; Irwin et al., 2005) is similar to that found between the cratered highlands of the northwest part of Terra Cimmeria and the lowland plains of the southeast zone of Nepenthes Mensae analyzed in this work. Both regions are characterized by the occurrence of a remarkable dichotomy escarpment (~2 km in local relief) and closed depressions in the lowlands interrupted by mesas and knobs made up of materials of the highland plateau. According to Irwin et al. (2004), the latter landforms probably correspond to residual reliefs resulting from fracture-controlled differential erosion acting along the edge of the escarpment. In these regions, as well as in Nilosyrtis Mensae, the highland residuals north of the escarpment show an increasing degree of degradation grading northward from mesas to sparse knobs (Irwin et al., 2004). The approximate alignment of mesa margins, buttes and knobs in Nilosyrtis Mensae, as well as the straightness and orientation of valleys, mostly parallel to the dichotomy escarpment, have been associated with the occurrence of Noachian-aged grabens along the crustal dichotomy (Levy et al., 2007). These transitional provinces show various morpho-tectonic features such as fracture-controlled linear valleys known as fretted valleys, extensional troughs forming chains of closed depressions in the lowlands, and lobate scarps ascribable to thrust faults in the adjacent highlands (McGill and Dimitriou, 1990; Watters, 2003a, 2003b; Watters and McGovern, 2006).

This work is focused on the highly contrasting transitional zone of NW Terra Cimmeria and SE Nepenthes Mensae, which remains as a poorly understood area (e.g., Skinner and Tanaka, 2018) and offers the opportunity for gaining insight into the processes involved in the development and evolution of the dichotomy escarpment. This area has been covered by multiple global and regional geologic maps produced by the United States Geological Survey (USGS, U.S. Department of the Interior) (e.g., King, 1978; Scott and Carr, 1978; Hiller, 1979; Greeley and Guest, 1987; Tanaka et al., 1992b; Tanaka et al., 2005; Tanaka et al., 2014). Recently, Skinner and Tanaka (2018) produced the regional-scale geologic map of the transition zone between Terra Cimmeria and Utopia Planitia, which is located northwest of our study area. Due to its proximity, this map provides a geological framework with which to compare our study. In the last few years, several authors have highlighted the important role played by surface water on the configuration of NW Terra Cimmeria and SE Nepenthes Mensae (e.g., Goudge and Fassett, 2018; Rivera-Hernández and Palucis, 2019; García-Arnay and Gutiérrez, 2020). In particular, putative deltas, shore platforms and paleolakes associated with a belt of closed depressions distributed along the foot of the dichotomy escarpment illustrate the value of geomorphic studies for understanding the role of the hydrosphere of Mars in the past (García-Arnay and Gutiérrez, 2020). However, despite its importance, there is a lack of detailed cartographic studies to furnish knowledge about the geological context and the evolution of this transitional zone. Areas located close to our study region have been selected as landing sites for several missions due to their low latitude, potential for paleoenvironmental research, and/or pervasive planarity (e.g., NASA's Mars Science Laboratory "Curiosity" and InSight missions settled in Gale crater and SW Elysium Planitia, respectively). The Nepenthes Planum region has been also targeted as a favorable landing site over time (e.g., NASA's Viking lander 1, Mars Pathfinder and Mars Exploration Rover missions or ESA's Beagle 2 mission), but finally discarded due to lack of sufficient knowledge about its geology (Skinner and Tanaka, 2018).

In this study, we have carried out a comprehensive local- and regional-scale geological study of NW Terra Cimmeria and SE Nepenthes Mensae largely based on cartographic work with the following purposes: (1) improve our knowledge on the geology and geomorphology of this transitional zone; (2) infer the processes responsible for the formation of the system of closed depressions that used to host paleolakes; (3) analyze the evolution of the dichotomy escarpment; and (4) reconstruct the geological-geomorphological history of the region. In order to achieve these objectives, we have produced a detailed geologic-geomorphic map identifying and describing the different units and features, analyzing their geometrical relationships, and correlating the units with those of the previous geological maps. We have also inferred the mineral composition of surface materials of paleoenvironmental interest, estimated the numerical age of the main mapped units, and interpreted subsurface structures from the analysis of radargrams.

2. Regional setting in the highland-lowland boundary

The study area is located in the Terra Cimmeria-Nepenthes Mensae Transitional Zone (CNTZ), comprising two contrasting geologic-geomorphic domains bounded by the dichotomy escarpment, in the equatorial region of Mars (Fig. 1). The sector of the CNTZ analyzed in this work corresponds to the northwest part of Terra Cimmeria and the southeast zone of Nepenthes Mensae. Terra Cimmeria forms part of the highland province, south of the dichotomy boundary, and was mapped as a Middle Noachian highland unit (mNh) characterized by moderately to heavily degraded terrains formed by undifferentiated impact, volcanic, fluvial and basin materials, according to the most recent global geological map of Mars (Tanaka et al., 2014). This heavily cratered region has been tectonically contracted, as indicated by the presence of numerous lobate scarps and wrinkle ridges (e.g., Watters and Robinson, 1999). It is also dissected by ancient V-shaped fluvial valleys (e.g., Irwin and Howard, 2002), which mouths are located along the dichotomy escarpment, with a local relief of around 2 km. The valleys seem to be locally disrupted by compressional tectonic deformation, as suggests the occurrence of beheaded channels associated with lobate scarps. They also show a clear structural control in the vicinity of the dichotomy, following the orientation of morpho-structural troughs both subparallel and subperpendicular to the escarpment, probably generated by extensional tectonic deformation and/or lateral spreading along the dichotomy (see Fig. 2a). Licus Vallis, which is the main ancient fluvial valley in the study area, shows an apparently poorly-evolved watershed, as suggested by its convex hypsometric curve and a very low drainage density (García-Arnay et al., 2018b). The paired terraces and knickpoints observed within this and other valleys seem to support base-level variations in the mouth area of the watersheds and/or rejuvenation by vertical tectonic movements (Goudge and Fassett, 2018). Furthermore, the majority of the valley networks, including Licus Vallis, show moderately preserved fan-shaped deposits at their mouths, most of them interpreted as Gilbert-type deltas and alluvial fans (e.g., Irwin et al., 2005; de Pablo and Pacifici, 2008; García-Arnay et al., 2018a, 2018b; Rivera-Hernández and Palucis, 2019; García-Arnay and Gutiérrez, 2020).

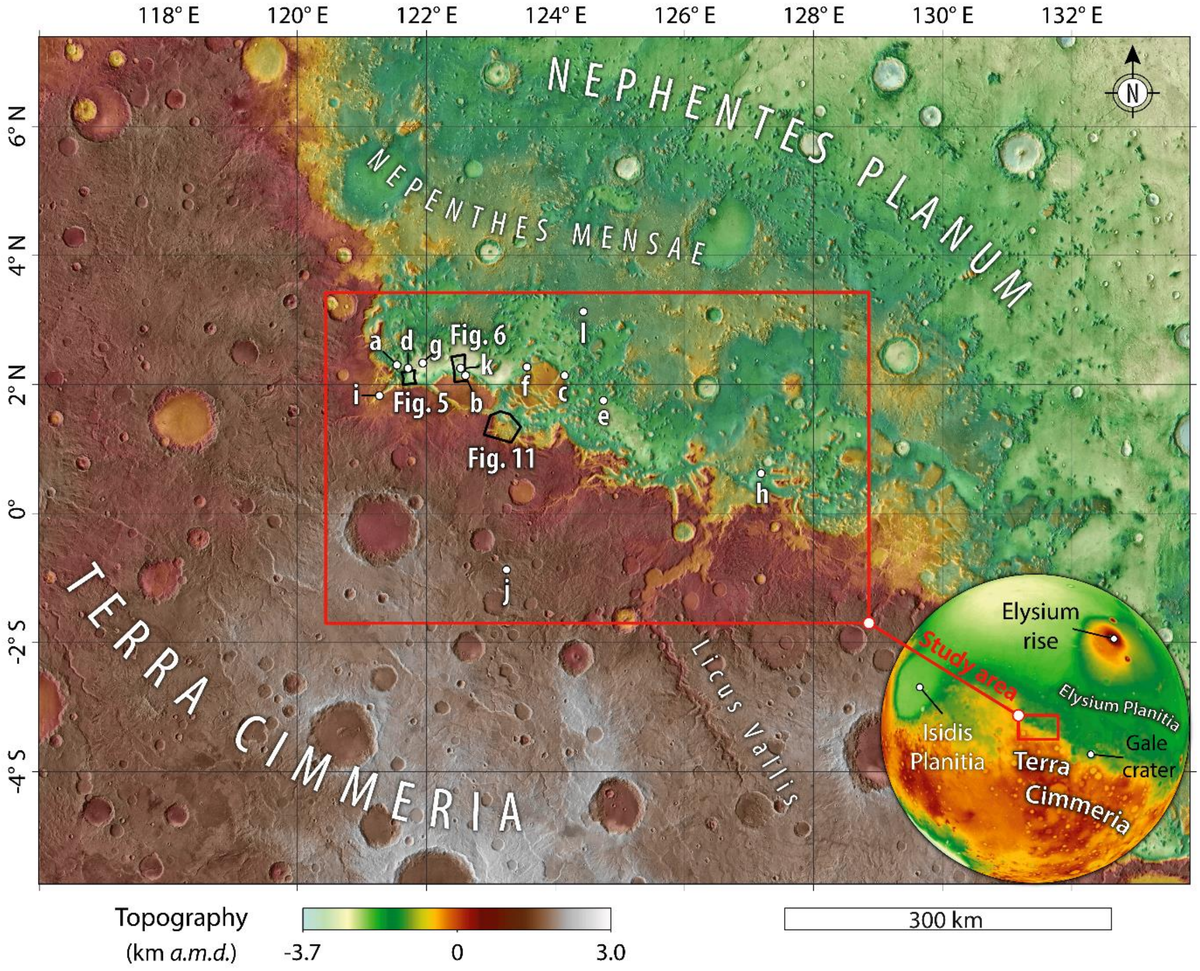

Fig. 1. Colorized elevation model (km above Martian datum) derived from HRSC-MOLA blended data over a base mosaic map of THEMIS-IR day images, with the study area framed by the red rectangle. The small white circles and their corresponding labels indicate the position of the images shown in Fig. 3. Black polygons indicate the area covered by the 3D model of Fig. 11, and the location of the CRISM images shown in Figs. 5 and 6.

The terrains north of Terra Cimmeria correspond to the region of Nepenthes Mensae, which is part of the transitional province north of the dichotomy. It was mapped as a Hesperian and Noachian transition unit (HNt) and described as Noachian impact breccias, volcanic rocks, and aprons formed by mass-wasted deposits during the Hesperian (Tanaka et al., 2014). This region displays two contrasting areas: (1) tectonically-contracted plateaus with eolian erosional landforms, and (2) a belt of interconnected NW-SE-trending closed depressions at the foot of the dichotomy escarpment in the knobby terrain (Irwin et al., 2004). These closed depressions together with the dichotomy escarpment are probably related to extensional deformation (Watters, 2003a; Watters and McGovern, 2006). Both areas display numerous residual reliefs (mesas and knobs) formed by highland materials. The presence of structural elements along the dichotomy may have also controlled the erosion pattern of the highlands, as suggested by fracture-controlled erosional troughs displayed by residual reliefs such as mesas (see Fig. 2a). The identification of fan-shaped deposits and coastal-like benches associated with the closed depressions, interpreted as putative Gilbert-type deltas and paleoshore platforms, respectively (García-Arnay and Gutiérrez, 2020), may be attributable to landforms developed along the shores of interconnected paleolakes.

3. Data and methods

Imagery, topographic and spectral data, as well as radar profiles were used to map and infer the geology, geomorphology, age, surface composition, and internal structure of the CNTZ. Visible imagery included panchromatic images acquired by the Context Camera (CTX, 5-6 m/pixel) (Malin et al., 2007), and additional images from the High Resolution Imaging Science Experiment (HiRISE, ~25-50 cm/pixel) (McEwen et al., 2007), both instruments on board NASA's Mars Reconnaissance Orbiter. The global CTX image mosaic (Dickson et al., 2018) covers the totality of the CNTZ, whereas HiRISE images cover specific zones of the study area. Infrared imagery comprised the daytime infrared image mosaic obtained by the Thermal Emission Imaging System (THEMIS, 100 m/pixel) (Christensen et al., 2004, 2013), on board NASA's Mars Odyssey. In order to differentiate surface materials on the basis of their thermophysical properties, we used the THEMIS-based thermal inertia (TI) (Fergason et al., 2006), which is derived from the nighttime infrared image mosaic captured by THEMIS.

Topographic data were extracted from Digital Elevation Models (DEMs) acquired by instruments with different spatial resolutions and coverages: laser altimeter point shots from the Mars Orbiter Laser Altimeter (MOLA, 463 m/pixel) (Zuber et al, 1992), on board NASA's Mars Global Surveyor, as well as stereo-pair images from the High Resolution Stereo Camera (HRSC, 50-75 m/pixel), on board ESA's Mars Express. The characterization and morphometric analysis of the landforms were carried out using, where possible, the HRSC-derived topographic data that displays the best spatial resolution. In order to cover areas where HRSC data are not available, we used a HRSC and MOLA blended DEM (Fergason et al., 2018, ~200 m/pixel). The imagery and topographic data were integrated into a Geographic Information System (ESRI's ArcGIS 10.5.1) to map and carry out multiple analyses. Spatial data were projected into the geographic coordinate system "GCS_Mars_2000_Sphere", with an equidistant cylindrical projection and a central meridian of 125°E, that is approximately located in the center of the CNTZ.

The geologic-geomorphic map (Fig. 2a) was produced applying methodologies and techniques used in planetary geological mapping (e.g., Greeley and Batson, 1990; Wilhelms, 1990), as well as in geological mapping of Mars (e.g., Skinner and Tanaka, 2003; Tanaka et al., 2014; Skinner and Tanaka, 2018). We mainly used a combination of imagery (visible and infrared) and topographic data that permitted the identification of the surface units essentially on the basis of their primary surface features (Skinner and Tanaka, 2003). This approach was also used for the characterization of the units, the analysis of their geometrical relationships, and their correlation. We used the THEMIS daytime infrared image mosaic as a primary base map to identify the lateral extent of the units. CTX and HiRISE images, as well as the TI mosaic, were used as supplementary datasets for refining the mapping of the boundaries of the units and interpreting their origin. The spectral data provided information on the mineral composition of some units of special interest (e.g., delta deposits and volcanic materials). The mapped units were named (see Fig. 2a) on the basis of their geographic location, where applicable, dominant landforms and/or genesis, as well as stratigraphic relations, in order to maintain the consistency (Hansen, 2000; Tanaka et al., 2005; Skinner and Tanaka, 2018). The units were also labeled and grouped (Fig. 2a) following an analogous methodology to that applied by Skinner and Tanaka (2018) for the geological map of Nepenthes Planum. The drainage network was initially mapped automatically using the toolset "Hydrology" in ArcGIS, and was later improved by removing manually numerous artifacts using visible imagery and TI data. The frequent occurrence of unconsolidated sediments (e.g., eolian deposits) in the valley floors, characterized by a lower apparent TI (Fig 2c), helped to improve the delineation of the drainage network. The mapping of the putative deltas and alluvial fans was challenging due to their moderate preservation conditions. We decided to delineate the proximal edges of the putative deltas and alluvial fans where the flows debouching from the fluvial valleys used to become unconfined (García-Arnay and Gutiérrez, 2020). Based on the new map, we present an updated summary table of both new and previously published putative deltas and alluvial fans located within and in the vicinity of the study area (Table 1). Elevation values were extracted from the slope break between the delta plain and the delta front junction, interpreted as the mean highstand level (e.g., Di Achille and Hynek, 2010). Several morphological features were also described such as layering, the occurrence of lobes and stepped profiles, or the type of watershed. All crater rims >5 km in diameter have been mapped. Well-preserved and pervasive crater materials with rim diameter ranging between 5 and 13 km were mapped as "Crater unit – undivided". This unit does not distinguish the different crater-related components due to their relatively small size in comparison with the map scale. In contrast, the preserved components (i.e., rim, wall, floor, peak, and ejecta) of craters ≥13 km in rim diameter were depicted in the map. Azimuth data from mapped landforms of interest (troughs and volcanic ridges) were extracted automatically with the "Minimum Bounding Geometry" tool available on "Data Management" toolbox of ArcGIS, and plotted on rose diagrams with GeoRose 0.5.1 software (Yong Technology Inc.) (see Fig. 4).

The mineral composition of the surficial material of units of interest was inferred from hyperspectral data obtained by the Compact Reconnaissance Imaging Spectrometer for Mars (CRISM, ~18-36 m/pixel) (Murchie et al., 2007), onboard NASA's Mars Reconnaissance Orbiter. The CRISM instrument is a visible-infrared imaging spectrometer with a wavelength range from 0.362 to 3.92 µm. We selected CRISM data with corrected I/F (radiance/solar irradiance) from the Targeted Empirical Record (TER) and the Map-projected Targeted Reduced Data Record (MTRDR). The spectral analysis was carried out using the CRISM Analysis Toolkit (CAT, version 7.3.1), an IDL/ENVI-based software system developed by the CRISM Science Team (Morgan et al., 2014). Spectral curves and spectral parameter maps were obtained, respectively, from the corrected I/F, and the refined spectral summary parameters (Viviano-Beck et al., 2014). We analyzed two CRISM scenes: FRT00017610 (~18 m/pixel, ~10x10 km) and HRL000134F5 (~36 m/pixel, ~10x20 km) in order to determine the composition of surface material in two different areas with paleoenvironmental interest. These CRISM scenes include fan-shaped deposits previously interpreted as deltas, and spatially associated fluvial and volcanic deposits (Figs. 5a and 6a). The occurrence of clay-bearing surfaces was identified on spectral parameter maps obtained by the PHY product (D2300 -red-, D2200 -green-, BD1900r2 -blue-) for both projected CRISM scenes following the procedure described by Viviano-Beck et al. (2014) (see Figs. 5b and 6c). Surfaces with olivine-bearing deposits were detected from the spectral parameter map derived from the MAF product (OLINDEX3 -red-, LCPINDEX2 -green-, HCPINDEX2 -blue-) for the projected CRISM scene HRL000134F5 (see Fig. 6b). In order to highlight these compositional units (i.e., clay- and olivine-bearing units), we adjusted the values displayed for each RGB channel applying stretch limits. I/F spectra were extracted from the unprojected CRISM scene FRT00017610 and averaged from a Region of Interest (ROI) selected for each compositional unit to obtain average spectra (s1). In order to minimize atmospheric contributions and instrument artifacts, these average spectra (s1) were ratioed to an average spectrum from a ROI of relatively spectrally featureless materials (s2) extracted from the CRISM scene. The ratioed I/F spectra (s1/s2) were compared with the CRISM and ENVI spectral libraries (Viviano-Beck et al., 2015) (Figs. 5c, d) in order to identify minerals that best match to CRISM spectra.

Numerical dating of surface units was carried out following the procedure proposed by Warner et al. (2015). Crater-counting areas for each unit of interest (Fig. 2b) and their associated crater populations were mapped and computed using the “CraterTools” toolset for ESRI’s ArcGIS (Kneissl et al., 2011). Depending on the spatial resolution and noise level of the visible imagery available (i.e., CTX or HRISE), all primary craters larger than 50 or 100 m in diameter (threshold values) with geometric centers within the count area were mapped manually based on three points selected along the crater rim. In general, we decided to exclude from our count areas the surfaces occupied by well-preserved ejecta blankets and their superposed crater populations because they represent the age of the impact event and postdate the target surface (Warner et al., 2015). However, crater populations on ejecta blankets were included when it was necessary to estimate the age of the associated impact event. In order to minimize the potential bias derived from the variable cratering pattern, we selected, where possible, crater-counting areas larger than 1,000 km^2 (Warner et al., 2015). Crater size-frequency diagrams for each sampling area (Fig. 7) were generated using CraterStats2 software (Michael and Neukum, 2010) and the absolute age models were derived from crater production and chronology functions defined by Hartmann (2005). The numerical age of the units (i.e., the age range estimated for the end of their formation), as well as the final age of the resurfacing events were estimated from simple and corrected cumulative data-dependent fits, respectively (see summarized age chart in Fig. 9). The assignation of the chronologic period(s) and epoch of Mars (Michael, 2013) to each mapped unit, which is indicated in the unit codes in capital letters (see map legend in Fig. 2a), was based on both the numerical age estimates obtained by crater counting and their relative chronology inferred from geometrical relationships.

The analysis of radargrams contributed to the interpretation of the subsurface structure of the CNTZ (see Fig. 8). We selected 8 radargrams located across the CNTZ (from West to East: S_01966502, S_02617902, S_01832001, S_02674602, S_02596802, S_01981001, S_01846503, S_02569101) that were obtained by the Mars Shallow Radar Sounder (SHARAD) (Seu et al., 2007), on board NASA’s Mars Reconnaissance Orbiter. These NE-SW-oriented radargrams were analyzed with the JMARS 5 software (ASU's Mars Space Flight Facility), which permitted us in combination with geomorphic data to identify possible tectonic and stratigraphic features. Geologic cross-sections shown in Figs. 10 and 12 summarize our interpretation of the subsurface stratigraphic relationships among the units, as well as the possible tectonic structures that occur along the profiles. They were constructed on the basis of the information provided by radargrams, topographic data, the geologic units, as well as the spectral analysis and formation ages of the units.

4. Results

4.1 Geology and geomorphology of the CNTZ

We have produced a detailed geological-geomorphological map of the CNTZ in order to identify and characterize the geologic units and the geomorphic features, establishing their spatial relationships and relative chronology (Fig. 2a). In our map we have recognized 18 units, which have been grouped according to their geographic distribution as follows: three units in the Cimmeria region of the highland province, two units in the Nepenthes Mensae region of the highland-lowland transitional province, seven impact crater units, and six spatially-dispersed units. Furthermore, we have depicted the main geomorphic features that occur within the units.

4.1.1 Description of the units

The Cimmeria region units include two Cimmeria dissected units ($\mathrm{Nhcd_a}$ and $\mathrm{Nhcd_b}$) and the Cimmeria basin unit ($\mathrm{Nhc_b}$) (Fig. 2a). Both Cimmeria dissected units are characterized by rugged and heavily cratered surfaces dissected by V-shaped valley networks (e.g., Tanaka et al., 2005, 2014; Skinner and Tanaka, 2018). These units represent two well-differentiated members. Member a ($\mathrm{Nhcd_a}$) crops out in the topographically higher portion of the highland province, mainly in the southwest sector of the mapped area. It displays a higher crater density than member b, lobate scarps with a dominant NW-SE orientation subparallel to the dichotomy, and less frequently ridge crests. Member b of the Cimmeria dissected unit ($\mathrm{Nhcd_b}$) occurs in the plateau situated south of the dichotomy escarpment at lower elevation than member a ($\mathrm{Nhcd_a}$), and is represented by residual reliefs (e.g., mesas and knobs) in the transitional province. This heavily dissected but less-cratered member exhibits deeper valleys with a dominant NE-SW orientation and a secondary NW-SE trend, the latter of which seem to be related to the numerous fracture-controlled troughs that occur in the vicinity of the dichotomy escarpment (see Figs. 2a and 4a). Member b locally exhibits NE-SW-oriented ridge crests in the eastern sector of the unit, and scarce occurrence of lobate scarps with NW-SE orientation. The boundary between members a and b is gradational, mainly defined by the slope break between

Fig. 2 (next page). *(a) Geologic-geomorphic map of the CNTZ showing the geologic units and the identified morphological and tectonic features over a THEMIS-IR day mosaic. (b) Colorized elevation model of the study area from HRSC-MOLA blended data over a mosaic of THEMIS-IR day images. Red polygons represent the crater-counting areas (1 to 12) selected for dating the main units (Fig. 7). The black line indicates the trace of the SHARAD profile "S_02596802" (Fig. 8) and that of the geological cross-section (A-A') shown in Fig. 10. The black polygon depicts the area covered by the bock diagram (Fig. 12) that interprets the subsurface geology along the B-B' profile. (c) Qualitative TI mosaic of the study area derived from THEMIS over a mosaic of THEMIS-IR day images.*

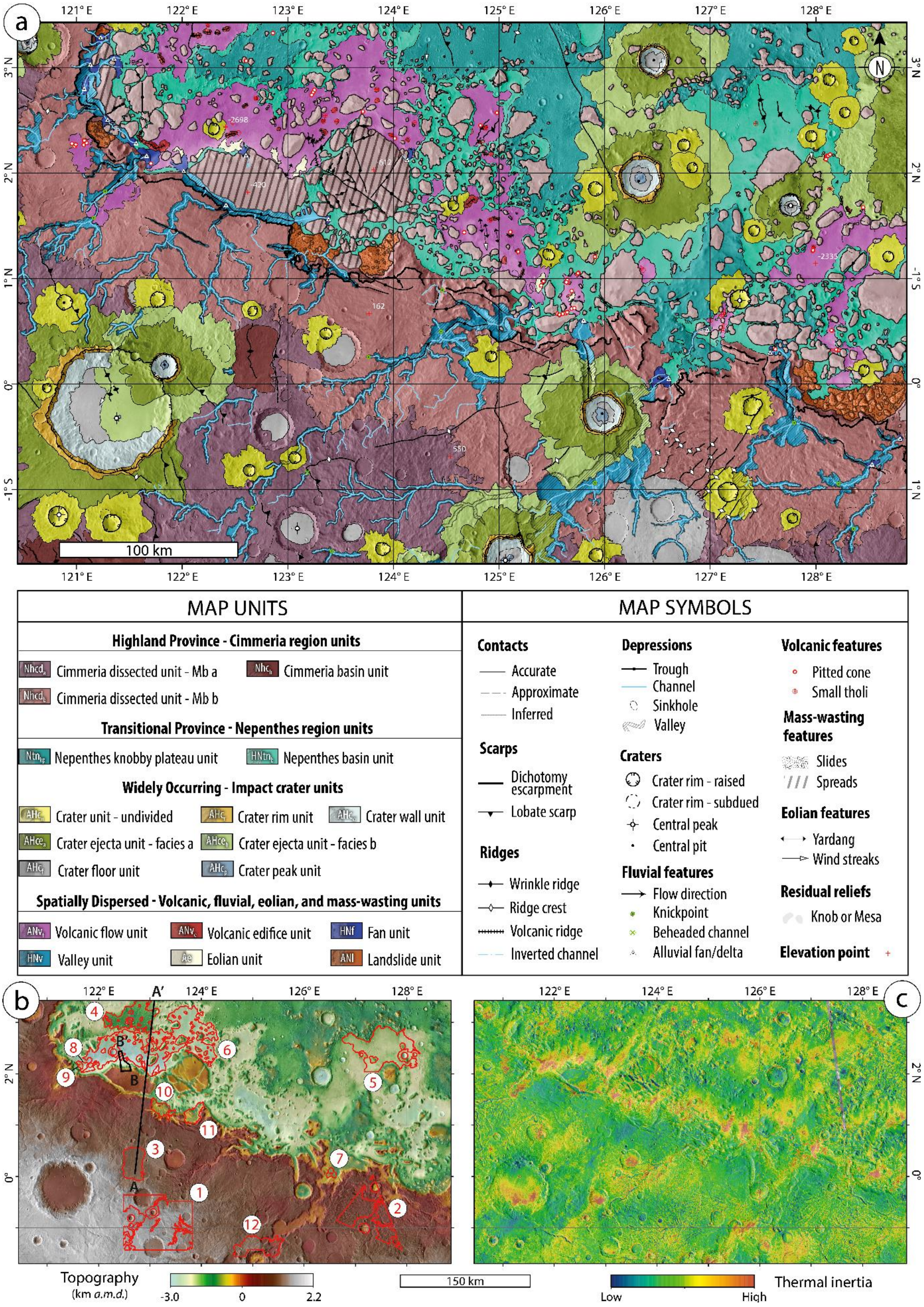
a
121° E
122° E
123° E
124° E
125° E
126° E
127° E
128° E
3° N
2° N
1° N
0°
-1° S
N
-2698
-420
412
-2335
162
550
100 km
MAP UNITS
Highland Province - Cimmeria region units
Nhcda Cimmeria dissected unit - Mb a
Nhcb Cimmeria basin unit
Nhcdb Cimmeria dissected unit - Mb b
Transitional Province - Nepenthes region units
Ntnkp Nepenthes knobby plateau unit
HNtnb Nepenthes basin unit
Widely Occurring - Impact crater units
AHcu Crater unit - undivided
AHcr Crater rim unit
AHcw Crater wall unit
AHcea Crater ejecta unit - facies a
AHceb Crater ejecta unit - facies b
AHcf Crater floor unit
AHcp Crater peak unit
Spatially Dispersed - Volcanic, fluvial, eolian, and mass-wasting units
ANvf Volcanic flow unit
ANve Volcanic edifice unit
HNf Fan unit
HNv Valley unit
Ae Eolian unit
ANl Landslide unit
MAP SYMBOLS
Contacts
Accurate
Approximate
Inferred
Scarps
Dichotomy escarpment
Lobate scarp
Ridges
Wrinkle ridge
Ridge crest
Volcanic ridge
Inverted channel
Depressions
Trough
Channel
Sinkhole
Valley
Craters
Crater rim - raised
Crater rim - subdued
Central peak
Central pit
Fluvial features
Flow direction
Knickpoint
Beheaded channel
Alluvial fan/delta
Volcanic features
Pitted cone
Small tholi
Mass-wasting features
Slides
Spreads
Eolian features
Yardang
Wind streaks
Residual reliefs
Knob or Mesa
Elevation point
b
122° E
A'
124° E
126° E
128° E
2° N
0°
B'
B
A
1
2
3
4
5
6
7
8
9
10
11
12
Topography
(km a.m.d.)
-3.0
0
2.2
150 km
c
122° E
124° E
126° E
128° E
2° N
0°
Low
High
Thermal inertia

the higher southern reliefs and the plateau. The Cimmeria basin unit (Nhc_b) corresponds to depressions of uncertain origin inset into member a and filled with sediments that display possible layering. It shows a smoother and less-cratered surface than those of the Cimmeria dissected units, pervasive wrinkle ridges, and absence of channels.

The Nepenthes region units comprise the Nepenthes knobby plateau unit (Ntn_{kp}) and the Nepenthes basin unit ($HNtn_b$) (Fig. 2a). The Nepenthes knobby plateau unit (Ntn_{kp}) crops out in the inter-crater plateau areas of Nepenthes Mensae. This moderately cratered unit features knobby terrains formed by degraded residual hills carved in materials of the unit $Nhcd_b$ and mass-wasted materials that form aprons around degraded reliefs (e.g., Tanaka et al., 2005). The unit also displays NW-SE-oriented lobate scarps and widely-distributed eolian erosional landforms such as yardangs with a prevailing NW-SE orientation (see detail in Fig. 3l). The Nepenthes basin unit ($HNtn_b$) corresponds to low-lying areas and the associated slopes of the Nepenthes Mensae region located between mesas and knobs, as well as on floors of ancient and highly-degraded impact basins. Depressions in Nepenthes Mensae show multiple evidence of enclosed paleolake basins (Rivera-Hernández and Palucis, 2019; García-Arnay and Gutiérrez, 2020). The Nepenthes basin unit is characterized by lower crater density than unit Ntn_{kp}, and relatively smooth surfaces locally interrupted by wrinkle ridges, as well as small tholi and pitted cones (see Fig. 3f). The boundary between units $HNtn_b$ and Ntn_{kp} is gradational.

Seven impact crater units have been differentiated on the basis of their morpho-structural components (i.e., rim, wall, floor, peak, and ejecta), following the classification proposed by Skinner and Tanaka (2018). The crater unit–undivided (AHc_u) includes well-preserved craters with rim diameter ranging between 5 and 13 km and the associated materials. This unit shows lobate ejecta morphologies, commonly hummocky crater floor, and scarce occurrence of central peak or pit. The rest of the impact crater units were ascribed to moderately to well-preserved impact craters with rim diameters ≥13 km. The crater peak unit (AHc_p) was mapped at or next to the center of impact craters. It is characterized by mounds with irregular and grooved surfaces, and the common presence of central pits. The crater floor unit (AHc_f) occurs between the foot of the crater wall and the central peak, and displays smooth, near-planar surfaces. Central peaks can be absent and pits may occur in the center of the crater. The crater wall unit (AHc_w) was mapped between the crater floor and rim units. This rough, and locally rugged unit is characterized by scarps, blocks, rockfalls and locally discontinuous terraces. The rim crater unit (AHc_r) is located along the continuous to discontinuous crested rim. It is characterized by an inward-facing steep scarp frequently dissected by gullies and grooves. The crater ejecta units are divided into two morpho-facies. The crater ejecta unit–facies a ($AHce_a$)

***Fig. 3 (next page)**. CTX images illustrating remarkable geomorphic features in the study area (locations indicated in Fig. 1). (a, b, c) Fan-shaped deposits attributable to Gilbert-type deltas (labelled as D# in our delta and alluvial fan catalogue presented in section 4.1). Putative volcanic features such as fissure vents (d, e), a pitted cone (f), lava fields, flows and channels (g, h). White arrows in (d) indicate the lower delta deposits of "D2" locally overlying those at the foot of the fissure vent and surrounding plains. (i) Fluvial valley showing a sharp break in the longitudinal profile (i.e., knickpoint). (j) Defeated and beheaded channel sections separated by a lobate scarp, attributable to a surface-rupturing thrust fault that disrupted the drainage. (k) Barchan dune fields indicating a dominant south-directed wind, as indicated by yellow arrows. (l) A detail of the knobby terrain that characterizes the Nepenthes knobby plateau unit (Ntn_{kp}). Note the presence of elongated erosional landforms with roughly parallel orientation ascribable to yardangs. North is up in all cases.*

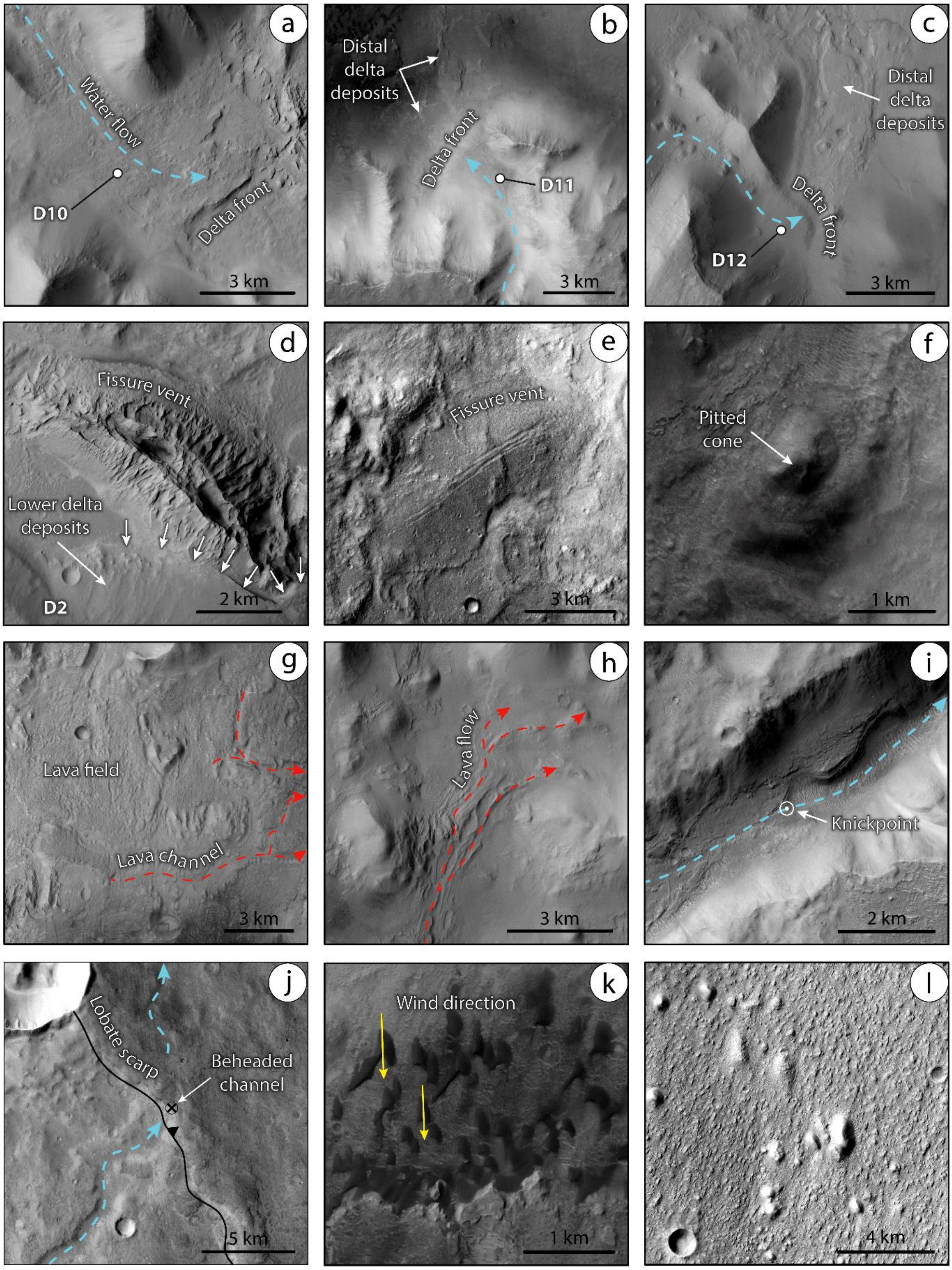
a
Water flow
D10
Delta front
3 km
b
Distal delta deposits
Delta front
D11
3 km
c
Distal delta deposits
Delta front
D12
3 km
d
Fissure vent
Lower delta deposits
D2
2 km
e
Fissure vent
3 km
f
Pitted cone
1 km
g
Lava field
Lava channel
3 km
h
Lava flow
3 km
i
Knickpoint
2 km
j
Lobate scarp
Beheaded channel
5 km
k
Wind direction
1 km
l
4 km

represents the proximal deposits. It is characterized by multiple overlapping rugged lobes with flowbands. The crater ejecta unit–facies b ($AHce_b$) is the outer unit, formed by multiple overlapping smooth flow-oriented lobes.

Six locally-distributed units have been mapped. The valley unit (HNv) corresponds to valleys carved in the Cimmeria region units $Nhcd_a$ and $Nhcd_b$, and rarely in the Nepenthes knobby plateau unit (Ntn_{kp}). This unit is characterized by high-TI, smooth deposits underlying the floors of valley networks with dendritic or trellis pattern. Licus Vallis, which is the longest, widest, and deepest valley in the study area, shows an apparently poorly-evolved watershed, as suggested by its convex hypsometric curve and a very low drainage density (García-Arnay et al., 2018b). Valley floors, generally characterized by a low THEMIS TI related to the presence of eolian deposits (see Fig. 2c), often show knickpoints (Fig. 3i) and rarely preserved incised or inverted channels. The degree of entrenchment of the valleys increases towards the dichotomy boundary, next to the paleolakes that controlled the position of the base level during their development, as indicates the presence of putative Gilbert-type deltas (e.g., García-Arnay and Gutiérrez, 2020). Some valleys are locally buried by ejecta deposits or disrupted by lobate scarps resulting in the formation of defeated and beheaded channels sections (see Fig. 3j). The fan unit (HNf), which is laterally associated with unit HNv, occurs at the mouth of the valleys, generally along the foot of the dichotomy. This unit corresponds to fan-shaped deposits with generally smooth surfaces, but sometimes corrugated due to differential erosion on layered sediments. Some fans show different lobes and rare channels carved into the surface (see Fig. 3a-c, and Fig. 3 from García-Arnay and Gutiérrez (2020)). The frontal slope of the fans can be continuous or stepped. Due to the paleoenvironmental interest of unit HNf, we present an updated catalogue of fan-shaped deposits identified within and near the study area in Table 1. The volcanic flow unit (ANv_f) shows poorly-cratered, uneven, and smooth to rugged surfaces with frequent grooves, channels (Fig. 3g), and overlapping lobes (Fig. 3h). This unit, which is darker in THEMIS daytime IR images than the surrounding plains, occurs in the deeper areas of the depressions of Nepenthes Mensae, and locally in the highland province near the dichotomy. It is locally modified by NE-SW-striking wrinkle ridges, NW-SE-aligned erosional eolian landforms such as yardangs, as well as small sinkhole-like depressions. This unit locally overlies units $Nhcd_b$ and $HNtn_b$, locally also underlies unit HNf, and grades into unit ANv_e. The volcanic edifice unit (ANv_e) is characterized by sloping, and rugged to smooth surfaces with isolated and coalesced fissures (see Figs. 3d, e), as well as small cone- and mound-shaped features (Fig. 3f). Cones and mounds often show small knobs and/or pits at their summit. Overlapping lobes related to the volcanic flow unit (ANv_f) seem to emanate from raised fissures, cones and mounds. The eolian unit (Ae) often consists of dune fields that mainly occur in the southern sector of the depressions of Nepenthes Mensae, near the foot of the dichotomy escarpment. This unit, which shows dark tones in CTX panchromatic images and bright tones in THEMIS daytime IR images, is formed by fields of barchan and longitudinal dunes indicating a dominant south-directed wind (see Fig. 3k). It locally overlies units ANv_f, $HNtn_b$ and $Nhcd_b$. The landslide unit (ANl) usually occurs associated with the ca. 2 km high dichotomy escarpment. It is characterized by rugged, rolling, and hummocky terrains with intervening large blocks that can

***Table 1 (next page)**. Characteristics of the fan-shaped features (identified as D# and F# for putative deltas and alluvial fans, respectively) recognized within and near the study area, as well as their associated basins. The front elevation for the stepped fans corresponds to the slope-break of the uppermost step. Features from D1 to D9 match with those referred by García-Arnay and Gutiérrez (2020). The basin type can be open (O) or closed (C). "N/A" = Not applicable.*

Delta/ Alluvial fan ID	Latitude (N)	Longitude (E)	Front elevation (m)	Visible layering	Multi-lobate	Morphology (Continuous/Stepped)	Basin type (O/C)	First reference
D1	3°5'31"	121°20'54"	-1865	✓	✓	Stepped	C	García-Arnay et al. (2018a)
D2	2°10'11"	121°39'29"	-1952	✓	✓	Stepped	C	Irwin et al. (2005)
D3	2°1'28"	122°00'31"	-1935	✓	✓	Stepped	C	García-Arnay et al. (2018a)
D4	1°34'7"	123°22'52"	-1793	✓	✓	Continuous	C	García-Arnay et al. (2018a)
D5	0°44'6"	125°18'55"	-1920	✓	✗	Continuous	C	García-Arnay et al. (2018a)
D6	0°36'33"	125°47'50"	-1975	✓	✗	Continuous	C	García-Arnay et al. (2018a)
D7	0°3'14"	126°36'20"	-1186	✓	✓	Continuous	O	García-Arnay et al. (2018a, 2018b)
D8	0°31'21"	126°58'19"	-1920	✓	✓	Continuous	C	García-Arnay et al. (2018a)
D9	0°18'8"	127°34'00"	-1783	✓	✓	Continuous	C	García-Arnay et al. (2018a)
D10	2°17'19"	121°33'25"	-2370	✓	✓	Continuous	C	This study
D11	2°10'26"	122°35'59"	-1906	✓	✓	Stepped	C	This study
D12	2°7'41"	124°7'40"	-1872	✓	✓	Stepped	C	This study
F1	-2°12'6"	120°57'9"	N/A	✗	✗	Continuous	O	This study
F2	2°48'16"	121°3'56"	N/A	✓	✓	Continuous	C	Rivera-Hernández & Palucis (2019)
F3	-1°55'21"	121°7'59"	N/A	✗	✓	Continuous	O	This study
F4	3°2'10"	121°7'28"	N/A	✓	✓	Continuous	C	Rivera-Hernández & Palucis (2019)
F5	3°17'25"	121°13'19"	N/A	✓	✓	Stepped	C	Rivera-Hernández & Palucis (2019)
F6	2°30'38"	121°17'13"	N/A	✓	✓	Stepped	C	Rivera-Hernández & Palucis (2019)
F7	1°42'6"	122°24'33"	N/A	✓	✗	Continuous	O	Rivera-Hernández & Palucis (2019)
F8	-2°59'40"	122°41'9"	N/A	✓	✓	Continuous	O	This study
F9	-4°10'27"	125°56'16"	N/A	✗	✓	Continuous	O	This study
F10	-0°45'21"	128°31'51"	N/A	✓	✓	Continuous	O	This study
F11	-0°30'47"	128°47'51"	N/A	✓	✓	Continuous	O	This study
F12	-1°11'53"	129°52'23"	N/A	✓	✓	Stepped	O	This study

be carved by channels (see details in the 3D image in Fig. 11). Locally, this unit overlies units Nhcd$_b$ and HNtn$_b$.

4.1.2 Geomorphology

We have also mapped the main geomorphic features in the CNTZ (Fig. 2a). Two types of scarps have been identified: lobate scarps, and those associated with the dichotomy boundary. Lobate scarps are ridge-like, linear to sinuous landforms in plan that display asymmetric cross profiles with convex and steep scarp faces (e.g., Watters and Robinson, 1999; Skinner and Tanaka, 2018), up to ~250 m high in the study area (Fig. 3j). These landforms mostly occur in the Cimmeria dissected units (Nhcd$_a$ and Nhcd$_b$) and the Nepenthes knobby plateau unit (Ntn$_{kp}$), showing a prevalent NW-SE orientation with often SW-facing scarps. In some cases, lobate scarps disrupt valleys and pre-existing crater floors (see locations at 0°48'11"S, 125°5'23"E; 0°0'25"N, 122°53'45"E and 1°29'17"S, 128°0'17"E), or appear interrupted by gaps related to impact craters that locally obliterated them. We mapped 22 lobate scarps that range in length from 4.5 to 103.1 km (27.7 km mean, 21.5 km median).

The dichotomy boundary displays a linear to sinuous escarpment ca. 2 km high that is dissected by numerous valleys, which often display conspicuous knickpoints. This major escarpment exhibits a dominant NW-SE orientation that turns to a N-S trend west of the map, and occurs in member b of the Cimmeria dissected unit (Nhcd$_b$). The foot of the escarpment generally defines the contact between the highland and transition units throughout the CNTZ. It is common the occurrence of gullies, as well as hummocky terrains with intervening large blocks associated to the landslide unit (ANl). We mapped 36 escarpment segments separated by valleys with a cumulative mapped length of 751.6 km.

Four types of ridges were mapped: wrinkle ridges, ridge crests, volcanic ridges, and inverted channels (Fig. 2a). Wrinkle ridges are linear to curvilinear ridges with asymmetric transverse profile, which crests are characterized by complex crenulations colloquially called “wrinkles” (e.g., Watters, 1988). In our map these landforms display two dominant orientations: a NW-SE trend that occurs in the plains of the basin units of the Cimmeria and Nepenthes regions (Nhc$_b$ and HNtn$_b$, respectively), and a NE-SW orientation within the volcanic flow unit (ANv$_f$). These crenulated ridges, which generally rise up to ~50 m above surrounding plains, commonly show the maximum width in the middle section. We mapped 18 wrinkle ridges ranging in length from 5.3 to 35.2 km (13.3 km mean, 9.4 km median).

Ridge crests, also called high-relief ridges, are characterized by a near symmetrical transverse profile and higher relief than the wrinkle ridges (e.g., Watters et al., 2009). These features mostly occur in the Cimmeria dissected units (Nhcd$_a$ and Nhcd$_b$) displaying lateral continuity across them. Although orientations vary across the map, ridge crests exhibit a dominant NE-SW orientation, and a secondary NW-SE strike. The conspicuous swarm with subparallel pattern east of the map is interrupted at an ancient and degraded impact crater 60 km in diameter, indicating an older age for the ridges (see Fig. 2a). We have mapped 28 ridge crests that range in length from 1.5 to 86.3 km (16.6 km mean, 11.5 km median).

Volcanic ridges correspond to raised fissure vents that occur in the volcanic edifice unit (ANv$_e$). These linear to curvilinear ridges reach up to ~600 m in local relief, exhibit pits and/or elongated depressions at the top, and smooth to rugged slopes carved by grooves and gullies (see Fig. 3d, e, and close-up view in Fig. 4b). The orientation of the volcanic ridges shows a rather scattered distribution, with weak NW-SE and NE-SW prevalent trends (Fig. 4b). We have mapped 21 volcanic ridges ranging in length from 1.1 to 12.5 km (4.4 km mean, 3.8 km median).

Channel ridges related to relief inversion, commonly known as “inverted channels”, are characterized by ridges with sinuous pattern in plan (e.g., Burr et al., 2010; Hayden et al., 2019; Clarke et al., 2020). In the map region we have identified sinuous ridges up to 3.8 km in length associated with the fan unit (HNf) that occurs in the eastern sector of the map area, specifically on the fan-shaped deposit F10 (Table 1).

Four types of negative relief features have been differentiated: troughs, valleys, channels, and sinkhole-like depressions. Troughs are rectilinear or slightly arcuate steep-walled depressions with maximum depths and widths of 1 and 7 km, respectively. These landforms are located along the northern Terra Cimmeria in the vicinity of the dichotomy escarpment, mainly cut into member b of the Cimmeria dissected unit (Nhcd$_\text{b}$) and into residual reliefs of this unit in Nepenthes Mensae to form fretted valleys (see close-up view in Fig. 4a). Troughs show a dominant NW-SE orientation and a secondary NE-SW trend, forming a distinctive polygonal pattern (Fig. 4a). We identified and mapped 72 troughs that range in length from 4.0 to 49.4 km (17.4 km mean, 13.7 km median).

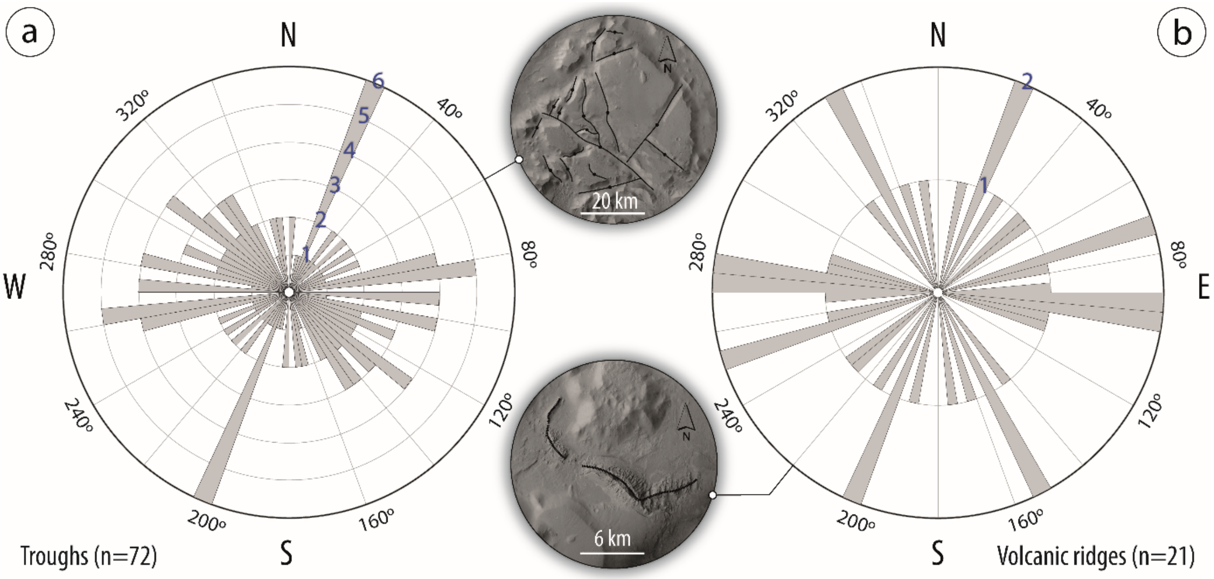

Fig. 4. Rose diagrams showing the distribution of the orientation of troughs (a) and volcanic ridges (b). Close-up views show examples of each case (CTX image mosaic). Note that the orientation of volcanic ridges displays higher dispersion than the troughs. Their higher dispersion may be partially due to the lower number of features (n).

Valleys are networks of V-shaped, elongate, steep-walled depressions with linear to sinuous trace and dendritic to trellis pattern. Valley networks often exhibit a pattern apparently controlled by lobate scarps, ridge crests and troughs. Some valleys disrupted by lobate scarps show evidence of later adaptation to these landforms, such as deflections. Their associated deposits comprise the valley unit (HNv) (see section 4.1.1). We mapped 32 valley networks within the map region that range in planimetric area from 6.9 to 2,400.7 km^2 (324.5 km^2 mean).

Channels are elongate, narrow and shallow depressions with linear to sinuous trace that occur in the valley floors and join in the downslope direction (e.g., Sharp and Malin, 1975). Channels associated to the valley unit (HNv) mostly occur in the Cimmeria dissected units (Nhcd$_\text{a}$ and Nhcd$_\text{b}$), and rarely in the Nepenthes knobby plateau unit (Ntn$_\text{kp}$). They locally display positive relief sections forming channel ridges related to relief inversion by differential erosion. Watersheds in the CNTZ are characterized by streams of up to fourth order using the Strahler's classification (Strahler, 1952), such as that of Licus Vallis (e.g., García-Arnay et al., 2018b). The channel network in the vicinity of the dichotomy tends to show a rectangular pattern, with channel sections following a dominant NE-SW trend and a secondary NW-SE orientation, probably controlled by fractures. We have mapped 248 channels in the study area ranging in length from 0.07 to 143.6 km (16.1 km mean, 10.3 km median).

Sinkhole-like depressions are elongated, closed depressions that commonly exhibit well-defined scarped boundaries (e.g., Parenti et al., 2020). These landforms locally occur in the volcanic flow unit (ANv$_f$), display major axes ranging from 10s to ~700 m, and a prevalent NW-SE trend that coincides with that of nearby yardangs and wind streaks.

Two types of cone- and mound-shaped landforms were identified within the volcanic edifice unit (ANv$_e$): pitted cones and small tholi. Pitted cones are conical hills with circular outline in plan and smooth slopes that exhibit a central pit in their summit (e.g., Skinner and Tanaka, 2018) (see Fig. 3f). These landforms occur either isolated or aligned, mainly associated with the volcanic flow unit (ANv$_f$), and less commonly in the Nepenthes knobby plateau and Nepenthes basin units (Ntn$_{kp}$ and HNtn$_b$, respectively). We have identified and mapped 47 pitted cones within the study area, ranging in diameter from 200 m to 1.2 km.

Small tholi are mounds with subtle slopes bounded by marginal scarps, and often showing central peaks (e.g., Skinner and Tanaka, 2018). These mounds of up to 2.7 km in diameter are frequently isolated, but in some cases form clusters. They generally occur associated with the volcanic flow unit (ANv$_f$), and rarely in the Nepenthes basin unit (HNtn$_b$). We mapped 30 small tholi in the map region.

4.2 Mineral composition of units of paleoenvironmental interest

The spectral analysis of the CRISM scenes FRT00017610 (~18 m/pixel, ~10x10 km) and HRL000134F5 (~36 m/pixel, ~10x20 km) was carried out in order to determine the composition of the surface material in two different areas of the CNTZ with paleoenvironmental interest. These CRISM observations (Figs. 5a and 6a) include fan-shaped deposits, and spatially associated distal fan deposits and surrounding plains (see locations in Fig 1). The layered fan-shaped deposits (unit HNf) shown in Fig. 5a occur within the landform identified as "D2" in Table 1. It is located in the western sector of the study area at the mouth of a canyon-type valley, and was interpreted as a delta for the first time by Irwin et al. (2005), displaying a stepped morphology (upper and lower delta). The PHY spectral parameter map (Fig. 5b) suggests the presence of two clay-bearing compositional units in the lower delta deposits: (1) laterally continuous patches of hydrated Fe/Mg-phyllosilicates occurring at different stratigraphic levels, which are the most common hydrated minerals on Mars (Carter et al., 2013); and (2) smaller isolated patches of hydrated Al-smectites and/or hydrated silica, shown by pink- and cyan-colored pixels, respectively (Fig. 5b). Aluminum smectites and/or hydrated silica occur in light-toned layered materials, as revealed by the HiRISE image ESP_016547_1820

***Fig. 5 (next page)**. (a) True color product of the CRISM map-projected scene "FRT00017610" (see location in Fig. 1). The close-up view shows a detail of the light-toned surfaces associated with the lower delta environment (HiRISE image ESP_016547_1820). (b) Phyllosilicate spectral parameter map (PHY product) generated for the same scene. Pink and cyan tones indicate the presence of hydrated Fe/Mg-smectites, and hydrated Al-smectites/hydrated silica, respectively. (c, d) CRISM ratioed I/F spectra (i.e., s1/s2) for hydrated Fe/Mg-smectites and hydrated Al-smectites/hydrated silica (above), compared to laboratory spectra (below). Vertical dashed lines indicate diagnostic absorption band depths, and blue and grey bands represent bandwidths for OH/H_2O, as well as Fe/Mg-OH and Al/Si-OH, respectively.*

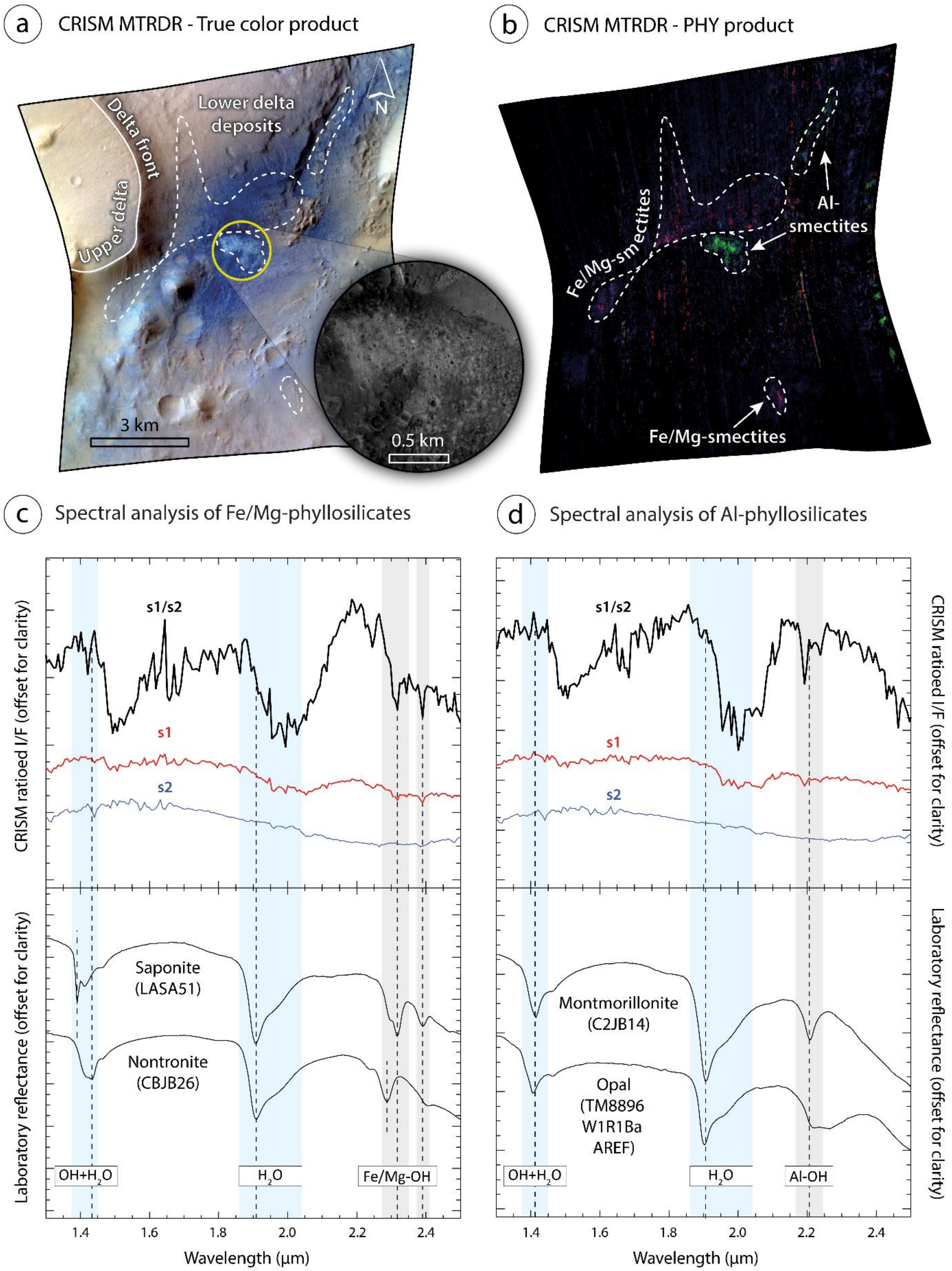

(close-up view in Fig. 5a). The ratioed I/F spectra (i.e., s1/s2) for both inferred compositional units reveal two sharp absorption bands at ~1.5 and ~2 μm related to structural H_2O and OH, and structural H_2O, respectively (Fig. 5c, d). These absorption bands associated with OH and/or H_2O in the ratioed spectra are shifted to longer wavelengths compared to those of laboratory spectra (i.e., ~1.4 and ~1.9 µm), which could be due to a higher degree of crystallinity and/or mineral mixing (e.g., Viviano-Beck et al., 2014). Furthermore, these ratioed spectra exhibit subtler absorption bands at ~2.31 and ~2.39 µm (Fig. 5c), and at ~2.2 µm (Fig. 5d) related to Fe/Mg- and Al/Si-OH bonds, respectively (Ehlmann et al., 2009; Viviano-Beck et al., 2014). These absorption bands, together with those related to OH/H_2O bonds, allow inferring the occurrence of hydrated Fe/Mg phyllosilicates (Fig. 5c), and hydrated Al-rich smectites and/or hydrated silica (Fig. 5d). Accordingly, the observed diagnostic features can be consistent with the presence of saponite (Mg-rich smectite) and nontronite (Fe-rich smectite) in the Fe/Mg-smectite unit, and montmorillonite (Al-rich smectite) and/or opal (hydrated silica) in the Al-smectite/hydrated silica unit, as indicated by the comparison between the ratioed spectra and those from the CRISM/ENVI spectral library (Viviano-Beck et al., 2015).

The fan-shaped deposits shown in Fig. 6a, labelled as "D11" in Table 1, are located at the mouth of a short valley (see details in Fig. 3b). The MAF and PHY spectral parameter maps indicate, respectively, extensive olivine-bearing deposits associated with the barchan dune field of the unit Ae (Fig. 6b), and patches of ferromagnesian phyllosilicates occurring along the distal fan deposits (unit HNf) with undetermined hydrated minerals (Fig. 6c). Cartographic relationships indicate that the distal fan deposits overlay the surrounding plains that form part of unit ANv$_f$, and are locally covered by the olivine-rich dark dunes.

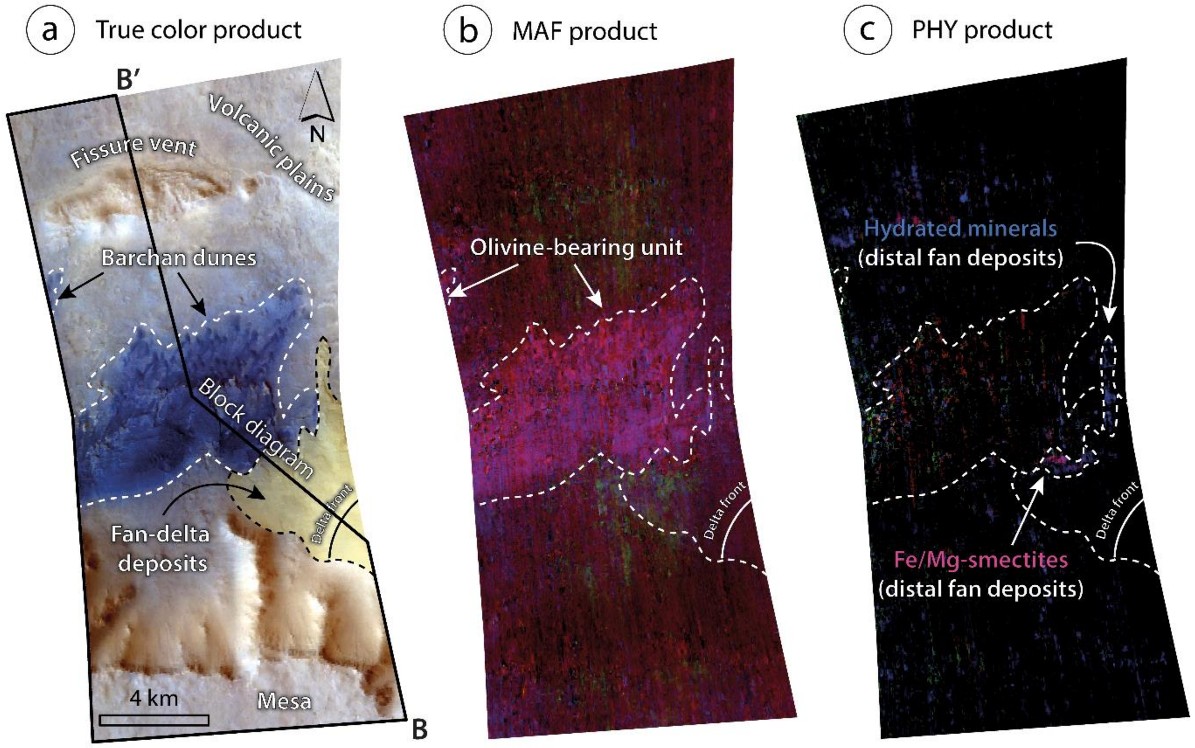

***Fig. 6**. (a) True color product of the CRISM map-projected scene "HRL000134F5" (see location in Fig. 1). The black-lined polygon indicates the area covered by the block diagram shown in Fig. 12, which shows an interpretation for the subsurface geology along the B-B' profile. (b, c) Mafic mineralogy and phyllosilicate spectral parameter maps (MAF and PHY products, respectively) for the same scene. Note the spatial association between clay- and olivine-bearing deposits around the distal fan environment.*

4.3 Numerical estimation of surface ages

The analysis of the crater size-frequency distribution (SFD) was performed in 12 counting areas representing the main map units, in order to obtain their age models (Fig. 7). We selected, where possible, crater-counting areas larger than 1,000 km^2 to minimize the impact of the local pattern variations in cratering (e.g., Warner et al., 2015). For clarity, the units have been grouped by regions and/or according to their spatial distribution, and ages have been ordered from older to younger. Average ages with error ranges of ± 0.0/0.0 are indicated by adding the symbol "~" before the age. In the Cimmeria region, we obtained average age estimates (red fit lines) of 4 ± 0.0/0.1 Ga (Early to Middle Noachian), and ~3.9 Ga (Middle Noachian) for the Cimmeria dissected units Nhcd$_a$ and Nhcd$_b$, respectively, as well as ~3.6 Ga (Late Noachian) for the Cimmeria basin unit (Nhc$_b$), considering counting areas of ~4,600, ~1,800 and ~790 km^2, respectively (Fig. 7a-c). In these diagrams we identified several kinks that suggest resurfacing events affecting to km-sized and smaller craters (blue and green fit lines), such as the large kink that occurs in the SFD shown in Fig. 7a at D <3 km, with a resulting average age of the resurfacing event of ~3.4 Ga (Early Hesperian). We estimated surface ages of ~3.8 Ga (Late Noachian) and 3.6 ± 0.1/0.1 Ga (Late Noachian to Early Hesperian) for the Nepenthes knobby plateau unit (Ntn$_{kp}$) and the Nepenthes basin unit (HNtn$_b$), with counting areas of ~1,200 and ~2,400 km^2, respectively (Fig. 7d, e). Among the spatially-dispersed units, we estimated the surface ages for the fan unit (HNf), the volcanic flow unit (ANv$_f$), and the landslide unit (ANl). For the fan unit (HNf), we selected three counting areas located in the largest fan-shaped deposits in order to reduce the potential impact of: (1) the spatial variability in cratering processes; and (2) the exclusion of larger craters associated with smaller counting areas (Warner et al., 2015). Thus, we obtained average ages of 3.6 ± 0.1/0.1 Ga (Late Noachian to Early Hesperian) for delta "D7" (see Table 1), and 3.6 ± 0.1/0.3 Ga (Late Noachian to Late Hesperian; lower delta) and 2.0 ± 0.4/0.4 Ga (Early Amazonian; upper delta) for "D2" (Fig. 7g-i), with counting areas of ~85.4, ~53, and ~41.1 km^2, respectively. For the volcanic flow unit (ANv$_f$), a fit to the D >450 m crater population provided an age estimate of 1.8 ± 0.2/0.2 Ga (Early Amazonian) (Fig. 7f), considering a counting area of ~9,000 km^2. Finally, we considered two counting areas for the landslide unit (ANl) of ~318 and ~314 km^2, with average age estimates of 1.0 ± 0.3/0.3 Ga (Early to Middle Amazonian) and 0.8 ± 0.2/0.2 Ga (Middle Amazonian), respectively (Fig. 7j, k).

In order to obtain a minimum age estimate for the cessation of fluvial activity in the main valley of Licus Vallis, we analyzed the crater size-frequency distribution of the crater population developed on the ejecta deposits of the unit AHce$_a$ overlapping the valley. These deposits are related to an impact crater 27 km in diameter formed near the middle course of Licus Vallis, with no evidence of reworking by fluvial activity. The fit for the D >0.3 km crater population provides an estimated age (minimum for fluvial activity) of 3.4 ± 0.1/0.1 Ga (Early to Late Hesperian), considering a counting area of ~860 km^2 (Fig. 7l).

Fig. 7 (next page). *(a-l) Cumulative crater size-frequency diagrams constructed for estimating the numerical age of the main surface units (above) and corresponding crater-counting areas from 1 to 12 (below) (see locations in Fig. 2b). Age models show simple cumulative fits for the formation ages (red fit lines), and corrected cumulative fits for the resurfacing events (blue and green fit lines). The grey shadow bands denote the time boundaries between Martian geological epochs according to Michael (2013). "D" and "Craters" refer to the minimum crater diameter and the number of counted craters considered for each counting area, respectively.*

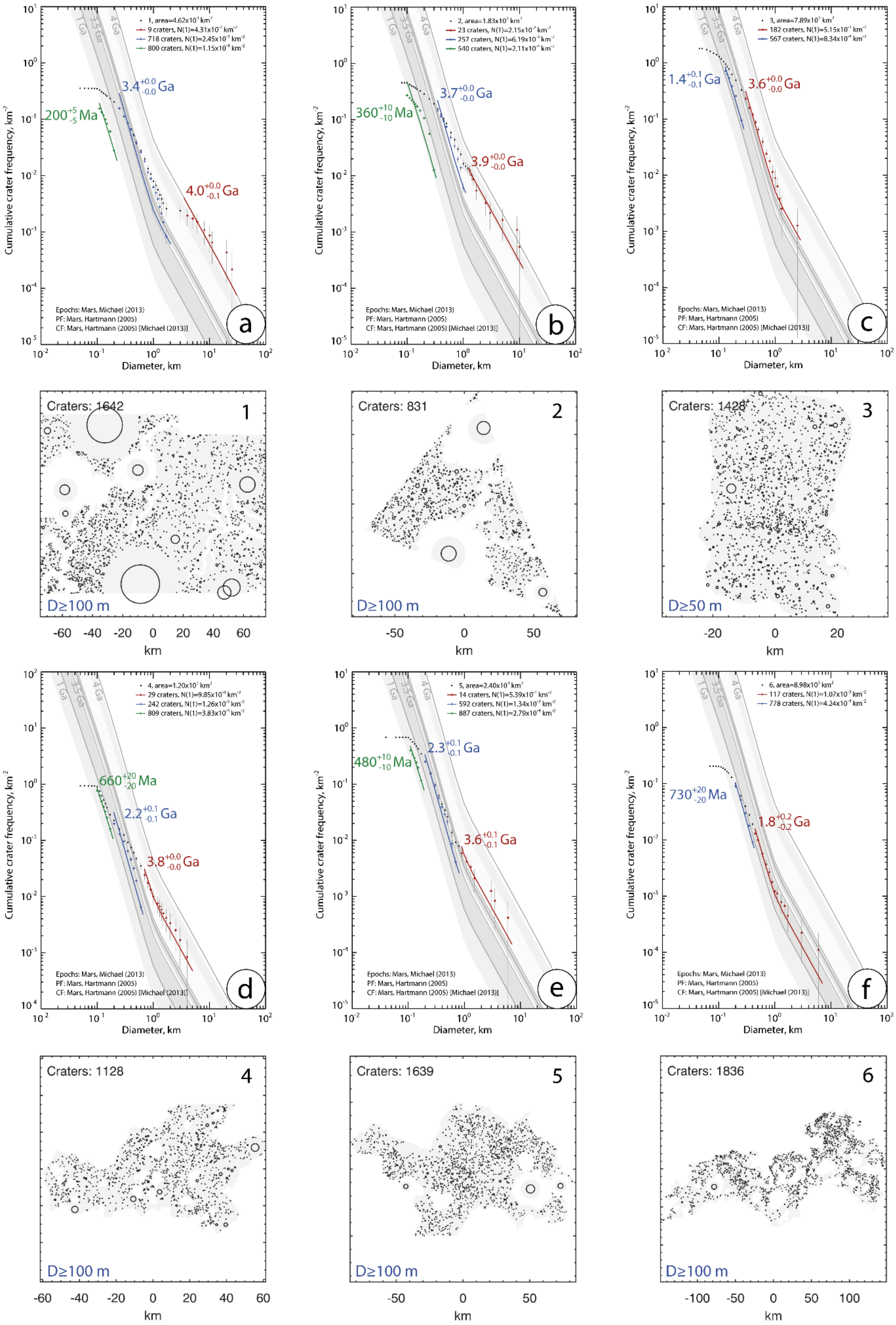
1, area=4.62x10^3 km^2
9 craters, N(1)=4.31x10^-2 km^-2
718 craters, N(1)=2.45x10^-3 km^-2
800 craters, N(1)=1.15x10^-4 km^-2
200 +5 -5 Ma
3.4 +0.0 -0.0 Ga
4.0 +0.0 -0.1 Ga
1 Ga
3.5 Ga
4 Ga
Epochs: Mars, Michael (2013)
PF: Mars, Hartmann (2005)
CF: Mars, Hartmann (2005) [Michael (2013)]
a
Cumulative crater frequency, km^-2
Diameter, km
2, area=1.83x10^3 km^2
23 craters, N(1)=2.15x10^-2 km^-2
257 craters, N(1)=6.19x10^-3 km^-2
540 craters, N(1)=2.11x10^-4 km^-2
360 +10 -10 Ma
3.7 +0.0 -0.0 Ga
3.9 +0.0 -0.0 Ga
b
3, area=7.89x10^2 km^2
182 craters, N(1)=5.15x10^-1 km^-2
567 craters, N(1)=8.34x10^-4 km^-2
1.4 +0.1 -0.1 Ga
3.6 +0.0 -0.0 Ga
c
Craters: 1642
1
D≥100 m
km
Craters: 831
2
D≥100 m
Craters: 1428
3
D≥50 m
4, area=1.20x10^3 km^2
29 craters, N(1)=9.85x10^-3 km^-2
242 craters, N(1)=1.26x10^-3 km^-2
809 craters, N(1)=3.83x10^-4 km^-2
660 +20 -20 Ma
2.2 +0.1 -0.1 Ga
3.8 +0.0 -0.0 Ga
d
5, area=2.40x10^3 km^2
14 craters, N(1)=5.39x10^-3 km^-2
592 craters, N(1)=1.34x10^-3 km^-2
887 craters, N(1)=2.79x10^-4 km^-2
480 +10 -10 Ma
2.3 +0.1 -0.1 Ga
3.6 +0.1 -0.1 Ga
e
6, area=8.98x10^3 km^2
117 craters, N(1)=1.07x10^-3 km^-2
778 craters, N(1)=4.24x10^-4 km^-2
730 +20 -20 Ma
1.8 +0.2 -0.2 Ga
f
Craters: 1128
4
D≥100 m
Craters: 1639
5
D≥100 m
Craters: 1836
6
D≥100 m

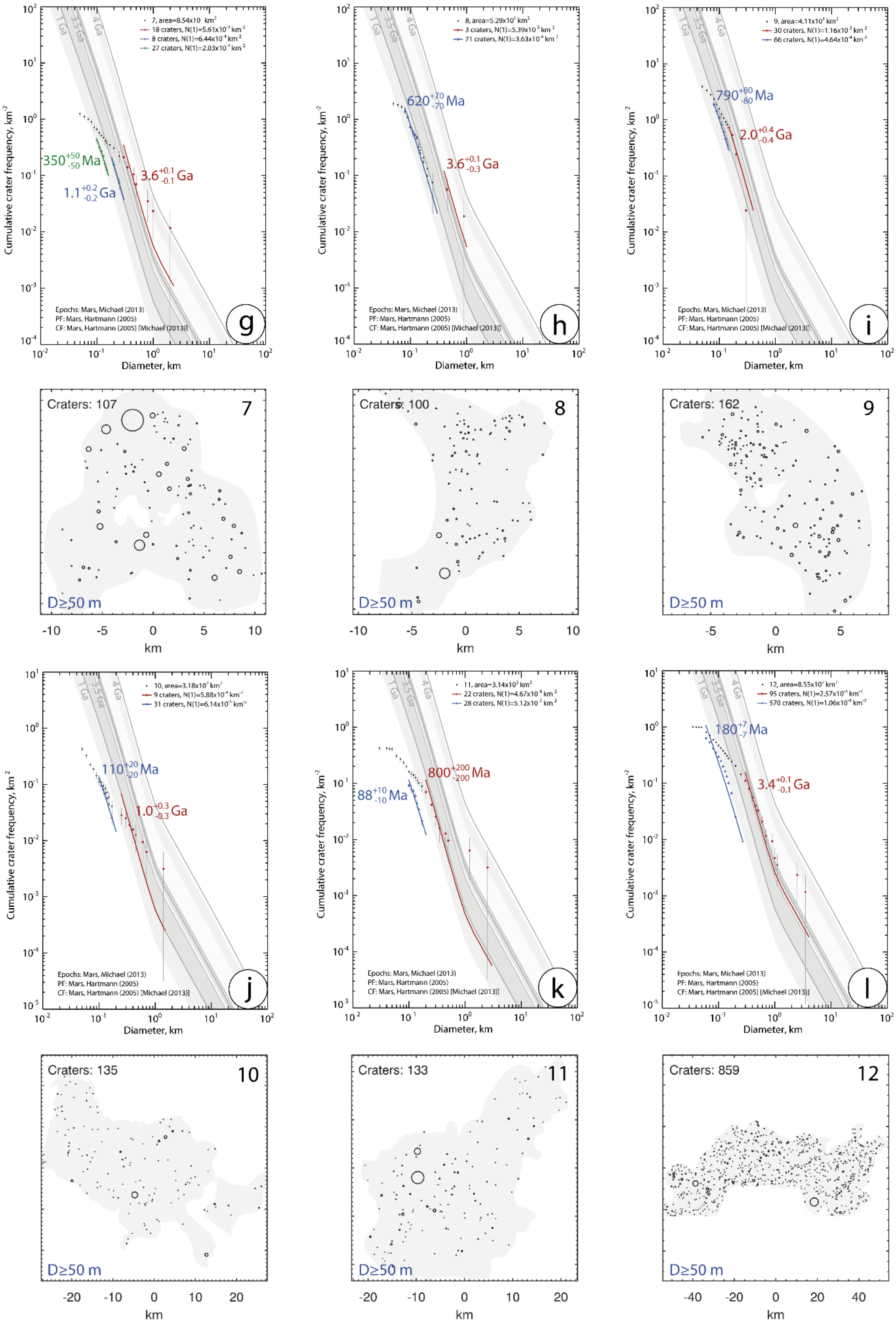
7, area=8.54×10 km^2
18 craters, N(1)=5.61×10^{-3} km^{-2}
8 craters, N(1)=6.44×10^{-4} km^{-2}
27 craters, N(1)=2.03×10^{-4} km^{-2}
1 Ga
3.5 Ga
4 Ga
350^{+50}_{-50} Ma
$1.1^{+0.2}_{-0.2}$ Ga
$3.6^{+0.1}_{-0.1}$ Ga
Epochs: Mars, Michael (2013)
PF: Mars, Hartmann (2005)
CF: Mars, Hartmann (2005) [Michael (2013)]
g
8, area=5.29×10^{1} km^2
3 craters, N(1)=5.39×10^{-3} km^{-2}
71 craters, N(1)=3.63×10^{-4} km^{-2}
620^{+70}_{-70} Ma
$3.6^{+0.1}_{-0.3}$ Ga
h
9, area=4.11×10^{1} km^2
30 craters, N(1)=1.16×10^{-3} km^{-2}
66 craters, N(1)=4.64×10^{-4} km^{-2}
790^{+80}_{-80} Ma
$2.0^{+0.4}_{-0.4}$ Ga
i
Cumulative crater frequency, km^{-2}
Diameter, km
Craters: 107
7
Craters: 100
8
Craters: 162
9
D≥50 m
km
10, area=3.18×10^{2} km^2
9 craters, N(1)=5.88×10^{-4} km^{-2}
31 craters, N(1)=6.14×10^{-5} km^{-2}
110^{+20}_{-20} Ma
$1.0^{+0.3}_{-0.3}$ Ga
j
11, area=3.14×10^{2} km^2
22 craters, N(1)=4.67×10^{-4} km^{-2}
28 craters, N(1)=5.12×10^{-5} km^{-2}
88^{+10}_{-10} Ma
800^{+200}_{-200} Ma
k
12, area=8.55×10^{2} km^2
95 craters, N(1)=2.57×10^{-4} km^{-2}
570 craters, N(1)=1.06×10^{-4} km^{-2}
180^{+7}_{-7} Ma
$3.4^{+0.1}_{-0.1}$ Ga
l
Craters: 135
10
Craters: 133
11
Craters: 859
12
-20 -10 0 10 20
-40 -20 0 20 40

4.4 Subsurface features

In order to infer possible subsurface structural and stratigraphic features and relationships, we analyzed eight NE-SW-oriented SHARAD ground-penetrating radar profiles acquired across the CNTZ (from west to east: S_01966502, S_02617902, S_01832001, S_02674602, S_02596802, S_01981001, S_01846503, S_02569101). In all these radargrams we have identified pervasive radar reflections related to dielectric discontinuities in the subsurface attributable to stratigraphic contacts and fractures with or without shear displacement (e.g., Seu et al., 2007; Castaldo et al., 2017). Here, we illustrate the radargram "S_02596802" because of its representativeness, clarity and significance (Fig. 8; location in Fig. 2b). It exhibits, from SW to NE, the following main reflective areas indicated by bright sectors (yellow arrows and dashed lines in Fig. 8a, b), and numbered from 1 to 5: (1) subparallel, closely-spaced reflections occurring in deposits of the Cimmeria basin unit (Nhc$_b$) that fill depressions inset into the Cimmeria dissected unit (Nhcd$_a$), and are also recognized in the radargram "S_02674602"; (2) spatially-dispersed and subparallel reflections reaching a depth of ~3.5 km across the Cimmeria dissected units (Nhcd$_a$ and Nhcd$_b$); (3) large detached and downdropped block associated with the dichotomy escarpment with backtilted reflections; other large detached blocks (i.e., mesas) with apparently deep fractures (e.g., clefts, gashes) (see Fig. 4a) have been recognized in the radargrams "S_01846503" and "S_01981001"; (4) reflections with an overall concave-upward geometry, apparently filling a fault-bounded basin ca. 1 km deep with triangular transverse geometry at the foot of the escarpment; and (5) discontinuous concave and convex reflections up to depths of 1.5 km across the Nepenthes basin and knobby plateau units (HNtnb and Ntnkp, respectively), beneath an overall rollover topography sloping toward the escarpment.

Steeply-dipping discontinuities expressed as dark narrow bands (red arrows and dashed lines in Fig. 8a, b) attributable to fractures and faults locally truncate the reflections described above (i.e., stratigraphic contacts). In the Cimmeria region and at the foot of the escarpment these fractures and faults dip consistently to the NE and occur associated with down-to-the north topographic drops and troughs. In the Nepenthes Mensae region they show an antithetic attitude, and together with the discontinuity at the foot of the escarpment mark the lateral boundaries of the sediment-filled basin with triangular section that has been also observed in radargrams "S_02569101", "S_01981001", "S_02674602", "S_01832001", "S_01966502" and, "S_02617902".

5. Discussion

The detailed mapping and description of the geology and geomorphology of the CNTZ (Figs. 2-4), together with the spectrally-inferred mineral composition (Figs. 5 and 6), the surface chronology based on both crater-density analysis (Fig. 7) and spatial relationships, and the stratigraphic and structural features interpreted in the radar-sounding data (Fig. 8), have permitted us to: (1) interpret the mapped units and landforms focusing on their formative pro-

***Fig. 8 (next page)**. (a, b) SHARAD radargram "S_02596802" (see location in Fig. 2b) with interpreted subsurface features marked by red and yellow arrows and dashed lines attributable to structural and stratigraphic features, respectively. (c) HRSC/MOLA blended DEM and (d) mapped geologic units, both over a THEMIS-IR day mosaic, showing the topography and geology of the area around the SHARAD profile, respectively. A-A' represents the trace of the radargram and that corresponding to the geological cross section shown in Fig. 10.*

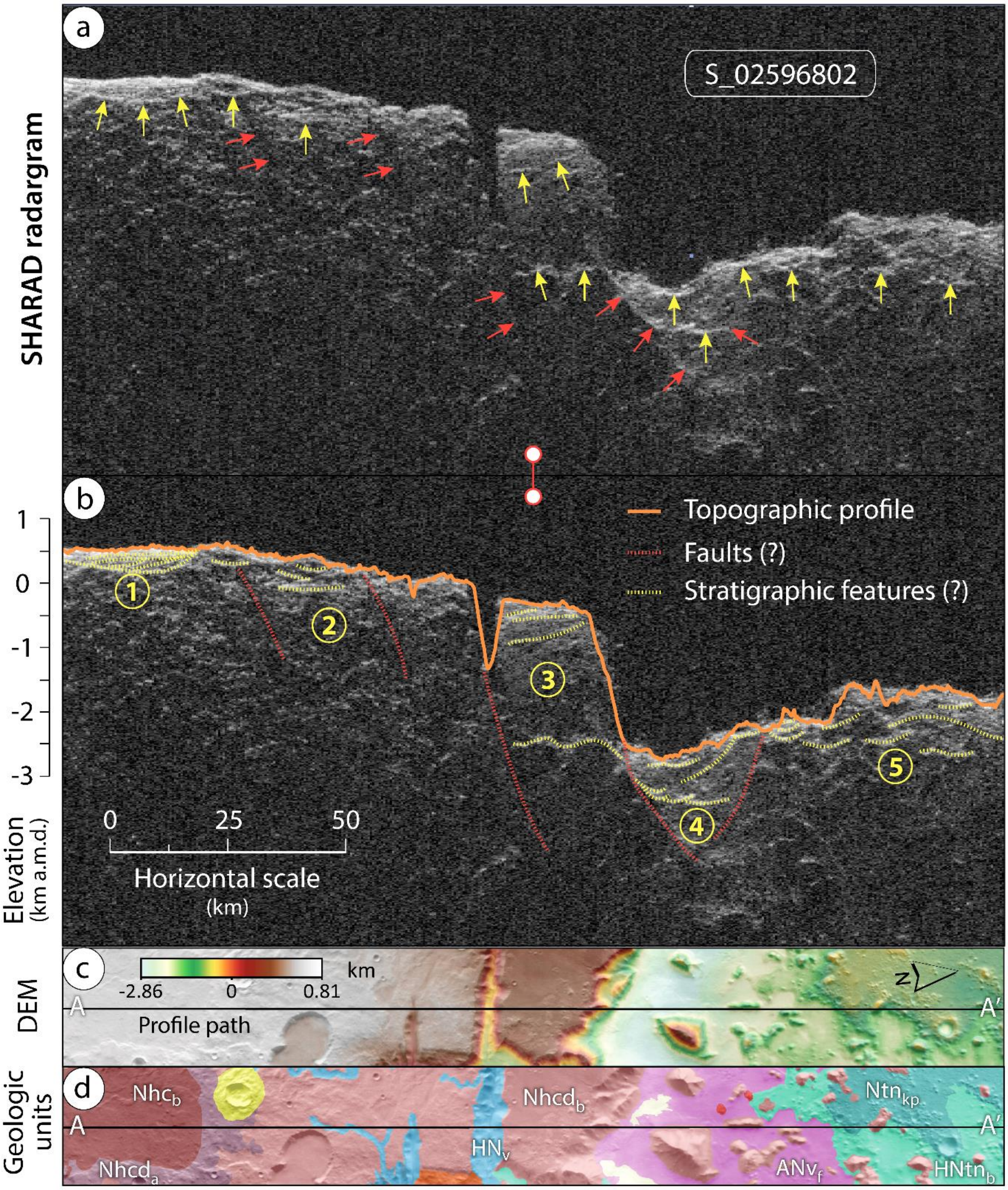

-cesses; (2) establish their stratigraphy and correlate them with those of previous geological maps; and (3) propose hypotheses about the landscape evolution and geological history of the area.

5.1 Unit interpretation, stratigraphy and correlation

The Cimmeria dissected units ($\mathrm{Nhcd_a}$ and $\mathrm{Nhcd_b}$) consist of heavily to moderately degraded highland materials, possibly formed by undifferentiated materials related to impact, volcanic, fluvial, and basin-fill processes. In the SHARAD radargrams these units show discontinuous reflections up to a depth of ~3.5 km interpreted as probable evidence of layering. In the vicinity of the dichotomy escarpment the reflections display southward dips attributable to detached and downdropped blocks tens of kilometers long that have experienced backtilting (Fig. 8a, b). The stratigraphically lower unit $\mathrm{Nhcd_a}$, Early to Middle Noachian in age (see summarized age chart in Fig. 9), is affected by locally- and regionally-distributed compressional tectonic morpho-structures, as indicated by the occurrence of ridge crests with local distribution, and widespread lobate scarps that indicate a prevalent NE-SW shortening direction subperpendicular to the dichotomy escarpment. Ridge crests and lobate scarps have been interpreted as the geomorphic expression of thrust or reverse faults (e.g., Watters and Robinson, 1999; Watters et al., 2009). The relatively younger unit $\mathrm{Nhcd_b}$ (Middle Noachian) (Fig. 9), locally affected by compressional lobate scarps and ridge crests, displays plateaus, mesas and knobs along the highland-lowland boundary, probably related to crustal extension and large slope movements (see Figs. 10 and 11). This interpretation is supported by (1) radar-inferred NE-dipping normal faults in the Cimmeria region and at the foot of the escarpment, that occur associated with down-to-the-northeast topographic drops and troughs along the dichotomy boundary (Fig. 8a, b); and (2) large detached coherent blocks of Cimmeria that match with arcuate scars in the escarpment, attributable to rock spreads. Both units $\mathrm{Nhcd_a}$ and $\mathrm{Nhcd_b}$ are integrated in the Middle Noachian highland unit (mNh) defined by Tanaka et al. (2014) in the last global-scale geologic map of Mars. Furthermore, we consider that the Cimmeria 1 unit ($\mathrm{Nhc_1}$; Early to Middle Noachian) defined by Skinner and Tanaka (2018) in the Nepenthes Planum region, northwest of our study area, probably correlates with our unit $\mathrm{Nhcd_b}$ due to their similar characteristics, age and topographic occurrence. The division of the Cimmeria region in the CNTZ into two units of different ages was also considered by Scott and Carr (1978) and King (1978) in their global and Mare Tyrrhenum quadrangle geologic maps. They defined for the Cimmeria lower and upper units two Noachian units of hilly and crater material (Nhc), and crater plateau material (Nplc), respectively, characterized by different degree of roughness in their inter-crater surfaces (Scott and Carr, 1978). The Cimmeria basin unit ($\mathrm{Nhc_b}$), Late Noachian in age (Fig. 9), consists of slightly to moderately degraded surfaces, underlain by undifferentiated materials probably corresponding to fluvial sediments and impact breccias that fill depressions inset into unit $\mathrm{Nhcd_a}$. These formations, which are tectonically contracted as indicated by the presence of wrinkle ridges ascribed to thrust faults (e.g., Andrews-Hanna, 2020), are characterized by radar-inferred subparallel, closely-spaced layering (Fig. 8a, b). This unit probably correlates with the Late Noachian highland unit (lNh) of Tanaka et al. (2014).

The Nepenthes knobby plateau unit ($\mathrm{Ntn_{kp}}$; Late Noachian) (Fig. 9) is underlain by deposits including an undifferentiated combination of impact breccias, volcanic products, and mass-wasted materials that form aprons around degraded mesas and knobs of highland rocks of the unit $\mathrm{Nhcd_b}$. The unit displays radar-inferred discontinuous layering with concave and convex geometries reaching depths of 1.5 km beneath the downthrown limb of a rollover anticline with topographic expression sloping toward the dichotomy escarpment (Figs. 8a, b and 10). This bending fold suggests a listric geometry for the master normal fault that controls the dichotomy escarpment. The Nepenthes knobby plateau unit shows evidence of compressional tectonics with a dominant NE-SW shortening trend, similar to that exhibited by member a of the Cimmeria dissected unit ($\mathrm{Nhcd_a}$), suggesting a common and coetaneous origin for the deformation structures. The unit $\mathrm{Ntn_{kp}}$ overlies member b of the Cimmeria dissected unit ($\mathrm{Nhcd_b}$), as inferred by the occurrence of relict reliefs (e.g., mesas and knobs) of the unit $\mathrm{Nhcd_b}$

that crop out as inliers north of the dichotomy escarpment, and locally underlies the Nepenthes basin unit (HNtn$_b$). The Nepenthes basin unit (HNtn$_b$; Late Noachian to Early Hesperian), locally showing compressional morpho-structures such as wrinkle ridges, displays pristine to degraded aggradational plains underlain by fluvial, lacustrine and/or mass-wasting deposits. These basins correspond to the belt of interconnected NW-SE-trending closed depressions at the foot of the dichotomy escarpment in Nepenthes Mensae that used to host putative paleolakes (e.g., García-Arnay and Gutiérrez, 2020). These depressions are inset into member b of the Cimmeria dissected unit (Nhcd$_b$). This unit shows reflections in the radargrams interpreted as layered deposits with an overall synformal geometry that fill a basin ca. 1 km deep. The basin fill at the foot of the escarpment displays a triangular cross-sectional geometry apparently bounded by synthetic and antithetic normal faults. This structure seems to correspond to a keystone graben associated with the master fault of a larger half-graben morpho-structure with rollover anticline (Figs. 8a, b and 10). In contrast, the basins of the unit HNtn$_b$ located to the northeast of our map are probably the result of the coalescence of degraded impact craters as indicated by their sub-circular shape in plan view, and partially-preserved knobby rims (see Fig. 2a). These two mapped units (Ntn$_{kp}$ and HNtn$_b$) were integrated into the Hesperian and Noachian transition unit (HNt) by Tanaka et al. (2014), as well as in the Nepenthes Mensae unit (HNn; Early Noachian to Early Hesperian) defined by Tanaka et al. (2005) in their geologic map of the northern plains of Mars. In the region of Nepenthes Planum, Skinner and Tanaka (2018) defined the Cimmeria 2 unit (Nhc$_2$; Middle to Late Noachian) and Cimmeria 3 unit (HNhc$_3$; Late Noachian to Early Hesperian) that possibly correlate with our mapped units Ntn$_{kp}$ and HNtn$_b$, respectively, as suggest their similar characteristics, stratigraphic position and chronology.

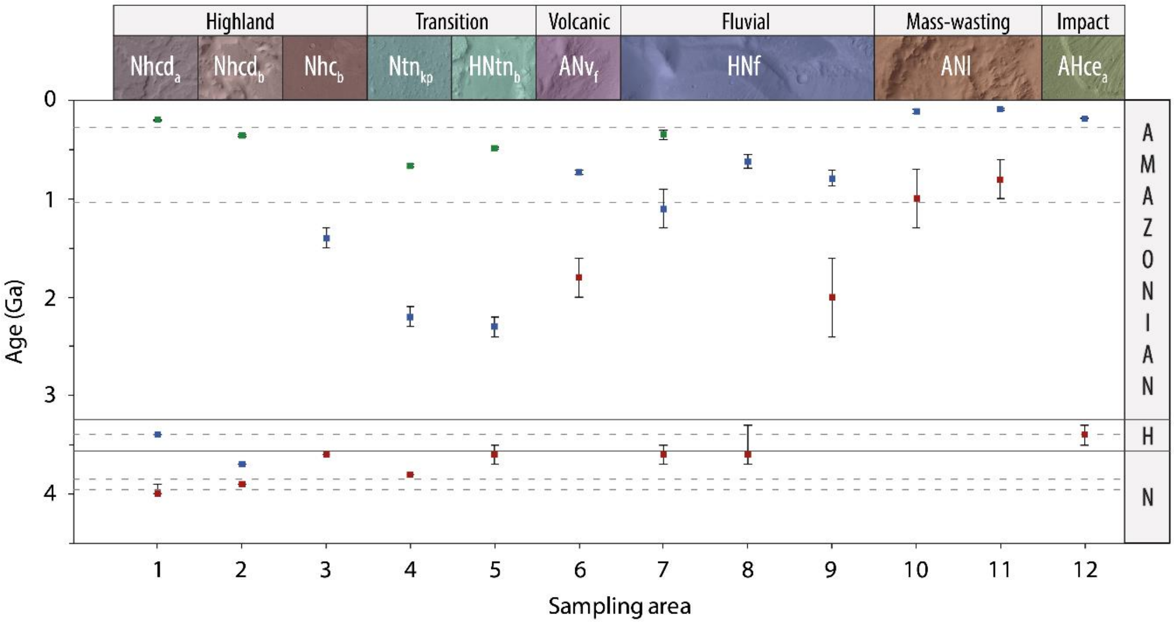

***Fig. 9**. Diagram showing formation (red boxes) and resurfacing (blue and green boxes) age estimations, as well as their error bars (vertical black lines) obtained for the main mapped units from the cumulative crater size-frequency diagrams constructed for each crater-counting area (Fig. 7) using the Hartmann chronology approach. Horizontal continuous and dashed lines indicate the boundaries between the Martian geological periods and epochs, respectively (Michael, 2013). The top of the diagram shows the geologic unit corresponding to each sampling area. Note that the colors of boxes indicating the ages in this diagram coincide with those shown in Fig. 7. N: Noachian; H: Hesperian.*

Tanaka et al. (1992b) defined in their geologic map of the Elysium region the undivided material unit HNu (Noachian to Early Hesperian) and the smooth-plains material unit Aps (Early Amazonian), that also correlate with our mapped units Ntn_{kp} and $HNtn_b$, respectively. The unit Aps defined by Tanaka et al. (1992b) shows poorly-constrained spatial boundaries and chronology, with a remarkable younger age than the age estimations obtained for those surfaces by Skinner and Tanaka (2018) and in this work.

The fan unit (HNf), Late Noachian to Late Hesperian in age (Fig. 9), corresponds to the fan-shaped deposits interpreted as putative Gilbert-type deltas and alluvial fans (e.g., Rivera-Hernández and Palucis, 2019; García-Arnay and Gutiérrez, 2020). These water-laid deposits show spectrally-inferred hydrated clay- and silica-bearing layered sediments (Figs. 5 and 6) in the deltas “D2” and “D11” (see Table 1). The spectra of the hydrated Fe/Mg-phyllosilicates and hydrated Al-phyllosilicates/silica are, respectively, consistent with an intermediate composition between end-member smectites saponite and nontronite, and between opal and the end-member smectite montmorillonite (Fig. 5c, d). The detection of hydrated minerals together with the morpho-sedimentary environment supports the presence of liquid water in the past (e.g., Poulet et al., 2005), and strengthens the hypothesis about the fan-delta origin of these deposits. Their high paleoenvironmental interest is also related to the relatively rapid aggradation rate that characterizes these sedimentary environments, favoring the preservation of potentially existing organic matter (e.g., Ehlmann et al., 2008). In order to estimate the chronology of this unit, we selected the two largest deltas in the CNTZ (i.e., “D2” and “D7”, Table 1). The areas of these deltas (<100 km^2) are significantly smaller than 1,000 km^2, which is the minimum threshold area for confidently assessing the age of a surface according to Warner et al. (2015). This implies that age estimations obtained for these surfaces may be affected to a greater extent by the spatial variability of cratering processes, as well as the exclusion of larger craters resulting in lower crater counts (i.e., potential age underestimation). We obtained a surface age of 2.0 ± 0.4/0.4 Ga (Early Amazonian) for the upper delta of “D2”, that represents the smaller delta area (~41.1 km^2). The upper delta partially overlies the lower delta of “D2” suggesting that the former is younger. In fact, its formation age is significantly younger than that estimated for the lower delta of “D2” (3.6 ± 0.1/0.3 Ga; Late Noachian to Late Hesperian). In contrast, the age estimated for the lower delta of “D2” is consistent with that estimated for the delta “D7” (3.6 ± 0.1/0.1 Ga; Late Noachian to Early Hesperian). Both ages are in agreement with the period of intense and widespread fluvial activity on Mars (e.g., Irwin III et al., 2005; Carr, 2012), and also fit with that estimated for the Nepenthes basin unit ($HNtn_b$) (3.6 ± 0.1/0.1 Ga; Late Noachian to Early Hesperian), probably filled by coeval deposits related to fluvial and lacustrine processes. Additionally, we obtained a minimum age estimate of 3.4 ± 0.1/0.1 Ga (Early to Late Hesperian) (Fig. 9) for the cessation of fluvial activity in Licus Vallis, the main watershed in the CNTZ. This age estimation is also compatible with the older ages obtained for the deltas “D7” and “D2” (lower delta), and the Nepenthes basin unit ($HNtn_b$). On the basis of these results, we assigned an age of Late Noachian to Late Hesperian to the valley unit (HNv). García-Arnay and Gutiérrez (2020) obtained a formation age of 3.88 ± 0.06/0.12 Ga (Middle Noachian to Late Noachian) for the delta “D7”, using the same approach as the one applied in the present work (the Hartmann chronology), but without establishing a minimum crater diameter (i.e., all primary craters observed were counted). The formation age obtained by García-Arnay and Gutiérrez (2020) is older than that estimated in this work (3.6 ± 0.1/0.1 Ga; Late Noachian to Early Hesperian). The difference between the closest extremes of the 1-sigma standard deviation error bars for each formation age is 600 Ma (3.76 vs. 3.7 Ga, respectively).

We interpret that this age difference is mainly due to exclusion in this work of the craters with diameters lower than the considered threshold value (50 m), as well as the inclusion of the delta front (larger counting area) potentially affected by erosion and slope instability processes (resurfacing). In summary, the chronological analysis indicates that (1) fluvial-lacustrine processes mainly occurred in the CNTZ from Late Noachian to Late Hesperian; (2) the higher impact of the spatial variability of cratering processes in smaller areas, as well as the minimum crater diameter considered in the computation (50 m) may have led to underestimated ages for the deltas; and (3) the formation age obtained for the upper delta of "D2", which overlies the lower delta (e.g., de Pablo and Pacifici, 2008), does not seem to be consistent with a period of intense fluvial activity during the Early Amazonian (~2 Ga), but seems to be related to the small size of the analyzed area and possible resurfacing events affecting its crater population.

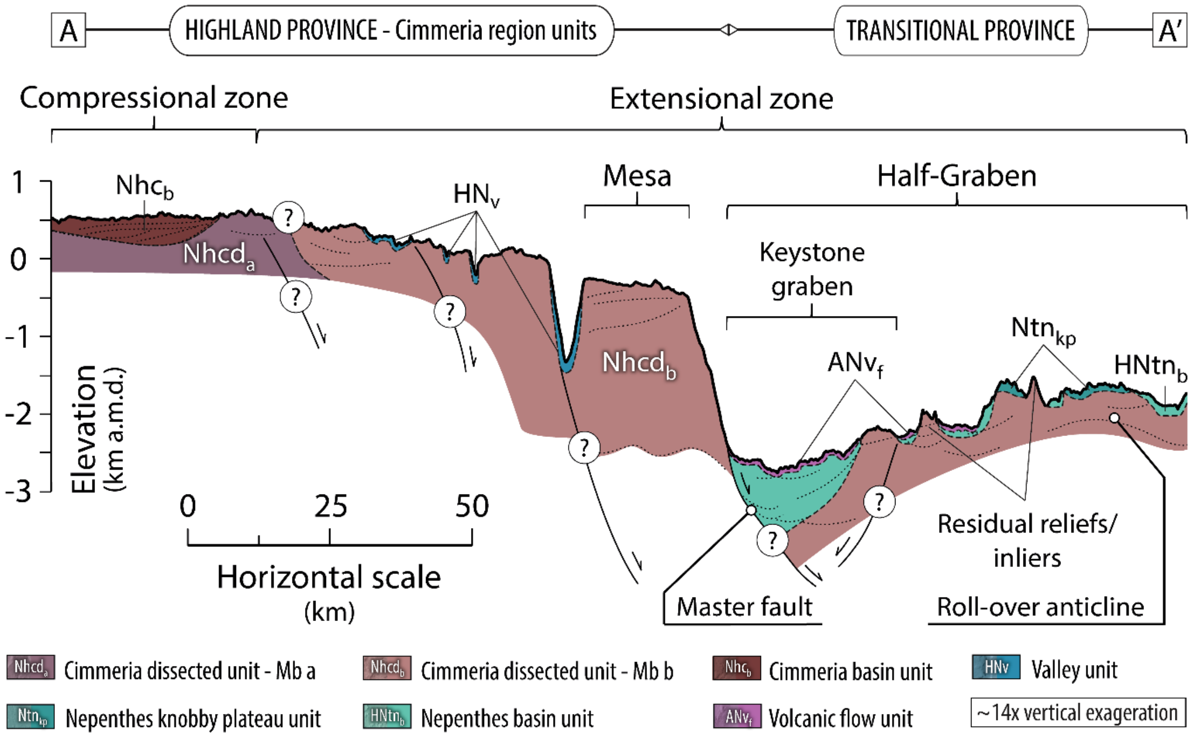

Fig. 10. Geological cross-section A-A' (see location in Fig. 2b) illustrating our interpretation of the subsurface stratigraphic and structural relationships in the CNTZ. This schematic cross-section has been constructed on the basis of the information provided by the radargram profile "S_02596802" shown in Fig. 8, topographic and chronological data, as well as cross-cutting and superposition relationships among geologic units. Colors coincide with those of the geologic units shown in Fig. 2a.

The volcanic flow unit (ANv_f) consists of high-TI plains most probably formed by lava fields, as indicated by the following lines of evidence: (1) frequent grooves and channels, as well as overlapping lobes often emanating from isolated and coalesced raised fissures, pitted cones and small tholi of the unit ANv_e, interpreted as different types of volcanic edifices genetically linked to the unit ANv_f, and thus, with an analogous age (see Fig. 3d-h); (2) extensive olivine-bearing deposits associated with barchan dune fields (unit Ae) that occur along the southern edges of the unit ANv_f (see Figs. 3k and 6); and (3) it generally occurs in the deepest areas of the depressions likely related to subsidence processes within an extensional tectonic environment (Figs. 10 and 12). The localized deformation of this unit by wrinkle ridges is probably associated to thermal contraction of cooling lava flows. We obtained for the volcanic flow unit an age estimate of 1.8 ± 0.2/0.2 Ga (Early Amazonian) (Fig. 9). However, we have corrected its formation age on the basis of more robust relative chronologies based on geometrical relationships (e.g., cross-cutting and superposition). The deposits corresponding to the lower delta of "D2" (unit HNf; Late Noachian to Late Hesperian) locally overlie the volcanic flow and volcanic edifice units (see details in Fig. 3d). We thus consider that the minimum age for the formation of the volcanic flow unit should be at least as old as that of the unit HNf (i.e., Late Noachian). The relatively young formation age obtained by crater counting for the unit ANv_f may be attributed to the obliteration of old craters as a result of the eolian erosion and/or locally younger volcanic activity. García-Arnay and Gutiérrez (2020) obtained a surface age of 3.71 ± 0.08/0.21 Ga (Late Noachian to Early Hesperian) for the low-lying terrains located east of the counting area "6" applying the same dating approach (i.e., the Hartmann chronology), but without considering any minimum crater diameter. This age fits with our minimum age estimate for the formation of the volcanic flow unit (Late Noachian). However, the counting area considered by García-Arnay and Gutiérrez (2020) also included zones corresponding to other geologic units and, as a result, the obtained age is not a reliable estimate for the volcanic flow unit. The unit ANv_f in the CNTZ is integrated into the Hesperian and Noachian transition unit (HNt) of Tanaka et al. (2014), and does not seem to be correlative to the Nepenthes flow unit (Htn_f) of the Nepenthes Planum region (Skinner and Tanaka, 2018).

The landslide unit (ANl) consists of mass-wasted highland materials derived from the dichotomy escarpment formed by unit $Nhcd_b$ and locally accumulated along the slopes of the dichotomy escarpment during the Late Noachian to Middle Amazonian. We have interpreted this unit as deposits of various types of large landslides based on the following features: (1) the presence of head scars that match with large detached blocks, back-tilted benches, as well as rugged, rolling, and hummocky surfaces locally with blocky texture; (2) their spatial association with the ca. 2 km high dichotomy escarpment; and (3) the extensional environmental that dominates the basins adjacent to the dichotomy. These large landslides, which occur along the dichotomy escarpment and have moved into the depressions in Nepenthes Mensae, are generally characterized by a limited runout. We have inferred different types of slope movements in the CNTZ based on the classification of Hungr et al. (2014): (1) detached, km-scale masses of coherent blocks, locally fractured and dilated, probably formed by lateral spreading related to weak basal materials (see an example in Fig. 4a), (2) deposits characterized by apparent internal deformation, slump blocks and often back-tilted benches possibly formed by rotational sliding (e.g., landslides 1 and 2 in Fig. 11), as well as (3) frequent rock falls. We obtained average age estimates of 1.0 ± 0.3/0.3 Ga (Early to Middle Amazonian) and 0.8 ± 0.2/0.2 Ga (Middle Amazonian) for each counting area considered (Fig. 9). However, the occurrence of a valley originating in the highlands (unit HNv; Late Noachian to Late Hesperian) and dissecting the landslide deposits (see Fig. 11) indicates that the minimum age estimation for the formation of the unit ANl may be as old as Late Noachian.

Fig. 11 (next page)*. 3D oblique view of two large landslides (ANl unit) occurring along the dichotomy escarpment in the CNTZ (location in Fig. 1; CTX images). The landslide 2 located on the right side to the image (labelled as "2") seems to overlap the larger landslide 1. Note the presence of hummocky topography on the landslide surfaces (circle: close-up view; CTX images). Landslide 1 is incised by a valley of the unit HNv. White dashed line indicates the toe of the landslide mass overriding the surrounding plains of the Nepenthes basin unit ($HNtn_b$). Blue and yellow dashed arrows indicate the paleoflow of the valley and the displacement direction of the landslides, respectively. The landslide of this 3D image corresponds with the counting area 10 (Figs. 7j and 9).*

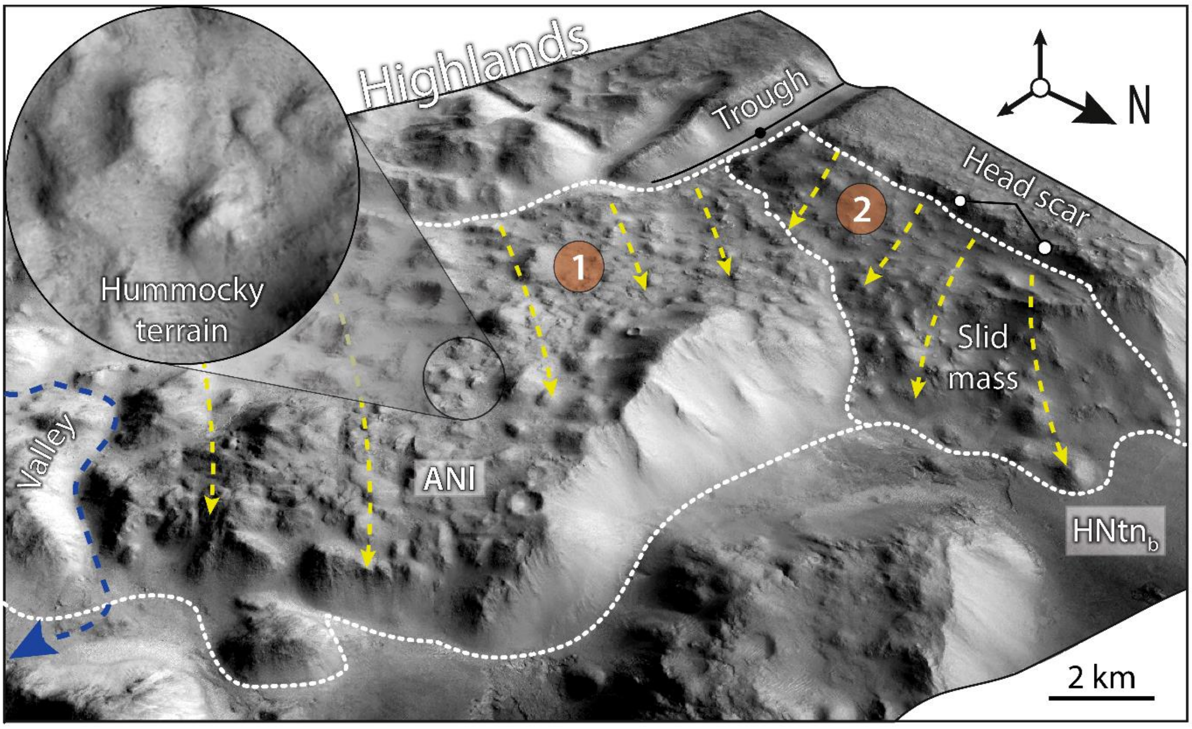

5.2 Geological-geomorphological history of the CNTZ

Here, we summarize the geological history and landscape evolution of the CNTZ inferred on the basis of the interpretation of the mapped units and landforms and their chronology. Our reconstruction is focused on the sequence of paleogeographic stages associated with the formation of the closed depressions that used to host large paleolakes and on the evolution of the dichotomy escarpment.

The explored record starts in the Early to Middle Noachian with the formation of the Cimmeria dissected units (the lower and upper members $Nhcd_a$ and $Nhcd_b$, respectively). Both units were affected by a phase of NE-SW-oriented tectonic shortening, recorded by prominent lobate scarps interpreted as the surface expression of thrust faults. These morpho-structures occur in the highland province (e.g., Watters and Robinson, 1999; Watters, 2003b), and less conspicuously in the Nepenthes knobby plateau unit (Ntn_{kp}, Late Noachian in age) of the transitional province. The disruption of fluvial valleys (Late Noachian to Late Hesperian in age) observed in the unit $Nhcd_a$ by lobate scarps unaffected by fluvial erosion, as well as the adaptation of some drainages to these compressional features (e.g., deflected fluvial valleys parallel to the toe of lobate scarps) suggest that the compressional stress field may have started as soon as the Late Noachian and probably ended sometime after the cessation of fluvial activity (Late Hesperian), which is roughly consistent with the global-scale compressional tectonic regime that occurred on Mars between the Late Noachian to Early Hesperian (e.g., Tanaka et al., 1991; Watters, 1993). During the Late Noachian, basins of uncertain origin were formed and filled of sediments on the unit $Nhcd_a$ to form the Cimmeria basin unit (Nhc_b) (see Fig. 10).

The topography of the Cimmeria dissected units in the CNTZ is analogous to that displayed in a large part of the highlands south the dichotomy, which is characterized by a topographically higher sector that gradually descends from the highlands into the northern lowlands and frequently ends abruptly along a steep escarpment that represents the dichotomy boundary (Watters and McGovern, 2006). The ca. 2 km high escarpment in the CNTZ defines the boundary between the highland and transitional provinces. The member b of the Cimmeria dissected units ($Nhcd_b$) associated with the dichotomy escarpment shows numerous troughs that controlled fretted valleys subparallel to the escarpment. The analyzed radargrams indicate that the escarpment and the troughs are related to a master and secondary normal faults that dip consistently to the NE indicating a NE-SW extension direction with major geomorphic imprint on the landscape (see Figs. 8 and 10). The extensional tectonics probably led to: (1) the plateau situated south of the dichotomy escarpment with down-to-the-north topographic drops associated with secondary normal faults; and (2) the chain of interconnected NW-SE-trending closed depressions located at the foot of the dichotomy escarpment. These basins are probably downthrown blocks (i.e., keystone graben) nested in the lower part of a larger half-graben morpho-structure (i.e., fault-angle depression), as inferred from the topography and the stratigraphic and structural relationships interpreted from the mapped units and radar reflections (see Figs. 8 and 10). According to Tanaka et al. (2005), the region of Nepenthes Mensae may have been affected by mass wasting and “basal sapping of volatiles” that may have generated the knobby terrain in this region. The belt of depressions in Nepenthes Mensae was also attributed to extensional tectonics by Watters (2003a) and Watters and McGovern (2006), reaching the maximum lithospheric deflection near the base of the dichotomy escarpment (Watters, 2003a). Other graben basins have been inferred along the crustal dichotomy in Nilosyrtis Mensae (Levy et al., 2007) and Protonilus Mensae (e.g., Watters, 2003a), located north of Terra Sabaea and Arabia Terra, respectively, as well as in Aeolis Mensae (e.g., Watters and McGovern, 2006), southeast of the CNTZ, exhibiting a topographic expression analogous to that in the study area. Our observations also suggest that, regardless of how and when the crustal dichotomy was originated, its current shape in the CNTZ is largely related to dip-slip displacement along a down-to-the-northeast normal fault system that controlled the formation of half-graben basins within this extensional environment in Nepenthes Mensae (see Figs. 10 and 12). The Nepenthes basin unit ($HNtn_b$), which is generally confined to the lower part of the half-graben basins (nested keystone graben) and seems to reach its greatest thickness in the vicinity of the fault-controlled escarpment (see Figs. 10 and 12), was accumulated from the Late Noachian to Early Hesperian based on crater densities. The probable syntectonic deposition of the unit $HNtn_b$ by fluvio-lacustrine and mass-wasting processes suggests that extensional tectonics in the CNTZ was active at least during the Late Noachian to Early Hesperian. The volcanic edifice/flow units (ANv_e and ANv_f, respectively), probably associated with extensional tectonics (i.e., fissure eruptions), were locally emplaced overlying the unit $HNtn_b$ from the Late Noachian to the Early Amazonian, as indicated by crater densities and geometrical relationships among units (see the block diagram in Fig. 12), what suggests that the extensional phase may have even been active until Early Amazonian times. The stratigraphic relationships between the volcanic units (ANv_e and ANv_f) and the fan unit (HNf; Late Noachian to Late Hesperian), which is rich in clay-bearing deposits (Figs. 5 and 6), reveal that the latter at least locally postdated the volcanic units (see an example in Fig. 12). However, their ages based on both crater densities and stratigraphic relationships suggest that the volcanic and the fluvio-lacustrine activity may have been at least partially coeval, between the Late Noachian and the Late Hesperian, coinciding with the period of fluvial activity and formation of paleolakes in the CNTZ (Fig. 12) (e.g., Rivera-Hernández and Palucis, 2019; García-Arnay and Gutiérrez, 2020). Our observations indicate that the inferred compressional and ex-

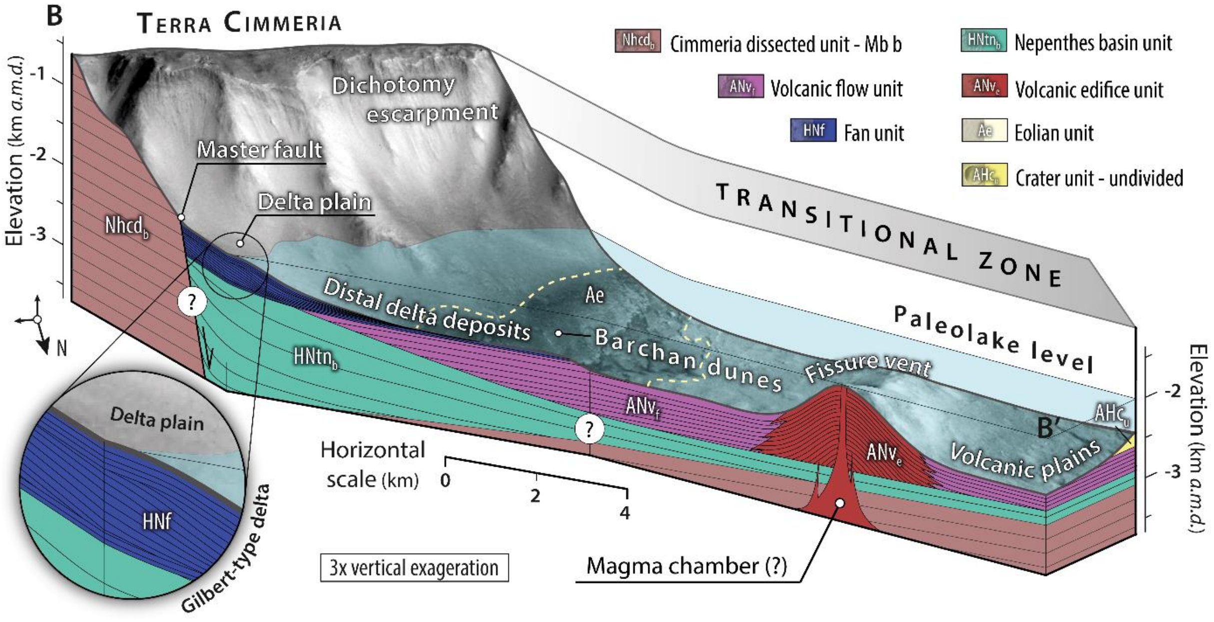

Fig. 12. Detailed block diagram of the CNTZ around the dichotomy escarpment that interprets the subsurface geology along the cross section B-B′ (location and details in Figs. 2b and 6a, respectively) integrating the information provided by topographic data, the geologic units, radargrams, formation ages and mineral composition of the units. It includes the reconstruction of the paleolake level at about −1,950 m, which is the mean water level of the main paleolake in Nepenthes Mensae during the Late Noachian-Early Hesperian transition according to García-Arnay and Gutiérrez (2020). Colors coincide with those of the geologic units shown in Fig. 2a. Circle: close-up view showing the interpreted depositional architecture of the putative Gilbert-type delta “D11” (see Table 1).

-tensional tectonic stresses in the CNTZ, which exhibit the same direction (i.e., NE-SW), seem to have largely occurred sometime from the Late Noachian to Late Hesperian, and even until more recent epochs, but not simultaneously. Several lines of evidence suggest that the extensional phase postdated the compressional deformation: (1) the compressional structures do not affect to the most recent units; (2) the extensional structures have formed the most recent morpho-structures (e.g., the present-day dichotomy escarpment or the basins in Nepenthes Mensae), as well as the accommodation space in which the units HNtn$_b$ and ANv$_f$ were deposited; and (3) the areas affected by extensional tectonics divide in half those that are tectonically contracted in the highland and transitional provinces. Other authors (e.g., McGill and Dimitriou, 1990; Watters and Robinson, 1999; Watters, 2003a, 2003b) indicated that the compressional and extensional deformation occurred along the dichotomy boundary in the Eastern Hemisphere from the Late Noachian to Early Hesperian. Different types of large landslides have been developed along the dichotomy escarpment favored by the large local relief, and probably also by its continuous tectonic rejuvenation and the weakening of the materials by extensional deformation (i.e., faulting, fracturing). Basal sapping suggested by Tanaka et al. (2005) may have contributed to the instability and development of the escarpment in Nepenthes Mensae. A tentative Late Noachian to Middle Amazonian age has been ascribed to the landslide unit (ANl) based on crater densities and stratigraphic relationships, although the different slope movements may have a wide range of chronologies. The presence of mechanically weak material in the basal part of the escarpment may have propitiated the development of large rock spreads, producing coherent blocks with dilated fractures of unit Nhcd$_b$ detached form the escarpment and displaced laterally into the depressions of Nepenthes Mensae (see an example of large rock spreads located ~15 km away from the dichotomy escarpment in Fig. 4a). During the Amazonian period, significant eolian erosion has mainly carved the surfaces of the knobby plateau and basin units in Nepenthes Mensae, as shown by the pervasive occurrence of yardangs that indicate a dominant S-directed wind (see Fig. 3l). Numerous barchan dune fields formed by olivine-bearing sands (Fig. 6) have been accumulated along the foot of the dichotomy escarpment in recent times (see Figs. 3k and 12).

6. Conclusions

The findings suggest that the exposed units mapped in the CNTZ formed over a long time-span, from the Early Noachian to recent times. The inferred compressional and extensional deformation have played a fundamental morphogenetic role in the configuration of the landscape at least from the Late Noachian to Late Hesperian. Extensional tectonics, which postdates the compressional phase, has contributed to the development of some of the most prominent geomorphic features of the region, including: (1) the plateau located to the south of the dichotomy in the highland province; (2) the 2-km-high dichotomy escarpment interpreted as a fault scarp related to the master normal fault (3) the formation of a half-graben at the foot of the escarpment with keystone grabens nested in its lower part that used to host paleolakes in Nepenthes Mensae; (4) the fissure-type volcanic activity in the deepest areas of the basins; and (5) the megalandslides (e.g., large rock spreads and slumps) derived from the dichotomy escarpment. Fluvial and lacustrine activity has also played an important morphogenetic role in the CNTZ. This interpretation is supported by the pervasive occurrence of tectonically-controlled fluvial valley networks carved into the Cimmeria dissected units, and putative fan-deltas, rich in hydrated clay-bearing layered sediments. The possible interaction during the Late Noachian to Late Hesperian between the heat sources associated with the volcanic activity and the liquid water occupying the basins in Nepenthes Mensae makes this region a potential landing site for the search of past life signatures on Mars. This work contributes to improve our knowledge about the geology and the landscape evolution in the CNTZ, and provides a detailed geologic framework to contextualize the recent findings about the paleohydrologic conditions in Nepenthes Mensae, as well as to compare future studies within the CNTZ and other areas along the highland-lowland transitional zone.

Acknowledgments

This research was supported by a PhD scholarship granted to ÁG-A (C237/2016) by the Gobierno de Aragón (Spain) and the European Social Fund, as well as by grants awarded by the Ibercaja-CAI mobility programme (CB 2/21; Universidad de Zaragoza, Fundación Bancaria Ibercaja and Fundación CAI) and the Erasmus+ Traineeship programme (53971; European Commission) to fund a research stay of ÁG-A at the International Research School of Planetary Sciences (Università degli Studi "G. D'Annunzio"). The work has been also supported by projects CGL2017-85045-P and PID2021-123189NB-I00 (Ministerio de Ciencia e Innovación, Gobierno de España).

References

Andrews-Hanna, J.C., 2020. The tectonic architecture of wrinkle ridges on Mars. Icarus 351, 113937. https://doi.org/10.1016/j.icarus.2020.113937.

Andrews-Hanna, J.C., Zuber, M.T., Banerdt, W.B., 2008. The Borealis basin and the origin of the martian crustal dichotomy. Nature 453(7199), 1212-1215. https://doi.org/10.1038/nature07011.

Burr, D.M., Williams, R.M., Wendell, K.D., Chojnacki, M., Emery, J.P., 2010. Inverted fluvial features in the Aeolis/Zephyria Plana region, Mars: Formation mechanism and initial paleodischarge estimates. J. Geophys. Res. Planets 115(E7). https://doi.org/10.1029/2009JE003496.

Carr, M.H., 2012. The fluvial history of Mars. Phil. Trans. R. Soc. A. 370(1966), 2193-2215. https://doi.org/10.1098/rsta.2011.0500.

Carter, J., Poulet, F., Bibring, J.-P., Mangold, N., Murchie, S., 2013. Hydrous minerals on Mars as seen by the CRISM and OMEGA imaging spectrometers: updated global view. J. Geophys. Res. Planets 118, 831–858. https://doi.org/10.1029/2012JE004145.

Castaldo, L., Mège, D., Gurgurewicz, J., Orosei, R., Alberti, G., 2017. Global permittivity mapping of the Martian surface from SHARAD. Earth Planet. Sc. Lett. 462, 55-65. https://doi.org/10.1016/j.epsl.2017.01.012.

Christensen, P.R., Jakosky, B.M., Kieffer, H.H., Malin, M.C., McSween, H.Y., Nealson, K., Mehall, G.L., Silverman, S.H., Ferry, S., Caplinger, M., Ravine, M., 2004. The thermal emission imaging system (THEMIS) for the Mars 2001 Odyssey Mission. Space Sci. Rev. 110 (1–2), 85–130. https://doi.org/10.1023/B:SPAC.0000021008.16305.94.

Christensen, P.R., Fergason, R.L., Edwards, C.S., Hill, J., 2013. THEMIS-derived thermal inertia mosaic of Mars: product description and science results. Lunar and Planetary Science Conference Abstracts vol. 44 (p. #2822).

Clarke, J., Pain, C.F., Rupert, S., 2020. Complex expressions of inverted and exhumed relief in central Utah, and some martian counterparts. Phys. Geogr. 1-18. https://doi.org/10.1080/02723646.2020.1839161.

de Pablo, M.Á., Pacifici, A., 2008. Geomorphological evidence of water level changes in Nepenthes Mensae, Mars. Icarus 196 (2), 667–671. https://doi.org/10.1016/j.icarus.2008.04.005.

Di Achille, G., Hynek, B.M., 2010. Ancient ocean on Mars supported by global distribution of deltas and valleys. Nat. Geosci. 3 (7), 459–463. https://doi.org/10.1038/ngeo891.

Dickson, J.L., Kerber, L.A., Fassett, C.I., Ehlmann, B.L., 2018. A global, blended CTX mosaic of Mars with vectorized seam mapping: a new mosaicking pipeline using principles of non-destructive image editing. Lunar and Planetary Science Conference Abstracts vol. 49 (p. #2480).

Ehlmann, B.L., Mustard, J.F., Fassett, C.I., Schon, S.C., Head III, J.W., Des Marais, D.J., Grant, J.A., Murchie, S.L., 2008. Clay minerals in delta deposits and organic preservation potential on Mars. Nat. Geosci. 1 (6), 355–358. https://doi.org/10.1038/ngeo207.

Ehlmann, B.L., Mustard, J.F., Swayze, G.A., Clark, R.N., Bishop, J.L., Poulet, F., Des Marais, D.J., Roach, L.H., Milliken, R.E., Wray, J.J., Barnouin-Jha, O.S., Murchie, S.L., 2009. Identification of hydrated silicate minerals on Mars using MRO-CRISM: geologic context near Nili Fossae and implications for aqueous alteration. J. Geophys. Res. Planets 114, E2. https://doi.org/10.1029/2009JE003339.

Elkins-Tanton, L.T., Hess, P.C., Parmentier, E.M., 2005. Possible formation of ancient crust on Mars through magma ocean processes. J. Geophys. Res. Planets 110(E12). https://doi.org/10.1029/2005JE002480.

Fergason, R.L., Christensen, P.R., Kieffer, H.H., 2006. High-resolution thermal inertia derived from the Thermal Emission Imaging System (THEMIS): Thermal model and applications. J. Geophys. Res. Planets 111(E12). https://doi.org/10.1029/2006JE002735.

Fergason, R.L., Hare, T.M., Laura, J., 2018. HRSC and MOLA Blended Digital Elevation Model at 200m v2, Astrogeology PDS Annex. U.S. Geological Survey http://bit.ly/HRSC_MOLA_Blend_v0.

Frey, H., Shultz, R.A., 1988. Large impact basins and the mega-impact origin for the crustal dichotomy on Mars. Geophys. Res. Lett. 15, 229–232. https://doi.org/10.1029/GL015i003p00229.

Frey, H.V., Schultz, R.A., Maxwell, T.A., 1986. The Martian crustal dichotomy: Product of accretion and not a specific event? Lunar and Planetary Science Conference Abstracts vol. 17, pp. 241-242.

García-Arnay, Á., Gutiérrez, F., de Pablo, M.Á., Fernández, S., 2018a. Characterization and interpretation of the fan-shaped and terrace-like features identified in Nepenthes Mensae, Mars. EGU General Assembly Conference Abstracts vol. 20 (p. # 808). Retrieved from https://figshare.com/articles/Characterization_and_interpretation_of_the_fanshaped_and_terrace-like_features_identified_in_Nepenthes_Mensae_Mars/9824609.

García-Arnay, Á., Fernández, S., de Pablo, M.Á., Gutiérrez, F., 2018b. The dominant morphogenetic role of surface runoff in Licus Vallis, Mars: results from geomorphological and morphometric analyses. Geogaceta 63, 63–66 Retrieved from. http://www.sociedadgeologica.es/archivos/geogacetas/geo63/geo63_16.pdf.

García-Arnay, Á., Gutiérrez, F., 2020. Reconstructing paleolakes in Nepenthes Mensae, Mars, using the distribution of putative deltas, coastal-like features, and terrestrial analogs. Geomorphology 359, 107129. https://doi.org/10.1016/j.geomorph.2020.107129.

Golabek, G.J., Keller, T., Gerya, T.V., Zhu, G., Tackley, P.J., Connolly, J.A., 2011. Origin of the Martian dichotomy and Tharsis from a giant impact causing massive magmatism. Icarus 215(1), 346-357. http://dx.doi.org/10.1016/j.icarus.2011.06.012.

Goudge, T.A., Fassett, C.I., 2018. Incision of Licus Vallis, Mars, from multiple lake overflow floods. J. Geophys. Res. Planets 123 (2), 405–420. https://doi.org/10.1002/2017JE005438.

Greeley, R., Guest, J., 1987. Geologic map of the eastern equatorial region of Mars. U.S. Geological Survey, IMAP 1802, Scale 1:5,000,000. https://doi.org/10.3133/i1802B.

Greeley, R., Batson, R.M., 1990. Planetary Mapping. Cambridge Univ. Press p. 296.

Hansen, V.L., 2000. Geologic mapping of tectonic planets. Earth Planet. Sc. Lett. 176(3–4), 527–542. https://doi.org/10.1016/S0012-821X(00)00017-0.

Hartmann, W.K., 2005. Martian cratering 8: isochron refinement and the chronology of Mars. Icarus 174 (2), 294–320. https://doi.org/10.1016/j.icarus.2004.11.023.

Hayden, A.T., Lamb, M.P., Fischer, W.W., Ewing, R.C., McElroy, B.J., Williams, R.M., 2019. Formation of sinuous ridges by inversion of river-channel belts in Utah, USA, with implications for Mars. Icarus 332, 92-110. https://doi.org/10.1016/j.icarus.2019.04.019.

Hiller, K.H., 1979. Geologic map of the Amenthes Quadrangle of Mars. U.S. Geological Survey, IMAP 1110, Scale 1:5,000,000. https://doi.org/10.3133/i1110.

Hungr, O., Leroueil, S., Picarelli, L., 2014. The Varnes classification of landslide types, an update. Landslides 11(2), 167-194. https://doi.org/10.1007/s10346-013-0436-y.

Irwin, R.P., Howard, A.D., 2002. Drainage basin evolution in Noachian Terra Cimmeria, Mars. J. Geophys. Res. Planets 107 (E7). https://doi.org/10.1029/2001JE001818.

Irwin III, R.P., Watters, T.R., Howard, A.D., Zimbelman, J.R., 2004. Sedimentary resurfacing and fretted terrain development along the crustal dichotomy boundary, Aeolis Mensae, Mars. J. Geophys. Res. Planets 109(E9). https://doi.org/10.1029/2004JE002248.

Irwin, R.P., Howard, A.D., Craddock, R.A., Moore, J.M., 2005. An intense terminal epoch of widespread fluvial activity on early Mars: 2. Increased runoff and paleolake development. J. Geophys. Res. Planets 110 (E12). https://doi.org/10.1029/2005JE002460.

Ke, Y., Solomatov, V.S., 2006. Early transient superplumes and the origin of the Martian crustal dichotomy. J. Geophys. Res. Planets 111(E10). https://doi.org/10.1029/2005JE002631.

King, E.A., 1978. Geologic map of the Mare Tyrrhenum Quadrangle of Mars. US Geological Survey Report, IMAP 1073. https://doi.org/10.3133/i1073.

Kneissl, T., van Gasselt, S., Neukum, G., 2011. Map-projection-independent crater size-frequency determination in GIS environments—new software tool for ArcGIS. Planet. Space Sci. 59 (11), 1243–1254. https://doi.org/10.1016/j.pss.2010.03.015.

Levy, J.S., Head, J.W., Marchant, D.R., 2007. Lineated valley fill and lobate debris apron stratigraphy in Nilosyrtis Mensae, Mars: Evidence for phases of glacial modification of the dichotomy boundary. J. Geophys. Res. Planets 112(E8). https://doi.org/10.1029/2006JE002852.

Malin, M.C., Bell, J.F., Cantor, B.A., Caplinger, M.A., Calvin, W.M., Clancy, R.T., Lee, S.W., 2007. Context camera investigation on board the Mars Reconnaissance Orbiter. J. Geophys. Res. Planets 112 (E5). https://doi.org/10.1029/2006JE002808.

McCauley, J.F., Carr, M.H., Cutts, J.A., Hartmann, W.K., Masursky, H., Milton, D.J., Sharp, R.P., Wilhelms, D.E., 1972. Preliminary Mariner 9 report on the geology of Mars, Icarus 17, 289. https://doi.org/10.1016/0019-1035(72)90003-6.

McEwen, A.S., Eliason, E.M., Bergstrom, J.W., Bridges, N.T., Hansen, C.J., Delamere, W.A., Grant, J.A., Gulick, V.C., Herkenhoff, K.E., Keszthelyi, L., Kirk, R.L., Mellon, M.T., Squyres, S.W., Thomas, N., Weitz, C.M., 2007. Mars reconnaissance orbiter's high resolution imaging science experiment (HiRISE). J. Geophys. Res. Planets 112 (E5). https://doi.org/10.1029/2005JE002605.

McGill, G.E., 2000. Crustal history of north central Arabia Terra, Mars. J. Geophys. Res. Planets 105(E3), 6945-6959. https://doi.org/10.1029/1999JE001175.

McGill, G.E., Dimitriou, A.M., 1990. Origin of the Martian global dichotomy by crustal thinning in the late Noachian or early Hesperian, J. Geophys. Res. 95, 12,595–12,605. https://doi.org/10.1029/JB095iB08p12595.

McGill, G.E., Squyres, S.W., 1991. Origin of the Martian crustal dichotomy: Evaluating hypotheses. Icarus 93(2), 386-393. https://doi.org/10.1016/0019-1035(91)90221-E.

Michael, G.G., 2013. Planetary surface dating from crater size–frequency distribution measurements: multiple resurfacing episodes and differential isochron fitting. Icarus 226 (1), 885–890. https://doi.org/10.1016/j.icarus.2013.07.004.

Michael, G.G., Neukum, G., 2010. Planetary surface dating from crater size–frequency distribution measurements: partial resurfacing events and statistical age uncertainty. Earth Planet. Sci. Lett. 294 (3), 223–229. https://doi.org/10.1016/j.epsl.2009.12.041.

Morgan, F., Seelos, F.P., Murchie, S.L., the CRISM Team, 2014. CRISM analysis toolkit (CAT). In: Gaddis, R.G., Hare, T., Beyer, R. (Eds.), Summary and Abstracts of the Planetary Data Workshop, June 2012: Open-File Report 2014-1056. U.S. Geological Survey, Reston, VA, USA, pp. 125–126.

Morgan, G.A., Head, J.W., Marchant, D.R., 2009. Lineated valley fill (LVF) and lobate debris aprons (LDA) in the Deuteronilus Mensae northern dichotomy boundary region, Mars: constraints on the extent, age and episodicity of Amazonian glacial events. Icarus 202(1), 22–38. https://doi.org/10.1016/j.icarus.2009.02.017.

Murchie, S., et al., 2007. Compact reconnaissance imaging spectrometer for Mars (CRISM) on Mars reconnaissance orbiter (MRO). J. Geophys. Res. Planets 112 (E5). https://doi.org/10.1029/2006JE002682.

Parenti, C., Gutiérrez, F., Baioni, D., García-Arnay, Á., Sevil, J., Luzzi, E., 2020. Closed depressions in Kotido crater, Arabia Terra, Mars. Possible evidence of evaporite dissolution-induced subsidence. Icarus 341, 113680. https://doi.org/10.1016/j.icarus.2020.113680

Poulet, F., Bibring, J.P., Mustard, J.F., Gendrin, A., Mangold, N., Langevin, Y., Arvidson, R.E., Gondet, B., Gomez, C., the Omega Team, 2005. Phyllosilicates on Mars and implications for early Martian climate. Nature 438 (7068), 623–627. https://doi.org/10.1038/nature04274.

Reese, C.C., Orth, C.P., Solomatov, V.S., 2010. Impact origin for the Martian crustal dichotomy: Half emptied or half filled? J. Geophys. Res. Planets 115(E5). https://doi.org/10.1029/2009JE003506.

Reese, C.C., Orth, C.P., Solomatov, V.S., 2011. Impact megadomes and the origin of the martian crustal dichotomy. Icarus 213(2), 433-442. https://doi.org/10.1016/j.icarus.2011.03.028.

Rivera-Hernández, F., Palucis, M.C., 2019. Do deltas along the crustal dichotomy boundary of Mars in the Gale crater region record a northern ocean? Geophys. Res. Lett. 46, 8689–8699. https://doi.org/10.1029/2019GL083046.

Roberts, J.H., 2015. Hemispheric Dichotomy (Mars). In: Hargitai H., Kereszturi Á. (eds) Encyclopedia of Planetary Landforms. Springer, New York, NY. https://doi.org/10.1007/978-1-4614-3134-3_649.

Roberts, J.H., Zhong, S., 2006. Degree-1 convection in the Martian mantle and the origin of the hemispheric dichotomy. J. Geophys. Res. Planets 111(E6). https://doi.org/10.1029/2005JE002668.

Scott, D.H., Carr, M.H., 1978. Geologic Map of Mars: U.S. Geological Survey Investigations Series, I-1083, Scale 1:25,000,000. http://pubs.er.usgs.gov/publication/i1083.

Seu, R., Phillips, R. J., Biccari, D., Orosei, R., Masdea, A., Picardi, G., Safaeinili, A., Campbell, B.A., Plaut, J.J., Marinangeli, L., Smrekar, S.E., Nunes, D.C., 2007. SHARAD sounding radar on the Mars Reconnaissance Orbiter. J. Geophys. Res. Planets 112(E5). https://doi.org/10.1029/2006JE002745.

Sharp, R.P., Malin, M.C., 1975. Channels on mars. Geol. Soc. Am. Bull. 86(5), 593-609. https://doi.org/10.1130/0016-7606(1975)86%3C593:COM%3E2.0.CO;2.

Skinner Jr, J.A., Tanaka, K.L., 2003. How should planetary map units be defined? Lunar and Planetary Science Conference Abstracts vol. 34 (p. #2100). Retrieved from: https://www.lpi.usra.edu/meetings/lpsc2003/pdf/2100.pdf.

Skinner Jr, J.A., Tanaka, K.L., 2018. Geological Map of the Nepenthes Planum Region, Mars. US Geological Survey Scientific Investigations Map 3389, Scale 1:1,506,000. https://doi.org/10.3133/sim3389.

Sleep, N.H., 1994. Martian plate tectonics. J. Geophys. Res. Planets 99(E3), 5639-5655. https://doi.org/10.1029/94JE00216.

Solomon, S.C., Aharonson, O., Aurnou, J.M., Banerdt, W.B., Carr, M.H., Dombard, A.J., Frey, H.V., Golombek, M.P., Hauck, S.A. II, Head, J.W. III, Jakosky, B.M., Johnson, C.L., McGovern, P.J., Neumann, G.A., Phillips, R.J., Smith, D.E., Zuber, M.T., 2005. New perspectives on ancient Mars. Science 307, 1214–1220, https://doi.org/10.1126/science.1101812.

Strahler, A.N., 1952. Hypsometric (area-altitude) analysis of erosional topography. Geol. Soc. Am. Bull. 63(11), 1117-1142. https://doi.org/10.1130/0016-7606(1952)63[1117:HAAOET]2.0.CO;2.

Tanaka, K.L., Golombek, M.P., Banerdt, W.B., 1991. Reconciliation of stress and structural histories of the Tharsis region of Mars. J. Geophys. Res. Planets 96(E1), 15617-15633. https://doi.org/10.1029/91JE01194.

Tanaka, K.L., Scott, D.H., Greeley, R., 1992a. Global stratigraphy. In: Kieffer HH, Jakosky BM, Snyder CW, Matthews MS (eds) Mars. University Arizona Press, Tucson, pp 345–382.

Tanaka, K.L., Chapman, M.G., Scott, D.H., 1992b. Geologic map of the Elysium region of Mars. US Geological Survey Report, IMAP 2147. https://doi.org/10.3133/i2147.

Tanaka, K.L., Skinner, J.A., Hare, T.M., 2005. Geologic map of the northern plains of Mars. US Geological Survey Scientific Investigations Map 2888, Scale 1:15,000,000. https://doi.org/10.3133/sim2888.

Tanaka, K.L., Skinner Jr., J.A., Dohm, J.M., Irwin III, R.P., Kolb, E.J., Fortezzo, C.M., Platz, T., Michael, G.G., Hare, T.M., 2014. Geologic Map of Mars. US Geological Survey Scientific Investigations Map 3292, Scale 1:20,000,000. pamphlet 43 p. https://doi.org/10.3133/sim3292.

Viviano, C.E., Seelos, F.P., Murchie, S.L., Kahn, E.G., Seelos, K.D., Taylor, H.W., Taylor, K., Ehlmann, B.L., Wiseman, S.M., Mustard, J.F., Morgan, M.F., 2014. Revised CRISM spectral parameters and summary products based on the currently detected mineral diversity on Mars. J. Geophys. Res. Planets 119(6), 1403–1431. https://doi.org/10.1002/2014JE004627.

Viviano-Beck, C.E., et al., 2015.MRO CRISM type spectra library. NASA Planetary Data System. Retrieved from. http://crismtypespectra.rsl.wustl.edu.

Warner, N.H., Gupta, S., Calef, F., Grindrod, P., Boll, N., Goddard, K., 2015. Minimum effective area for high resolution crater counting of Martian terrains. Icarus 245, 198–240. https://doi.org/10.1016/j.icarus.2014.09.024.

Watters, T.R., 1988. Wrinkle ridge assemblages on the terrestrial planets. J. Geophys. Res. Solid Earth 93(B9), 10236-10254. https://doi.org/10.1029/JB093iB09p10236.

Watters, T.R., 1993. Compressional tectonism on Mars. J. Geophys. Res. Planets 98(E9), 17049-17060. https://doi.org/10.1029/93JE01138.

Watters, T.R., 2003a. Lithospheric flexure and the origin of the dichotomy boundary on Mars, Geology 31, 271–274. https://doi.org/10.1130/0091-7613(2003)031%3C0271:LFATOO%3E2.0.CO;2.

Watters, T.R., 2003b. Thrust faults along the dichotomy boundary in the eastern hemisphere of Mars, J. Geophys. Res. Planets 108(E6), 5054. https://doi.org/10.1029/2002JE001934.

Watters, T.R., Robinson, M.S., 1999. Lobate scarps and the Martian crustal dichotomy. J. Geophys. Res. Planets 104(E8), 18981-18990. https://doi.org/10.1029/1998JE001007.

Watters, T.R., McGovern, P.J., 2006. Lithospheric flexure and the evolution of the dichotomy boundary on Mars. Geophys. Res. Lett. 33(8). https://doi.org/10.1029/2005GL024325.

Watters, T.R., Solomon, S.C., Robinson, M.S., Head, J.W., André, S.L., Hauck II, S.A., Murchie, S.L., 2009. The tectonics of Mercury: The view after MESSENGER's first flyby. Earth Planet. Sc. Lett. 285(3-4), 283-296. https://doi.org/10.1016/j.epsl.2009.01.025.

Wilhelms, D.E., 1990. Geologic mapping. In: Greeley, R., Batson, R.M. (Eds.), Planetary Mapping. Cambridge University Press, NY, pp. 208-260.

Wilhelms, D.E., Squyres, S.W., 1984. The Martian hemispheric dichotomy may be due to a giant impact. Nature 309(5964), 138-140. https://doi.org/10.1038/309138a0.

Zhong, S., Zuber, M.T., 2001. Degree-1 mantle convection and the crustal dichotomy on Mars. Earth Planet. Sc. Lett. 189(1-2), 75-84. https://doi.org/10.1016/S0012-821X(01)00345-4.

Zuber, M.T., Smith, D.E., Solomon, S.C., Muhleman, D.O., Head, J.W., Garvin, J.B., 1992. The Mars Observer laser altimeter investigation. J. Geophys. Res. Planets 97 (E5), 7781–7797. https://doi.org/10.1029/92JE00341.

Zuber, M.T., Solomon, S.C., Phillips, R.J., Smith, D.E., Tyler, G.L., Aharonson, O., Balmino, G., Banerdt, W.B., Head, J.W., Johnson, C.L., Lemoine, F.G., McGovern, P.J., Neumann, G.A., Rowlands, D.D., Zhong, S., 2000. Internal structure and early thermal evolution of Mars from Mars Global Surveyor topography and gravity. Science 287(5459), 1788-1793. https://doi.org/10.1126/science.287.5459.1788.

CHAPTER

---

5. Fluvial and coastal landforms in NW Terra Cimmeria and SE Nepenthes Mensae

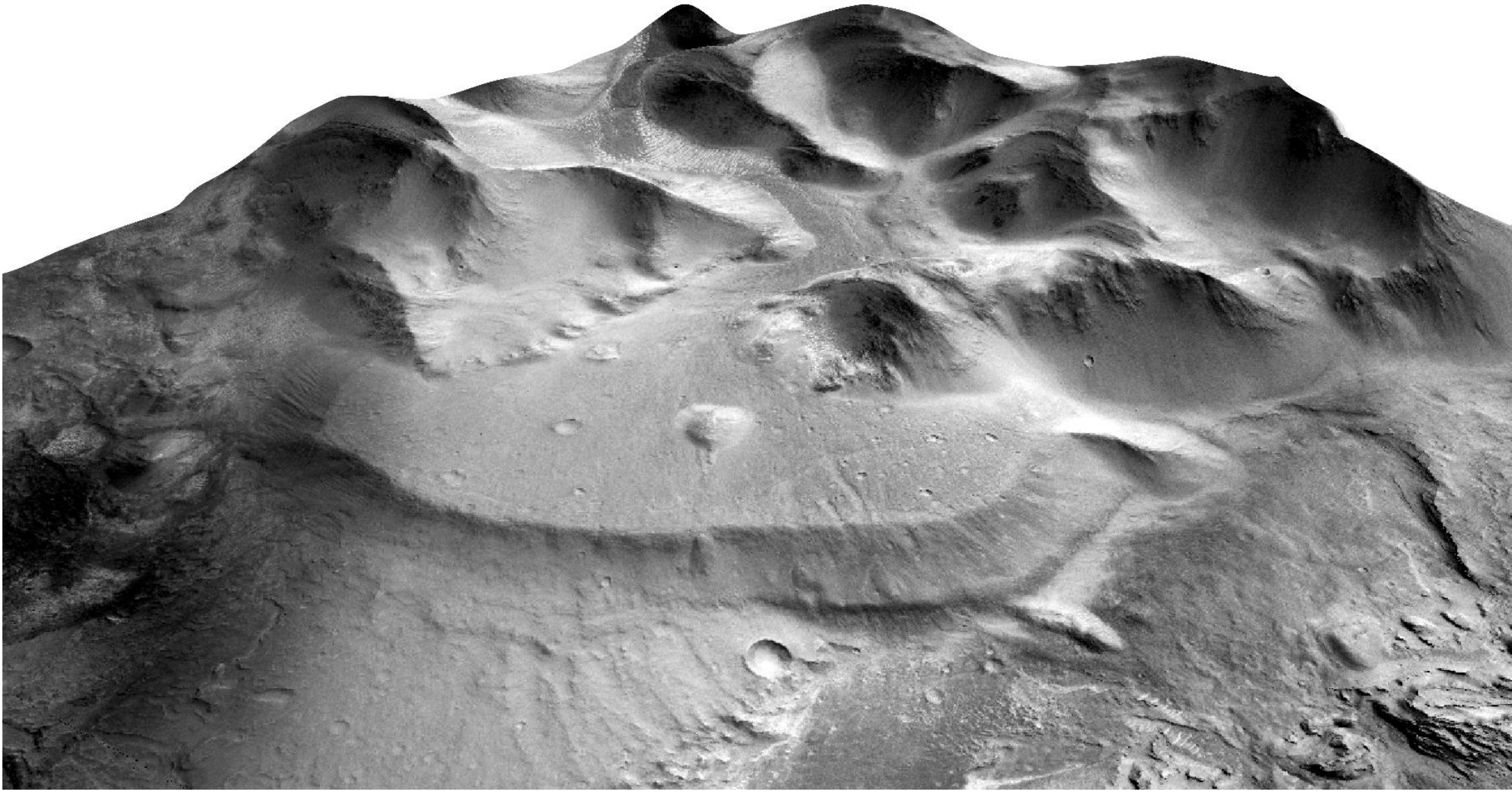

INTRODUCTION AND GOALS

The surface of Mars shows frequent fluvial- and coastal-like landforms suggesting that liquid water was abundant and has played an important morphogenetic role during the early stages of its history (e.g., Baker, 2001; Bibring et al., 2006; Carr, 2012), as well as during relatively short periods in more recent times (e.g., Malin and Edgett, 2000). Well-developed valley networks carved into the Noachian highlands, such as those located in NW Terra Cimmeria, may be the result of past fluvial erosion (e.g., Irwin et al., 2005), and/or a combination of both runoff and groundwater sapping erosional processes (Malin and Carr, 1999; Harrison and Grimm, 2005).

Fan-shaped deposits attributable to deltas and alluvial fans have been widely reported on Mars (e.g., Kleinhans, 2005; Di Achille and Hynek, 2010a). These landforms are located at the mouth of stream networks where the flow becomes unconfined, such as at impact craters (e.g., Goudge et al., 2015) or along the highland-lowland dichotomy escarpment (e.g., Fassett and Head III, 2008). Numerous fan-shaped deposits ascribed to Gilbert-type deltas and alluvial fans have been identified in SE Nepenthes Mensae (e.g., Irwin et al., 2005; de Pablo and Pacifici, 2008; Rivera-Hernández and Palucis, 2019). The fan-shaped aggradational landforms documented in this Chapter were presented for the first time by García-Arnay (2016) and García-Arnay et al. (2018a, 2018b), and described in detail by García-Arnay and Gutiérrez (2020). In addition, an updated cartographic inventory of putative deltas and alluvial fans mapped along the CNTZ, as well as those reported by other authors, is presented in Chapter 4. The presence of deltas supports the existence in the past of long-lived liquid water bodies forming ancient lakes, or even a possible ocean developed in the Martian lowlands (e.g., Head III et al., 1999; Carr and Head III, 2003; Di Achille and Hynek, 2010b; Fawdon et al., 2018). Laterally continuous benches with nearly consistent elevation located along the margins of depressions and lowlands, and very probably associated with ancient masses of water, have been interpreted as erosional and/or aggradational coastal landforms attributable to paleoshorelines (e.g., Parker et al., 1993; Ghatan and Zimbelman, 2006).

In this Chapter, we carry out two studies, which results are presented in two peer-reviewed scientific papers, consisting of: (1) A morphometric analysis, largely based on geomorphological mapping, in the catchment of Licus Vallis, which is the largest drainage basin in the study area of the CNTZ. The main objective of this work is to shed light into the morphogenetic role played by liquid water in the past, assessing the relative contribution of runoff and groundwater sapping erosional processes in valley formation. (2) A detailed study focused on the morphometry, spatial distribution, age, surface composition and origin of fan-shaped deposits and coastal-like benches in SE Nepenthes Mensae, reconstructing the paleogeography of the inferred paleolakes and proposing terrestrial analogs.

The dominant morphogenetic role of surface runoff in Licus Vallis, Mars: results from geomorphological and morphometric analyses

El papel morfogenético dominante de la escorrentía superficial en Licus Vallis, Marte: resultados del análisis geomorfológico y morfométrico

Ángel García-Arnay[1, 2], Susana Fernández[2], Miguel Ángel de Pablo[3] and Francisco Gutiérrez[1]

[1] Departamento de Ciencias de la Tierra. Universidad de Zaragoza, 50009 Zaragoza, Spain; arnay@unizar.es; fgutier@unizar.es
[2] Departamento de Geología, Universidad de Oviedo, C/ Jesús Arias de Velasco s/n, 33005 Oviedo, Spain; fernandezmsusana@uniovi.es
[3] Departamento de Geología, Geografía y Medio Ambiente, Universidad de Alcalá, 28805 Alcalá de Henares, Spain; miguelangel.depablo@uah.es

ABSTRACT

A watershed analysis was performed to assess the morphogenetic role of surface water on the development of Licus Vallis, an ancient river valley located in the equatorial region of Mars. Terrain analysis in a GIS environment allowed the identification of numerous relict fluvial features such as channels, paired terraces and a delta. Licus Vallis has the characteristics of a young watershed with a non-equilibrium profile, fourth-order streams, V-shaped valleys, very low drainage density, and a dendritic drainage pattern. Erosion related to surface runoff appears to be the dominant process involved in the formation of Licus Vallis. Nevertheless, the presence of theatre-like valley heads seems to indicate that sapping erosion associated with springs may have played some role in the headward expansion of valleys. Moreover, the finding, for the first time in this work, of a possible Gilbert-type delta at the mouth of the fluvial system permitted to define the paleobase level of the drainage basin and suggests the existence of an ancient sea in the region.

Key-words: *Mars, surface runoff, morphometric analysis, fluvial landforms.*

RESUMEN

Se ha analizado la cuenca de Licus Vallis, un antiguo cauce situado en la región ecuatorial de Marte, con la finalidad de evaluar el papel morfogenético que tuvo el agua superficial en su desarrollo. El análisis geomorfológico llevado a cabo en un entorno SIG ha permitido identificar numerosas morfologías fluviales relictas como canales, terrazas simétricas y un delta. Licus Vallis presenta una cuenca con rasgos propios de un relieve joven, con un perfil en desequilibrio, canales de cuarto orden, valles en V, una densidad de drenaje muy baja, y un patrón dendrítico. La erosión generada por la escorrentía superficial parece ser el proceso dominante en la formación de Licus Vallis. Sin embargo, la presencia de valles con cabecera semicircular parece indicar que la erosión asociada a surgencias pudo contribuir a la expansión por erosión remontante de los valles. Además, el hallazgo, por primera vez en este trabajo, de un posible delta de tipo Gilberten la desembocadura del sistema fluvial permitió definir el nivel de base de la cuenca y plantear la posible existencia de un antiguo mar en la región.

Palabras clave: *Marte, escorrentía superficial, análisis morfométrico, morfologías fluviales.*

Geogaceta, 63 (2018), 63-66
ISSN (versión impresa): 0213-683X
ISSN (Internet): 2173-6545

Recepción: 30 de junio de 2017
Revisión: 20 de octubre 2017
Aceptación: 23 de octubre 2017

Introduction

The surface of Mars is currently too cold and dry to allow the presence of stable, long-standing liquid water. However, the existence of numerous relict fluvial and coastal landforms such as channels, paleolakes, terraces, deltas and probable shorelines seems to indicate that large volumes of liquid water flowed over the Martian surface in the past (Carr, 2012). A combination of surface runoff and sapping (erosion processes associated with springs) has been proposed to explain the formation of valley networks on Mars (*e.g.*, Harrison and Grimm, 2005). Nevertheless, the relative contribution of surface-water erosion and groundwater sapping in valley formation is not yet well understood (*e.g.*, Mest *et al.*, 2010).

A watershed analysis was performed in the catchment of Licus Vallis, an ancient river valley located in the equatorial region of Mars, close to the Martian highland-lowland boundary. The main objectives of this analysis were to shed light on the morphogenetic role played by liquid water in the past and assess the relative contribution of the dominant erosional process, namely runoff versus sapping.

Geographic and geological setting

Licus Vallis is located in the northeastern part of Mare Tyrrhenum quadrangle (centered at 3°S, 126°E) (Fig. 1). This region is incised by channel networks whose mouths terminate at the dichotomy boundary, near the Nepenthes Mensae area, and may have formed during the Late Noachian (Fassett and Head, 2008). Geologically, the Licus Vallis area is situated in the Middle Noachian highland unit (unit mNh), characterised by ancient highland basalts heavily cratered and dissected by fluvial networks (Tanaka *et al.*, 2014).

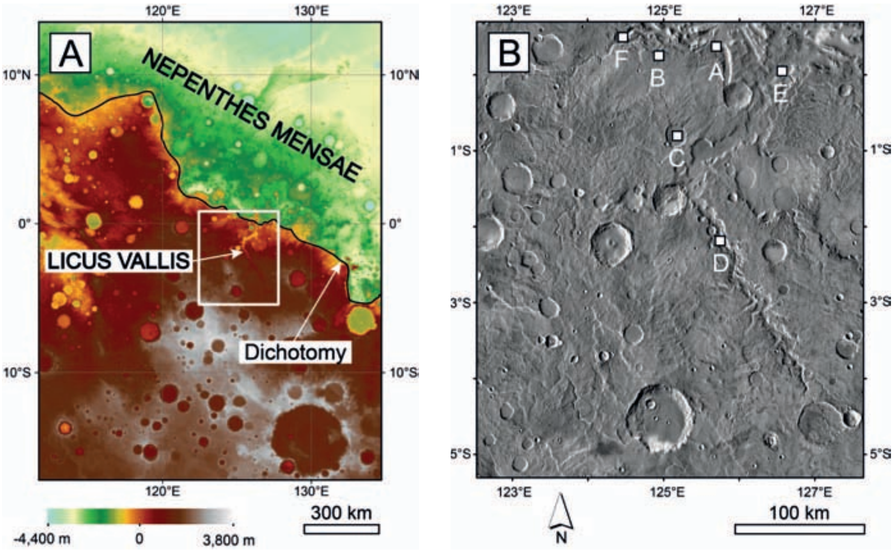

Fig. 1.- A) Regional setting of Licus Vallis (the study area is indicated by the white box) (MOLA topography, NASA). B) Image mosaic of the study area (labelled white boxes are locations of images shown in Fig. 2) (THEMIS-IR day images, NASA). See color figure in the web.

Fig. 1.- A) Situación regional de Licus Vallis (el área de estudio se indica con el recuadro blanco) (topografía MOLA, NASA). B) Mosaico de imágenes del área de estudio (los recuadros blancos etiquetados indican la localización de las imágenes mostradas en la Fig. 2) (Imágenes THEMIS-IR diurnas, NASA). Ver figura en color en la web.

Materials and methods

Topographic and imagery data were used to analyse the geomorphology and morphometry of the study area. Topographic data were extracted from a Digital Elevation Model (DEM) derived from images acquired by the High Resolution Stereo Camera (HRSC) instrument on board the ESA's Mars Express, with a resolution of 50 or 75 m per pixel. Imagery data consisted of panchromatic images from Context Camera (CTX) instrument, on board the NASA's Mars Reconnaissance Orbiter, and HRSC instrument (~6 m and 12.5 m in resolution, respectively). These data were integrated into a Geographic Information System (GIS) for carrying out multiple watershed analyses and describing the identified landforms. The stream network and watershed boundaries were initially mapped automatically using GIS tools. The flow accumulation tool permitted to preliminarily delineate the stream network by applying a threshold value of 14,000 cells (equivalent to an area of 35 km^2) to select cells with a high accumulated flow. The resulting stream network, including numerous artefacts, was improved manually.

Morphometric analysis

To analyse the drainage basin morphometry, we ranked the stream network using Strahler's classification (Strahler, 1952), and calculated morphometric parameters based on Horton's Laws (Horton, 1945). This analysis includes the consideration of linear, areal and relief aspects of the drainage basin. The linear aspects are outlined in Table I.

Drainage density (D_d) is a fundamental areal parameter that appraises the degree of fluvial dissection in a drainage basin, which in planet Earth is related to several factors like local climate, relief, substrate, runoff coefficient or vegetation cover. According to Horton (1945), drainage density (D_d) is defined as the total length of streams of all orders in a drainage basin (L_T), divided by the total basin area (A). It is expressed by the formula:

$$D_d = L_T/A \qquad (1)$$

If all other factors remain equal, higher drainage density values indicate low permeability and highly erodible substrate, while low drainage density occurs in areas of highly resistant and/or permeable substrate.

The relief aspects include, among others, the mean stream slope as a function of order, which is the average gradient expressed in degrees measured along all the stream segments of each order. Another relief parameter is the hypsometric curve. Hypsometric analysis relates the normalised elevation versus the normalised area of a drainage basin. This curve is used to estimate the geomorphic maturity of catchments.

Parameter	Formula	Ref.
Stream order (u)	Hierarchical rank	Strahler (1952)
Number of streams (N_u)	The total number of stream segments of a given order 'u'	Horton (1945)
Stream length (L_u)	The total length for each stream order 'u'	Horton (1945)
Bifurcation ratio (R_b)	$R_b = N_u/N_{u+1}$	Horton (1945)
Mean length ($\bar{L}_u$)	$\bar{L}_u = L_u/N_u$	Horton (1945)
Cumulative mean length ($\bar{L}_\mu$)	The sum of the mean stream length of a given order 'μ' and the mean lengths of all lower orders	Horton (1945)
Length ratio (R_L)	$R_L = \bar{L}_\mu/\bar{L}_{\mu-1}$	Horton (1945)

Table I.- Linear parameters used to analyse the drainage basin of Licus Vallis.

Tabla I.- Parámetros lineales utilizados para analizar la cuenca de drenaje de Licus Vallis.

Results and discussion

Main landforms

Terrain analysis allowed the identification of the most relevant landforms on the study area, such as the Martian dichotomy, impact craters, crater paleolakes, fluvial terraces and a delta.

The Martian dichotomy divides the poorly cratered northern lowlands from the heavily cratered southern highlands. It is characterised by a prominent escarpment around 1700 m in local relief, whose upper limit is at an elevation of about 0 m (Fig. 2A).

All impact craters larger than 2 km in diameter were mapped. The presence of rampart craters, characterised by distinctive features ascribable to fluidised ejecta, may indicate evidence of near-surface water or ice (Fig. 2B). Some impact craters may contain paleolakes, which were probably fed by fluvial channels. These relict lake basins may contain terraces and lake sediments (Fig. 2C).

The middle course of the main channel of Licus Vallis shows the development of paired terraces. These terraces, continuous for

Stream order, u	Number of stream, N_u	Bifurcation ratio, R_b	Stream length, L_u (km)	Mean length, $\bar{L}_u$ (km)	Cumulative mean length, $\bar{L}_\mu$ (km)	Length ratio R_L	Max stream slope (º)	Min stream slope (º)	Mean stream slope (º)	Stream area (km^2)
1	121	4.17	1413.96	11.69	11.69	0.33	39.99	0	4.37	89.50
2	29	3.63	689.95	23.79	35.48	0.34	42.60	0	4.90	43.60
3	8	8	555.77	69.47	104.95	0.24	35.40	0	4.80	35.00
4	1		340.03	340.03	444.97		25.20	0	4.50	21.72

Table II.- Results of the morphometric analysis of the drainage network of Licus Vallis.

Tabla II.- Resultados del análisis morfométrico de la red de drenaje de Licus Vallis.

tens of kilometres, possibly record the rejuvenation of the river valley due to a lowering of its base level (Fig. 2D).

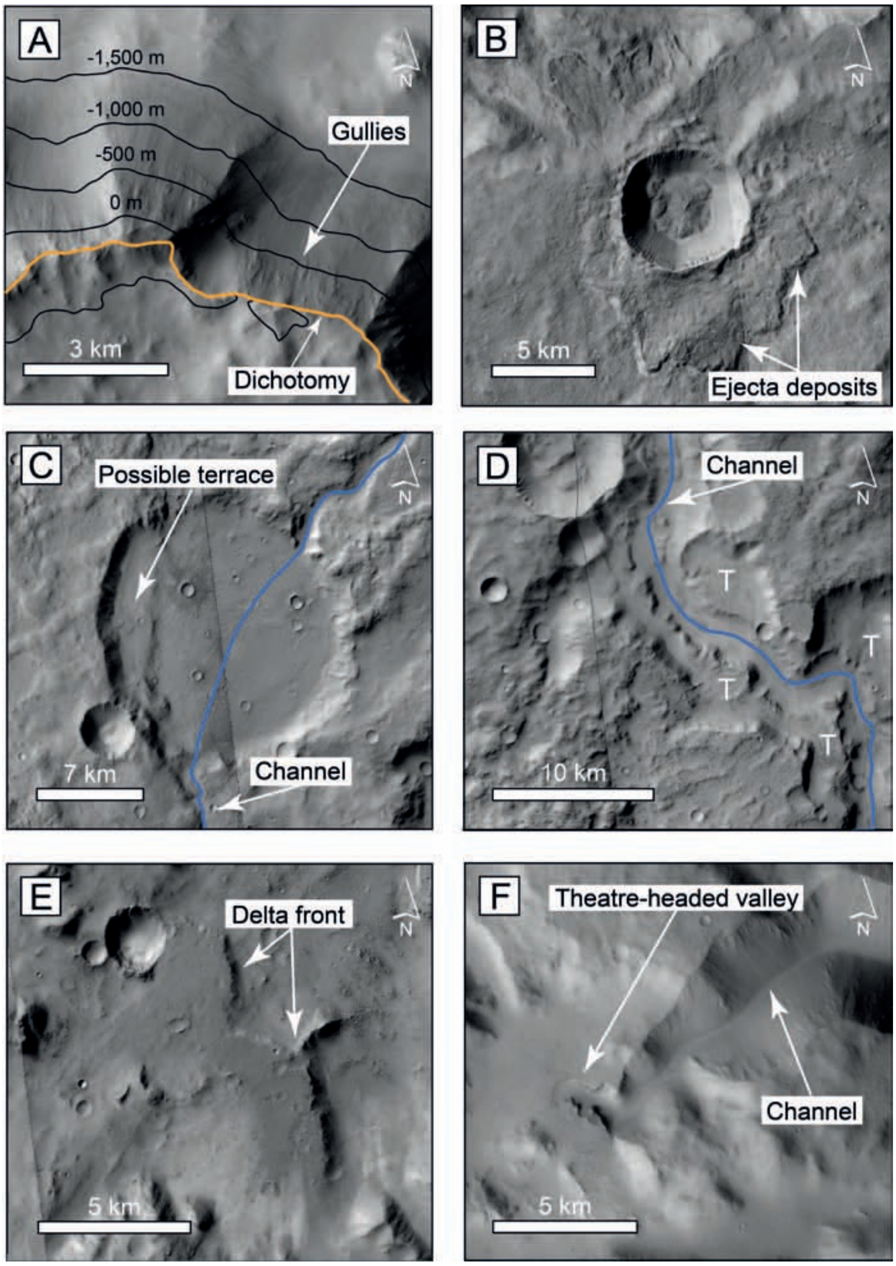

Fig. 2.- A) Martian dichotomy. B) Rampart crater. C) Crater paleolake with a possible terrace. D) Paired terraces (T) in the middle course of Licus Vallis. E) Gilbert-type delta. F) Theatre-like valley head and V-shaped valley (CTX images, NASA). See color figure in the web.

Fig. 2.- A) Dicotomía marciana. B) Cráter amurallado. C) Paleolago de cráter con una posible terraza. D) Terrazas simétricas (T) en el curso medio de Licus Vallis. E) Delta de tipo Gilbert. F) Valle con cabecera remontante y valle en V (Imágenes CTX, NASA). Ver figura en color en la web.

A possible Gilbert-type delta composed of two delta lobes was identified, for the first time, at the mouth of the river basin of Licus Vallis (Fig. 2E). The delta plain occupies an area of 90.1 km^2 with a mean depositional slope of ~3.4º. This delta defines a paleobase level of the drainage basin at -1186 m, given by the edge of the delta plain. Moreover, it seems to record a persistent water level of the ancient sea that possibly occupied the Lowlands at Nepenthes Mensae area (de Pablo and Pacifici, 2008).

Morphometric analysis

The watershed of Licus Vallis presents V-shaped valleys and occupies an area of 55672.6 km^2, with the highest and lowest elevation at 2442 and -1591 m, respectively. The lowest elevation corresponds to an intrabasinal impact crater, rather than to the mouth of the basin. Some valley heads display theatre-like morphologies and lack any evidence of surface runoff, which may be related to sapping erosion (Fig. 2F). Sapping causes the headward migration of channels by preferential erosion (undermining and cliff recession) associated with springs (Goldspiel and Squyres, 2000).

The drainage basin presents a fourth-order network, with a dendritic drainage pattern (Fig. 3A), and low average stream gradients (Table II). Most of the streams are first order and their number declines as the order increases. The mapped streams have a total length of 2999.7 km and the drainage basin has an area of 55672.6 km^2, yielding a drainage density of 0.05 km^{-1}. This is a very low value, in terms of terrestrial drainage density values (*e.g.*, Carr and Chuang, 1997), characteristic of a basin located in a region with a wet climate and resistant substrate, like the basalts (unit mNh) of the area of Licus Vallis. The mean bifurcation ratio is 5.2, which is larger than terrestrial values, typically ranging between 2 and 4 (Horton, 1945). The bifurcation ratio of 8 for third to fourth order channels increases the mean value. It is much larger than the bifurcation ratios obtained with lower

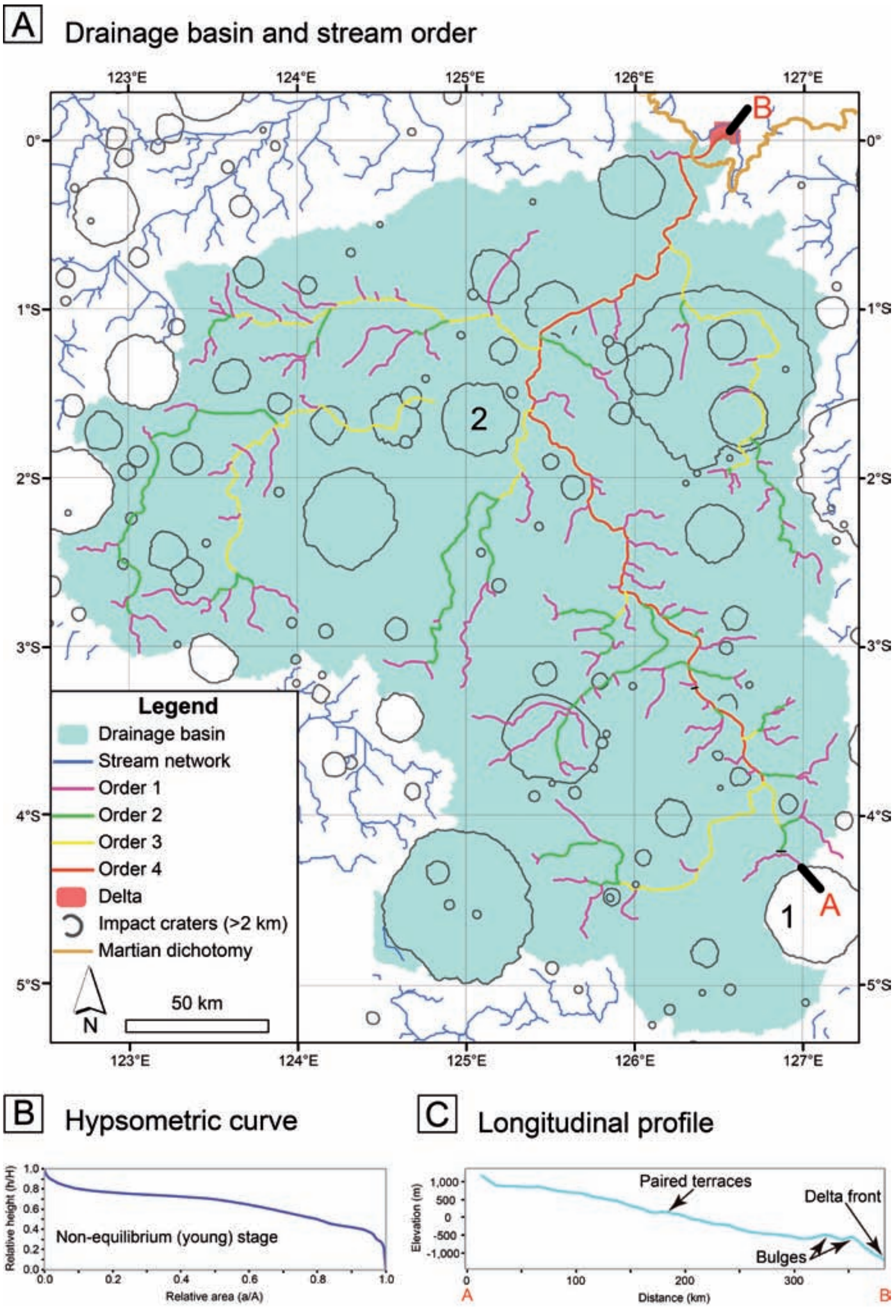

Fig. 3. A) Licus Vallis basin and stream ordering according to Strahler's classification. 1: Impact crater with a possible paleolake that eventually overflowed; 2: Channel interrupted by impact craters. B) Hypsometric curve of the basin. C) Smoothened profile of the main channel. See color figure in the web.

Fig. 3.- A) Cuenca de Licus Vallis y orden de canales según la clasificación de Strahler. 1: cráter de impacto que albergó un posible paleolago que alimentaba al canal principal; 2: canal interrumpido por cráteres de impacto. B) Curva hipsométrica de la cuenca. C) Perfil suavizado del cauce principal. Ver figura en color en la web.

order channels (Table II), which may indicate a poorly developed stream network. The hypsometric curve of the drainage basin shows that Licus Vallis has an immature topography (Fig. 3B), as corroborated by its non-equilibrium profile (Fig. 3C). Bulges near the mouth are probably related to tectonic deformation, as supported by the presence of morphostructural lineaments along the dichotomy boundary (Martín-González *et al*., 2007).

Conclusions

The analysis of the identified landforms and their spatial relationships permitted the identification of water-related landforms like channels, paleolakes, paired terraces and a delta. Licus Vallis presents a young watershed, as indicated by its hypsometric curve and its non-equilibrium profile. The V-shaped valleys and a dendritic drainage pattern suggest that surface runoff was the main morphogenetic process in the formation of Licus Vallis. The presence of some valleys with theatre-like headcuts supports that sapping may have played a role in their headward expansion. In fact, the existence of rampart craters indicates the presence of large amounts of near-surface water or ice in the region during the impact events. On the other hand, the mapped putative Gilbert-type delta defines a paleobase level of the drainage basin and indicates the possible existence of an ancient standing body of water in the Lowlands. River terraces and the shape of the non-equilibrium profile may indicate an episodic water level drop of the ancient sea.

Acknowledgements

We thank Rosana Menéndez and an anonymous reviewer for their comments and suggestions which helped to improve the paper.

References

Carr, M.H. (2012). *Philosophical Transactions of the Royal Society* 370(1966), 2193-2215.

Carr, M.H. and Chuang, F.C. (1997). *Journal of Geophysical Research: Planets* 102(E4), 9145-9152.

de Pablo, M.A. and Pacifici, A. (2008). *Icarus* 196, 667-671.

Fassett, C.I. and Head, J.W. (2008). *Icarus* 195(1), 61-89.

Goldspiel, J.M. and Squyres, S.W. (2000). *Icarus* 148(1), 176-192.

Harrison, K.P. and Grimm, R.E. (2005). *Journal of Geophysical Research: Planets* 110(E12).

Horton, R.E. (1945). *Geological Society of America Bulletin* 56, 275-370.

Martín-González, F., de Pablo, M.A. and Pacifici, A. (2007). *Geophysical Research Abstracts* 9, 07796.

Mest, S.C., Crown, D.A. and Harbert, W. (2010). *Journal of Geophysical Research: Planets* 115(E9).

Strahler, A.N. (1952). *Geological Society of America Bulletin* 63(11), 1117-1142.

Tanaka, K.L., Skinner, J.A., Jr., Dohm, J.M., Irwin, R.P., III, Kolb, E.J., Fortezzo, C.M., Platz, T., Michael, G.G. and Hare, T.M. (2014). *Geologic Map of Mars, USGS Scientific Investigations Map 3292.* US Geological Survey, Flagstaff, AZ.

Geomorphology 359 (2020) 107129

Contents lists available at ScienceDirect

Geomorphology

journal homepage: www.elsevier.com/locate/geomorph

Reconstructing paleolakes in Nepenthes Mensae, Mars, using the distribution of putative deltas, coastal-like features, and terrestrial analogs

Ángel García-Arnay *, Francisco Gutiérrez

Departamento de Ciencias de la Tierra, Universidad de Zaragoza, 50009 Zaragoza, Spain

ARTICLE INFO

Article history:
Received 4 December 2019
Received in revised form 6 February 2020
Accepted 27 February 2020
Available online 2 March 2020

Keywords:
Mars
Hydrology
Fan-shaped deposit
Paleo-water level
Desiccated lake

ABSTRACT

Nepenthes Mensae is an equatorial region situated north of the Martian dichotomy, northwest of Gale crater. It is characterized by a NW-SE-oriented belt of interconnected depressions, Late Noachian to Early Hesperian in age, with knobby terrains with residual relief. The highlands south of Nepenthes Mensae, Middle Noachian in age, correspond to the Licus Vallis region, which is dissected by drainage networks with valley mouths located along the dichotomy boundary scarp. This work presents a detailed geomorphological analysis of ten fan-shaped and fifty-four coastal-like benches identified in Nepenthes Mensae. The combination of detailed mapping, morphological and morphometric analyses, spatial-altitudinal distribution relationships, crater counting, spectral analysis, and comparison with terrestrial analogs suggest that (1) the fan-shaped and coastal-like benches are likely putative Gilbert-type deltas and paleoshore platforms, respectively, and (2) these features may be attributable to paleoshorelines developed along the margins of an ancient inner sea or interconnected paleolakes. These findings reveal the important morphogenetic role that liquid water played in the evolution of Nepenthes Mensae and Licus Vallis regions during the Late Noachian-Early Hesperian transition, and contribute to contextualize the continuous findings on the environmental and climatic conditions of the nearby Gale crater during such time period.

1. Introduction

Multiple geomorphological and geochemical lines of evidence indicate that liquid water has played an instrumental role during the early evolutionary stages of Mars (e.g., Baker, 2001; Bibring et al., 2006), as well as during relatively short periods in recent times (e.g., Malin and Edgett, 2000). Numerous valley networks carved into the Noachian highlands may be the result of past runoff erosion (e.g., Irwin et al., 2005), and/or a combination of runoff and groundwater sapping erosional processes (Malin and Carr, 1999; Harrison and Grimm, 2005). Large outflow channels developed during the Hesperian and Amazonian periods are attributed to the catastrophic release of large amounts of groundwater (Andrews-Hanna and Phillips, 2007). Fan-shaped deposits associated with the mouth of stream networks debouching at various types of depressions have been widely reported on Mars (e.g., Kleinhans, 2005; Di Achille and Hynek, 2010a). Such features, which show morphologic characteristics analogous to those of deltas on Earth, occur in spatially restricted closed basins such as impact craters (e.g., Goudge et al., 2015), some of them with outlet valleys, and in large basins, commonly where valley networks reach the edge of depressions or the upland-lowland boundary (e.g., Fassett and Head III, 2008). Some of the best-known delta-like features on Mars are probably the Jezero and the Eberswalde deltas, which show multiple lobes with clearly visible distributary channels with a meandering pattern (Wood, 2006; Pondrelli et al., 2008; Schon et al., 2012). The presence of deltas supports the existence in the past of long-standing liquid water bodies in paleolakes and an ancient ocean developed in the Martian lowlands (e.g., Head III et al., 1999; Carr and Head III, 2003; Di Achille and Hynek, 2010b; Fawdon et al., 2018). Laterally continuous benches with consistent elevation along the margins of the Lowlands and depressions have been interpreted as possible erosional and/or aggradational coastal landforms that record paleoshorelines (e.g., Parker et al., 1993; Ghatan and Zimbelman, 2006).

Irwin et al. (2005) reported fan-shaped deposits and ascribed them to a Gilbert-type delta in Nepenthes Mensae, which was also analyzed by de Pablo and Pacifici (2008). The rest of fan-shaped deposits documented in this work (i.e., 9 out of 10) were presented, for the first time, by García-Arnay (2016) and García-Arnay et al., 2018b, 2018c. Recently, Rivera-Hernández and Palucis (2019) have also documented some of these landforms that can be used as possible paleoshoreline markers in the equatorial region of Nepenthes Mensae (e.g., de Pablo and Pacifici, 2008; de Pablo and Pacifici, 2009; Valenciano et al., 2009; García-Arnay, 2016; García-Arnay et al., 2018a). These features may

---

[*] Corresponding author.
E-mail address: arnay@unizar.es (Á. García-Arnay).

https://doi.org/10.1016/j.geomorph.2020.107129
0169-555X/© 2020 Elsevier B.V. All rights reserved.

record the past existence of a long-lived body of liquid water related to the putative Martian ocean.

In this work, we present a geomorphological analysis of Nepenthes Mensae, largely based on detailed geomorphic mapping. It explores features attributable to deltas and shore platforms related to an ancient inner sea or a system of paleolakes, and reinforces this interpretation using possible terrestrial analogs. These putative paleoshore markers are characterized by analyzing their morphometric features and their surface composition, and estimating their numerical age. Paleowater-level elevations derived from the putative deltas and shore platforms are used to reconstruct the paleogeography of the inferred paleolakes (e.g., extent, depth, volume).

2. Study area

The study area is located in an equatorial region of the eastern hemisphere of Mars, astride two contrasting geomorphic domains divided by the Martian dichotomy boundary scarp: Nepenthes Mensae and Licus Vallis region (Fig. 1). Nepenthes Mensae (centered at 2°N, 124°E) is situated north of the dichotomy (upland-lowland boundary), east of Isidis Planitia, and northwest Gale crater. This region is characterized by a belt of interconnected NW-SE-trending depressions (de Pablo and Pacifici, 2009) with knobby terrains of residual relief (mesas and knobs) related to the erosion of the Martian highlands along the dichotomy (Caprarelli, 2015). The dichotomy displays steep slopes ~2 km in local relief. Nepenthes Mensae was mapped as Hesperian-Noachian transition unit (HNt) and interpreted as volcanic deposits, impact breccias, and sediments of Noachian in age with aprons formed by Hesperian mass-wasted deposits, according to the most recent global geological map of Mars (Tanaka et al., 2014). The highlands south of Nepenthes Mensae correspond to the Licus Vallis region (centered at 4°S, 125°E), an ancient fluvial valley (e.g., Irwin and Howard, 2002) located in the northeastern part of Mare Tyrrhenum quadrangle. It was mapped as middle Noachian highland unit (mNh), which is interpreted as "moderately to heavily degraded" "undifferentiated impact, volcanic, fluvial and basin materials" (Tanaka et al., 2014). The heavily cratered terrains of Licus Vallis region are dissected by V-shaped valley networks related to fluvial erosion, whose mouths are located along the dichotomy. Sapping erosion may also have contributed to the headward expansion of valleys, as supported by the existence of theater-shaped valley heads (Valenciano and de Pablo, 2010). Licus Vallis shows a very low drainage density and an apparently poorly-developed watershed, as suggested by its convex hypsometric curve (García-Arnay et al., 2018c). The knickpoints, slope breaks and paired terraces recognized within the valleys support

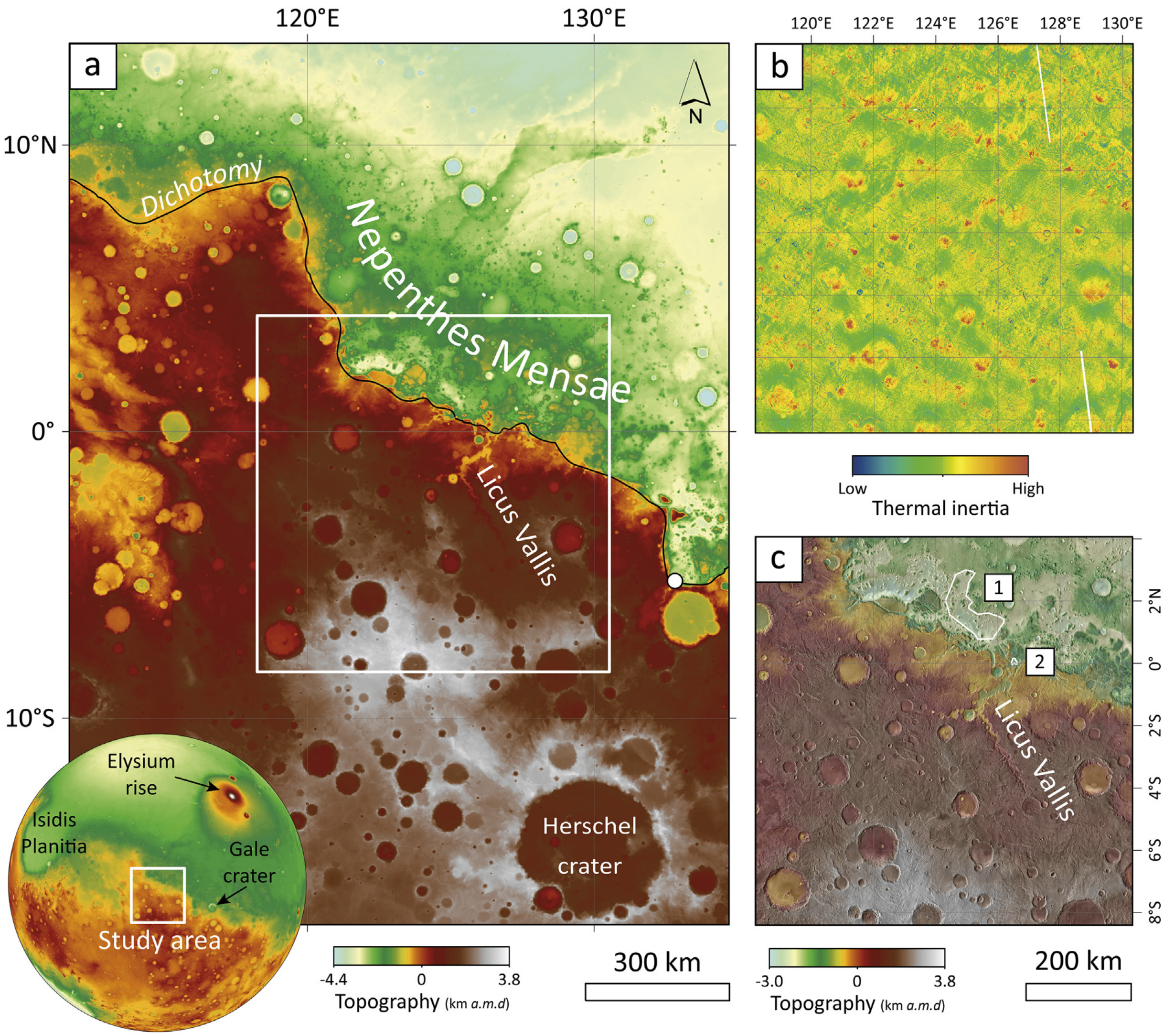

Fig. 1. (a) Colorized elevation model (kilometers above Martian datum, a.m.d.) derived from MOLA, with the study area framed by the white box. The small white circle east of study area marks the position of the fan-delta whose surface composition was inferred by CRISM spectral analysis. (b) Qualitative thermal inertia mosaic of the study area derived from THEMIS. (c) Colorized elevation model of the study area derived from HRSC-MOLA blended data over a mosaic of THEMIS-IR day images. White-lined polygons represent the crater-counting areas delineated for dating the depressions and the largest delta (labelled as 1 and 2, respectively).

base-level changes that could be related to water-level variations in the mouth area and/or vertical tectonic movements (Goudge and Fassett, 2018). The transition between both geomorphic domains is dominated by the presence of morpho-structural lineaments (Martín-González et al., 2007) that may have controlled the erosion of the highlands as well as the drainage pattern along the dichotomy.

3. Data and methods

Imagery as well as topographic and spectral data were used to characterize the geomorphology and surface composition of the analyzed region. Visible imagery included panchromatic images acquired by the High Resolution Stereo Camera (HRSC, 12.5 m/pixel) (Neukum et al., 2004) on board the ESA's Mars Express, as well as by the Context Camera (CTX, 5–6 m/pixel) (Malin et al., 2007; Dickson et al., 2018) and the High Resolution Imaging Science Experiment (HiRISE, ~25–50 cm/pixel) (McEwen et al., 2007), both instruments on board the NASA's Mars Reconnaissance Orbiter. Additional information was extracted from the qualitative thermal inertia image mosaic derived from nighttime infrared images obtained by the Thermal Emission Imaging System (THEMIS, 100 m/pixel) (Christensen et al., 2004, 2013) on board NASA's Mars Odyssey. Thermal inertia (TI) permits the differentiation of surface materials based on their thermophysical properties. In this work, TI data helped in identifying and mapping drainage networks because unconsolidated sediments such as eolian deposits, characterized by lower apparent TI, mainly occur in low-lying areas such as fluvial valleys.

Topographic data were extracted from Digital Elevation Models (DEMs) derived from laser altimeter point shots acquired by the Mars Orbiter Laser Altimeter (MOLA, 463 m in resolution) (Zuber et al., 1992), on board NASA's Mars Global Surveyor, as well as images from the HRSC instrument (50–75 m/pixel). In order to cover areas where no HRSC data were available, we used a blend of DEM data derived from MOLA and HRSC (Fergason et al., 2018, ~200 m/pixel). The spatial resolution of the HRSC-derived topography, that covers almost all the study area, is appropriate for analyzing the landforms of interest for this work. Imagery and topographic data were integrated into a Geographic Information System (ArcGIS 10.5.1, ESRI) for mapping and carrying out multiple morphological and morphometric analyses. Spatial data were projected into the same geographic coordinate system with sinusoidal projection and central meridian located in the center of the study area (125°E).

Surface composition was inferred from hyperspectral data acquired by the Compact Reconnaissance Imaging Spectrometer for Mars (CRISM, ~18 m/pixel) aboard NASA's Mars Reconnaissance Orbiter, a visible-infrared imaging spectrometer sensitive to light from 0.362 to 3.92 μm (Murchie et al., 2007). Spectral data were retrieved from the PDS Geosciences Node Mars Orbital Data Explorer (ODE) (available at: https://ode.rsl.wustl.edu/mars/) in corrected I/F (radiance/solar irradiance) using Targeted Empirical Record (TER) and Map-projected Targeted Reduced Data Record (MTRDR) products. We carried out the spectral analysis using the corrected I/F to obtain spectral diagrams, and the refined spectral summary parameters to derive spectral parameter maps (Viviano-Beck et al., 2014). Spectral data were processed using the CRISM Analysis Toolkit (CAT, version 7.3.1), an IDL/ENVI-based software system developed by the CRISM Science Team (Morgan et al., 2014). Due to its paleoenvironmental interest, clay-bearing surfaces were highlighted in a spectral parameter map obtained by the PHY product (D2300 (red), D2200 (green), BD1900r2 (blue)) for the projected CRISM observation FRT000064CE (~18 m/pixel, and ~10 km across) (Fig. 4b) following the procedure described by Viviano-Beck et al. (2014). The values displayed for each RGB channel were adjusted applying stretch limits to highlight the clay-bearing materials. The I/F spectrum was extracted from the unprojected CRISM cube and averaged from a Region of Interest (ROI) drawn for the compositional unit. This average spectrum (s1) was ratioed to an average spectrum from a ROI of spectrally unremarkable terrains (s2) from the CRISM scene to minimize atmospheric contributions and instrument artifacts. The ratioed I/F spectrum (i.e., s1/s2) was compared with the CRISM spectral library (available at: http://crismtypespectra.rsl.wustl.edu/) (Viviano-Beck et al., 2015). The choice of this CRISM scene was determined by (1) the absence of TER products for fan-shaped deposits within the study area, and (2) the scene corresponds to a previously interpreted fan delta located close to the study area.

In order to identify equipotential surfaces corresponding to paleolevels of possible long-standing liquid-water bodies, we extracted the elevation values (expressed in meters above Martian datum, a.m.d.) from the mapped putative deltaic and coastal-like landforms (e.g., Irwin and Zimbelman, 2012). In the case of putative deltas, we considered the slope break at the junction between the delta plain and the delta front, which was interpreted as the mean highstand (e.g., Di Achille and Hynek, 2010b). In spite of the difficulties to infer the water level from the elevation of shore platforms on Earth (e.g., Trenhaile, 1987; Sunamura, 1992), we decided to consider the inner edge, also called the “shoreline angle” (e.g., Figueiredo et al., 2014; Zazo et al., 2013; Hearty et al., 2007) (Fig. 2). The spatial-altitudinal distribution of the putative deltas and benches (Fig. 8) permitted us to constrain their elevation range, and reconstruct the distribution of ancient liquid-water bodies (Fig. 9). The approximate volume of the largest mass of liquid water was measured using the ArcGIS tool “Polygon volume”. It calculates the volume resulting from the intersection between the lake bottom derived from a TIN model and a horizontal surface defined by the mean elevation estimated for the water level. The maximum depth was estimated by the difference between the mean elevation of the water level and the elevation of the deepest bathymetry point, which was calculated using the ArcGIS tool “Zonal Statistics as Table”, while the mean depth is given by the difference between the mean water level elevation and the average elevation of the bathymetry of the depression. In this research, we assumed that (1) the present regional topography is similar to the one that existed during the development of the analyzed landforms, and (2) the landforms formed when the Martian hydrosphere was persistent and a long-standing body of liquid water was present in the region (e.g., Di Achille and Hynek, 2010b). The stream network and watershed boundaries were mapped using the toolset “Hydrology” of ArcGIS. The drainage network generated automatically, which included numerous artifacts, was improved manually using imagery and TI data. Watershed boundaries were delineated considering the local base levels defined by each putative delta at the mouth of drainage basins.

The mapping of some putative deltas was challenging due to their spatially variable preservation conditions and geomorphic setting. The proximal edges of the deltas were delineated where the ancient flow debouching from the fluvial valley became unconfined (Fig. 2). The areas estimated for some deltas should be considered as minimum values due to surface reduction related to erosional processes (e.g., landsliding). The delta-shape index, or elongation of the delta, is a dimensionless morphometric parameter defined by the expression $S_d = W_d/2L_d$, where L_d is the delta length given by the maximum distance parallel to the paleoflow direction and W_d is the delta width, defined as the maximum distance across the foot of the delta front and perpendicular to W_d. S_d values of 1 correspond to semicircular deltas, while $S_d > 1$ and $S_d < 1$ indicate oblate and prolate deltas with long axes perpendicular or parallel to the paleoflow direction, respectively. These definitions were adapted for this work from Caldwell and Edmonds (2014) (see Fig. 2). We also estimated the mean slope for the deltaic plains and fronts, as well as several morphological attributes as defined by Di Achille and Hynek (2010a) in order to characterize qualitatively: (1) the type of drainage network, distinguishing between poorly-developed stream networks (Lw) and steep canyons (C); (2) the morphology of the delta front, differentiating between steep simple fronts (M1) and stepped fronts with benches or slope breaks (M2); (3) evidence of avulsion (multi-lobate deltas); and (4) visible layering (see Table 1).

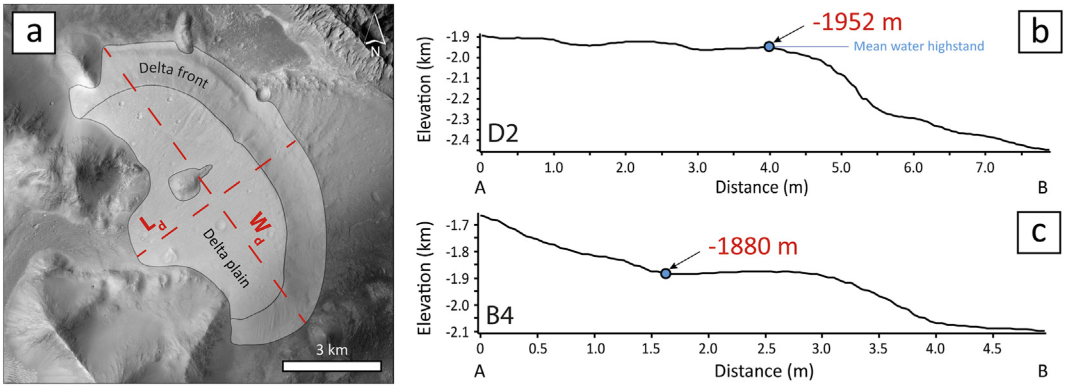

Fig. 2. (a) CTX image of the D2 feature showing the mapped delta plain and front as well as the morphometric parameters L_d (length) and W_d (width) used to calculate the delta-shape index (S_d). (b) and (c) Topographic profiles corresponding to delta D2 and bench B4, respectively (see trace of profiles in Fig. 3). The arrows and blue dots indicate the slope break of the topographic profile used to infer the past water-level elevation from fan-shaped features and benches, as described in the text.

Surface dating was carried out using the crater size-frequency distribution (CSFD) method (e.g., Neukum et al., 2001; Hartmann and Neukum, 2001) in order to estimate the age of the morphogenetic surface and resurfacing events. Impact craters and crater-counting areas (Fig. 1c) were mapped using the CraterTools toolset for ArcGIS (Kneissl et al., 2011). Crater size-frequency diagrams were generated using CraterStats2 software (Michael and Neukum, 2010), and age estimates (Fig. 6) were derived using the production and chronology functions defined by Hartmann (2005). The clustering of the crater population and the confidence level of its adjustment was determined by the randomness analysis (Michael et al., 2012).

4. Results and discussion

4.1. Description of the fan-shaped and bench-like landforms

We analyzed ten fan-shaped features and fifty-four coastal-like benches. Fan-shaped landforms (labelled as D# in Fig. 3) occur at the mouth of past high-gradient rivers that used to debouch into an unconfined low-lying area. The majority of fan-shaped deposits are linked to drainage basins characterized by poorly-ranked stream networks (Lw). In contrast, D3 and D6 seem to be the only fan-shaped landforms associated with steep canyons (C). These features are distributed along a NW-SE oriented belt associated with the southern margin of interconnected depressions with latitude and longitude coordinates that range from 0°18′8″N to 3°5′31″N and from 121°20′54″E to 127°34′00″E, respectively. The fan-shaped features range from ~3.0 km^2 to ~85.4 km^2 in area and display two well-differentiated parts: low-gradient plains with mean slopes from ~2.3° to ~5.2°, and steep fronts with variable preservation conditions and average gradients from ~3.4° to ~15.8° (see Table 1). The more degraded fan-shaped features (i.e., D1a, D1b and D8), display a lower gradient difference (<2°) between the plains and their fronts, probably due to erosion in the upper part of the slope and accumulation in the footslope (Table 1). In some cases, the plains are dissected by small and rather subdued channels as illustrated in Fig. 5b. The measurement of the width (W_d) and length (L_d) allowed the calculation of the delta-shape index (S_d) for each feature, which ranges between 0.56 (prolate geometry) and 1.02 (oblate geometry). These values are analogous to those from protruding deltas on Earth (e.g., Mikhailova, 2015). Most features display visible layering on their fronts, strongly suggesting that they are formed by stratified sediments (Fig. 5a). The lack of visible or unambiguous layering in some features may be related to a topographic surface concordant with the bedding, as is commonly the case in delta fronts (dip slope) (e.g., Hampson and Storms, 2003), or to the presence of eolian dust and sand. In the cases where layering is exposed in the front of the delta due to erosion, the slope probably does not represent the foreset inclination. The majority of the features have one defined lobe, whereas D1b, D7 and D9 show two clear lobes, and D2 has two probable frontal lobes, although very poorly defined (Figs. 3 and 5b). These multi-lobe features have in common the presence of bedrock inliers, likely relict relief that protrudes over their plains. Most of the features show a steep front with a continuous slope (M1). However, D1 displays a stepped front with benches and slope breaks (M2) (Fig. 3).

The coastal-like benches are generally located along the margins of the depressions and encircling isolated massifs and knobs within the depressions. These features have not been identified outside the depressions. A selection of them are shown in Fig. 3 (labelled as B#) and in Fig. 5d. These benches display smooth, subhorizontal or gently-sloping surfaces, with lateral continuity, elevation consistency, and steep slopes associated with their outer edges. In some cases, such as B1 (B1 in Fig. 3), paired benches occur on both sides of the depression at consistent elevation. The relationship between the coastal-like benches and putative deltas is analyzed from their elevation values and spatial distribution (Fig. 8).

4.2. Spectral analysis of the delta deposits

We carried out the spectral analysis of the CRISM scene FRT000064CE in order to identify possible hydrated minerals. The spectral analysis of this CRISM scene has been also performed by Ehlmann and Buz (2014, 2015). The observation displays a fan-shaped deposit located east of the study area, at the mouth of a valley carved into the southwest side of the Robert Sharp crater rim, east of the study area (Fig. 1a). This deposit was interpreted as fan delta by Irwin III et al. (2004) (Fig. 4a). The PHY spectral parameter map reveals that the scene is dominated by hydrated Fe/Mg-phyllosilicates (Ehlmann and Buz, 2015), the most common hydrated minerals on Mars (Carter et al., 2013), as highlighted by the pink-colored pixels in Fig. 4b. The ratioed I/F spectrum (i.e., s1/s2) shows a subtle absorption band feature at ~1.4 μm due to structural H_2O and OH, a sharp absorption feature at ~1.9 μm indicating structural H_2O, as well as an absorption band at ~2.31 μm related to Fe/Mg-OH bond and a subtler band at ~2.39 μm also related to these bonds (Ehlmann et al., 2009; Viviano-Beck et al., 2014) (Fig. 4c). Absorption features are consistent with the presence of saponite (Mg-rich smectite) and nontronite (Fe-rich smectite), as shown by the comparison between the ratioed spectrum and laboratory spectra (Viviano-Beck et al., 2015). These ferromagnesian smectites occur in light-toned layered deposits with apparently meter-scale polygonal fractures along the delta front and at its foot, as revealed by the HiRISE image PSP_001884_1750 (close-up view in Fig. 4a). Clay minerals may either have formed during transport or by near-surface weathering and subsequently transported and deposited as detrital particles (Ehlmann and Buz, 2014).

Table 1
Morphometric and morphological parameters of the fan-shaped features and their associated drainage networks.

Delta	Latitude (N)	Longitude (E)	Delta front elevation (m)	W_d (m)	L_d (m)	Delta-shape index	Mean plain slope (°)	Mean front slope (°)	Visible layering	Multi-lobate	Stepped morphology	Drainage network	Drainage area (km^2)	Delta area (km^2)	First reference
D1a	3°5′31″	121°20′54″	−1865	3627	2971	0.61	4.18	6.05	✔	✗	M2?	Lw	1510.37	7.76	García-Arnay et al. (2018b)
D1b	3°4′30″	121°23′59″	−1972	11,124	5529	1.01	4.07	5.44	✔	✔	M2?	Lw	1510.37	40.49[a]	García-Arnay et al. (2018b)
D2	2°10′11″	121°39′29″	−1952	10,430	6045	0.86	3.86	15.38	✔	✔	M1	Lw	20,268.25	41.13	Irwin et al. (2005)
D3	2°1′28″	122°00′31″	−1935	2371	1885	0.63	5.19	8.68	✔	✗	M1	C	113.19	2.98	García-Arnay et al. (2018b)
D4	1°34′7″	123°22′52″	−1793	5602	2844	0.98	4.77	14.41	✔	✔	M1	C/Lw	28,000.94	10.91[a]	García-Arnay et al. (2018b)
D5	0°44′6″	125°18′55″	−1920	4740	3500	0.68	2.34	15.82	✔	✗	M1	Lw	8189.85	11.93	García-Arnay et al. (2018b)
D6	0°36′33″	125°47′50″	−1975	4704	2304	1.02	2.95	5.64	✗	✗	M1	C	1908.04	8.53	García-Arnay et al. (2018b)
D7	0°3′14″	126°36′20″	−1186	12,621	11,069	0.57	3.41	7.76	✔	✔	M1	Lw	156,377.80	85.40	García-Arnay et al., 2018b, 2018c
D8	0°31′21″	126°58′19″	−1920	2458	2176	0.56	2.66	3.40	✔	✔	M1	Lw	–	3.65[a]	García-Arnay et al. (2018b)
D9	0°18′8″	127°34′00″	−1783	5424	3520	0.77	3.49	7.56	✗	✔	M1	Lw	10,753.31	12.55	García-Arnay et al. (2018b)

(–) no flow accumulation data available to derive the drainage area. Mean slopes correspond to those of the current topographic surface. In the cases where layering is exposed in the front of the delta due to erosion, the slope probably does not represent the foreset inclination. Latitude and longitude coordinates correspond to the point along the topographic profile used to extract the elevation of the delta front (see Fig. 8).

[a] Delta surface presents ambiguous and/or eroded limits.

Other minerals within Robert Sharp crater such as carbonates and akaganéite, which is an oxide mineral related to acidic and oxidizing conditions in a drying lagoon, were reported by Carter et al. (2015). Clay-bearing layered deposits support the presence of liquid water in the past (e.g., Poulet et al., 2005), and are considered potential sites for organic matter preservation due to relatively rapid burial (e.g., Ehlmann et al., 2008). We consider that these findings strengthen the possible deltaic origin of this fan-shaped deposit and its composition could be analogous to deltas in the study area.

4.3. Interpretation of landforms

Based on the morphologic and morphometric characteristics of the described landforms, their spatial distribution, and spectral analysis, we interpret the fan-shaped features as putative relict Gilbert-type deltas linked to the mouth of drainage basins. The interpreted deltas show an overall convex and segmented longitudinal profile, whereas alluvial fans are characterized by continuous concave long profiles. Furthermore, the presence of steep fronts hundreds of meters in local relief is strongly inconsistent with the interpretation of these features as alluvial or fluvial fans and argues for the presence of a deep water body. Nonetheless, the mapped deltas are expected to have a proximal subaerial component, and as such could be also designated as fan-deltas (Blair and McPherson, 1994).

Some of the ten putative deltas analyzed in this work also have been documented by other authors (e.g., Irwin et al., 2005; de Pablo and Pacifici, 2008; Rivera-Hernández and Palucis, 2019). On Earth, Gilbert-type deltas, which were first described by Gilbert (1884), typically occur in lakes where the near-shore water is relatively deep (e.g., Bird, 2011), and tend to be associated with homopycnal flows (e.g., Penland and Kulp, 2005), in which the density of the river water is very similar to that of the standing mass of water in the basin (Bates, 1953). These flows commonly occur in lacustrine environments and produce rapid deposition to form deltas characterized by steep delta fronts (Fig. 5a–c). Some deltas show multi-lobate fronts (e.g., D1b, D2, D7 and D9, Fig. 3) that may indicate flow bifurcation and/or channel avulsion processes. The presence of bedrock inliers protruding through their plains probably controlled flow bifurcation and the consequent development of two lobes. Deltas D4 and D8 display two apparent lobes, although their shape is probably related to post-depositional landsliding (D4, Fig. 5a) and/or erosion (D8, Fig. 3). The origin of the stepped topography of some delta fronts (D1, Fig. 3) could be either related to erosional benches developed during stages of relatively stable water level that punctuated the overall regression trend, or to differential erosion. Kraal et al. (2008) ascribed the stepped longitudinal profile of an alluvial fan, comprising a sequence of risers and treads, to the episodic decline of the water level and the development of benches during periods of stability. Finally, the possible deltaic origin of the fan-shaped deposits in Nepenthes Mensae is strengthen by the occurrence of phyllosilicate minerals in the front of the analyzed delta, which supports the presence of liquid water in the past.

Based on the morphologic characteristics of the described landforms, their spatial distribution, altitudinal relationship with the deltas, and resemblance with possible terrestrial analogues, we interpret the benches as possible shore platforms developed by coastal erosion along paleoshorelines at different water-level elevations. Shore platforms with rounded outer edges in plan view located around isolated massifs and knobs are common in the northern lowlands, as indicated by Parker et al. (1993). These "stepped massifs", such as those located in Cydonia Mensae, display the same characteristics as the ones described in this work at Nepenthes Mensae (Parker et al., 1993; Parker and Currey, 2001). Parker et al. (1989, 1993) interpreted these features as possible wave-cut island formed by coastal erosion of the pre-existent rocks during highstands of an ancient liquid-water ocean and/or by erosional processes associated with the floating sea ice on a frozen ocean that occupied the northern lowlands of Mars (Clifford and

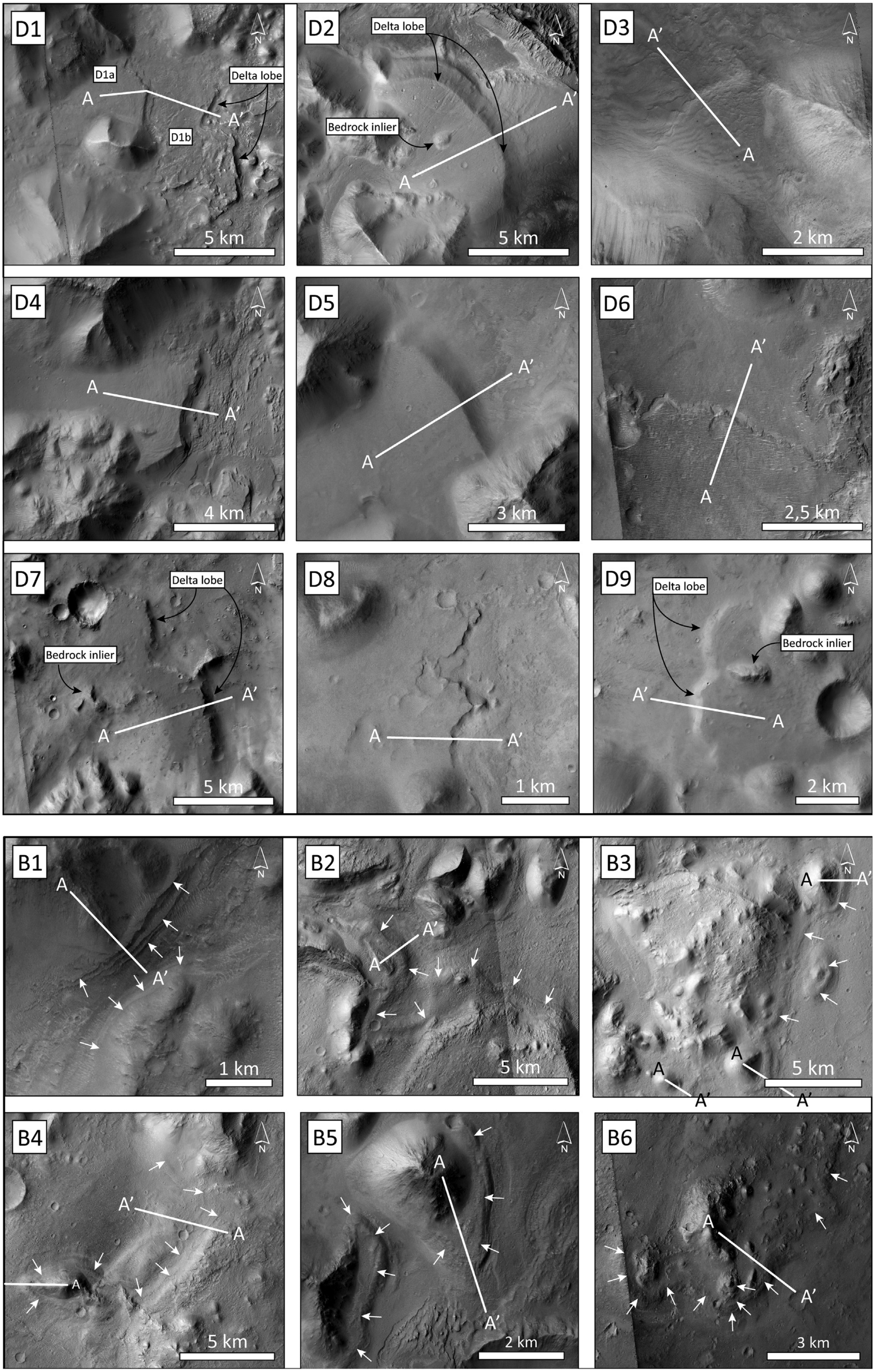
D1
D1a
D1b
Delta lobe
A
A'
5 km
D2
Delta lobe
Bedrock inlier
A
A'
5 km
D3
A'
A
2 km
D4
A
A'
4 km
D5
A'
A
3 km
D6
A'
A
2,5 km
D7
Delta lobe
Bedrock inlier
A'
A
5 km
D8
A
A'
1 km
D9
Delta lobe
Bedrock inlier
A'
A
2 km
B1
A
A'
1 km
B2
A'
A
5 km
B3
A
A'
A
A'
A
A'
5 km
B4
A'
A
A
5 km
B5
A
A'
2 km
B6
A
A'
3 km
N

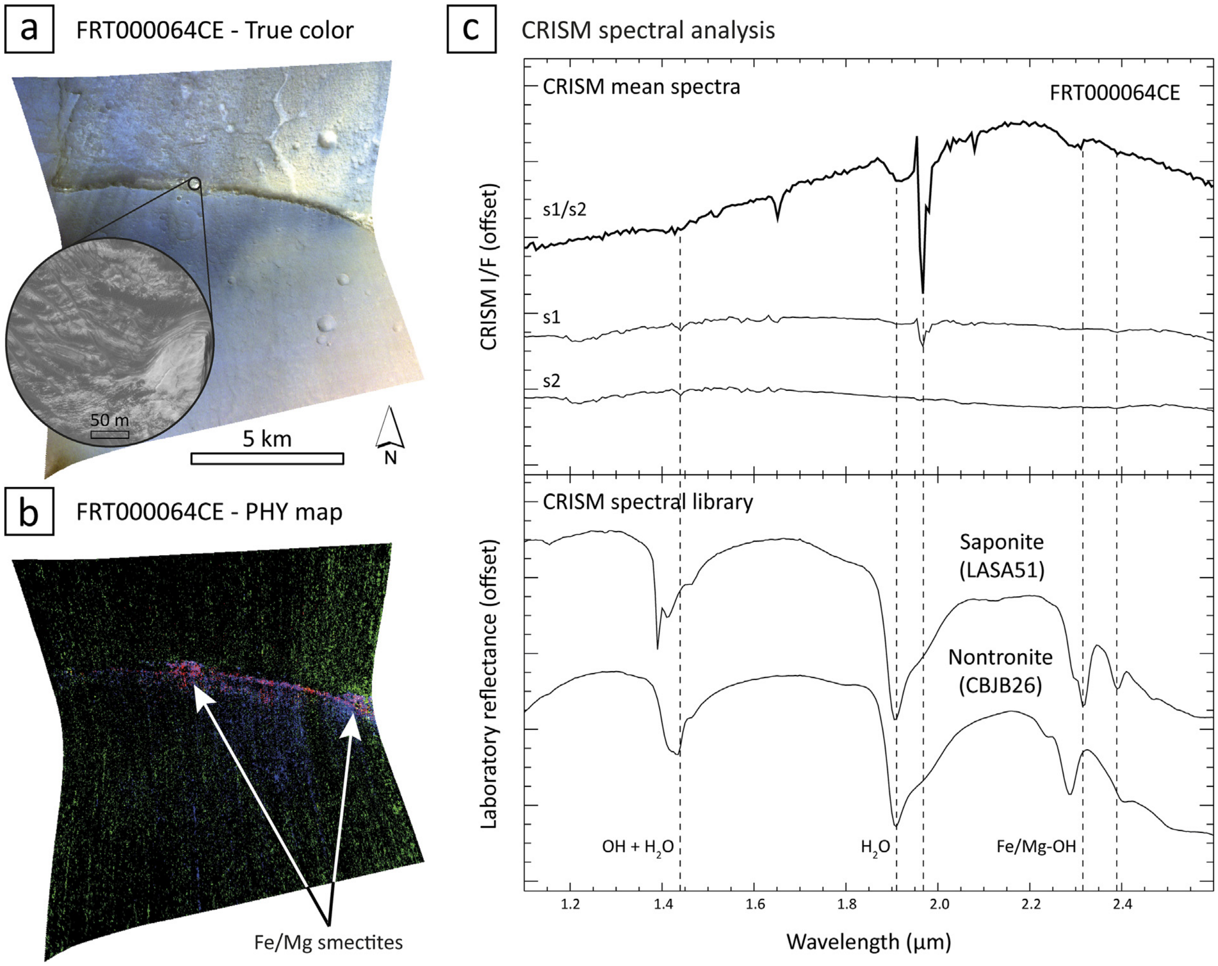

Fig. 4. (a) True color image of the CRISM scene FRT000064CE. The close-up view shows a detail of the light-toned layered deposits occurring at the delta front. (b) Spectral parameter map (PHY product) for the same scene. Pink tones indicate the presence of Fe/Mg- phyllosilicates outcropping along the delta front. (c) CRISM ratioed I/F spectrum compared to CRISM library spectra (vertical dashed lines indicate observed absorption band features).

Parker, 2001). The formation of wave-cut platforms implies that the available fetch, the atmospheric pressure, and wind speed were sufficient to produce these erosional landforms (e.g., Kraal et al., 2006; Banfield et al., 2015). On Earth, lakes with <50 km of open water are considered 'fetch-limited' (e.g., Nordstrom and Jackson, 2012). Eolian landforms developed in the largest depression of Nepenthes Mensae after its desiccation such as dune fields, yardangs and wind streaks indicate predominant NW- and NE-oriented winds. Based on the dimensions of the reconstructed paleolakes (Fig. 9) and the inferred wind directions, fetch values would range from ~40 km to ~100 km. These values are similar to those estimated for the Carson Desert sub-basin of the pluvial Lake Lahontan, United States, during the Pleistocene highstand, ranging from ~50 km to ~110 km (Morrison, 1964). As explained below, this pluvial paleolake displays well-developed shore platforms. Nonetheless, the estimation of the effective fetch of the inferred paleolakes would require to know the predominant wind direction when the erosional benches were formed. Moreover, the unknown erodibility of the materials exposed in the coastal areas play a critical role in the development of these landforms. Alternative processes have been proposed to explain the formation of benches and stepped massifs in other regions of Mars, including differential erosion in layered bedrock (e.g., Carr and Head III, 2003) and eolian erosion (e.g., Manent and El-Baz, 1986). Kraal et al. (2006) proposed alternative processes for the development of Martian landforms interpreted as 'bedrock shoreline features' such as the erosional action of ice in the surface of lakes or seas. An ice-covered lake was also the preferred hypothesis of Howard and Moore (2004) to explain the formation of benches and scarps in the Gorgonum Basin. Sholes et al. (2019) indicate that lineaments and terraces in Cydonia Mensae, which are considered as one of the better candidates for putative paleoshoreline features in the literature, do not show lateral or altitudinal consistency. Consequently, Sholes et al. (2019) considered that those landforms better resemble eroded and exposed bedding surfaces. These interpretations seem to be highly unlikely in our study area since the benches do not show any lithostratigraphic control or any preferred orientation.

4.4. Chronology of the delta and paleolake systems

The surface age of the delta D7 and of the main depression were calculated using crater-size frequency distribution statistics. This delta was selected due to its large area (~80 km^2) in order to reduce uncertainties on the age model (e.g., Warner et al., 2015). We obtained average age estimates of ~3.88 Ga (Middle Noachian) for the delta D7 (Fig. 6a, b), and ~3.71 Ga (Late Noachian) for the depression, considering a counting area of ~6200 km^2 in the latter (Fig. 6c, d). Both ages are consistent with those assigned to the geological units where these features are located

Fig. 3. CTX images illustrating features attributable to putative Gilbert-type deltas and shore platforms in the study area (labelled as D# and B#, respectively). A-A′ lines indicate the trace of the topographic profiles used to infer the mean water level from each feature (Fig. 8). White arrows indicate laterally continuous benches (e.g., B1, B4), some of them associated with residual relief and showing rounded geometry in plan view (e.g., B2, B3, B5 and B6).

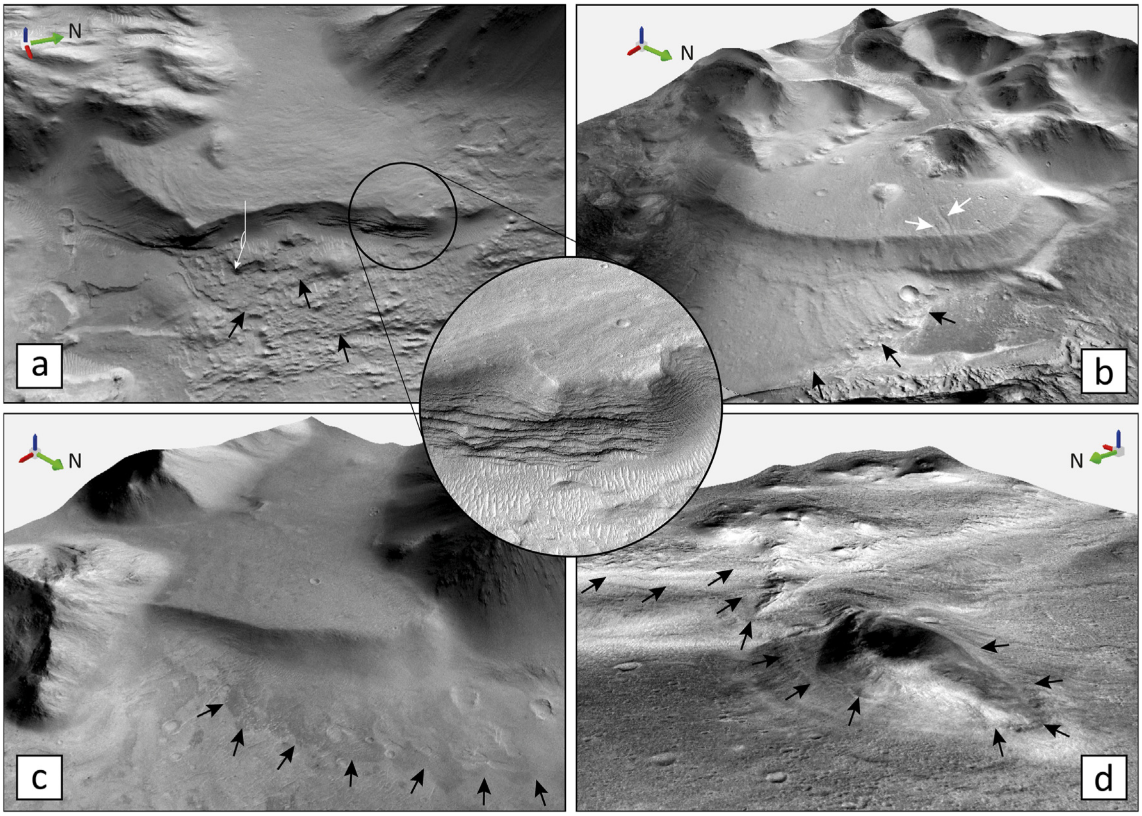

Fig. 5. 3D oblique views of some fan-shaped and coastal-like features (CTX images). (a) The D4 feature shows a steep front scalloped by a long-runout landslide in its central part, which permits observation of inner layering or clinoforms (circle: close-up view of HiRISE image ESP_058612_1815). Note that the lateral extent of the concave headscar of the landslide matches with the hummocky terrain situated at the foot, attributable to a blocky landslide deposits (black arrows). (b) The D2 feature shows two overlapping morpho-stratigraphic units. The oldest apron (foot indicated by black arrows) is partially overlain by the younger one, whose upper plain is carved by subtle channels (white arrows). (c) The D5 feature may also record several phases of development as suggested by the low-albedo apron located at the foot of its front (black arrows). (d) Laterally continuous benches corresponding to B4 at different elevations (black arrows) around a residual relief, which apparently connected to the "mainland" resembling an older isthmus and a peninsula.

and/or genetically related. According to Tanaka et al. (2014), the deltas associated with the drainage networks occur in the mNh unit (Middle Noachian), and the depressions in the HNt unit (Late Noachian-Early Hesperian). In spite of the age consistency between delta D7 and the depressions, the age model for delta D7 may present more uncertainties than that for the depressions. Its lower counting area (~80 km^2) can imply a higher spatial variability in cratering processes, as well as the exclusion of larger craters (Warner et al., 2015). Furthermore, the significant higher elevation of the delta D7 with respect to other deltas in the study area and the depressions do not permit confidence in associating its age with them.

According to Brossier et al. (2015), the estimated age of the delta located at the southwestern part of the Robert Sharp crater (Fig. 1a) is ~1.30 ± 0.37 Ga (Early Amazonian), with delta front elevation at around −2400 m, and an area of ~120 km^2. The remarkable age difference between the delta D7 and that located at the Robert Sharp crater could be either related to different formation ages or to resurfacing events associated with possible later aqueous phases that would have obliterated the oldest craters on the delta at Robert Sharp crater. Ejecta deposits related to an impact crater 23 km in diameter seem to obstruct the outlet of the ancient fluvial valley of Licus Vallis. These ejecta deposits probably prevented the fluvial reactivation of delta D7. Additionally, according to Warner et al. (2015), the selected area for confidently assessing the age of a surface should exceed 1000 km^2, whereas the mentioned deltas have significantly smaller areas.

The randomness analysis reveals that the clustering trend of the crater population in the main depression is significantly larger than in the delta, which is more ordered (Fig. 6a, e), with craters ranging from around 100 m to 300 m in diameter in the depression (Fig. 6c, f). Several resurfacing events have been identified, one of them affecting both features ~3.5 Ga ago (Early Hesperian), probably related to late episodes of aqueous activity (Fig. 6b, d). In summary, the chronological analysis indicates that (1) fluvial-lacustrine processes occurred in the region during the Noachian; and (2) the later occurrence of resurfacing events probably related to renewed flooding during the Early Hesperian or later.

4.5. Terrestrial analogs

In order to compare the putative paleolakes and the associated coastal-like features of Nepenthes Mensae with analog landforms on Earth, we focused our attention on Lake Bonneville and Lake Lahontan, two large and deep pluvial lakes that used to be located in the Great Basin of western North America during the Pleistocene (e.g., Broecker and Orr, 1958). Lake Lahontan and Lake Bonneville reached their maximum water level around 15 kyr ago during the Late Pleistocene, covering areas of 22,300 km^2 and 51,300 km^2, respectively (Benson et al., 2011). These paleolakes, partially desiccated at the present time, and their relict landforms (e.g., wave-cut platforms, beach ridges, spits, barriers, bars) have been proposed as terrestrial analogs for putative ancient lakes and oceans on Mars by multiple authors (e.g., Clifford and Parker, 2001; Zimbelman et al., 2004, 2005; Parker et al., 2010; Irwin and Zimbelman, 2012). We chose these pluvial paleolakes for comparison with our study area due to the following reasons: (1) the presence of well-preserved paleoshorelines recorded by laterally continuous shore platforms and beach ridges developed at different water-level elevations (Fig. 7b, c) (e.g., Oviatt, 2015); (2) these relict coastal features resemble those identified along the edges of the depressions and around the residual reliefs in Nepenthes Mensae (Fig. 7a); (3) the presence of multiple former deltas located at the mouth of fluvial valleys such as the Bonneville-level delta at American Fork (Godsey et al.,

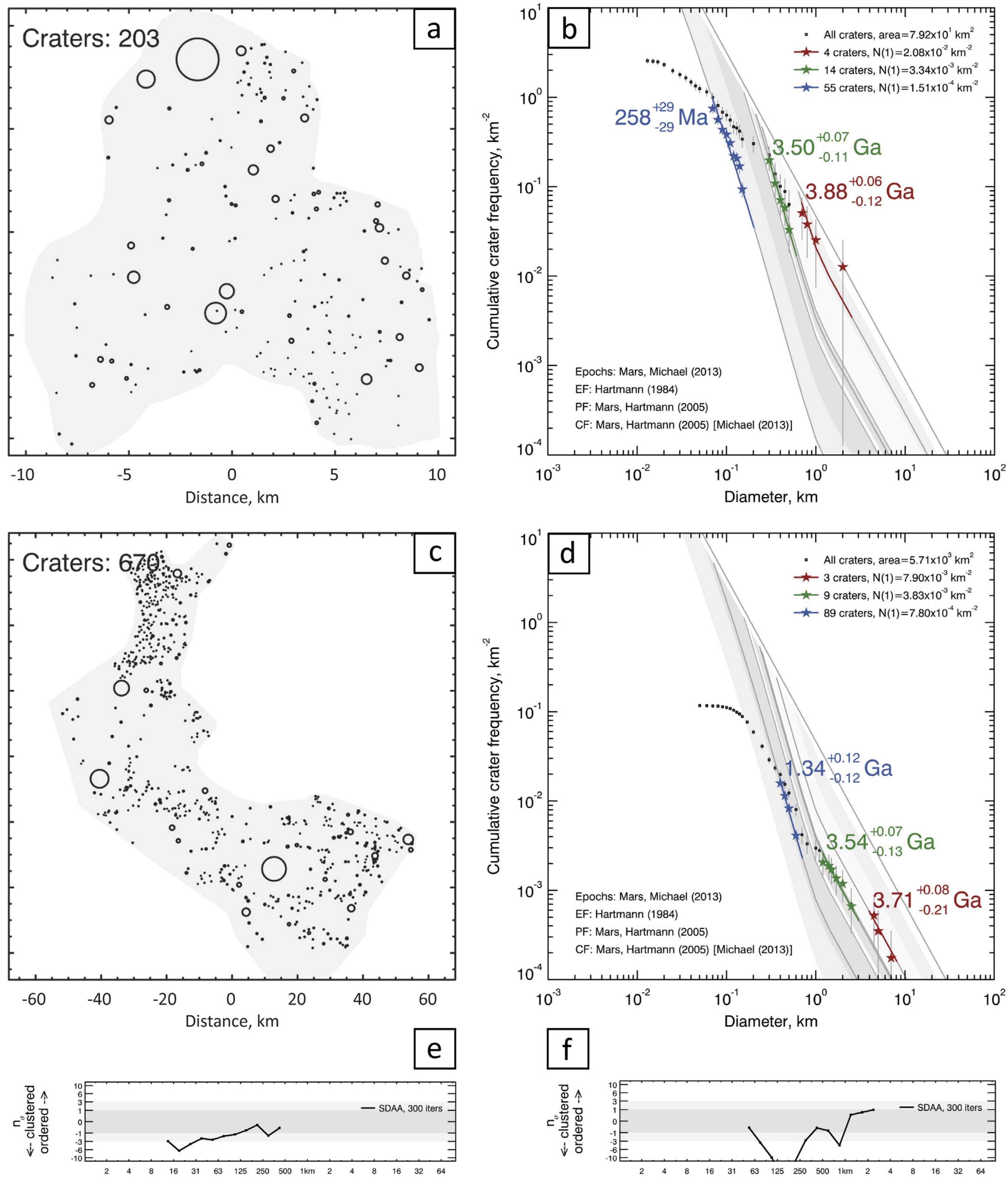

Fig. 6. (a, c) Crater-counting areas used for estimating the numerical age of delta D7 and the main depression, respectively (see location in Fig. 1c). (b, d) Age models showing simple cumulative fit for the formation age (red fit line), and corrected cumulative fits for the resurfacing events (green and blue fit lines) of the delta D7 and the main depression, respectively. The grey shadow bands represent the boundaries between the different Martian geological epochs (Michael, 2013). (e, f) Randomness analysis for the crater population of the delta and the depression, respectively.

2005), which was first analyzed by Gilbert (1890); (4) these coarse-grained deltas (Gilbert-type deltas) were fed by high-gradient rivers associated with canyons and small watersheds (Lemons and Chan, 1999); (5) both terrestrial paleolakes are located within endorheic basins as seems to be the case of those in Nepenthes Mensae; and (6) the extent covered by the Lake Lahontan during its highstand (22,300 km^2) is

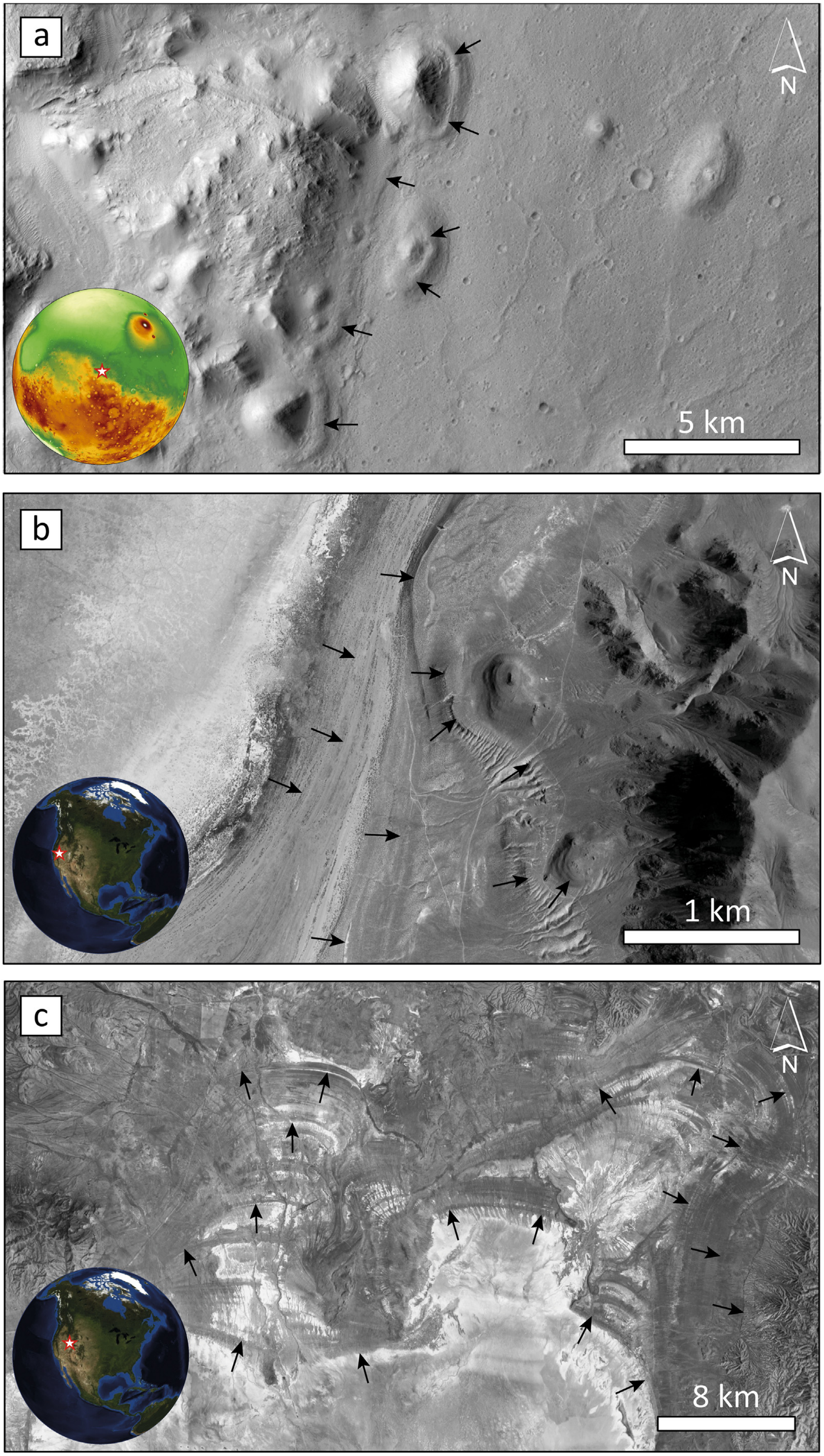
a
N
5 km
b
N
1 km
c
N
8 km

comparable to the sum of the surface areas of the paleolakes in Nepenthes Mensae during the mean highstand yielding a total area of ~19,000 km^2 (Fig. 9).

The strong resemblance (i.e., morphology, morphometry, spatial relationships) between the analyzed landforms on Mars and the terrestrial analogs is used to support our geomorphic and paleohydrologic interpretations.

4.6. Paleohydrological reconstruction

Elevations extracted from the putative deltas and shore platforms occur within the elevation ranges −1186 m to −1975 m, and −1811 m to −2150 m, respectively (Fig. 8). Elevation values are rather scattered and collectively do not define a clear equipotential surface. This fact can be related to several disconnected water bodies and multiple water levels. Delta fronts yield a mean elevation of −1830 m (standard deviation of 236 m). If the anomalous elevation of D7 is not considered, delta fronts yield an average elevation of −1902 m (standard deviation of 72 m). Collectively, benches yield a mean elevation value of −1978 m (standard deviation of 57.6 m). Deltas and benches associated with the main paleolake (i.e., deltas D2, D3, D5, and D6; and forty-four out of the fifty-four benches) yield mean elevations of −1946 m (standard deviation of 24 m) for deltas, and −1986 m (standard deviation of 56 m) for benches (see dashed lines in Fig. 8). The mean elevations among deltas and benches are consistent and define a contour along the edges of the depressions. In addition, these mean elevations are coherent with the average elevation of deltas within the main paleolake obtained by Rivera-Hernández and Palucis (2019), whose value is −1934 ± 33 m. These authors used two deltas documented within the main paleolake (deltas D2 and D5, as are identified in our work) for calculating that average elevation. It seems to correspond to a paleowater level of a former inland sea or of a series of potentially interconnected lakes with sufficient persistence to have a significant geomorphic imprint in the landscape. Using the mean elevation value from deltas of the main paleolake (around −1950 m), we have reconstructed the paleogeography of the paleolakes that used to occupy the depressions of Nepenthes Mensae (Fig. 9). According to this reconstruction, the largest paleolake reached an area of ~12,787 km^2, an estimated water volume of 3648 km^3, and mean and maximum depths of ~290 m and ~1000 m, respectively. Estimations for the area of the largest paleolake and its volume are similar to those calculated by Rivera-Hernández and Palucis (2019), whose values are 12,830 km^2 and 3890 km^3, respectively. The sum of the areas of the paleolakes in Nepenthes Mensae reached ~19,000 km^2 during the mean highstand. The surface of the depressions below the reconstructed paleolake level shows a smoother surface than that located above this level and outside the basin. This morphological feature, which is also observed in terrestrial paleolakes such as Lake Bonneville and Lake Lahontan, may be attributed to sediment aggradation in the bottom of the paleolakes and exposure to erosional processes during a shorter time span, after the desiccation of the lakes.

The deltas associated with the main depression (i.e., D2, D3, D5 and D6) show consistent delta-front elevations. However, the elevation of the front of the majority of the deltas that are not spatially associated with the main depression do not fall within their elevation range (i.e., D1a, D4, D7, and D9), with the exception of D1b and D8. Deltas D1a, D4, D7 and D9 show delta front elevations above −1900 m. This fact may be due to different water-level elevations. We propose that the anomalous elevation of delta D7, which is the largest of the study area (~85 km^2), is related to the presence in the past of a small enclosed depression at the mouth of Licus Vallis, perched above and disconnected from the main system of depressions, with a local base level located at an elevation of around −1200 m (Fig. 8). A small valley occurs below this inferred basin, which may receive two non-excluding interpretations: (1) an overflow channel of the depression; (2) the stream that captured the perched depression. The delta D8 occurs at the mouth of this valley at an elevation of around −1920 m, which is consistent with the mean water level calculated for deltas of the main paleolake. The anomalous elevation difference (~720 m) cannot be explained by differential vertical displacements due to the lack of discrete tectonic structures between deltas D7 and D8, situated ~34 km apart (Fig. 10). Black et al. (2017) proposed that regional tectonic activity was low during the period of formation of valley networks on Mars, and Goudge and Fassett (2018) inferred that regional uplift was not an important factor during the configuration of the drainage network of Licus Vallis. Therefore, we consider that the present topography is similar to what existed during the incision of the drainage network and the development of the deltas.

Multiple "levels" interpreted as paleoshorelines have been identified on Mars (e.g., Carr and Head III, 2003; Webb, 2004; Ghatan and Zimbelman, 2006). The "Contact 1", defined by Parker et al. (1989), and renamed as "Arabia shoreline" by Clifford and Parker (2001), is the topographically highest level of the putative Martian ocean, which shows significant elevation variations along the northern plains of up to several kilometers, attributable to subsequent regional deformation caused by true polar wander (Perron et al., 2007). Di Achille and Hynek (2010b) inferred an equipotential surface (referred to as "S" level) from elevation values of 17 putative delta fronts located in open basins along the margins of the Martian lowlands. This level lies at a mean elevation of −2540 m (standard deviation of 177 m), which is consistent with the mean elevation inferred for the Arabia level (−2499 m) (Clifford and Parker, 2001; Di Achille and Hynek, 2010b). This level is ~500 m lower than the one inferred in this work at Nepenthes Mensae (around −1950 m) from putative deltas of the main depression. However, these deltas were probably associated with an

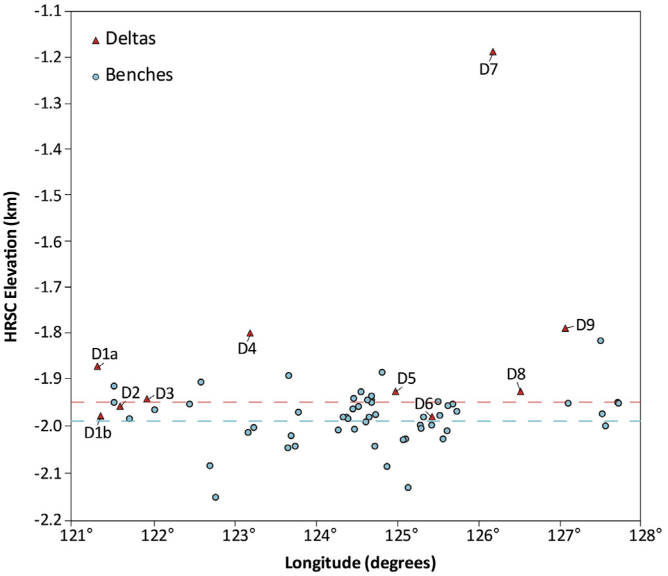

Fig. 8. Elevation values from each putative delta (plain-front junction, Table 1) and shore platform (inner edge) used to infer the past water levels. The dashed red and blue lines indicate, respectively, the mean elevation for deltas and shore platforms situated within the main paleolake. Note that delta D7 is located at an anomalous elevation compared with the rest of measured coastal landforms.

Fig. 7. (a) Comparison between the putative coastal landforms in Nepenthes Mensae (Mars, image centered at 2°24′2″N, 124°44′10″E), and (b) those in terrestrial paleolakes such as Lake Lahontan (Nevada, USA; image centered at 40°14′3″N, 119°17′4″W) and (c) Lake Bonneville (Utah, USA; image centered at 41°29′55″N, 113°25′53″W). Arrows point to laterally continuous benches with consistent elevation and strandlines that record paleowater levels.
Images from CTX and Google Earth.

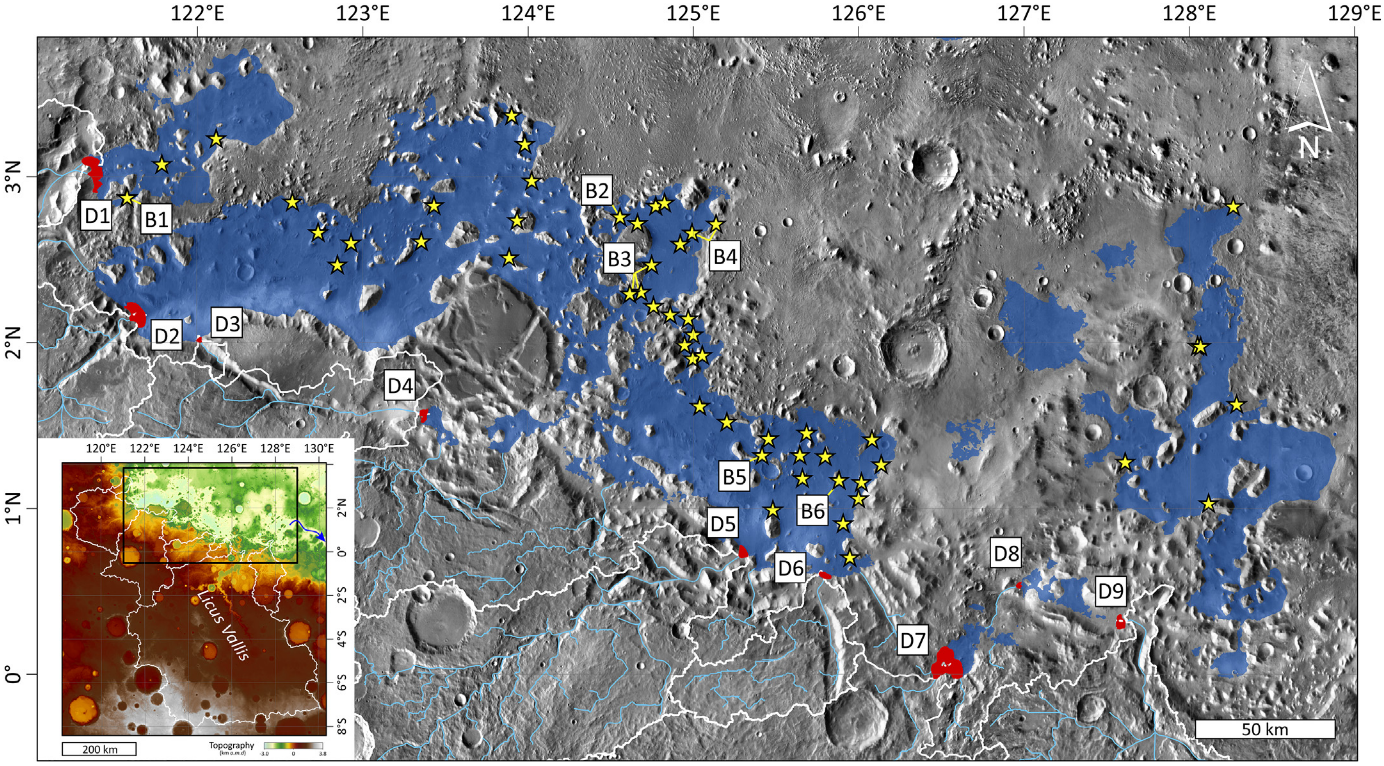

Fig. 9. Inset: elevation model of the study area showing the watershed boundaries (white lines) and the area depicted in the overview (black polygon). The blue arrow indicates that the depressions probably used to connect eastward with the northern lowlands (HRSC-MOLA blended topography). Overview: paleogeographic reconstruction of the paleolakes (blue polygons), based on the mean elevation (~−1950 m) of the paleo-water level recorded by the putative deltas of the main paleolake. Deltas and shore platforms are indicated by red areas and yellow stars, respectively. The stream network is represented with light-blue lines. The labels indicate the location of the images shown in Fig. 3 (base map mosaic from THEMIS-IR day images).

endorheic basin occupied by an inner sea or large interconnected paleolakes. It is possible that, at some stage, these basins became connected to the putative Oceanus Borealis before the water level dropped, supported by the fact that the depressions connect eastward to the northern lowlands (Fig. 9). However, this possible connection to a northern ocean would require a more detailed investigation.

4.7. Geomorphological history

In order to summarize the geomorphological evolution of the study area, focusing on the history of the paleolakes, we propose the following possible sequence of events: (1) The large depressions that hosted the paleolakes were formed along the dichotomy boundary during the Noachian. The origin of these basins could be related to various types of large-scale deformation processes, although it remains uncertain. (2) Fluvial processes initiated with the presence of liquid water and runoff resulted in the development of valleys carved into the mNh unit in the highlands. These N-directed drainage systems fed the paleolakes developed in the endorheic depressions located along the dichotomy. (3) The presence of long-standing water bodies and relatively long periods of lake-level stability permitted the formation of deltas at the mouth of the valleys and coastal benches along the margins of the depressions and around residual reliefs. (4) The paleolakes probably experienced a long-term water-level decline punctuated by periods of stability, as supported by inset benches at different elevations. (5) The resurfacing events suggested by the chronological analysis carried out in the bottom of the depressions could be related to new flooding events during the Early Hesperian or later. (6) Finally, hydrological activity in the region declined and as a result the paleolakes desiccated. This situation allows the observation of the relict geomorphic features related to former base levels, as occurs in the proposed pluvial paleolakes as terrestrial analogs. At the present time, the landscape is being modified by depositional and erosional eolian processes as recorded by dune fields and yardangs.

5. Conclusions

The fan-shaped and terrace-like features identified in Nepenthes Mensae are likely relict Gilbert-type deltas and shore platforms, respectively, developed along paleoshorelines. This interpretation is supported by several lines of evidence: (1) their spatial distribution, with putative deltas linked to the mouth of drainage networks, and benches located along the margins of the depressions and around prominent residual reliefs; (2) their morphological resemblance with other Martian landforms attributed by other authors to relict deltas and markers of paleoshorelines; (3) the lateral continuity along kilometers of the gently-sloping benches; (4) the elevation consistency among the benches and deltas as shown by their altitudinal distribution; (5) the detection of hydrated minerals (Fe/Mg smectites) occurring in the surface of the front of a delta analyzed near the study area, indicative of the existence of liquid water in the past; and (6) the analogy between these ancient Martian landforms and those documented in Pleistocene paleolakes, such as Lake Bonneville and Lake Lahontan, including the extent and endorheic nature of these terrestrial paleolakes and those inferred in Nepenthes Mensae. Assuming that the current regional topography is similar to the one that existed during the development of the analyzed landforms, their elevations permitted us to approximately determine the mean water level at around −1950 m corresponding to an ancient inner sea or a system of interconnected paleolakes that occupied the belt of NW-SE trending depressions. This past water level is consistent with the mean elevation reported for the mean Arabia level. The paleolakes may have experienced a long-term water-level decline punctuated by periods of stability, as supported by inset benches at different

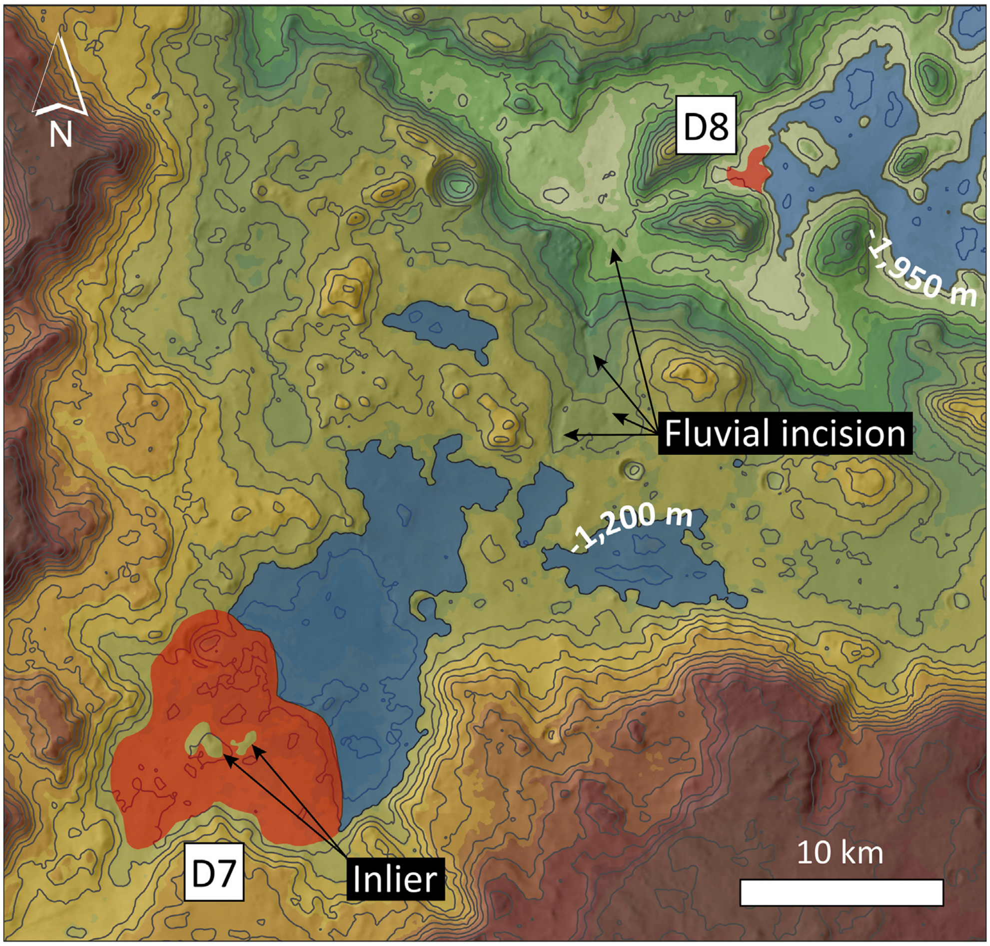

Fig. 10. Context map with 100 m contour lines showing the spatial-altitudinal distribution of deltas D7 and D8 (red polygons), as well as the respective paleolakes (blue polygons). Delta D7 includes interior high points likely representing bedrock inliers, which probably controlled the formation of two delta lobes (CTX mosaic over HRSC topography).

elevations. These findings shed light into the paleogeography and paleohydrologic conditions in the Nepenthes Mensae region during the Late Noachian-Early Hesperian transition. They also contribute to contextualize the continuous findings on the environmental and climatic conditions in nearby Gale crater at a similar time; and illustrates the important morphogenetic role that liquid water may have played on Mars in the past.

Declaration of competing interest

The authors declare that they have no known competing financial interests or personal relationships that could have appeared to influence the work reported in this paper.

Acknowledgments

This research was supported by a PhD scholarship granted to ÁG-A (C237/2016) by the Gobierno de Aragón (Spain) and the European Social Fund, by project CGL2017-85045-P (Ministerio de Ciencia, Innovación y Universidades, Gobierno de España), and by the Ibercaja-CAI mobility program (CB 5/18) funded by Universidad de Zaragoza, Fundación Bancaria Ibercaja and Fundación CAI (mobility funding for research stay of Á.G-A. at the Centro de Astrobiología (INTA-CSIC)). We would like to thank Dr. Joel Davis and an anonymous reviewer for their valuable comments and suggestions which helped to improve the paper. We also grateful to Dr. Jim Head for his interest in our paper and his suggestions in a previous version of the manuscript.

References

Andrews-Hanna, J.C., Phillips, R.J., 2007. Hydrological modeling of outflow channels and chaos regions on Mars. J. Geophys. Res. Planets 112 (E8). https://doi.org/10.1029/2006JE002881.

Baker, V.R., 2001. Water and the Martian landscape. Nature 412 (6843), 228. https://doi.org/10.1038/35084172.

Banfield, D., Donelan, M., Cavaleri, L., 2015. Winds, waves and shorelines from ancient Martian seas. Icarus 250, 368–383. https://doi.org/10.1016/j.icarus.2014.12.001.

Bates, C.C., 1953. Rational theory of delta formation. AAPG Bull. 37 (9), 2119–2162.

Benson, L.V., et al., 2011. The rise and fall of Lake Bonneville between 45 and 10.5 ka. Quat. Int. 235 (1–2), 57–69. https://doi.org/10.1016/j.quaint.2010.12.014.

Bibring, J.P., et al., 2006. Global mineralogical and aqueous Mars history derived from OMEGA/Mars Express data. Science 312 (5772), 400–404. https://doi.org/10.1126/science.1122659.

Bird, E.C., 2011. Coastal Geomorphology: An Introduction. John Wiley & Sons (436 pp).

Black, B.A., Perron, J.T., Hemingway, D., Bailey, E., Nimmo, F., Zebker, H., 2017. Global drainage patterns and the origins of topographic relief on Earth, Mars, and Titan. Science 356, 727–731. https://doi.org/10.1126/science.aag0171.

Blair, T.C., McPherson, J.G., 1994. Alluvial fans and their natural distinction from rivers based on morphology, hydraulic processes, sedimentary processes, and facies assemblages. J. Sediment. Res. 64 (3a), 450–489. https://doi.org/10.1306/D4267DDE-2B26-11D7-8648000102C1865D.

Broecker, W.S., Orr, P.C., 1958. Radiocarbon chronology of Lake Lahontan and Lake Bonneville. Geol. Soc. Am. Bull. 69 (8), 1009–1032. https://doi.org/10.1130/0016-7606(1958)69[1009:RCOLLA]2.0.CO;2.

Brossier, J., Le Deit, L., Hauber, E., Mangold, N., Carter, J., Jaumann, R., 2015. Reconstructing the infilling history within Robert Sharp Crater, Mars: insights from morphology and stratigraphy. European Planetary Science Congress Abstracts. vol. 10 (EPSC2015-735).

Caldwell, R.L., Edmonds, D.A., 2014. The effects of sediment properties on deltaic processes and morphologies: a numerical modeling study. J. Geophys. Res. Earth 119 (5), 961–982. https://doi.org/10.1002/2013JF002965.

Caprarelli, G., 2015. Stratigraphic relations of Hesperian transition units in the Nepenthes region, Mars. Lunar and Planetary Science Conference Abstracts. vol. 46 (p#1584).

Carr, M.H., Head III, J.W., 2003. Oceans on Mars: an assessment of the observational evidence and possible fate. J. Geophys. Res. Planets 108 (E5). https://doi.org/10.1029/2002JE001963.

Carter, J., Poulet, F., Bibring, J.-P., Mangold, N., Murchie, S., 2013. Hydrous minerals on Mars as seen by the CRISM and OMEGA imaging spectrometers: updated global view. J. Geophys. Res. Planets 118, 831–858. https://doi.org/10.1029/2012JE004145.

Carter, J., Viviano-Beck, C., Loizeau, D., Bishop, J., Le Deit, L., 2015. Orbital detection and implications of akaganeite on Mars. Icarus 253, 296–310. https://doi.org/10.1016/j.icarus.2015.01.020.

Christensen, P.R., et al., 2004. The thermal emission imaging system (THEMIS) for the Mars 2001 Odyssey Mission. Space Sci. Rev. 110 (1–2), 85–130. https://doi.org/10.1023/B:SPAC.0000021008.16305.94.

Christensen, P.R., Fergason, R.L., Edwards, C.S., Hill, J., 2013. THEMIS-derived thermal inertia mosaic of Mars: product description and science results. Lunar and Planetary Science Conference Abstracts. vol. 44 (The Woodlands, Texas, p. # 2822).

Clifford, S.M., Parker, T.J., 2001. The evolution of the Martian hydrosphere: implications for the fate of a primordial ocean and the current state of the northern plains. Icarus 154 (1), 40–79. https://doi.org/10.1006/icar.2001.6671.

Di Achille, G., Hynek, B.M., 2010a. Deltas and valley networks on Mars: implications for a global hydrosphere. Lakes on Mars, pp. 223–248. https://doi.org/10.1016/C2009-0-06633-1.

Di Achille, G., Hynek, B.M., 2010b. Ancient ocean on Mars supported by global distribution of deltas and valleys. Nat. Geosci. 3 (7), 459–463. https://doi.org/10.1038/ngeo891.

Dickson, J.L., Kerber, L.A., Fassett, C.I., Ehlmann, B.L., 2018. A global, blended CTX mosaic of Mars with vectorized seam mapping: a new mosaicking pipeline using principles of non-destructive image editing. Lunar and Planetary Science Conference Abstracts. 49 (p#2480).

Ehlmann, B.L., Buz, J., 2014. Hydrology and aqueous alteration in the Watershed of Gale, Sharp, and Knobel craters: a regional context for Curiosity's exploration. Lunar and Planetary Science Conference Abstracts. 45 (p#2587).

Ehlmann, B.L., Buz, J., 2015. Mineralogy and fluvial history of the watersheds of Gale, Knobel, and Sharp craters: a regional context for the Mars Science Laboratory Curiosity's exploration. Geophys. Res. Lett. 42 (2), 264–273. https://doi.org/10.1002/2014GL062553.

Ehlmann, B.L., Mustard, J.F., Fassett, C.I., Schon, S.C., Head III, J.W., Des Marais, D.J., Grant, J.A., Murchie, S.L., 2008. Clay minerals in delta deposits and organic preservation potential on Mars. Nat. Geosci. 1 (6), 355–358. https://doi.org/10.1038/ngeo207.

Ehlmann, B.L., Mustard, J.F., Swayze, G.A., Clark, R.N., Bishop, J.L., Poulet, F., Des Marais, D.J., Roach, L.H., Milliken, R.E., Wray, J.J., Barnouin-Jha, O.S., Murchie, S.L., 2009. Identification of hydrated silicate minerals on Mars using MRO-CRISM: geologic context near Nili Fossae and implications for aqueous alteration. J. Geophys. Res. Planets 114, E2. https://doi.org/10.1029/2009JE003339.

Fassett, C.I., Head III, J.W., 2008. Valley network-fed, open-basin lakes on Mars: distribution and implications for Noachian surface and subsurface hydrology. Icarus 198 (1), 37–56. https://doi.org/10.1016/j.icarus.2008.06.016.

Fawdon, P., Gupta, S., Davis, J.M., Warner, N.H., Adler, J.B., Balme, M.R., Bell, J.F., Grindrod, P.M., Sefton-Nash, E., 2018. The Hypanis Valles delta: the last highstand of a sea on early Mars? Earth Planet. Sc. Lett. 500, 225–241. https://doi.org/10.1016/j.epsl.2018.07.040.

Fergason, R.L., Hare, T.M., Laura, J., 2018. HRSC and MOLA Blended Digital Elevation Model at 200m v2, Astrogeology PDS Annex. U.S. Geological Survey http://bit.ly/HRSC_MOLA_Blend_v0.

Figueiredo, P.M., Cabral, J., Rockwell, T.K., 2014. Recognition of Pleistocene marine terraces in the Southwest of Portugal (Iberian Peninsula): evidences of regional Quaternary uplift. Ann. Geophys. 56 (6). https://doi.org/10.4401/ag-6276.

García-Arnay, Á., Gutiérrez, F., Fernández, S., 2018a. Coastal-like features in Nepenthes Mensae, Mars as paleowater-level indicators, and a terrestrial analog. Lunar and Planetary Science Conference Abstracts. 49 p#2595. Retrieved from. https://www.hou.usra.edu/meetings/lpsc2018/pdf/2595.pdf.

García-Arnay, Á., Fernández, S., de Pablo, M.Á., Gutiérrez, F., 2018c. The dominant morphogenetic role of surface runoff in Licus Vallis, Mars: results from geomorphological and morphometric analyses. Geogaceta 63, 63–66 Retrieved from. http://www.sociedadgeologica.es/archivos/geogacetas/geo63/geo63_16.pdf.

García-Arnay, Á., Gutiérrez, F., de Pablo, M.Á., Fernández, S., 2018b. Characterization and interpretation of the fan-shaped and terrace-like features identified in Nepenthes Mensae, Mars. EGU General Assembly Conference Abstracts. 20 p# 808. Retrieved from. https://figshare.com/articles/Characterization_and_interpretation_of_the_fan-shaped_and_terrace-like_features_identified_in_Nepenthes_Mensae_Mars/9824609.

García-Arnay, J.Á., 2016. Cartografía geomorfológica de la región de Nepenthes Mensae, Marte: evidencias de un antiguo mar. Universidad de Zaragoza, Zaragoza, Spain Master's thesis. Retrieved from. https://zaguan.unizar.es/record/58648/files/TAZ-TFM-2016-821.pdf.

Ghatan, G.J., Zimbelman, J.R., 2006. Paucity of candidate coastal constructional landforms along proposed shorelines on Mars: implications for a northern lowlands-filling ocean. Icarus 185 (1), 171–196. https://doi.org/10.1016/j.icarus.2006.06.007.

Gilbert, G.K., 1884. The topographical features of lake shores. United States Geological Survey Annual Report. vol. 5, pp. 104–108.

Gilbert, G.K., 1890. Lake Bonneville. vol. 1. US Government Printing Office.

Godsey, H.S., Atwood, G., Lips, E., Miller, D.M., Milligan, M., Oviatt, C.G., 2005. Don R. Currey memorial field trip to the shores of Pleistocene Lake Bonneville. In: Pederson, J.L., Dehler, C.M. (Eds.), Interior Western United States. Geological Society of America Field Guide 6, pp. 419–448. https://doi.org/10.1130/2005.fld006(19).

Goudge, T.A., Fassett, C.I., 2018. Incision of Licus Vallis, Mars, from multiple lake overflow floods. J. Geophys. Res. Planets 123 (2), 405–420. https://doi.org/10.1002/2017JE005438.

Goudge, T.A., Aureli, K.L., Head, J.W., Fassett, C.I., Mustard, J.F., 2015. Classification and analysis of candidate impact crater-hosted closed-basin lakes on Mars. Icarus 260, 346–367. https://doi.org/10.1016/j.icarus.2015.07.026.

Hampson, G.J., Storms, J.E., 2003. Geomorphological and sequence stratigraphic variability in wave-dominated, shoreface-shelf parasequences. Sedimentology 50 (4), 667–701. https://doi.org/10.1046/j.1365-3091.2003.00570.x.

Harrison, K.P., Grimm, R.E., 2005. Groundwater-controlled valley networks and the decline of surface runoff on early Mars. J. Geophys. Res. Planets 110 (E12). https://doi.org/10.1029/2005JE002455.

Hartmann, W.K., 2005. Martian cratering 8: isochron refinement and the chronology of Mars. Icarus 174 (2), 294–320. https://doi.org/10.1016/j.icarus.2004.11.023.

Hartmann, W.K., Neukum, G., 2001. Cratering chronology and the evolution of Mars. In: Kallenbach, R., Geiss, J., Hartmann, W.K. (Eds.), Chronology and Evolution of Mars. Space Sciences Series of ISSI vol 12. Springer, Dordrecht. https://doi.org/10.1007/978-94-017-1035-0_6.

Head III, J.W., Hiesinger, H., Ivanov, M.A., Kreslavsky, M.A., Pratt, S., Thomson, B.J., 1999. Possible ancient oceans on Mars: evidence from Mars Orbiter Laser Altimeter data. Science 286 (5447), 2134–2137. https://doi.org/10.1126/science.286.5447.2134.

Hearty, P.J., Hollin, J.T., Neumann, A.C., O'Leary, M.J., McCulloch, M., 2007. Global sea-level fluctuations during the Last Interglaciation (MIS 5e). Quat. Sci. Rev. 26 (17–18), 2090–2112. https://doi.org/10.1016/j.quascirev.2007.06.019.

Howard, A.D., Moore, J.M., 2004. Scarp-bounded benches in Gorgonum Chaos, Mars: formed beneath an ice-covered lake? Geophys. Res. Lett. 31, L01702. https://doi.org/10.1029/2003GL018925.

Irwin III, R.P., Watters, T.R., Howard, A.D., Zimbelman, J.R., 2004. Sedimentary resurfacing and fretted terrain development along the crustal dichotomy boundary, Aeolis Mensae, Mars. J. Geophys. Res. Planets 109, E09011. https://doi.org/10.1029/2004JE002248.

Irwin, R.P., Howard, A.D., 2002. Drainage basin evolution in Noachian Terra Cimmeria, Mars. J. Geophys. Res. Planets 107 (E7). https://doi.org/10.1029/2001JE001818.

Irwin, R.P., Zimbelman, J.R., 2012. Morphometry of Great Basin pluvial shore landforms: implications for paleolake basins on Mars. J. Geophys. Res. Planets 117 (E7). https://doi.org/10.1029/2012JE004046.

Irwin, R.P., Howard, A.D., Craddock, R.A., Moore, J.M., 2005. An intense terminal epoch of widespread fluvial activity on early Mars: 2. Increased runoff and paleolake development. J. Geophys. Res. Planets 110 (E12). https://doi.org/10.1029/2005JE002460.

Kleinhans, M.G., 2005. Flow discharge and sediment transport models for estimating a minimum timescale of hydrological activity and channel and delta formation on Mars. J. Geophys. Res. Planets 110 (E12). https://doi.org/10.1029/2005JE002521.

Kneissl, T., van Gasselt, S., Neukum, G., 2011. Map-projection-independent crater size-frequency determination in GIS environments—new software tool for ArcGIS. Planet. Space Sci. 59 (11), 1243–1254. https://doi.org/10.1016/j.pss.2010.03.015.

Kraal, E.R., Asphaug, E., Moore, J.M., Lorenz, R.D., 2006. Quantitative geomorphic modeling of Martian bedrock shorelines. J. Geophys. Res. Planets 111. https://doi.org/10.1029/2005JE002567 E03001.

Kraal, E.R., Van Dijk, M., Postma, G., Kleinhans, M.G., 2008. Martian stepped-delta formation by rapid water release. Nature 451 (7181), 973. https://doi.org/10.1038/nature06615.

Lemons, D.R., Chan, M.A., 1999. Facies architecture and sequence stratigraphy of fine-grained lacustrine deltas along the eastern margin of late Pleistocene Lake Bonneville, northern Utah and southern Idaho. AAPG Bull. 83 (4), 635–665.

Malin, M.C., Carr, M.H., 1999. Groundwater formation of Martian valleys. Nature 397 (6720), 589. https://doi.org/10.1038/17551.

Malin, M.C., Edgett, K.S., 2000. Evidence for recent groundwater seepage and surface runoff on Mars. Science 288 (5475), 2330–2335. https://doi.org/10.1126/science.288.5475.2330.

Malin, M.C., Bell, J.F., Cantor, B.A., Caplinger, M.A., Calvin, W.M., Clancy, R.T., Lee, S.W., 2007. Context camera investigation on board the Mars Reconnaissance Orbiter. J. Geophys. Res. Planets 112 (E5). https://doi.org/10.1029/2006JE002808 E05S04.

Manent, L.S., El-Baz, F., 1986. Comparison of knobs on Mars to isolated hills in eolian, fluvial and glacial environments. Earth Moon Planet. 34 (2), 149–167. https://doi.org/10.1007/BF00055132.

Martín-González, F., de Pablo, M.A., Pacifici, A., 2007. Alignments mapping and structural analysis of western sector of Nepenthes Mensae, Mars. Geophys. Res. Abstr. 9, 07796.

McEwen, A.S., Eliason, E.M., Bergstrom, J.W., Bridges, N.T., Hansen, C.J., Delamere, W.A., Grant, J.A., Gulick, V.C., Herkenhoff, K.E., Keszthelyi, L., Kirk, R.L., Mellon, M.T., Squyres, S.W., Thomas, N., Weitz, C.M., 2007. Mars reconnaissance orbiter's high resolution imaging science experiment (HiRISE). J. Geophys. Res. Planets 112 (E5). https://doi.org/10.1029/2005JE002605 E05S02.

Michael, G.G., 2013. Planetary surface dating from crater size–frequency distribution measurements: multiple resurfacing episodes and differential isochron fitting. Icarus 226 (1), 885–890. https://doi.org/10.1016/j.icarus.2013.07.004.

Michael, G.G., Neukum, G., 2010. Planetary surface dating from crater size–frequency distribution measurements: partial resurfacing events and statistical age uncertainty. Earth Planet. Sci. Lett. 294 (3), 223–229. https://doi.org/10.1016/j.epsl.2009.12.041.

Michael, G.G., Platz, T., Kneissl, T., Schmedemann, N., 2012. Planetary surface dating from crater size–frequency distribution measurements: spatial randomness and clustering. Icarus 218 (1), 169–177. https://doi.org/10.1016/j.icarus.2011.11.033.

Mikhailova, M.V., 2015. Morphometry of river deltas. Water Res. 42 (1), 52–62. https://doi.org/10.1134/S009780781501008X.

Morgan, F., Seelos, F.P., Murchie, S.L., the CRISM Team, 2014. CRISM analysis toolkit (CAT). In: Gaddis, R.G., Hare, T., Beyer, R. (Eds.), Summary and Abstracts of the Planetary Data Workshop, June 2012: Open-File Report 2014-1056. U.S. Geological Survey, Reston, VA, USA, pp. 125–126.

Morrison, R.B., 1964. Lake Lahontan: Geology of Southern Carson desert, Nevada. 401. US Government Printing Office Retrieved from. https://pubs.usgs.gov/pp/0401/report.pdf.

Murchie, S., et al., 2007. Compact reconnaissance imaging spectrometer for Mars (CRISM) on Mars reconnaissance orbiter (MRO). J. Geophys. Res. Planets 112 (E5). https://doi.org/10.1029/2006JE002682.

Neukum, G., Ivanov, B.A., Hartmann, W.K., 2001. Cratering records in the inner solar system in relation to the lunar reference system. In: Kallenbach, R., Geiss, J., Hartmann, W.K. (Eds.), Chronology and Evolution of Mars. Space Sciences Series of ISSI vol. 12. Springer, Dordrecht. https://doi.org/10.1007/978-94-017-1035-0_3.

Neukum, G., Jaumann, R., the HRSC Co-Investigator and Experiment Team, 2004. HRSC: the high resolution stereo camera of Mars Express. In: Wilson, A. (Ed.), Mars Express: The Scientific Payload. ESA, Noordwijk, The Netherlands, pp. 17–35 SP-1240.

Nordstrom, K.F., Jackson, N.L., 2012. Physical processes and landforms on beaches in short fetch environments in estuaries, small lakes and reservoirs: a review. Earth Sci. Rev. 111 (1–2), 232–247. https://doi.org/10.1016/j.earscirev.2011.12.004.

Oviatt, C.G., 2015. Chronology of Lake Bonneville, 30,000 to 10,000 yr BP. Quat. Sci. Rev. 110, 166–171. https://doi.org/10.1016/j.quascirev.2014.12.016.

de Pablo, M.Á., Pacifici, A., 2008. Geomorphological evidence of water level changes in Nepenthes Mensae, Mars. Icarus 196 (2), 667–671. https://doi.org/10.1016/j.icarus.2008.04.005.

de Pablo, M.Á., Pacifici, A., 2009. Chain of depressions and the watershed evolution in Nepenthes Mensae, Mars. Lunar and Planetary Science Conference Abstracts. vol. 40 (p#1095).

Parker, T.J., Currey, D.R., 2001. Extraterrestrial coastal geomorphology. Geomorphology 37 (3–4), 303–328. https://doi.org/10.1016/S0169-555X(00)00089-1.

Parker, T.J., Saunders, R.S., Schneeberger, D.M., 1989. Transitional morphology in west Deuteronilus Mensae, Mars: implications for modification of the lowland/upland boundary. Icarus 82 (1), 111–145. https://doi.org/10.1016/0019-1035(89)90027-4.

Parker, T.J., Gorsline, D.S., Saunders, R.S., Pieri, D.C., Schneeberger, D.M., 1993. Coastal geomorphology of the Martian northern plains. J. Geophys. Res. Planets 98 (E6), 11061–11078. https://doi.org/10.1029/93JE00618.

Parker, T.J., Grant, J.A., Franklin, B.J., 2010. The northern plains: a Martian oceanic basin. Lakes on Mars, pp. 249–273. https://doi.org/10.1016/B978-0-444-52854-4.00009-X.

Penland, S., Kulp, M.A., 2005. Deltas. In: Schwartz, M. (Ed.), Encyclopedia of Coastal Science. Springer, pp. 362–386.

Perron, J.T., Mitrovica, J.X., Manga, M., Matsuyama, I., Richards, M.A., 2007. Evidence for an ancient Martian ocean in the topography of deformed shorelines. Nature 447 (7146), 840. https://doi.org/10.1038/nature05873.

Pondrelli, M., Rossi, A.P., Marinangeli, L., Hauber, E., Gwinner, K., Baliva, A., Di Lorenzo, S., 2008. Evolution and depositional environments of the Eberswalde fan delta, Mars. Icarus 197 (2), 429–451. https://doi.org/10.1016/j.icarus.2008.05.018.

Poulet, F., Bibring, J.P., Mustard, J.F., Gendrin, A., Mangold, N., Langevin, Y., Arvidson, R.E., Gondet, B., Gomez, C., the Omega Team, 2005. Phyllosilicates on Mars and implications for early Martian climate. Nature 438 (7068), 623–627. https://doi.org/10.1038/nature04274.

Rivera-Hernández, F., Palucis, M.C., 2019. Do deltas along the crustal dichotomy boundary of Mars in the Gale crater region record a northern ocean? Geophys. Res. Lett. 46, 8689–8699. https://doi.org/10.1029/2019GL083046.

Schon, S.C., Head, J.W., Fassett, C.I., 2012. An overfilled lacustrine system and progradational delta in Jezero crater, Mars: implications for Noachian climate. Planet. Space Sci. 67 (1), 28–45. https://doi.org/10.1016/j.pss.2012.02.003.

Sholes, S.F., Montgomery, D.R., Catling, D.C., 2019. Quantitative High-Resolution Reexamination of a Hypothesized Ocean Shoreline in Cydonia Mensae on Mars. J. Geophys. Res. Planets 124 (2), 316–336. https://doi.org/10.1029/2018JE005837.

Sunamura, T., 1992. Shore platforms. Geomorphology of Rocky Coasts. vol. 302. Wiley, Chichester, pp. 139–183.

Tanaka, K.L., Skinner Jr., J.A., Dohm, J.M., Irwin III, R.P., Kolb, E.J., Fortezzo, C.M., Platz, T., Michael, G.G., Hare, T.M., 2014. Geologic Map of Mars: U.S. Geological Survey Scientific Investigations Map 3292, Scale 1:20,000,000. pamphlet 43 p. https://doi.org/10.3133/sim3292.

Trenhaile, A.S., 1987. Shore platforms. The Geomorphology of Rock Coasts. Oxford University Press, USA, pp. 192–239.

Valenciano, A, de Pablo, M.A., 2010. La importancia del agua en el modelado de la región de Nepenthes Mensae, Marte. Tecnología y desarrollo 8, 30 Retrieved from. https://revistas.uax.es/index.php/tec_des/article/view/563.

Valenciano, A., de Pablo, M.Á., Pacifici, A., 2009. The role of water on the evolution of the Nepenthes Mensae region of Mars. Lunar and Planetary Science Conference Abstracts. vol. 40 (p#1052).

Viviano-Beck, C.E., et al., 2014. Revised CRISM spectral parameters and summary products based on the currently detected mineral diversity on Mars. J. Geophys. Res. Planets 119 (6), 1403–1431. https://doi.org/10.1002/2014JE004627.

Viviano-Beck, C.E., et al., 2015. MRO CRISM type spectra library. NASA Planetary Data System Retrieved from. http://crismtypespectra.rsl.wustl.edu.

Warner, N.H., Gupta, S., Calef, F., Grindrod, P., Boll, N., Goddard, K., 2015. Minimum effective area for high resolution crater counting of Martian terrains. Icarus 245, 198–240. https://doi.org/10.1016/j.icarus.2014.09.024.

Webb, V.E., 2004. Putative shorelines in northern Arabia Terra, Mars. J. Geophys. Res. Planets 109 (E9). https://doi.org/10.1029/2003JE002205.

Wood, L.J., 2006. Quantitative geomorphology of the Mars Eberswalde delta. Geol. Soc. Am. Bull. 118 (5–6), 557–566. https://doi.org/10.1130/B25822.1.

Zazo, C., Goy, J.L., Dabrio, C.J., Lario, J., González-Delgado, J.A., Bardají, T., Hillaire-Marcel, C., Cabero, A., Ghaleb, B., Borja, F., Silva, P.G., Roquero, E., Soler, V., 2013. Retracing the Quaternary history of sea-level changes in the Spanish Mediterranean–Atlantic coasts: geomorphological and sedimentological approach. Geomorphology 196, 36–49. https://doi.org/10.1016/j.geomorph.2012.10.020.

Zimbelman, J.R., Williams, S.H., Johnston, A.K., Head, J.W., 2004. Lake shorelines: earth analogs for hypothesized Martian coastal features. Lunar and Planetary Science Conference Abstracts. vol. 35 (p#1683).

Zimbelman, J.R., Williams, S.H., Irwin, R.P., Rivera, J.E., Graves, L., Ghatan, G., 2005. Shorelines in the western United States as analogs for hypothesized shoreline features on Mars. Lunar and Planetary Science Conference Abstracts. vol. 36 (p#1733).

Zuber, M.T., Smith, D.E., Solomon, S.C., Muhleman, D.O., Head, J.W., Garvin, J.B., 1992. The Mars Observer laser altimeter investigation. J. Geophys. Res. Planets 97 (E5), 7781–7797. https://doi.org/10.1029/92JE00341.

CHAPTER

6. Morphometry, spatial distribution and origin of sinkhole-like depressions in Kotido Crater

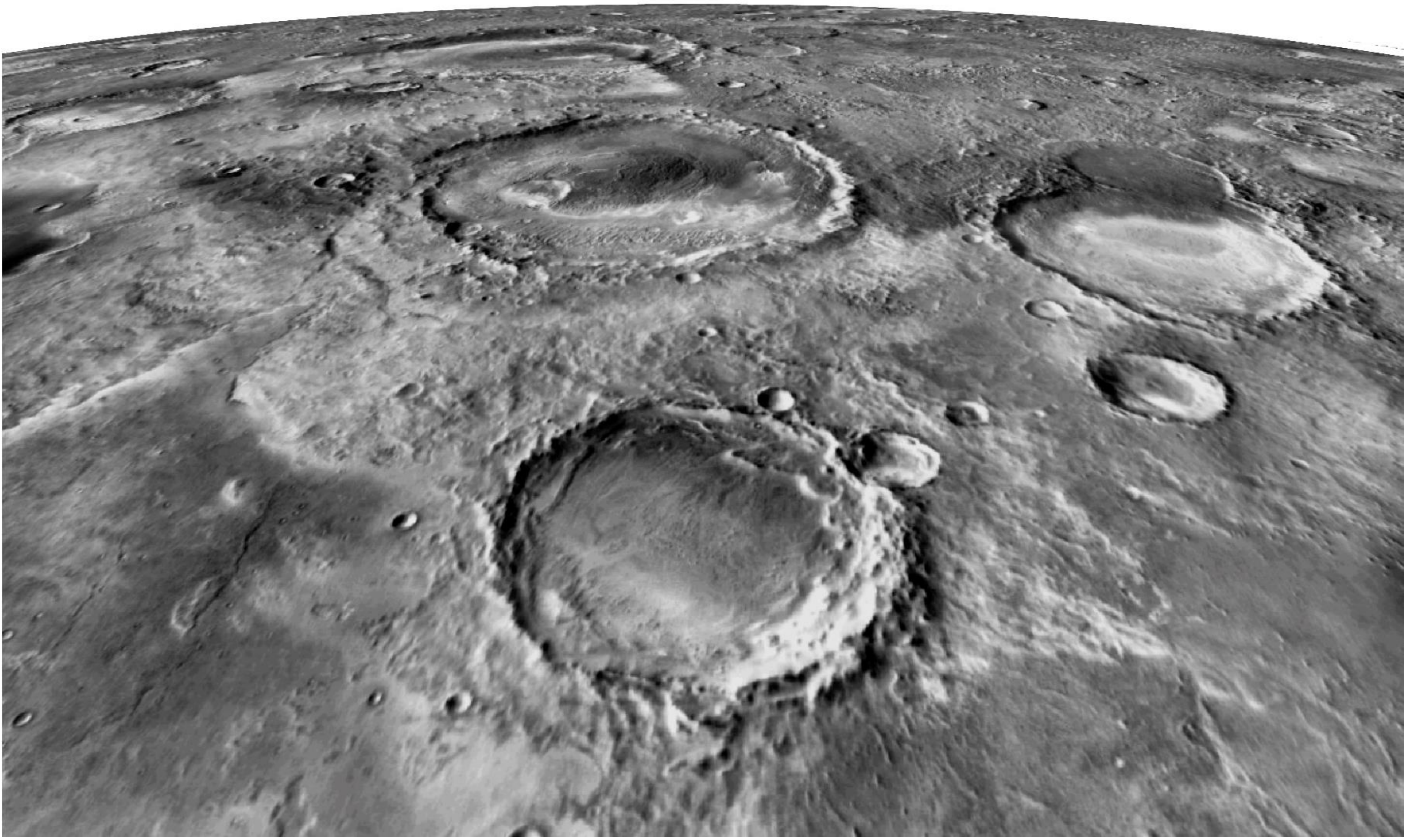

INTRODUCTION AND GOALS

The existence of sinkholes and karst landforms has been hypothesized in many regions of Mars since the first images of the Viking Orbiter became available (Schaeffer, 1990; Kargel et al., 2004; Preuschmann et al., 2006; Wyrick et al., 2004). The Martian surface contains soluble evaporite-bearing formations in numerous regions, as indicated by sulphate minerals detected on the surface from spectral data collected by several spectroscopic instruments onboard different missions (e.g., Bibring et al., 2006; Murchie et al., 2007). A significant number of recent works based on high-resolution images provide strong evidence of the presence of remarkable sinkholes developed on Martian evaporite sediments (e.g. Baioni et al., 2009; Baioni and Wezel, 2010; Flahaut et al., 2015; Baioni and Sgavetti, 2013; Baioni and Tramontana, 2017), which are widely regarded as the main diagnostic surface landform in karst areas (Ford and Williams, 2007). In addition, these landforms are postulated as useful lithological indicators and valuable markers of past paleoclimatic and paleohydrological conditions, since dissolution requires the presence of liquid water.

A number of previous studies related to enclosed depressions on Mars, attributable to the dissolution of evaporitic sediments, provide interpretations that are mainly supported by morphological descriptions and some morphometric parameters. However, to our knowledge, there is a lack of detailed cartographic inventories including comprehensive morphometric and spatial distribution analyses, which may contribute to provide some clues on the geomorphic evolution and origin of this type of depressions.

The Kotido Crater, located in SW Arabia Terra, displays the occurrence of numerous sinkhole-like depressions developed on evaporite-bearing layered deposits, found in a wide range of geomorphic settings in the equatorial belt of Mars (e.g., Okubo et al., 2009; Pondrelli et al., 2019).

In this chapter, we carry out a comprehensive cartographic study, which results are presented in a peer-reviewed scientific paper, consisting of: (1) the detailed mapping of the closed depressions and fractures developed on evaporitic layered deposits within the Kotido Crater; (2) the analysis of their morphometric parameters, and distribution patterns and the spatial relationships with other features; and (3) the interpretation of the morphogenetic processes and controlling factors involved in the development of the depressions.

Icarus 341 (2020) 113680

Contents lists available at ScienceDirect

Icarus

journal homepage: www.elsevier.com/locate/icarus

Closed depressions in Kotido crater, Arabia Terra, Mars. Possible evidence of evaporite dissolution-induced subsidence

Carlotta Parenti[a], Francisco Gutiérrez[b,*], Davide Baioni[c], Ángel García-Arnay[b], Jorge Sevil[b], Erica Luzzi[d]

[a] Dipartimento di Scienze Chimiche e Geologiche, Università degli Studi di Modena e Reggio Emilia, Italy
[b] Departamento de Ciencias de la Tierra, Universidad de Zaragoza, Spain
[c] Dipartimento di Scienze Pure e Applicate, Università degli Studi di Urbino Carlo Bo, Italy
[d] Department of Physics and Earth Sciences, Jacobs University Bremen, Germany

ARTICLE INFO

Keywords:
Sinkholes
Evaporite karst
Aeolian erosion
Frequency-size relationships

ABSTRACT

The identification of karst sinkholes in Mars may provide evidence of dissolution processes caused by liquid water and information on paleoclimatic and paleohydrological conditions. This work presents a comprehensive cartographic inventory of 513 closed depressions developed on evaporite-bearing Equatorial Layered Deposits (ELDs) within Kotido crater, Arabia Terra. Detailed mapping, morphometric analyses and spatial distribution relationships reveal a number of features supporting that the depressions correspond to collapse sinkholes related to evaporite dissolution: (1) suitable topographic and litho-structural conditions for the development of a fracture-controlled epigene evaporite karst; (2) presence of open fissures at the foot of the scarped margins; (3) dimensions and frequency-size distributions comparable with those reported on Earth; (4) spatial association with high-permeability zones (i.e., fractures). Some characteristics of the depressions indicate that they have been re-shaped and enlarged by wind erosion: (1) dominant orientation consistent with the prevalent one-directional winds; (2) differing morphological characteristics on the downwind- and upwind-sides; and (3) nested depressions associated with the upwind sector. The relatively fresh appearance of the depressions and the lack of impact craters suggest a poorly constrained Amazonian karstification phase in the region.

1. Introduction

Unravelling the origin of closed depressions is frequently a challenging geomorphological problem, especially when subsurface data gathered by intrusive and/or non-intrusive methods is not available. The formation of closed depressions may be related to several genetic mechanisms acting individually or in combination (e.g., Waltham, 1989): (1) differential mechanical erosion of the ground surface (e.g., deflation basins); (2) lowering of the ground by preferential surface dissolution at specific locations (e.g., solution sinkholes); (3) accumulation of deposits with an irregular top surface (e.g., moraines, landslides, dunes); (4) explosive activity (e.g., explosion craters); (5) impact of a solid body (e.g., impact craters); and (6) subsidence due to mass and/or volume depletion in the subsurface (e.g., subsidence sinkholes, thermokarst depressions, collapse calderas, sinkholes related to the collapse of lava tubes, compaction/consolidation-related depressions). Mechanisms 4, 5 and 6 involve the deformation of the ground and 4 and 5 are commonly accompanied by the ejection of material.

According to Johnson (2008), four basic conditions are required for evaporite karst development: (1) the presence of soluble evaporitic sediments; (2) a supply of liquid water unsaturated with respect to the evaporitic minerals; (3) an outlet whereby the solution (or brine) can scape; and (4) a gradient causing water to flow through the system. All these conditions can be found on Mars. The Martian surface contains soluble evaporite minerals in numerous regions, as demonstrated by data gathered with instruments of several missions (e.g., Bibring et al., 2006; Murchie et al., 2007). The presence of liquid water at the surface and in the subsurface has been widely demonstrated (e.g., Carr, 2012; Schon et al., 2012; García-Arnay et al., 2018). Suitable subsurface flow conditions can be assured by the presence of permeability features (e.g., fractures) and hydraulic gradients largely governed by the topography. In fact, a number of studies based on the analysis of high-resolution images propose the presence of karst landforms attributable to evaporite dissolution (Grindrod and Balme, 2010; Flahaut et al., 2015; Baioni,

---

* Corresponding author at: Edificio Geológicas, Pedro Cerbuna 12, 50009 Zaragoza, Spain.
E-mail address: fgutier@unizar.es (F. Gutiérrez).

https://doi.org/10.1016/j.icarus.2020.113680
Received 17 May 2019; Received in revised form 15 January 2020; Accepted 28 January 2020

2018 and references therein), notably sinkholes, which are widely regarded as the main diagnostic surface landform in karst areas (Ford and Williams, 2007). These geomorphic features are postulated as useful lithological indicators, and valuable markers of past paleoclimatic and paleohydrological conditions since dissolution requires the presence of liquid water.

The existence of karst landforms and sinkholes have been hypothesized in many regions of Mars since the first images of the Viking Orbiter became available (Schaeffer, 1990; Kargel et al., 2004; Preuschmann et al., 2006; Wyrick et al., 2004). The first account was probably published by Schaeffer (1990), who noted three major localities in the northern plains of Mars (Arcadia Planitia, western Utopia Planitia, and eastern Acidalia Planitia) with "thumbprint" terrain riddled by depressions that could be related to differential solution of extensive carbonate deposits in low-lying areas. In a brief note, Smith et al. (2006) indicated that Mars hosts environments with evaporite sediments favourable for karst development and has a weaker gravitational field that should allow the formation of subsurface cavities larger than those occurring on Earth before their collapse. These authors, using low-resolution imagery identified a number of possible sinkholes in Kasei, Tiu and Simud Valles. Grindrod and Balme (2010) proposed a conceptual hydrogeological model for Hebes Chasma, whereby groundwater flow from the central elevated mound could discharge in the surrounding basin floor, leading to the crystallization of hydrated minerals, in which karst landforms including solution possible dolines have developed. A number of recent works based on high-resolution images provide strong evidence of the presence of sinkholes in Martian evaporite deposits (e.g. Baioni et al., 2009; Baioni and Wezel, 2010; Flahaut et al., 2015). Baioni and Sgavetti (2013) interpreted sinkholes related to evaporite dissolution in the northern Sinus Meridiani region, based on the presence of sulphates indicated by spectral analyses and the morphological and morphometric similarity of the depressions with sinkholes developed on Earth. These authors proposed that the observed variable degree of karst development could be related to variations in the solubility of different lithological units. Baioni and Tramontana (2015) documented putative sinkholes related to dissolution of sulphate-bearing layered deposits in Iani Chaos. Their interpretation was mainly based on the morphological analogy with terrestrial sinkholes and a discard analysis considering other potential genetic mechanisms. The authors suggested that the depressions record a single wet period, probably related to ice melting in the late Amazonian. Similar landforms have been documented in Meridiani Planum (Baioni, 2019), Tyrrhena Terra (Baioni and Tramontana, 2016), Coprates Chasma (Baioni et al., 2011), Tithonium Chasma (Baioni, 2013) and Juventae Chasma (Baioni and Tramontana, 2017). Large closed depressions of the order of kilometres or tens of kilometres long have been also attributed to dissolution-induced subsidence. In an early work, Croft (1989) addressed the controversial origin of the numerous large-volume ($\geq 10^2$ km^3) enclosed depressions (chasmata) associated with the canyons linked to Valles Marineris. The author advocated for a combined karst-tectonic model, involving both collapse induced by structurally controlled dissolution of carbonate rocks and extensional tectonics. Recently, Rodriguez et al. (2016) attributed the origin of the elongated enclosed depressions several tens of kilometres long of Noctis Labyrinthus to collapse processes. These authors explain the subsidence phenomenon by conduit development by structurally-controlled groundwater flow along salt-rich deposits, from the Tharsis volcanic rise towards Valles Marineris. In the bottom of one of the linear troughs of Noctic Labyrinthus, which is underlain by sulphate-bearing light-toned deposits, Baioni (2018) characterised shallow rimless pits mostly tens to hundreds of meters long. The author ascribed these depressions to a relict evaporite karst.

A number of works provide detailed descriptions of enclosed depressions on Mars attributable to the dissolution of evaporitic sediments, generally supported by some morphometric data and selected images. However, to our knowledge, such previous studies lack detailed cartographic inventories and comprehensive morphometric and spatial distribution analyses, which may contribute to infer more robust genetic interpretations. Additionally, most previous works analyse sinkholes individually, without considering their relationships with other landforms that may provide some clues on the origin and morphological evolution. In this work we present a cartographic inventory of closed depressions developed on evaporitic layered deposits in Kotido crater, Arabia Terra. The detailed map, including other features such as fractures and data on wind direction, has been used to extract and analyse morphometric parameters and the spatial distribution of the depressions. The morphometric analyses include the production of frequency-size relationships, which are compared with scaling relationships generated for karst sinkholes on Earth. The resulting qualitative and quantitative data provides the objective basis for discussing the origin and controlling factors of the depressions.

2. Study area

The study area is located in the east-central sector of Kotido crater (cantered at 9.1°W, 1°N), situated in Arabia Terra (Fig. 1). This equatorial region, characterised by a gently sloping topography, represents a gradual transition between the highlands and lowlands of Mars, in contrast with the sharp dichotomy observed in other regions. The Kotido crater is one of the many crater basins that hosts Equatorial Layered Deposits (ELDs). This is the informal term used to collectively designate the light-toned layered deposits found in a wide range of geomorphic settings within the equatorial regions of Mars (e.g., Okubo et al., 2009; Pondrelli et al., 2019). The stratigraphic distribution of the ELDs ranges from the Noachian-Hesperian transition to the lower Hesperian (e.g., Pondrelli et al., 2005), and according to spectral data they include monohydrated and/or polyhydrated sulphates (e.g., Gendrin et al., 2005; Bibring et al., 2006; Mangold et al., 2008). These sulphate-bearing sediments postdate Noachian argillaceous units and are thought to record a major environmental change in the history of Mars (Bibring et al., 2006).

The Kotido crater is a circular topographic basin 40 km across and around 1 km deep, from the rim to the floor. The substratum in which the Kotido crater was formed and that underlies the ELDs is formed by rocks of the "Middle Noachian highland unit" (mNh) (Tanaka et al., 2014). The ELDs correspond to the "Undivided etched unit" ($HnMe_u$) mapped by Hynek and Di Achille (2017) within the crater and in the nearby inter-crater plains. These authors indicate that the surfaces of unit $HnMe_u$ are "tabular to rugged and intensely affected by aeolian erosion". Pondrelli et al. (2019), using the equations of Garvin et al. (2003) and Robbins and Hynek (2013), reconstructed the original geometry of the crater, inferring a rough estimate for the thickness of its sedimentary fill of 1 km. Pondrelli et al. (2019) mapped the ELDs of Kotido crater at 1:20,000 scale, where they show significant variability and good exposure conditions with limited dust cover. They analysed their characteristics (i.e., morphology, texture, composition) and architectural features in order to infer the depositional environment and processes.

The ELDs exposed in Kotido crater consist of interbedded light- and dark-toned deposits, locally with interspersed intermediate-tone mounds (Pondrelli et al., 2019). The light-toned sediments are composed of well-stratified layers or packages of meter-scale thickness forming undulated surfaces. The dark-toned layers are made of more erodible material with smoother texture that tend to occur in topographically lower areas. The attitude of the ELDs of Kotido crater show spatial variations. In the central sector of the crater they mainly lie horizontally or show gentle dips, whereas in the marginal areas are affected by gentle folds.

Pondrelli et al. (2019) reported and illustrated the following morphological features in the layered deposits of Kotido crater: (1) Mounds in lateral continuity with the layered deposits, displaying a rounded depositional geometry, occasionally with an apical pit, and

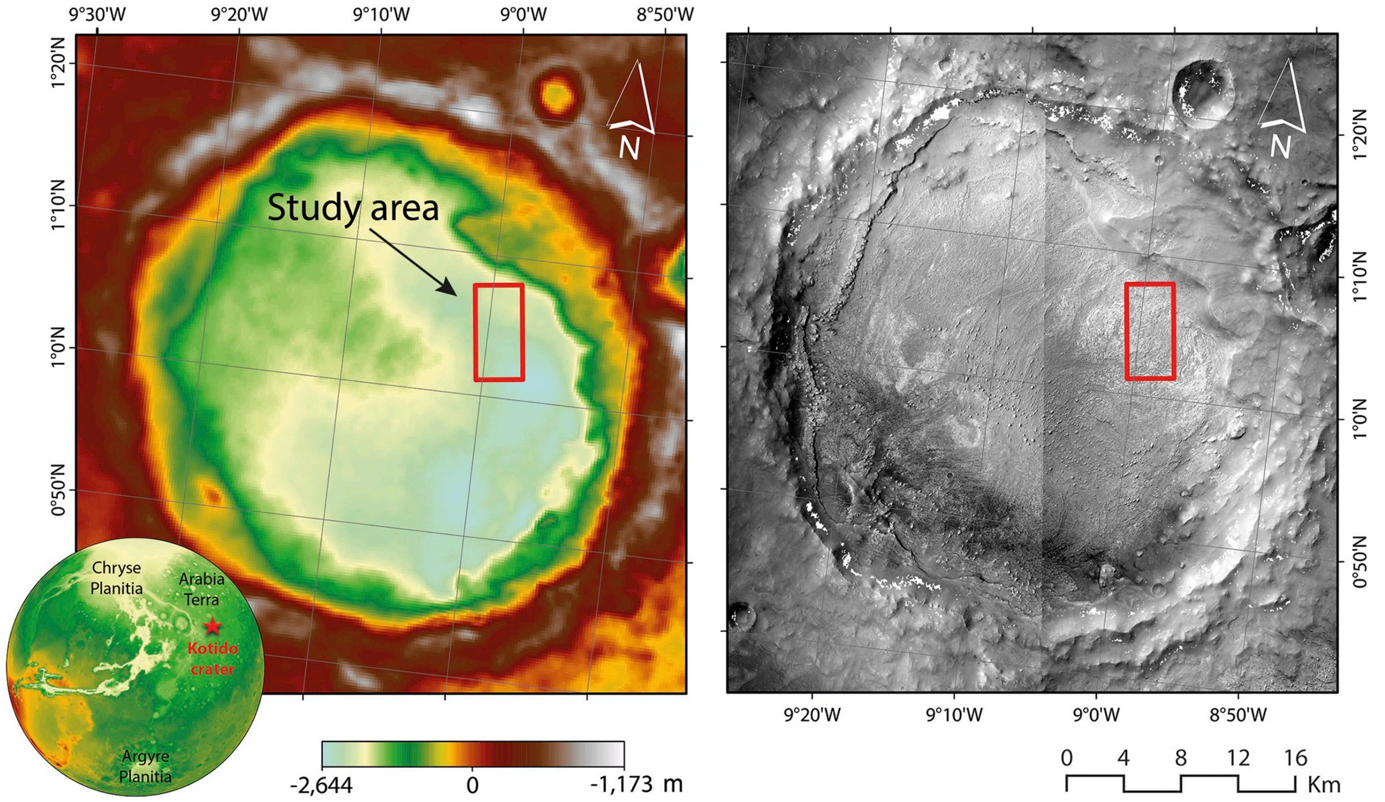

Fig. 1. General position of Kotido crater, Arabia Terra, in the equatorial region of Mars and location of the study area within the floor of Kotido crater, indicated in a DEM (~200 m/pixel) (left) (Fergason et al., 2018) and a CTX image mosaic from images F05_037663_1794 and B18_016776_1818 (right).

commonly forming alignments. (2) Straight to sinuous scarps, mesas, buttes and cuestas controlled by the more resistant horizontal or dipping light-toned beds, acting as caprocks. (3) Elongated yardangs with a prevalent NE trend generated by aeolian erosion. (4) Kilometre-scale linear layered ridges made up of resistant material and locally in spatial association with the mounds. These structurally controlled features are interpreted as fissure ridges formed by the upwelling of material through fractures or faults. According to Pondrelli et al. (2019), these lineaments show a roughly radial or circular distribution, suggesting that they are influenced by fracturing associated with the formation of the impact crater. (5) Numerous closed depressions that riddle the ELDs, which are the focus of this investigation. Regarding these depressions, Pondrelli et al. (2019) indicate that their “characteristics are comparable both in shape and size with dissolution-related morphologies typical, although not exclusive, of evaporite rocks. They also point that “aeolian erosion has been invoked to explain similar morphologies in the etched terrains of Arabia Terra. Pondrelli et al. (2019) interpret that the ELDs of Kotido crater were deposited in a playa-lake environment with spring mounds and fissure ridges fed by salt-rich pressurized groundwater. Sedimentation was characterised by alternating periods of evaporitic (light-toned layers) and fine-grained detrital sedimentation (dark-toned layers). They propose that the gentle dips and antiforms observed in the strata could be related to deposition over an inherited topography (i.e. sediments draping a paleorelief) or post-sedimentary deformation. A similar interpretation was proposed by Pondrelli et al. (2015) for the ELDs occurring inside and around the nearby Firsoff crater. Other authors relate ELDs occurring all over the region to deposition in groundwater discharge areas (Ori and Baliva, 1999; Malin and Edgett, 2000; Rossi et al., 2008; Oehler and Allen, 2008; Pondrelli et al., 2011; Franchi et al., 2014; Luzzi et al., 2018). Andrews-Hanna et al. (2010) proposed that oscillations of the regional groundwater table may have played an important role in the deposition of ELDs.

The ELDs in the mapped sector of Kotido crater are unconformably overlain by dark-toned dune fields, mainly concentrated in topographic lows, and slope deposits with distinctive rockfalls. The latter are typically associated with steep-slopes controlled by resistant light-toned deposits (caprock), including the scarped margins of the closed depressions and residual reliefs.

3. Data and methodology

A sector within the floor of Kotido Crater, covering 21.7 km^2 and underlain by ELDs, was selected for investigating the closed depressions. This area includes numerous depressions with variable geomorphic features and is large enough to perform statistically significant analyses. The landforms were mapped and analysed in a GIS environment (ArcGIS 10.5.1) using the stereo-pair images ESP_016776_1810 and ESP_016921_1810 (0.5 m/pixel) from the High Resolution Imaging Science Experiment (HiRISE) instrument (McEwen et al., 2007) onboard NASA's Mars Reconnaissance Orbiter. A DEM was produced from these stereo pairs (~0.58 m in resolution) by means of ASP (Ames Stereo Pipeline, NASA). It was bundle adjusted to the global topography provided by the MOLA dataset and aligned to HRSC. Spatial data was projected on the coordinate system Mars2000 Equidistant Cylindrical. DEMS generated using the NASA ASP may include non-consistent elevation data along shadowed areas (e.g., inner part of the depression rims) because the stereo correlation in these zones does not capture clear distinctive boundaries easily matched between the stereo-pair images (Watters et al., 2017; Beyer et al., 2018). As a result, the DEM used in the cartographic analysis includes some no-data gaps in these areas, which can be observed in Figs. 1 and 3. Elevation data corresponding to these areas were interpolated in order to minimize their effect in the calculation of volume parameters.

Our mapping was mainly focused on the manual digitizing of the enclosed depressions on the HiRISE images. Automatic mapping using the DEM was discarded since these procedures tend to generate a high proportion of false positives and overlook numerous sinkholes (e.g., Doctor and Young, 2013; De Carvalho-Junior et al., 2014). Eventually, topographic profiles constructed with the DEM aided in the identification and precise mapping of the depression edges. The cartographic inventory includes simple depressions and compound basins resulting from the coalescence of several adjoining depressions. It excludes potential former closed depressions opened by erosion whose mapping would be highly subjective. The geomorphological map also contains other features that may shed some light into genetic processes and controlling factors such as dune fields and the inferred prevalent wind direction, and fractures (Fig. 2).

The map produced, together with the DEM, were used to extract morphometric parameters, analyse frequency-size relationships and perform spatial analyses. The following morphometric parameters were obtained for the depressions: major axis, orientation of major axis, area, elongation ratio, perimeter, circularity ratio, mean elevation of the perimeter, volume, elevation of deepest point and depth. Table 1 includes the definition of these parameters and the procedure used for their measurement. The approximate volume of the depressions was calculated with the polygon volume tool of ArcGIS following the procedure explained in Table 1. However, a null volume was obtained for 29 depressions (<6% of the inventory) of limited area (<550 m^2), probably related to artefacts in the DEM and a small offset between the images used for mapping and the DEM. The volume of these depressions has been indirectly estimated using an exponential regression with a reasonable goodness of fit ($y = 0.0012 \times ^{1.8598}$; $R^2 = 0.689$) that relates the area of the sinkholes smaller than 5000 m^2 and their volume. Table 2 includes maximum, minimum and average values of some of the parameters, as well as the standard deviation. Azimuth data was plotted on rose diagrams with the GeoRose software. The frequency-size relationships of the depressions have been analysed considering their major axis, area and volume and generating best-fit regression functions.

The spatial distribution analysis includes, in addition to qualitative observations, the production of density maps of depressions and fractures, the calculation of the nearest neighbour index (NNI) for the depressions, and the comparison of rose diagrams generated with the orientation of the depressions, fractures and wind direction. Two types of sinkhole density models were generated computing the number of depressions and the proportion of the area occupied by depressions within a search radius. The density model by number was generated with the centroids of the depressions (Feature to Point tool) and applying a uniform Kernel function (Kernel Density tool). The areal density map was generated transforming the depression polygons into raster and then into points (Polygon to Raster and Raster to Point tools) and applying a uniform Kernel function (Kernel Density tool). In both cases, the default search radius was used, calculated specifically to the input dataset using a spatial variant of Silverman's Rule of Thumb that is robust to spatial outliers (i.e., points far away from the rest) (Silverman, 1986). The NNI of the depressions was calculated with their centroids with the Average Nearest Neighbour tool to quantify dispersion versus clustering.

4. Results

4.1. General features and morphometric parameters

The general topography in the investigated sector of Kotido crater is characterised by undulating erosional plains, riddled by numerous closed depressions and locally interrupted by residual reliefs (Fig. 3). The elevation ranges from −3079 m to −2850 m, and its mean elevation is situated around 120 m above the deepest point of the crater floor. The area is underlain by ELDs, showing an alternation of resistant light-toned beds and more erodible dark-toned units. Locally, this stratified material shows gentle dips and open folds. The residual reliefs include prominent steep-sided mesas and buttes capped by resistant beds, as well as some NE-oriented elongated hills with well-defined crests attributable to yardangs (Pondrelli et al., 2019).

The mapped closed depressions show a wide range of morphologies and dimensions. The major axis ranges from 8 m to 342 m (average 55 m) and the area from 44 m^2 to 29,371 m^2 (average 1615 m^2) (Table 2). Some depressions show a subcircular morphology in plan view, however, a significant proportion of them have an elongated shape (Fig. 3). Around 48% and 21% of the depressions have elongation ratios lower than 0.7 and 0.6, respectively. The orientation of the major axis of the depressions show a broad NE prevalent trend; N20-80E (Fig. 4A). The edges of most of the depressions show a continuous trace, whereas some show a rather irregular outline. The perimeter of the depressions varies from 24 m to 1248 m (average 149 m), and the mean circularity ratio is 0.71, with values as low as 0.22 for the depressions with irregular edges (Table 2).

The closed depressions commonly display well-defined scarped edges controlled by resistant light-toned layers. These caprocks form free-face scarps, whereas the underlying more erodible material is generally covered by slope deposits (debris slopes), including distinctive rock-falls. Other depressions have prominent ridge-like edges or poorly defined boundaries (Fig. 3A, B). The floor of the depressions tends to be mantled by dark-toned deposits, mostly dunes, which locally overlap the edges of the depressions. In addition, planar bedrock outcrops occur in the bottom of the depressions. The NE-oriented elongated depressions typically display different morphological features on the opposite ends. The SW edges tend to be sharper and steeper, whereas the NE edges show gentler slopes, seldom with vaguely-defined boundaries. Moreover, the outline of these NE sides tends to be more irregular (Fig. 3A, B, C). Some depressions show a tear-drop morphology, with a subcircular shape interrupted on the NE side by an outward projection (Fig. 3A). The area also includes depressions with smaller nested depressions, typically associated with the SW portion of the larger basin (Fig. 3D).

The depressions are rather shallow with maximum and average depths of 12 m and 2.8 m, respectively. The volume of the depressions, roughly estimated with the DEM, reaches 124.51 m^3, with an average of 3149 m^3. The whole set of inventoried depressions has an aggregate volume of 1615,650 m^3. This value, together with the area of the mapped zone (21,725,412 m^2), yields an average lowering of the ground surface by depression-forming processes of 7.4 cm.

Several depressions show wide-open arcuate fissures along the foot of the scarped edge, with the inner block apparently tilted (toppled) towards the centre of the basin. These features are commonly observed on the western and southwestern edge of the depressions (Fig. 3E, F). Depressions and depression alignments are frequently associated with fractures (Fig. 3B, C). The latter may have a variable expression: (1) low-relief ridges indicative of more resistant material; (2) darker tone lineaments without topographic expression; and (3) linear scarps attributable to differential erosion and/or dip-slip fault displacement.

4.2. Frequency-size relationships

The frequency-size distribution of the 513 mapped depressions has been analysed plotting various morphometric parameters in logarithmic scale (Ma: major axis; A: area; V: volume) against cumulative frequency (Fc; proportion of depressions equal or larger than a given size value) (Fig. 5). The empirical data show a general linear trend in the semi-log graph that can be fitted with a high goodness of fit with logarithmic functions. A higher correlation coefficient is obtained for the major axis and the area (R^2: 0.96) than for the volume (R^2: 0.94), which was measured with significantly lower accuracy, especially for the small depressions (Table 1). The major axis, area and volume data range cover 1.6, 2.8 and 7.5 orders of magnitude, respectively, given by log (maximum value / minimum value) (Table 2). The empirical major axis and area data show a slight deviation from the fitted regressions for the extreme-size values of the distribution (upper and lower cut-offs or truncations). The adjusted relationships predict higher cumulative

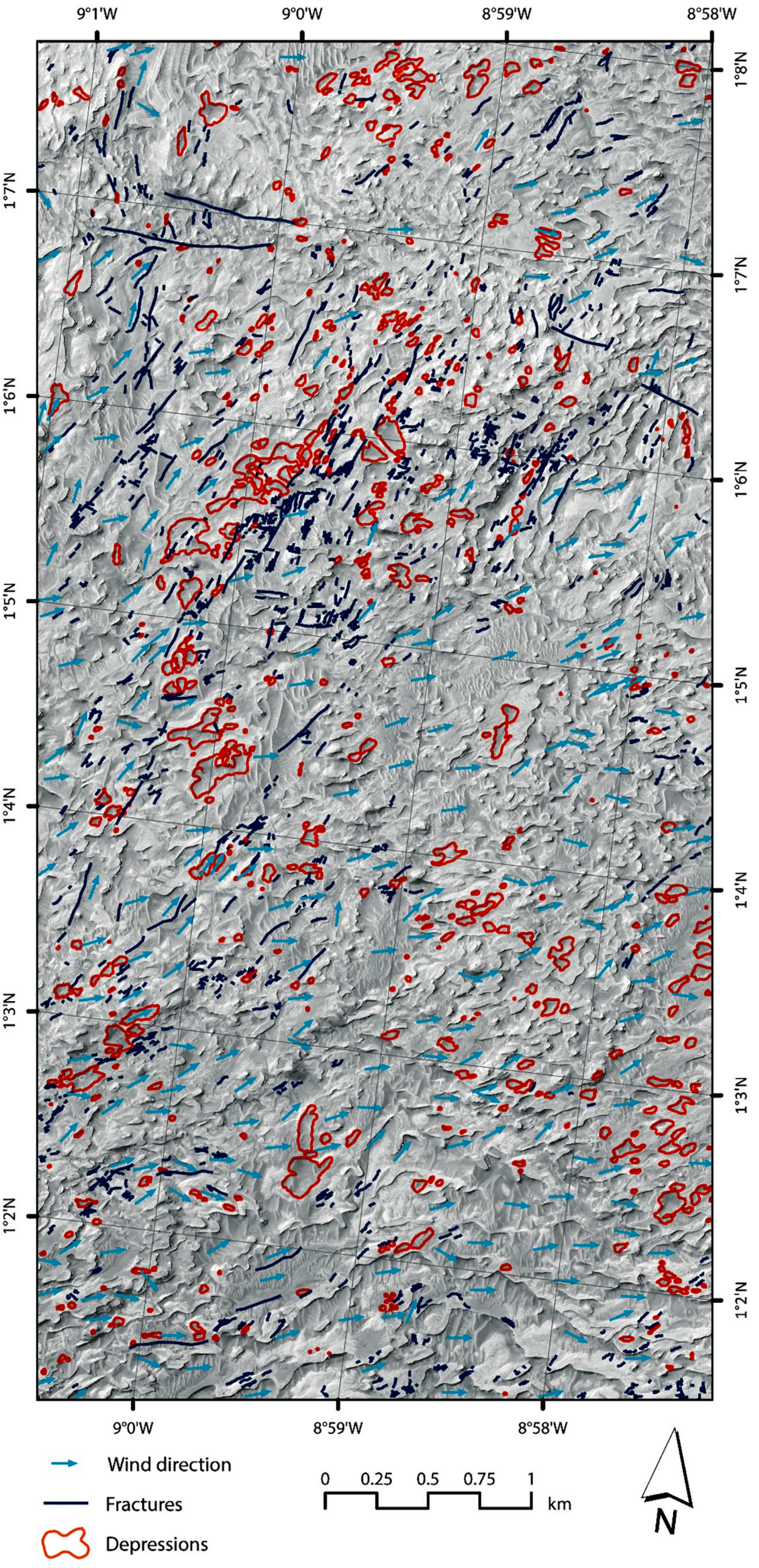

Fig. 2. Geomorphological map of the study area showing the distribution of closed depressions and fractures, as well as the wind-direction vectors inferred from dune fields.

Table 1
Code, brief definition of the morphometric parameters and spatial distribution index of the depressions and procedure used for their measurement.

Parameter	Code	Definition	Procedure
Major axis	Ma	Straight line between most distant points of perimeter. Indicates elongation direction	Longest distance between two vertexes of convex hull polygons generated with the depressions using the Minimum Bounding Geometry tool (Data Management Tools; Features)
Orientation of major axis	OMa	Azimuth of major axis	Attribute calculated automatically by the Minimum Bounding Geometry tool (Data Management Tools; Features)
Elongation ratio	Re	Ratio between the diameter of a circle with the same area as that of the depression and the major axis (Schumm, 1956)	$Re = D/Ma$ Virtual circle diameter given by $D = 2\sqrt{(A/\pi)}$
Area	A	Area enclosed within the mapped edges	Using calculate geometry with the attribute table of the depressions
Perimeter	P	Length of mapped edge	Using calculate geometry with the attribute table of the depressions
Circularity ratio (Rc)	Rc	Ratio between the area of the depression (A) and the area of a circle having a circumference equal to the perimeter of the depression (Miller, 1953)	$Rc = A/Ac$ Circle area given by $P^2/4\pi$
Mean elevation of perimeter	MzP	Average elevation of line that outlines the edge of the depression	(1) Transform 2D shapefile of depressions into a 3D shapefile with z values for the perimeter (3D Analyst Tools, Functional Surface, Interpolate Shape); (2) Obtain mean z value of perimeter (3D Analyst Tools, 3D Features, Add Z Information)
Volume	V	Since the edges of the depressions have a variable elevation, the approximate volume has been estimated calculating the volume of a 3D polygon defined by intersecting the surface of the depressions and a horizontal surface at an elevation given by the mean elevation of the depression perimeter (MPz).	(1) Extract DEM of areas enclosed by the depressions (Spatial Analyst Tools, Extraction, Extract by Mask). (2) Generate contour lines with 2 m interval (Spatial Analyst Tools, Surface, Contour). (3) Generate TIN (triangulated irregular network) of depressions from contour lines (3D Analyst Tools, Data Management, TIN, create TIN). (4) Calculate volume between TIN of depressions and horizontal plane at MPz elevation (3D Analyst Tools, Triangulated Surface, Polygon Volume).
Minimum elevation	Mz	Elevation of deepest point of the depression	Combining the depressions layer and the DEM, the "Zonal Statistics as Table" tool provides the minimum elevation.
Depth	D	Difference between the mean elevation of the perimeter and the elevation of deepest point	$D = MzP - Mz$
Nearest Neighbour Index	NNI	Quantifies the clustering or dispersion of depressions (centroids) within the study area	Ratio between the observed mean distance between each centroid (La) and its nearest neighbour and the expected mean distance for the centroids in a theoretical field with random pattern and the same density ($Le = 0.5/\sqrt{D}$). Average Nearest Neighbour tool (Spatial Statistic Tools; Analysing Patterns)

Table 2
Main values of the morphometric parameters derived from the close depressions inventoried in the study area.

Parameter	Maximum	Minimum	Average	Standard deviation
Major axis (m)	342.33	8.58	55.57	45.90
Elongation ratio	0.96	0.40	0.70	0.11
Area (m^2)	29,371.82	44.23	1615.25	3067.68
Perimeter (m)	1248.75	24.76	149.70	139.07
Circularity ratio	0.99	0.22	0.71	0.17
Volume (m^3)	124,515.21	0.004	3149.42	11,213.36
Depth (m)	12.01	0.01	2.82	2.51

frequency for the small depressions and lower cumulative frequency for the largest ones. These truncations affect to a larger size range for the volume data, particularly for the small-volume depressions that include outliers. It should be noted that the volume of some of the smaller depressions was indirectly estimated with a regression that relates the area and the volume of the depressions.

4.3. Spatial distribution analysis

The relative spatial distribution of the mapped sinkholes can be analysed through the nearest neighbour index (NNI; see formulation in Table 1). This index, extensively used for the characterization of sinkholes (Gutiérrez, 2016 and references therein), quantifies the degree of clustering versus dispersion of features distributed within a particular area and varies from 0 to 2.15 (Clark and Evans, 1954; Williams, 1972). A NNI equal to 2.15 indicates maximum dispersion with uniform hexagonal pattern, 1 indicates perfect random distribution and 0 indicates maximum clustering (virtual sinkhole field in which the centroids of all sinkholes are attached to another). A NNI of 0.82 has been calculated for the study area, with a z-score of −7.52 and a *p*-value of 0.0. This index indicates an overall random distribution with some clustering. Visual inspection of the geomorphological map reveals that the depressions show a clear clustered pattern in some sectors, whereas in other zones sinkholes are very scarce and show a more dispersed distribution (Fig. 2). These patterns can be analysed through the production of sinkhole density models.

A total of 513 sinkholes have been mapped in an area covering 21.7 km^2, yielding a density of 23.6 depressions/km^2. Baioni (2018) estimated a density of 10.4 depressions/km^2 in a putative evaporite karst area of Western Noctis Labrinthus. The value obtained in Kotido crater is probably biased by the selection of a sector with a high number of closed depressions. The inventoried closed depressions, with an aggregate area of 0.83 km^2, have an areal density of 3.8%. Note that this is the percentage of the area covered by closed depressions, and excludes open former enclosed depressions. The spatially-distributed density models of depressions by number and area show very similar patterns (Fig. 6A, B). These maps highlight the areas with higher number of depressions or

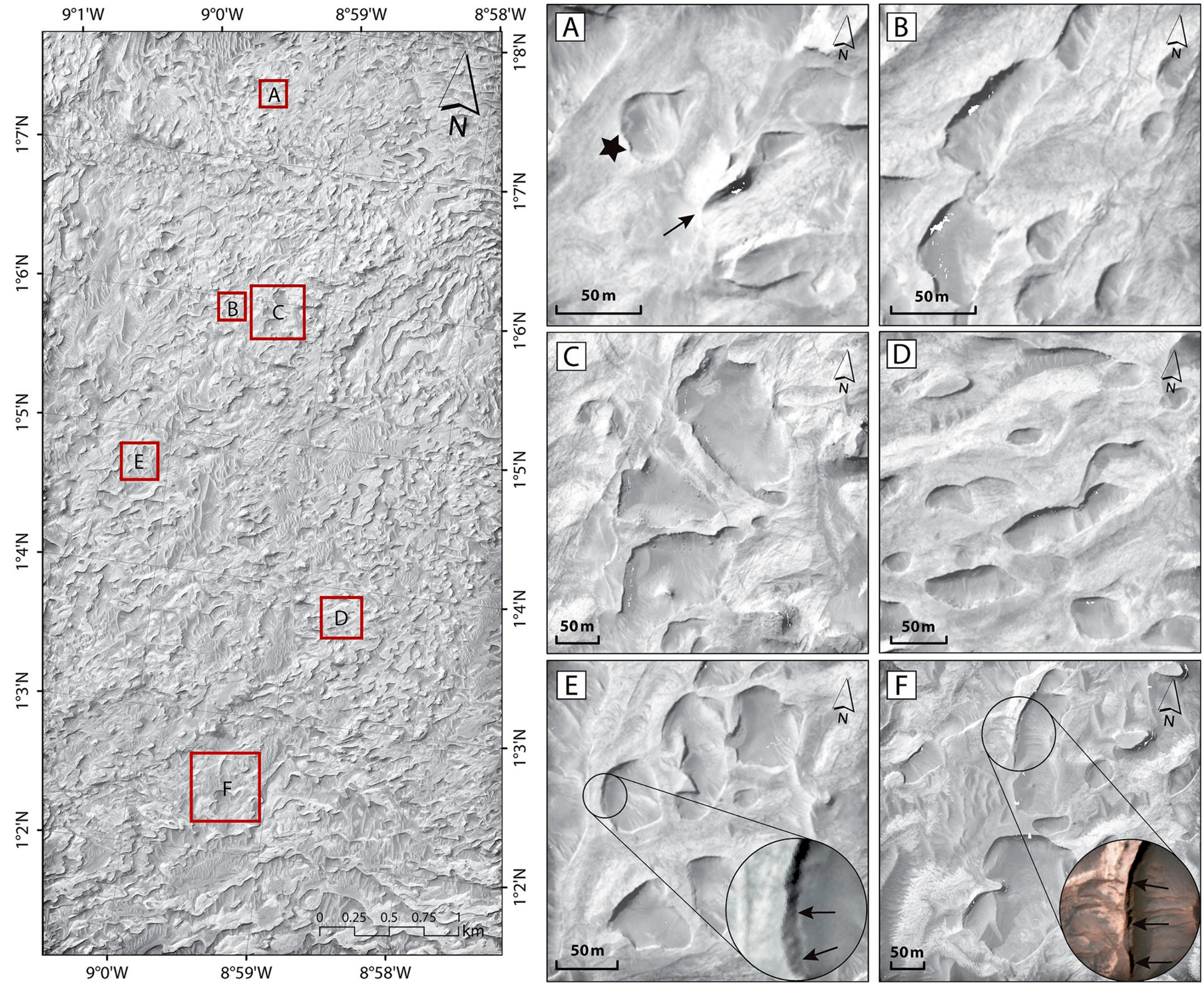

Fig. 3. HiRISE images (ESP_016776_1810 and ESP_016921_1810) illustrating some of the main features of the study area and the mapped closed depressions. A: Elongated depressions with a broader and steeper SW side and a pointed and a gentler NE edge (star). Sharp-crested NE-oriented ridge attributable to a yardang (arrow). B: Aligned and partially coalesced elongated depressions associated with fractures with a prevalent NNE trend. Note the difference between the gentler NE and steeper SW sides of the depressions and the prominent ridge-like morphology of some edges. C: Composite depressions with scarped edges developed on fractured light-toned resistant layers. The floor of the depressions is largely mantled by aeolian deposits a scattered fallen blocks. D: Elongated scarp-edged depressions some of them with stepped floors and nested basins associated with the SW sector. E and F: Depressions with fissures at the foot of the marginal scarps indicative of ground deformation. Butte capped by a resistant layer in the NE corner of the image. Inset images show enlarged fissures. Inset in Fig. F corresponds to a RGB image.

depression coverage, and their comparison allow identifying zones with few but large sinkholes or with many but small depressions. Both models, as well as the geomorphological map, show an uneven sinkhole distribution, with similar areas characterised by high density by number (>34 depressions/km^2) and area (>23%), and relatively large zones with very low density (<8 depressions/km^2 and < 2%). Grossly, the high density zones include a NNE oriented belt located in the NW half of the study area and a shorter NW-SE oriented band in the SE quadrant.

A total of 1341 fractures have been mapped, ranging in length from 4.7 to 835 m, and with an average length of 46.7 m (Fig. 2). The orientation of the fractures shows a clear unimodal distribution, with a preferred NNE-SSW trend; N10–50E (Fig. 4B). A Kernel fracture density model, which expresses the number of fractures by area, shows some high fracture density zones in the northern and western sectors (>6.98 fractures/km^2) of the study area and a very low density zone in the SE quadrant (<0.96 fractures/km^2) (Fig. 6C). The comparison of the density models of depressions and fractures indicate both some spatial correlation in the NE half of the study area and the opposite in the SE quadrant, with high depression density and very low fracture density.

A total of 250 dune fields have been mapped in the study area (not shown in the geomorphological map). The wind direction has been inferred for each of them on the basis of the orientation of the crest of transverse dunes and the position of the steeper downwind side of the dunes (Figs. 2, 4C). The distribution of the wind vectors shows a well-defined ENE-directed wind (N60–80E).

5. Discussion

The cartographic, morphometric and spatial distribution analyses carried out with the 513 depressions inventoried in the selected zone of Kotido crater, covering 21.7 km^2, provide a comprehensive basis for the characterization of these landforms associated with ELDs, and for discussing their potential origin. Several lines of evidence concurrently point to evaporite-dissolution subsidence as a likely genetic mechanism,

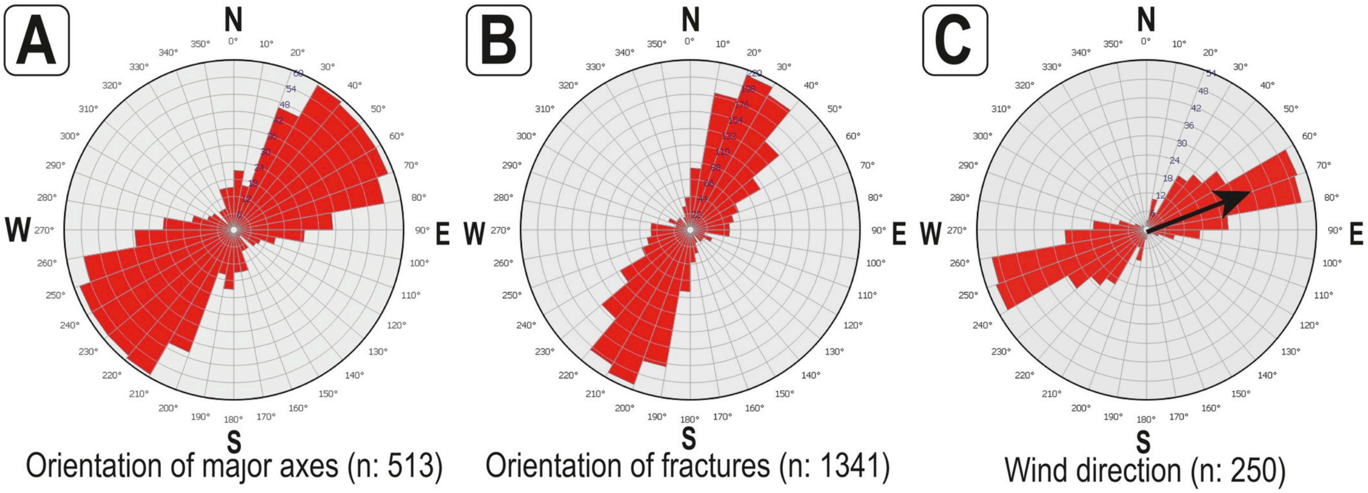

Orientation of major axes (n: 513)

Orientation of fractures (n: 1341)

Wind direction (n: 250)

Fig. 4. Rose diagrams showing the distribution of the orientation of the major axis of the depressions (A) and the fractures (B), and the wind directions inferred from fields of transverse dunes (C). (n: number of data). (For interpretation of the references to colour in this figure legend, the reader is referred to the web version of this article.)

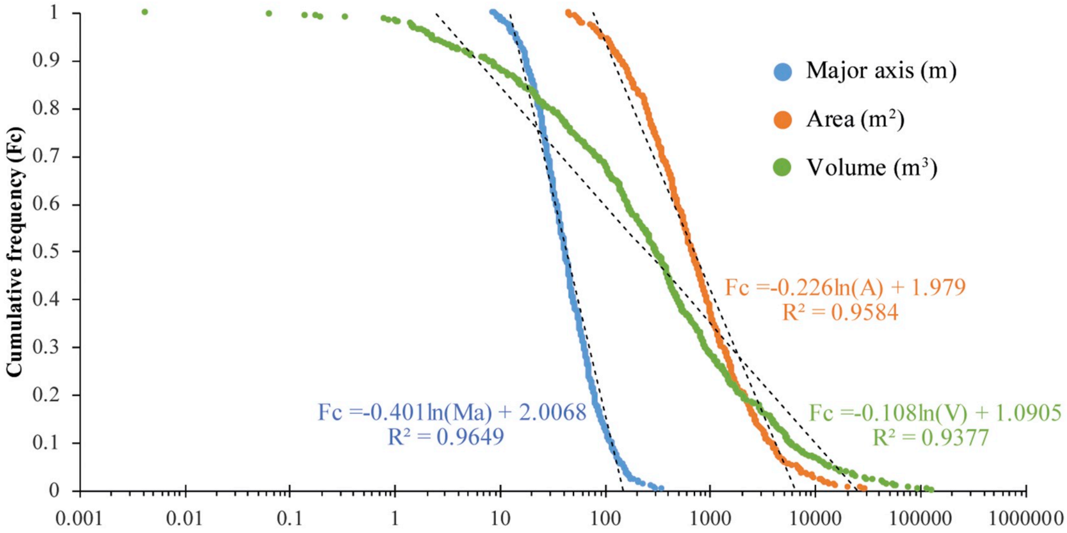

Fig. 5. Semi-log graphs of cumulative frequency (Fc) versus major axis (Ma), area (A), and volume (V) of the closed depressions, and best-fit regressions functions (dashed lines).

which entails subsurface dissolution by liquid water and subsidence of the overlying undermined sediments (Waltham et al., 2005; Gutiérrez and Cooper, 2013; Gutiérrez et al., 2014):

- Spectral data indicate that the ELDs include soluble hydrated sulphates (Gendrin et al., 2005; Bibring et al., 2006; Mangold et al., 2008). Consistently, the layered deposits of Kotido crater have been interpreted as evaporitic sediments formed in a playa-lake environment fed by salt-rich groundwater rising from a confined aquifer (artesian flow), preferentially along fractures (Pondrelli et al., 2019). These data strongly suggest that the area is underlain by a suitable substratum for the development of karts features; i.e., fractured evaporites.
- Some depressions display open fissures along the foot of the scarped edges, with the downthrown side apparently toppled towards the centre of the depression (Fig. 3E, F). These surface ruptures provide evidence of ground deformation related to mass depletion in the subsurface, attributable to the development of dissolution cavities and the collapse of the roof material. These extensional fissures are commonly found along the edge of the bottom of collapse sinkholes developed in karst rocks, and especially in evaporites, characterised by a more ductile rheology. The evaporitic sediments underlain by a cavity tend to bend downwards (sagging), experiencing centripetal contraction. The radial shortening is counterbalanced by the development of annular extensional fissures at the margins associated with the collapse ring faults (e.g., Gutiérrez et al., 2008; Gutiérrez, 2016). Fig. 7A, B shows examples of comparable fissures at the foot of the marginal scarps of collapse sinkholes developed on well-bedded sub-horizontal evaporites deposited in a playa-lake environment in the Ebro Cenozoic Basin, NE Spain (Gutiérrez et al., 2005).
- The inventoried depressions of Kotido crater display morphologic and morphometric characteristics comparable to those reported for other enclosed depressions on Mars attributed to dissolution, such as Tithonium Chasma (Baioni and Wezel, 2010; Baioni and Sgavetti, 2013), Coprates Chasma (Baioni et al., 2011), Hebes Chasma (Grindrod and Balme, 2010), Sinus Meridiani (Baioni and Sgavetti, 2013; Flahaut et al., 2015), Iani Chaos (Baioni and Tramontana, 2015), Tyrrhena Terra (Baioni and Tramontana, 2016), Western

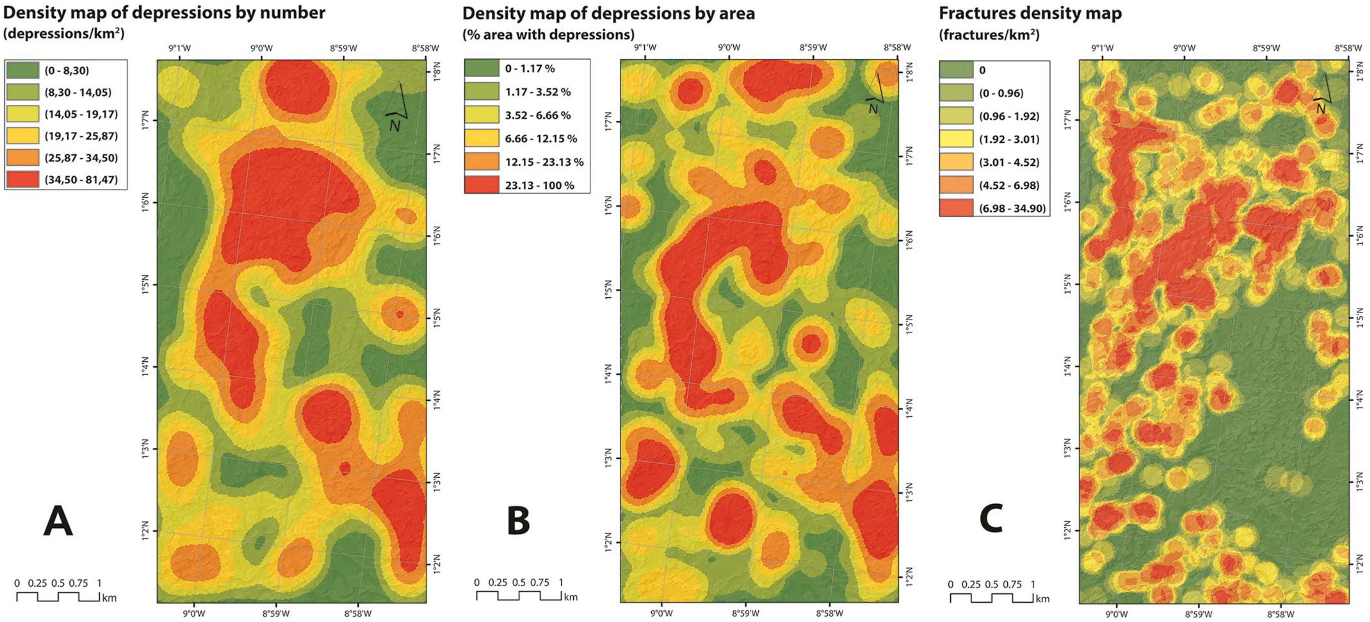

Fig. 6. Kernel density models of depressions by area (A) and number (B) and of fractures (C).

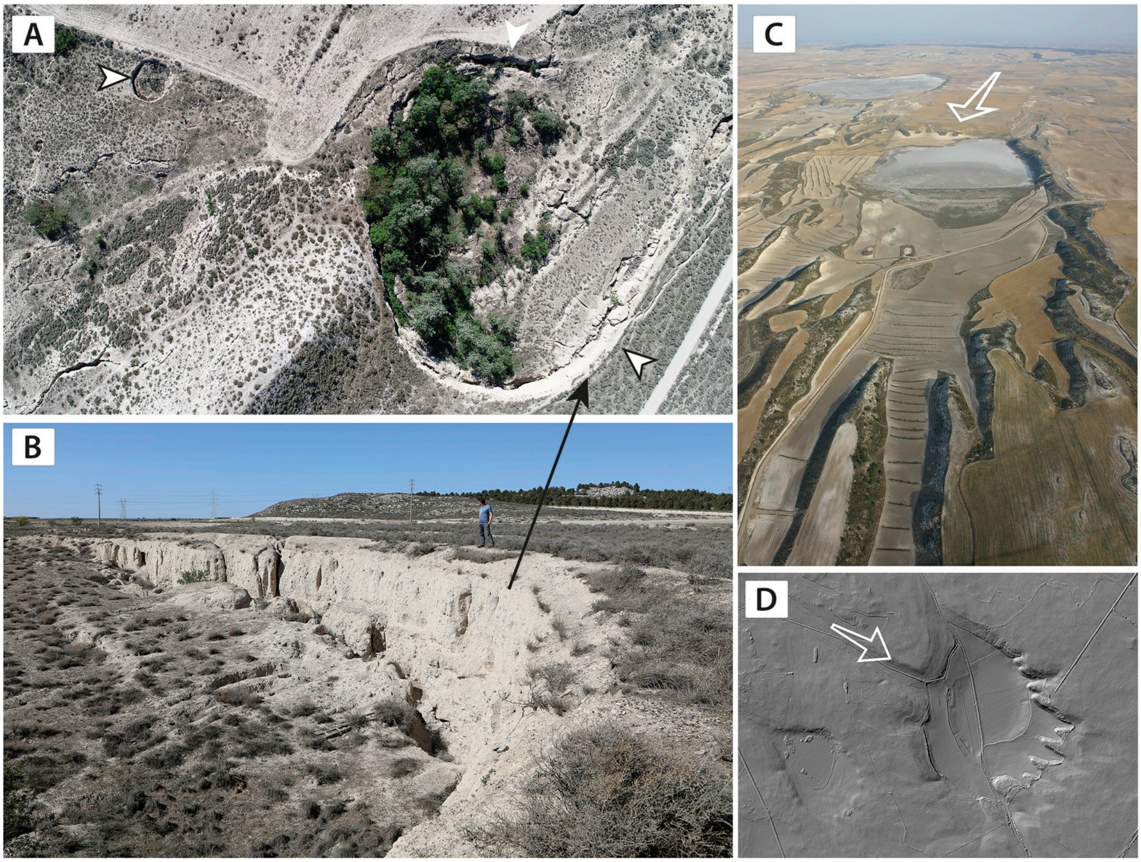

Fig. 7. Images of sinkholes developed on horizontally lying Tertiary evaporites in the Ebro Basin, NE Spain. A: Vertical view of collapse sinkholes with open fissures at the foot of the scarped margins (white arrows). The large sinkhole with tree vegetation is 85 m long and is centred at 41°38.810′N 0°45.501′W. B: Field view of a scarped margin with an open fissure. C: Sinkhole developed on gypsum strata re-shaped by aeolian erosion. Note the irregular downwind edge with wind-fluted yardangs. Arrow indicates prevalent wind direction. The playa-lake in the foreground is centered at 41°24.760′N 0°9.086′W. D: Shaded relief model of a sinkhole with digitated donwwind edge and a nested depression associated with the upwind sector of the basin. Arrow indicates wind direction. Depression centred at 41°24.183′N 0°4.717′W.

Noctis Labyrinthus (Baioni, 2018), and other regions (McKay and Nedell, 1988; Schaeffer, 1990; Spencer and Fanale, 1990).

- Some morphometric parameters of the depressions, such as the major axis (8–342 m), the area (44–29,371 m^2), the volume (average 3149 m^3), and the depth (average 2.8 m), are comparable with the broad range of values documented for sinkholes on Earth. A summary table with morphometric data can be found in Baioni (2018) although these metrics have a limited diagnostic meaning. Nonetheless, the large number of depressions mapped in Kotido crater offers the opportunity to generate statistically significant frequency-size relationships and comparing them with those produced with datasets of karst sinkholes from different karst settings on Earth (i.e., evaporites and carbonates, mantled and interstratal karst, epigene and hypogene karst). In the case of Kotido crater, the best fit between different size parameters (major axis, area, and volume) and their cumulative frequency is obtained with logarithmic functions ($R^2 \geq 0.94$) (Fig. 5). Similarly, regressions generated with the major axis of sinkholes on Earth developed in: (1) a limestone karst mantled by a thin alluvial cover (Val d'Orleans, France; Gombert et al., 2015); (2) a limestone karst mantled by a thick cohesive cover (Hamedan plains, Iran; Taheri et al., 2015); (3) a salt karst with a residual caprock (Gotvand salt pillow, Iran; Gutiérrez and Lizaga, 2016); (4) an epigene evaporite karst with both caprocks and covers (Fluvia valley, NE Spain; Gutiérrez et al., 2016); and (5) a hypogene interstratal evaporite karst (Sant Miquel valley, NE Spain; Gutiérrez et al., 2019), also show a high correlation ($R^2 \geq 0.92$) between the empirical data and logarithmic functions (Fig. 8). The variable slopes and size distributions of those datasets from different settings are attributed to factors such as the nature, thickness and mechanical strength of the cavity-roof materials (Gutiérrez et al., 2019). Corral and González (2019), using large datasets of karst depressions from the limestone karsts of Kentucky and Florida, and the mantled salt karst of the Dead Sea, obtained better fits with log-normal distributions. However, most of the depressions from Florida and Kentucky are not subsidence sinkholes, but solution sinkholes, and a great part of the depressions inventoried in the Dead Sea are uvalas (i.e., compound sinkholes). In Kotido crater and in the different areas on Earth indicated above, there is typically a deviation between the empirical data and the regressions for extreme-size values. The upper tail (small-size values), with lower empirical frequencies, is generally attributed to the incompleteness of the inventories and to mechanical thresholds. The first factor, typically related to lack of resolution of the remote-sensed data, presence of vegetation and human activity (e.g., anthropogenic filling), does not seem to be applicable to Kotido crater. The lower tail (large-size values), with higher observed frequencies, can be attributed to the coalescence of depressions (e.g., Corral and González, 2019; Gutiérrez et al., 2019). The process of coalescence involves a reduction in the number of depressions and an abrupt increase in the size of some depressions, which may plot as outliers. Overall, the depressions of Kotido crater show larger dimensions than those mapped in epigene evaporite karst terrains on Earth, showing a striking parallelism with those of the Gotvand salt karst of Iran (Fig. 8). Potential collapse sinkholes on Mars should attain larger dimensions than on Earth under equivalent geometrical and mechanical conditions, given the lower gravitational acceleration (3.7 ms^{-2} versus 9.8 ms^{-2}) (Smith et al., 2006). For instance, a cylindrical cavity roof (i.e., flat ceiling) on Mars should have a diameter 1.6 times larger than that on Earth with the same weight. Moreover, as explained below, the depressions of Kotido crater seem to have been significantly reshaped and enlarged by long-sustained erosion.
- The orientation of the major axis of the elongated depressions show a broad prevalent N20-80E trend. This range covers the dominant orientation of the 1341 mapped factures (N10–50) and the wind direction inferred from the 250 mapped dune fields (N60–80E) (Fig. 4). The depressions tend to occur spatially associated with fractures (Fig. 3B, C) and the highest density of depressions concurs with the zone showing the highest density of fractures (Fig. 6). These data support that the fracture system has played a significant role on the development and distribution of the depressions. In karst systems, fractures are major elements controlling the formation of subsurface cavities and the associated collapse sinkholes. These discontinuities provide preferential pathways for groundwater flow, which enlarge by dissolution through a self-accelerating process (e.g., Dreybrodt and Gabrovsek, 2004; Ford and Williams, 2007; Palmer, 2007). They also contribute to reduce the rock-mass strength, favouring the collapse of cavity roofs. For instance, Dogan and Ozel (2005) found a good correlation between the distribution and orientation of collapse sinkholes in the epigene gypsum karst of Sivas, Turkey, and the fracture system. Another striking example is given by the high density of collapse sinkholes (ring of cenotes) associated with the margin of the Chicxulub impact crater in

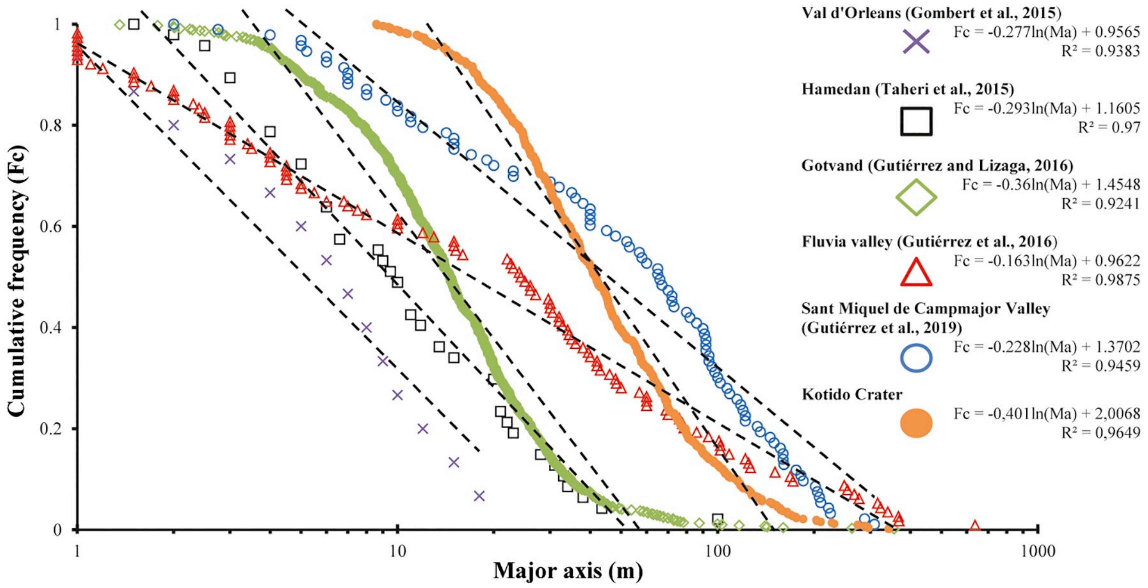

Fig. 8. Frequency-size relationships constructed with the major axis of the depressions mapped in Kotido crater and sinkhole inventories from different karst regions of the Earth. See explanation in the text.

Yucatán, related to the higher degree of fracturing in the carbonate bedrock (Perry et al., 1995).

- Two main karst systems can be differentiated from the speleogenetic perspective: epigene and hypogene (Palmer, 2007; Klimchouk, 2007; Gutiérrez et al., 2019). Epigene systems are characterised by a dominant downward groundwater flow from recharge areas towards a topographically lower discharge zone, controlled by the base level of erosion and the associated water table. In hypogene systems karstification is caused by rising groundwater flows coming from an underlying aquifer, typically under confined conditions (artesian aquifer). According to Pondrelli et al. (2019), the ELDs of Kotido crater were deposited in a playa-lake environment fed by artesian groundwater flows. Significant karstification during this stage was unlikely, since the groundwater was presumably highly mineralized leading to the precipitation of evaporites. However, the layered deposits in which the depressions have been formed are perched around 120 m above the deepest point of the crater. These are adequate topographic conditions for the development of an epigene karst system in the study area, which could be affected by downward groundwater flows towards a topographic base level. In epigene systems karst is generally expressed through widely distributed features such as caves and sinkholes, whereas in hypogene environments those features tend to form dense clusters separated by regions of minimal karst development (Klimchouk, 2003; Frumkin and Fischhendler, 2005; Gutiérrez et al., 2019). The NNI of 0.82 calculated for the depressions of study area, which indicates overall limited clustering of the depressions, is consistent with an epigene environment characterised by karst landforms distributed over the entire investigated zone (Fig. 2).

The depressions display a number of features and spatial relationships strongly suggesting that they have been re-shaped and enlarged by aeolian erosion, probably under the current wind regime. The rose diagram constructed with the wind directions inferred from the dune fields show a prevalent one-directional N60–80 trend (sense of flow), coherent with the NE-oriented yardangs documented in the area (Pondrelli et al., 2019) and the dominant azimuth of the major axes of the depressions (N20-80E) (Fig. 4). Numerous depressions show a markedly asymmetric morphology, with more subdued and irregular edges on the downwind NE edge, where the wind has a higher erosional capability due to flow concentration and higher vorticity (Whitney, 1978) (Fig. 3A, B, C). Moreover, some depressions show a stepped floor with smaller nested depressions typically associated with the SW sector (Fig. 3D). This type of geomorphic arrangement with nested surfaces is frequently observed in the floor of pans generated by aeolian deflation (e.g., Goudie and Wells, 1995). Fig. 7C, D illustrates a comparable situation in the central sector of the Ebro Cenozoic Basin, NE Spain, where sinkholes related to gypsum dissolution show a very irregular downwind edge related to wind erosion and the development of yardangs (Gutiérrez-Elorza et al., 2002). These basins that may host saline ephemeral lakes also show nested depressions associated the upwind sector that record deepening phases attributed to periods with more intense aeolian action (Gutiérrez et al., 2013).

Other hypotheses could be proposed to explain the origin of the closed depressions mapped in Kotido crater. However, the available data tends to either refute them or strongly question their potential validity: (1) Wind erosion: although wind erosion may have played a significant role in the morphological evolution and expansion of the depressions as explained above, it cannot explain the ground deformation features associated with the rims of the depressions, which are indicative of brittle collapse. Moreover, blowout hollows develop by differential deflation on loose dune deposits (Hesp, 2002; Kuznetsov et al., 2005), whereas the analysed depressions formed on over-consolidated layered sediments. (2) Impact craters: these features can be ruled out by the non-circular geometry of the depressions (e.g., Barlow and Bradley, 1990; De Pablo and Komatsu, 2009), with an average elongation ratio of 0.7 (Table 2), and the lack of raised rims and ejecta. Impact craters in which the rims have been removed by backwearing are characterised by parabolic or super-parabolic cross-sections (Forsberg-Taylor et al., 2004; Watters et al., 2015), and the crater walls show a progressive slope decrease towards the bottom of the depression (Craddock et al., 2008). These morphological features are not observed in the depressions of Kotido crater, characterised by flat or stepped floors and steep walls. (3) Volcanic processes: depressions related to volcanic activity and products such as calderas, explosion craters or sinkholes related to the collapse of lava tubes can be confidently ruled out due to the lack of volcanic materials and landforms, the size of the depressions, and their spatial patterns (e.g., Palmer, 2007; Soare et al., 2013; Gutiérrez and Gutiérrez, 2016). (4) Hydrothermal processes: depressions related to the upwelling of groundwater can be ruled out by the aggregate volume of the depressions (ca. 1.6×10^6 m^3), their elongated shape and the lack of features such as vents, rimstones or outflow channels (e.g., Pellicer et al., 2014). (5) Thermokarst: subsidence related to the loss of ground ice by sublimation typically produces depressions with a desiccated regolith in their floor riddled by pockmarks and pits (Soare et al., 2007; Dundas et al., 2015). Moreover, these depressions are typically associated with patterned ground, as documented in the Utopia and western Elysium Planitia, and Astepus Colles regions (Soare and Osinski, 2009). Such landforms are considered to be diagnostic of periglacial activity (Soare et al., 2012).

The closed depressions mapped in the evaporite-bearing ELDs of Kotido crater are likely related to past subsurface dissolution by liquid water and the subsidence of the overlying sediments. The resulting collapse depressions seem to have been reshaped by aeolian erosion, acting more intensively on their NE side, and rock-falls from the scarped margins, both causing enlargement of the depressions and eventually leading to their coalescence. The liquid water responsible for the dissolution may have been derived from the melting of snow and/or ice, including permafrost, as it has been proposed to explain the karst-like landforms found in other regions of Mars (Baioni et al., 2009; Grindrod and Balme, 2010; Jackson et al., 2011; Baioni and Sgavetti, 2013; Flahaut et al., 2015; Baioni and Tramontana, 2016; Baioni, 2018).

Episodic changes in Martian obliquity may explain the origin of the ice and/or snow that melted and generated these putative karst landforms in this equatorial region (Mustard et al., 2001; Laskar et al., 2004). Theoretical considerations about the stability of water ice and numerical climatic simulations predict that accumulation areas of ice and/or snow at the surface may have shifted repeatedly between polar, middle, tropical and equatorial latitudes in response to changes in the Martian axial tilt and atmospheric characteristics in the past (Forget et al., 2006; Madeleine et al., 2009; Wordsworth et al., 2013). According to some simulations, the net ice accumulation rates might have exceeded 20 mm/yr in locations around the Martian equator. Such shifts may have been necessary to achieve the Amazonian environmental conditions, given the current composition of the atmosphere (Madeleine et al., 2009), and other physical conditions (e.g., insolation, atmospheric circulation) in the past (Wordsworth et al., 2013). Moreover, recent retrospective studies have hypothesized the presence of ice in the tropical regions, as well as the presence of ground ice in equatorial zones (Shean, 2010; Mège and Bourgeois, 2011; Gourronc et al., 2014).

Some studies illustrate that impact craters and troughs may function as preferential areas for the accumulation of ice. Their interior behave as cold traps that tend to shield volatile elements from ablative insolation and wind circulation, favouring the preservation of icy bodies that would not persist in open plains. In the craters snow or ice accumulation presumably resulted from concentrated synoptic precipitation (Shean, 2010; Weiz et al., 2013), whichmay have resulted into significant runoff upon melting (Shean, 2010; Grant and Wilson, 2012 Weiz et al., 2013). In fact, in equatorial regions, the melting of rapidly emplaced and localized snow with the albedo of dust is possible for a subset of orbital conditions, even with the weak present-day greenhouse effect (Kite et al., 2011). Moreover, recent works reveal the possibility of the presence of liquid water on the Martian surface in many regions even during the Amazonian epoch (Chapman et al., 2010; Morgan et al., 2011; Soare et al., 2013; Johnsson et al., 2014; de Haas et al., 2015; Salese et al., 2016; Frances et al., 2017; Hargitai and Gulick, 2018).

Regarding the chronology of the depressions, cartographic and geomorphic relationships indicate that they were formed after the deposition of the ELDs, with a poorly constrained early Hesperian age (Pondrelli et al., 2015), and most probably after the erosional phase within Kotido crater that placed the ELDs in a perched position with respect to the deepest zone of the crater. The absence of impact craters supports a young age for the depressions. Moreover, the presence of open marginal fissures suggests recent subsidence activity. It should be taken into account that the depressions are interpreted to be related to two processes that do not necessarily operate concomitantly: subsurface dissolution and collapse (Gutiérrez, 2016). In many regions on Earth, a significant time lag has been documented between the karstification periods and the timing of sinkhole development (e.g., Youssef et al., 2016). The formation of sinkholes may be related to the collapse of cavities formed long time before. Most probably, the subsurface dissolution responsible for the development of the depressions in Kotido crater occurred sometime in the past under climatic conditions different from the present day, and the fissures may be the manifestation of residual subsidence activity related to the presence of relict cavities. The geomorphic appearance of the depressions of Kotido crater (e.g., degradation of margins, infill) suggests a similar or younger age to those observed in other region of Mars ascribed to the early Amazonian (Baioni and Wezel, 2010; Baioni et al., 2011; Baioni and Tramontana, 2016), and appear to be older than others of late Amazonian age (Baioni and Tramontana, 2015; Baioni, 2018).

6. Conclusions

The analysed closed depressions, which developed in the ELDs within Kotido crater are likely related to subsurface dissolution of evaporites and collapse processes (i.e., collapse sinkholes). The development of underground voids and the collapse of cavity roofs is supported by the presence of open fissures at the foot of the scarped margins of some depressions. The dimensions of the depressions, including compound basins related to coalescence, are comparable with those reported for sinkholes on Earth and Mars. Moreover, the cumulative frequency of the major axis of the depressions in Kotido crater follow a logarithmic distribution, like in numerous evaporite and carbonate karst regions of Earth. The apparently larger size of the depressions of Kotido crater, compared with other epigene evaporite karst areas on Earth may be related to the lower gravitational acceleration of Mars. The spatial association between depressions and fractures, and the preferred orientation of the elongated depressions (N20-80E) and the fractures (N10–50E), suggest that both dissolution and subsidence processes were influenced by these permeability and mechanical-weakness features. The topographic conditions, with the area perched >100 m above the deepest zone of the crater, and the overall random distribution of the inventoried depressions (NNI: 0.82), are consistent with an epigene karst in which dissolution was caused by downward groundwater flows. The putative karst depressions seem to have been enlarged and reshaped by long-sustained wind erosion. This is supported by (1) the trend of the one-directional winds (N60–80E) inferred from dune fields, coherent with the orientation of the elongated depressions (N20-80E); (2) the presence of NE-oriented yardangs; and (3) the frequent asymmetry of the depressions, with a more irregular and degraded NE margin and nested depressions associated to the upwind side.

The investigated depressions are most probably relict landforms related to dissolution of evaporites in the past. These may be indicative markers of past paleoclimatic and paleohydrological conditions during which there was significant underground circulation of liquid water, presumably derived from the melting of snow and/or ice. The fissures observed at the margins of some depressions are consistent with residual subsidence activity related to the presence of subsurface cavities formed in the past. The relatively fresh appearance of the depressions, the lack of impact craters, and the comparison with depressions documented in other regions suggest a loosely constrained Amazonian age.

Acknowledgements

This work has been supported by project CGL2017-85045-P (Ministerio de Ciencia, Innovación y Universidades, Gobierno de España).

References

Andrews-Hanna, J.C., Zuber, M.T., Arvidson, R.E., Wiseman, S.M., 2010. Early Mars hydrology: Meridiani playa deposits and the sedimentary record of Arabia Terra. J. Geophys. Res. Planets 115 (E6). https://doi.org/10.1029/2009JE003485.

Baioni, D., 2013. Morphology and geology of an interior layered deposit in the westernTithonium Chasma, Mars. Planet. Space Sci. 89, 140–150. https://doi.org/10.1016/j.pss.2013.09.019.

Baioni, D., 2018. Karst Landforms as Markers of Recent Climate Change on Mars: An Example from a Late Amazonian Epoch Evaporate-Karst within a Trough in Western Noctis Labyrinthus. Recent and Current Landscape Evolution of the Red Planet. Elsevier, Amsterdam, Netherlands, Dynamic Mars, pp. 411–429. https://doi.org/10.1016/B978-0-12-813018-6.00014-5.

Baioni, D., 2019. Very recent karst landforms within Cagli crater, Sinus Meridiani, Mars. Ital. J. Geosci. 138, 262–273. https://doi.org/10.3301/IJG.2019.05.

Baioni, D., Sgavetti, M., 2013. Karst terrains as possible lithologic and stratigraphic markers in northern sinus Meridiani. Mars. Planetary and Space Science 75 (1), 173–181. https://doi.org/10.1016/j.pss.2012.08.011.

Baioni, D., Tramontana, M., 2015. Evaporite karst in three interior layered deposits in Iani Chaos, Mars. Geomorphology 245, 15–22. https://doi.org/10.1016/j.geomorph.2015.05.018.

Baioni, D., Tramontana, M., 2016. Possible karst landforms in two unnamed craters in Tyrrhena Terra, Mars. Planet. Space Sci. 132, 57–65. https://doi.org/10.1016/j.pss.2016.08.011.

Baioni, D., Tramontana, M., 2017. Possible evaporite karst in an interior layered deposit in Juventae Chasma. Mars. International Journal of Speleology 46, 181–189. https://doi.org/10.5038/1827-806X.46.2.2085.

Baioni, D., Wezel, F.C., 2010. Morphology and origin of an evaporitic dome in Tithonium Chasma. Mars. Planetary and Space Science 58, 847–857. https://doi.org/10.1016/j.pss.2010.01.009.

Baioni, D., Zupan, Hajna N., Wezel, F.C., 2009. Karst landforms in a Martian evaporitic dome. Acta Carsologica 38 (1), 9–18. Retrieved from. https://search.proquest.com/docview/869787639?accountid=14795.

Baioni, D., Zupan, H.N., Wezel, F.C., 2011. Karst landforms in an interior layered deposit within Coprates chasma, Mars. Acta Carsologica 40 (3), 473–481. Retrieved from. https://search.proquest.com/docview/1668230512?accountid=14795.

Barlow N. G., Bradley T. L., 1990. Martian impact craters: Dependence of ejecta and interior morphologies on diameter, latitude, and terrain. Icarus, 87, 156–179. doi: doi.org/10.1016/0019-1035(90)90026-6.

Beyer, R.A., Alexandrov, O., McMichael, S., 2018. The Ames stereo pipeline: NASA's open source software for deriving and processing terrain data.Earth and space. Science 5 (9), 537–548.

Bibring, J.P., Langevin, Y., Mustard, J.F., Poulet, F., Arvidson, R., Gendrin, A., Gondet, B., Mangold, N., Pinet, P., Forget, F., the OMEGA team, 2006. Global mineralogical and aqueous Mars history derived from OMEGA/Mars express data. Science 312 (5772), 400–404. https://doi.org/10.1126/science.1122659.

Carr M. H., 2012. The fluvial history of Mars. Philosophical transactions of the Royal Society a: mathematical, Phys. Eng. Sci., 370(1966), 2193–2215. doi: https://doi.org/10.1098/rsta.2011.0500.

Chapman, M.G., Neukum, G., Dumke, A., Michae, G., van Gasselt, S., Kneissl, T., Zuschneid, W., Hauber, E., Mangold, N., 2010. Amazonian geologic history of the Echus Chasma and Kasei Valles system on Mars: new data and interpretations. Earth Planet. Sci. Lett. 294 (3–4), 238–255. https://doi.org/10.1016/j.epsl.2009.11.034.

Clark, P.J., Evans, F.C., 1954. Distance to nearest neighbor as a measure of spatial relationships in populations. Ecology 35 (4), 445–453. https://doi.org/10.2307/1931034.

Corral, Á., González, Á., 2019. Power-law size distributions in geoscience revisited. Earth and Space Science 6. https://doi.org/10.1029/2018EA000479.

Craddock, R. A., Ansan, V., Howard, A. D., Mangold, N., 2008. Crater modification processes in the aeolis region of Mars. In: Lunar and Planetary Science Conference Abstracts, vol. 39. The Woodlands, Texas, p. #1617.

Croft, S.K., 1989. Spelunking on Mars: The carbonate-tectonic hypothesis for the origin of Valles Marineris. In: Watters, T.R., Golombek, M.P. (Eds.), MEVTV Workshop on Tectonic Features on Mars, vols. 89-06, pp. 21–24. Lunar and Planetary Institute Report.

De Carvalho-Junior O. A., Fontes-Guimaraes R., Montgomery D. R., Gillispie A. R., Trancoso-Gomes R. A., de Souza-Martins E., Correira-Silva N., 2014. Karst depression detection using ASTER, ALOS/PRISM and SRTM-derived digital elevation models in the Bambuí Group, Brazil. Remote Sensing, 6, 330–351. doi: https://doi.org/10.3390/rs6010330.

De Haas T., Hauber E., Conway S.J., van Steijn H., Johnsson A., Kleinhans M. G., 2015. Earth-like aqueous debris-flow activity on Mars at high orbital obliquity in the last million years. Nature Communication, 6, 7543. doi: https://doi.org/10.1038/ncomms8543.

De Pablo, M.A., Komatsu, G., 2009. Possible pingo fields in the Utopia basin, Mars: geological and climatical implications. Icarus 199 (1), 49–74. https://doi.org/10.1016/j.icarus.2008.09.007.

Doctor, D.H., Young, J.A., 2013. An evaluation of automated GIS tools for delineating karst sinkholes and closed depressions from 1-meter LIDAR-derived digital elevation data. In: Land, L., Doctor, D.H., Stephenson, J.B. (Eds.), Sinkholes and the Engineering and Environmental Impacts of Karst. National Cave and Karst Research Institute, Carlsbad, pp. 449–458. https://doi.org/10.5038/9780979542275.1156.

Dogan, U., Ozel, S., 2005. Gypsum karst and its evolution east of Hafik (Sivas, Turkey). Geomorphology 71 (3–4), 373–388. https://doi.org/10.1016/j.geomorph.2005.04.009.

Dreybrodt W., Gabrovsek F., 2004. Speleogenesis: computer models. In: Gunn, J. (Ed.). Encyclopedia of Caves and Karst Science. Fitzroy Dearborn, 677–681.

Dundas, C.M., Byrne, S., McEeven, A.S., 2015. Modelling the development of Martian sublimation thermokarst landforms. Icarus 262, 154–169. https://doi.org/10.1016/j.icarus.2015.07.033.

Fergason, R.L., Hare, T.M., Laura, J., 2018. HRSC and MOLA blended digital elevation model at 200m v2, astrogeology PDS annex, U.S. Geological Survey. In: URL. http://bit.ly/HRSC_MOLA_Blend_v0.

Flahaut, J., Carter, J., Poulet, F., Bibring, J.P., van Westrenen, W., Davies, G.R., Murchie, S.L., 2015. Embedded clays and sulfates in Meridiani Planum. Mars. Icarus 248, 269–288. https://doi.org/10.1016/j.icarus.2014.10.046.

Ford D., Williams P., 2007. Karst Hydrogeology and Geomorphology. Wiley, 562.

Forget, F., Haberle, R.M., Montmessin, F., Levrard, B., Head, J.W., 2006. Formation of glaciers on Mars by atmospheric precipitation at high obliquity. Science 311 (5759), 368–371. https://doi.org/10.1126/science.1120335.

Forsberg-Taylor N. K., Howard A. D., Craddock R. A., 2004. Crater degradation in the Martian highlands: Morphometric analysis of the Sinus Sabaeus region and simulation modeling suggest fluvial processes. Journal of Geophysical Research: Planets,109(E5),. doi: 10.1029/2004JE002242.

Frances, E.G., Butcher, G., Balme, M.R., Gallagher, C., Arnold, S.J., Conway, S.J., Hagermann, A., Lewis, S.R., 2017. Recent basal melting of a mid-latitude glacier on Mars. J. Geophys. Res. Planets 122 (12), 2445–2468. https://doi.org/10.1002/2017JE005434.

Franchi, F., Rossi, A., Pondrelli, M., Cavalazzi, B., 2014. Geometry, stratigraphy and evidences for fluid expulsion within Crommelin crater deposits, Arabia Terra, Mars. Planet. Space Sci. 92, 34–48. https://doi.org/10.1016/j.pss.2013.12.013.

Frumkin, A., Fischhendler, I., 2005. Morphometry and distribution of isolated caves as a guide for phreatic and confined paleohydrological conditions. Geomorphology 67. https://doi.org/10.1016/j.geomorph.2004.11.009 (457–451).

García-Arnay, Á., Gutiérrez, F., Fernández, S., 2018. Coastal-Like Features in Nepenthes Mensae, Mars as Paleowater-Level Indicators, and a Terrestrial Analog. In: Lunar and Planetary Science Conference Abstracts, vol. 49. The Woodlands, Texas, p#2595.

Garvin, J.B., Sakimoto, S., Frawley, J.J., 2003. Craters on Mars: Global geometric properties from gridded MOLA topography. In: Sixth international conference on Mars. In: Abstract #3277.

Gendrin, A., Mangold, N., Bibring, J.P., Langevin, Y., Gondet, B., Poulet, F., Bonello, G., Quantin, C., Mustard, J., Arvidson, R., 2005. Sulfates in martian layered terrains: the OMEGA/Mars express view. Science 307 (5715), 1587–1591. https://doi.org/10.1126/science.1109087.

Gombert, P., Orsat, J., Mathon, D., Alboresha, R., Al Heib, M., Deck, O., 2015. Role des efondrements karstiques sur les desordres survenus sur les digues de Loire dans le Val D'Orleans (France). Bull. Eng. Geol. Environ. 74 (1), 125–140. https://doi.org/10.1007/s10064-014-0594-8.

Goudie, A.S., Wells, G.L., 1995. The nature, distribution and formation of pans in arid zones. Earth Sci. Rev. 38 (1), 1–69. https://doi.org/10.1016/0012-8252(94)00066-6.

Gourronc, M., Bourgeois, O., Megè, D., Pochat, S., Bultei, B., Massè, M., Le Deil, L., Le Mouèlic, S., Mercier, D., 2014. One million cubic kilometers of fossil ice in Valles Marineris: relicts of a 3.5 Gy old glacial landsystem along the Martian equator. Geomorphology 204, 235–255. https://doi.org/10.1016/j.geomorph.2013.08.009.

Grant, J.A., Wilson, S.A., 2012. A possible synoptic source of water for alluvial fan formation in southern Margaritifer Terra, Mars. Planet. Space Sci. 72 (1), 44–52. https://doi.org/10.1016/j.pss.2012.05.020.

Grindrod P. M., Balme M. R., 2010. Groundwater processes in Hebes Chasma, Mars. Geophysical Research Letters 37(13), L13202. doi: https://doi.org/10.1029/2010GL044122, 2010.

Gutiérrez, F., 2016. Sinkhole Hazards. Oxford Research Encyclopedia of Natural Hazard Science. Oxford University Press, pp. 1–92. https://doi.org/10.1016/j.toxicon.2016.11.002.

Gutiérrez, F., Cooper, A., 2013. Surface morphology of gypsum karst. Treatise on geomorphology, karst. Geomorphology 6, 425–437. https://doi.org/10.1016/B978-0-12-374739-6.00114-7.

Gutiérrez, F., Gutiérrez, M., 2016. Landforms of the Earth. An illustrated guide. Springer 270. https://doi.org/10.1007/978-3-319-26947-4.

Gutiérrez, F., Lizaga, I., 2016. Sinkholes, collapse structures and large landslides in an active salt dome submerged by a reservoir: the unique case of the Ambal ridge in the Karun River, Zagros Mountains, Iran. Geomorphology 254, 88–103. https://doi.org/10.1016/j.geomorph.2015.11.020.

Gutiérrez, F., Gutiérrez-Elorza, M., Marín, C., Desir, G., Maldonado, C., 2005. Spatial distribution, morphometry and activity of La Puebla de Alfindén sinkhole field in the Ebro river valley (NE Spain): applied aspects for hazard zonation. Environ. Geol. 48 (3), 360–369. https://doi.org/10.1007/s00254-005-1280-8.

Gutiérrez, F., Johnson, K., Cooper, A., 2008. Evaporite karst processes, landforms, and environmental problems. Environ. Geol. 53 (5), 935–936. https://doi.org/10.1007/s00254-007-0715-9.

Gutiérrez, F., Valero-Garcés, B., Desir, G., González-Sampériz, P., Gutiérrez, M., Linares, R., Zarroca, M., Moreno, A., Guerrero, J., Roqué, C., Arnold, L.J., Demuro, M., 2013. Late Holocene evolution of playa lakes in the central sector of the Ebro depression based on geophysical surveys and morpho-stratigraphic analysis of lacustrine terraces. Geomorphology 196, 177–197. https://doi.org/10.1016/j.geomorph.2012.02.013.

Gutiérrez, F., Parise, M., De Waele, J., Jourde, H., 2014. A review on natural and human-induced geohazards and impacts in karst. Earth Sci. Rev. 138, 61–88. https://doi.org/10.1016/j.earscirev.2014.08.002.

Gutiérrez, F., Fabregat, I., Roqué, C., Carbonel, D., Guerrero, J., García-Hermoso, F., Zarroca, M., Linares, M., 2016. Sinkholes and caves related to evaporite dissolution in a stratigraphically and structurally complex setting, Fluvia Valley, eastern Spanish Pyrenees. Geological, geomorphological and environmental implications. Geomorphology 267, 76–97. https://doi.org/10.1016/j.geomorph.2016.05.018.

Gutiérrez, F., Fabregat, I., Roqué, C., Carbonel, D., Zarroca, M., Linares, R., Yechieli, Y., García-Arnay, Á., Sevil, J., 2019. Sinkholes in hypogene versus epigene karst systems, illustrated with the hypogene gypsum karst of the Sant Miquel de Campmajor Valley, NE Spain. Geomorphology 328, 57–78. https://doi.org/10.1016/j.geomorph.2018.12.003.

Gutiérrez-Elorza, M., Desir, G., Gutiérrez-Santolalla, F., 2002. Yardangs in the semiarid central sector of the Ebro depression (NE Spain). Geomorphology 44 (1–2), 155–170. https://doi.org/10.1016/S0169-555X(01)00151-9.

Hargitai, H.I., Gulick, V.C., 2018. Late Amazonian–Aged Channel and island systems located east of Olympus Mons, Mars. In: Mars, D. (Ed.), Recent and Current Landscape Evolution of the Red Planet. Elsevier, Amsterdam, Netherlands, pp. 121–154. https://doi.org/10.1016/B978-0-12-813018-6.00004-2.

Hesp, P., 2002. Foredunes and blowouts: initiation, geomorphology and dynamics. Geomorphology 48 (1–3), 245–268. https://doi.org/10.1016/S0169-555X(02)00184-8.

Hynek, B.M., Di Achille, G., 2017. Geologic map of Meridiani Planum. Mars. US Geological Survey Scientific Investigations Map 3356.

Jackson, M.P.A., Adams, J.B., Dooley, A.R., Montgomery, D.R., 2011. Modelling the collapse of Hebes Chasma, Valles Marineris. Mars. Geological Society of America Bulletin 123 (7–8), 1596–1627. https://doi.org/10.1130/B30307.1.

Johnson, K.S., 2008. Evaporite-karst problems and studies in the USA. Environ. Geol. 53 (5), 937–943. https://doi.org/10.1007/s00254-007-0716-8.

Johnsson, A., Reiss, D., Hauber, E., Hiesinger, H., Zanetti, M., 2014. Evidence for very recent melt-water and debris flow activity in gullies in a young mid-latitude crater on Mars. Icarus 235, 37–54. https://doi.org/10.1016/j.icarus.2014.03.005.

Kargel, J.S., Dougherty, A., Feldman, W., Hogenboom, D., Marion, G., McCarthy, C., Prieto-Ballesteros, O., 2004. Hydrated salts: dehydration, dissolution, and incongruent melting in terrestrial evaporites and at Meridiani Planum, Mars. In: AGU Fall Meeting Abstracts. P21A-0205.

Kite, E.S., Michaels, T.I., Rafkin, S., Manga, M., Dietrich, W.E., 2011. Localized precipitation and runoff on Mars. Journal of Geophysical Research: Planets 116 (E7). https://doi.org/10.1029/2010JE003783.

Klimchouk, A.B., 2003. Conceptualization of speleogenesis in multi-story artesian systems: a model of transverse speleogenesis. Speleogenesis and Evolution of Karst Aquifers 1, 1–18.

Klimchouk A. B., 2007. Hypogene speleogenesis: hydrogeological and morphogenetic perspective. National Cave and Karst Research Institute. Special paper 1, 106.

Kuznetsov I. V., Kuzmin R. O., Greeley R., 2005. Wind-related erosion depressions within a small impact craters in Chryse and Elysium Planitia, Mars. In: Lunar and Planetary Science Conference Abstracts, vol. 36. The Woodlands, Texas, p#1810, DOI: https://doi.org/10.3390/10091074.

Laskar, J., Correia, A.C.M., Gastineau, M., Joutel, F., Levrard, B., Robutel, P., 2004. Long term evolution and chaotic diffusion of the insolation quantities of Mars. Icarus 170 (2), 343–364. https://doi.org/10.1016/j.icarus.2004.04.005.

Luzzi, E., Rossi, A.P., Pozzobon, R., Oehler, D.Z., Etiope, G., 2018. Becquerel crater radial faults: a possible target for methane seepage investigations. Lunar and Planetary Science Conference 49.

Madeleine, J.B., Forget, F., Head, J.W., Levrard, B., Montmessin, F., Millaur, E., 2009. Amazonian northern mid-latitude glaciation on Mars: a proposed climate scenario. Icarus 203 (2), 390–405. https://doi.org/10.1016/j.icarus.2009.04.037.

Malin, M.C., Edgett, K.S., 2000. Sedimentary rocks of early Mars. Science 290 (5498), 1927–1937. https://doi.org/10.1126/science.290.5498.1927.

Mangold, N., Gendrin, A., Gondet, B., LeMouelic, S., Quantin, C., Ansan, V., Bibring, J.P., Langevin, Y., Masson, P., Neukum, G., 2008. Spectral and geological study of the sulfate-rich region of West Candor Chasma, Mars. Icarus 194 (2), 519–543. https://doi.org/10.1016/j.icarus.2007.10.021.

McEwen, A.S., Eliason, E.M., Bergstrom, J.W., Bridges, N.T., Hansen, C.J., Delamere, W. A., Grant, J.A., Gulick, V.C., Herkenhoff, K.E., Keszthelyi, L., Kirk, R.L., Mellon, M.T., Squyres, S.W., Thomas, N., Weitz, C.M., 2007. Mars reconnaissance orbiter's high-resolution imaging science experiment (HiRISE). Journal of Geophysical Research: Planets 112 (E5). https://doi.org/10.1029/2005JE002605.

McKay, C.P., Nedell, S.S., 1988. Are there carbonate deposits in Valles Marineris, Mars? Icarus 73 (1), 142–148. https://doi.org/10.1016/0019-1035(88)90088-7.

Mège, D., Bourgeois, O., 2011. Equatorial glaciations on Mars revealed by gravitational collapse of Valles Marineris wall slope. Earth Planet. Sci. Lett. 310 (3–4), 182–191. https://doi.org/10.1016/j.epsl.2011.08.030.

Miller, V.C., 1953. A quantitative geomorphic study of drainage basin characteristics in the clinch mountain area. In: Technical Report 3. Columbia University, Department of Geology.

Morgan, G.A., Head, J.W., Marchant, D.R., 2011. Preservation of Late Amazonian Mars ice and water-related deposits in a unique crater environment in Noachis Terra: age relationships between lobate debris tongues and gullies. Icarus 211 (1), 347–365. https://doi.org/10.1016/j.icarus.2010.08.004.

Murchie S., Arvidson R., Bedini P., Beisser K., Bibring J. P., Bishop J., Boldt J., Cavender P., Choo T., Clancy R. T., Darlington E. H., Des Marais D., Espiritu R., Fort D., Green R., Guinness E., Hayes J., Hash C., Heffernan K., Hemmler J., Heyler G., Humm D., Hutcheson J., Izenberg N., Lee R., Lees J., Lohr D., Malaret E., Martin T., McGovern J. A., McGuire P., Morris R., Mustard J., Pelkey S., Rhodes E., Robinson M., Roush T., Schaefer E., Seagrave G., Seelos F., Silverglate P., Slavney S., Smith M., Shyong W. J., Strohbehn K., Taylor H., Thompson P., Tossman B., Wirzburger M., Wolff M., 2007. Compact reconnaissance imaging spectrometer for Mars (CRISM) on Mars reconnaissance orbiter (MRO). Journal of Geophysical Research: Planets, 112(E5). doi: https://doi.org/10.1029/2006JE002682.

Mustard, J.F., Cooper, C.D., Rifkin, M.K., 2001. Evidence for recent climate change on Mars from the identification of youthful near-surface ground ice. Nature 412 (6845), 411–414. https://doi.org/10.1038/35086515.

Oehler D. Z., Allen C. C., 2008. Ancient hydrothermal springs in Arabia Terra, Mars. In: Lunar and Planetary Science Conference Abstracts, Vol. 39, p. #1391, DOI: https://doi.org/10.1109/IEMBS.2008.4650211.

Okubo, C.H., Schultz, R.A., Chan, M.A., Komatsu, G., 2009. Deformation band clusters on Mars and implications for subsurface fluid flow. Geol. Soc. Am. Bull. 121 (3–4), 474–482. https://doi.org/10.1130/B26421.1.

Ori G., Baliva A., 1999. Large bulges at the center of impact craters on Mars. In: Lunar and Planetary Science Conference Abstracts, Vol. 30, DOI: https://doi.org/10.1248/yakushi1947.119.11_868.

Palmer, A.N., 2007. Cave geology. Cave Books, Daytom 454.

Pellicer, X.M., Linares, R., Gutiérrez, F., Comas, X., Roqué, C., Carbonel, D., Zarroca, M., Rodríguez, J.A.P., 2014. Morpho-stratigraphic characterization of a tufa mound complex in the Spanish Pyrenees using ground penetrating radar and trenching, implications for studies in Mars. Earth Planet. Sci. Lett. 388, 197–210. https://doi.org/10.1016/j.epsl.2013.11.052.

Perry, E., Marin, L., McClain, J., Velázquez, G., 1995. Rig of cenotes (sinkholes), Northwest Yucatán, Mexico: its hydrogeologic characteristics and possible association wit hthe Chicxulub impact crater. Geology 23 (1), 17–20. https://doi.org/10.1130/0091-7613(1995)023<0017:ROCSNY>2.3.CO;2.

Pondrelli M., Baliva A., Di Lorenzo S., Marinangeli L., Rossi A. P., 2005. Complex evolution of paleolacustrine systems on Mars: an example from the Holden crater. J. Geophys. Res. Planets, 110(E4). doi: https://doi.org/10.1029/2004JE002335.

Pondrelli, M., Rossi, A.P., Ori, G., van Gasselt, S., Praeg, D., Ceramicola, S., 2011. Mud volcanoes in the geologic record of Mars: the case of Firsoff crater. Earth Planet. Sci. Lett. 304 (3–4), 511–519. https://doi.org/10.1016/j.epsl.2011.02.027.

Pondrelli, M., Rossi, A.P., Le Deit, L., Fueten, F., van Gasselt, S., Glamoclija, M., Cavalazzi, B., Hauber, E., Franchi, F., Pozzobon, R., 2015. Equatorial layered deposits in Arabia Terra, Mars: Facies and process variability. Geol. Soc. Am. Bull. 127 (7–8), 1064–1089. https://doi.org/10.1130/B31225.1.

Pondrelli M., Rossi A. P., Le Deit L., Schmidt G. W., Pozzobon R., Hauber E. and Salese F., 2019. Groundwater control and process variability on the equatorial layered deposits of Kotido crater, Mars. J. Geophys. Res. Planets, 124(E3), 779–800. doi: https://doi.org/10.1029/2018JE005656.

Preuschmann S., Benkkert D., Wagner R., Neukum, G., the HRSC Co-Investigator Team, 2006. Karst-like topography within the Ganges Chasma region. Geophys. Res. Abstr., 8: 09383.

Robbins, S., Hynek, B., 2013. Utility of laser altimeter and stereoscopic terrain models: application to Martian craters. Planet. Space Sci. 86, 57–65. https://doi.org/10.1016/j.pss.2013.06.019.

Rodriguez, J.A.P., Zarroca, M., Linares, R., Gulick, V., Weitz, C.M., Yan, J., Fairén, A.G., Miyamoto, H., Platz, T., Baker, V., Kargel, J., Glines, N., Higuchi, K., 2016. Groundwater flow induced collapse and flooding in Noctic Labyrinthus, Mars. Planet. Space Sci. 124, 1–14. https://doi.org/10.1016/j.pss.2015.12.009.

Rossi, A., Neukum, G., Pondrelli, M., Gasselt, S.V., Zegers, T., Hauber, E., Chicarro, A., Foing, B., 2008. Large-scale spring deposits on Mars? J. Geophys. Res. Planets 113 (E8). https://doi.org/10.1029/2007JE003062.

Salese F., Di Achille, G., Neesemann A., Ori G. G., Hauber E., 2016. Hydrological and sedimentary analyses of well-preserved paleofluvial-paleolacustrine systems at moa Valles, Mars. J. Geophys. Res. Planets, 121(2), 194–232. doi: https://doi.org/10.1002/2015JE004891.

Schaeffer, M., 1990. Geochemical evolution of the northern plains of Mars: early hydrosphere, carbonate development and present morphology. J. Geophys. Res. Solid Earth 95 (B9), 14291–14300. https://doi.org/10.1029/JB095iB09p14291.

Schon, S.C., Head, J.W., Fassett, C.I., 2012. An overfilled lacustrine system and progradational delta in Jezero crater, Mars: implications for Noachian climate. Planet. Space Sci 67 (1), 28–45. https://doi.org/10.1016/j.pss.2012.02.003.

Schumm, S.A., 1956. Evolution of drainage systems and slopes in badlands at Perth Amboy, New Jersey. Geol. Soc. Am. Bull. 67 (5), 597–646. https://doi.org/10.1130/0016-7606(1956)67[597:EODSAS]2.0.CO;2.

Shean, D.E., 2010. Candidate ice-rich material within equatorial craters on Mars. Geophys. Res. Lett. 37 (24), L24202 https://doi.org/10.1029/2010GL045181.

Silverman, B.W., 1986. Density Estimation for Statistics and Data Analysis. Chapman & Hall, London.

Smith, Z.E., Tullis, J.A., Steele, K.F., Malfavon, L., 2006. Martian sinkholes: Implications for large scale evaporite deposits. 37th Annual Lunar and Planetary Science Conference.

Soare, R.J., Osinski, G.R., 2009. Stratographical evidence of late Amazonian periglaciation and glaciation in the Astapus Colles region of Mars. Icarus 202 (1), 17–21. https://doi.org/10.1016/j.icarus.2009.02.009.

Soare, R.J., Kargel, J.S., Osinski, G.R., Costard, F., 2007. Thermokarst processes and the origin of crater-rim gullies in utopia and western Elysium Planitia. Icarus 191 (1), 95–112. https://doi.org/10.1016/j.icarus.2007.04.018.

Soare, R.J., Costard, F., Pearce, G.D., Sèjournè, A., 2012. A re-interpretation of the recent stratigraphical history of utopia Planitia, Mars: implications for late-Amazonian periglacial and ice-rich terrain. Planet. Space Sci. 60 (1), 131–139. https://doi.org/10.1016/j.pss.2011.07.007.

Soare, R.L., Conway, S.J., Pearce, G.D., Dohm, J.M., Grindrod, P.M., 2013. Possible crater-based pingos, paleolakes and periglacial landscapes at the high latitudes of utopia Planitia, Mars. Icarus 225 (2), 971–981. https://doi.org/10.1016/j.icarus.2012.08.041.

Spencer, J.R., Fanale, P.F., 1990. New models for the origin of Valles Marineris closed depressions. J. Geophys. Res. 95 (B9), 14301–14313. https://doi.org/10.1029/JB095iB09p14301.

Taheri, K., Gutiérrez, F., Mohseni, H., Raeisi, E., Taheri, M., 2015. Sinkhole susceptibility mapping using the analytical hierarchy process (AHP) and magnitude frequency relationship: a case study in Hamadan province, Iran. Geomorphology 234, 64–79. https://doi.org/10.1016/j.geomorph.2015.01.005.

Tanaka, K., Skinner, J., Dohm, J., Irwin, R., Kolb, E., Fortezzo, C., Platz, T., Michael, G., Hare, T., 2014. Geologic map of Mars. USGS Scientific Investigations Map 3292. https://doi.org/10.3133/sim3292.

Waltham, A.C., 1989. Ground Subsidence. Blackie, Glasgow and London (202 p).

Waltham, T., Bell, F., Culshaw, M., 2005. Sinkholes and Subsidence. Springer, Chichester, p. 382.

Watters, W.A., Geiger, L.M., Fendrock, M., Gibson, R., 2015. Morphometry of small recent impact craters on Mars: size and terrain dependence, short-term modification. J. Geophys. Res. Planets 120 (2), 226–254. https://doi.org/10.1002/2014JE004630.

Watters, W.A., Geiger, L.M., Fendrock, M., Gibson, R., Hundal, C.B., 2017. The role of strength defects in shaping impact crater planforms. Icarus 286, 15–34. https://doi.org/10.1016/j.icarus.2016.12.024.

Weiz, C.M., Bishop, J.L., Grant, J.A., 2013. Gypsum, opal and fluvial channels within a trough of Noctis Labyrinthus, Mars: implications for aqueous activity during the late Hesperian to Amazonian. Planet. Space Sci. 87, 130–145. https://doi.org/10.1016/j.pss.2013.08.007.

Whitney, M.I., 1978. The role of vorticity in developing lineation by wind erosion. Geol. Soc. Am. Bull. 89 (1), 1–18. https://doi.org/10.1130/0016-7606(1978)89<1:TROVID>2.0.CO;2.

Williams, M., 1972. Success and failure in analysis. Primary envy and the fate of the good. J. Anal. Psychol. 17 (1) https://doi.org/10.1111/j.1465-5922.1972.00007.x (7-6).

Wordsworth, R., Forget, F., Millour, E., Head, J.W., Madeleine, J.B., Charnay, B., 2013. Global modelling of the early Martian climate under a denser CO2 atmosphere: water cycle and ice evolution. Icarus 222 (1), 1–19. https://doi.org/10.1016/j.icarus.2012.09.036.

Wyrick, D., Ferril, D.A., Morris, A.P., Colton, S.L., Sims, D.W., 2004. Distribution, morphology, and origin of Martian pit crater chains. J. Geophysical Research 109. E06005.

Youssef, A.M., Al-Harbi, H.M., Gutiérrez, F., Zabramwi, Y.A., Bulkhi, A.B., Zahrani, S.A., Bahamil, A.M., Zahrani, A.J., Otaibi, Z.A., El-Haddad, B.A., 2016. Natural and human-induced sinkhole hazards in Saudi Arabia: distribution, investigation, causes and impacts. Hydrogeol. J. 24 (3), 625–644. https://doi.org/10.1007/s10040-015-1336-0.

CHAPTER

7. Summary, analysis and way forward

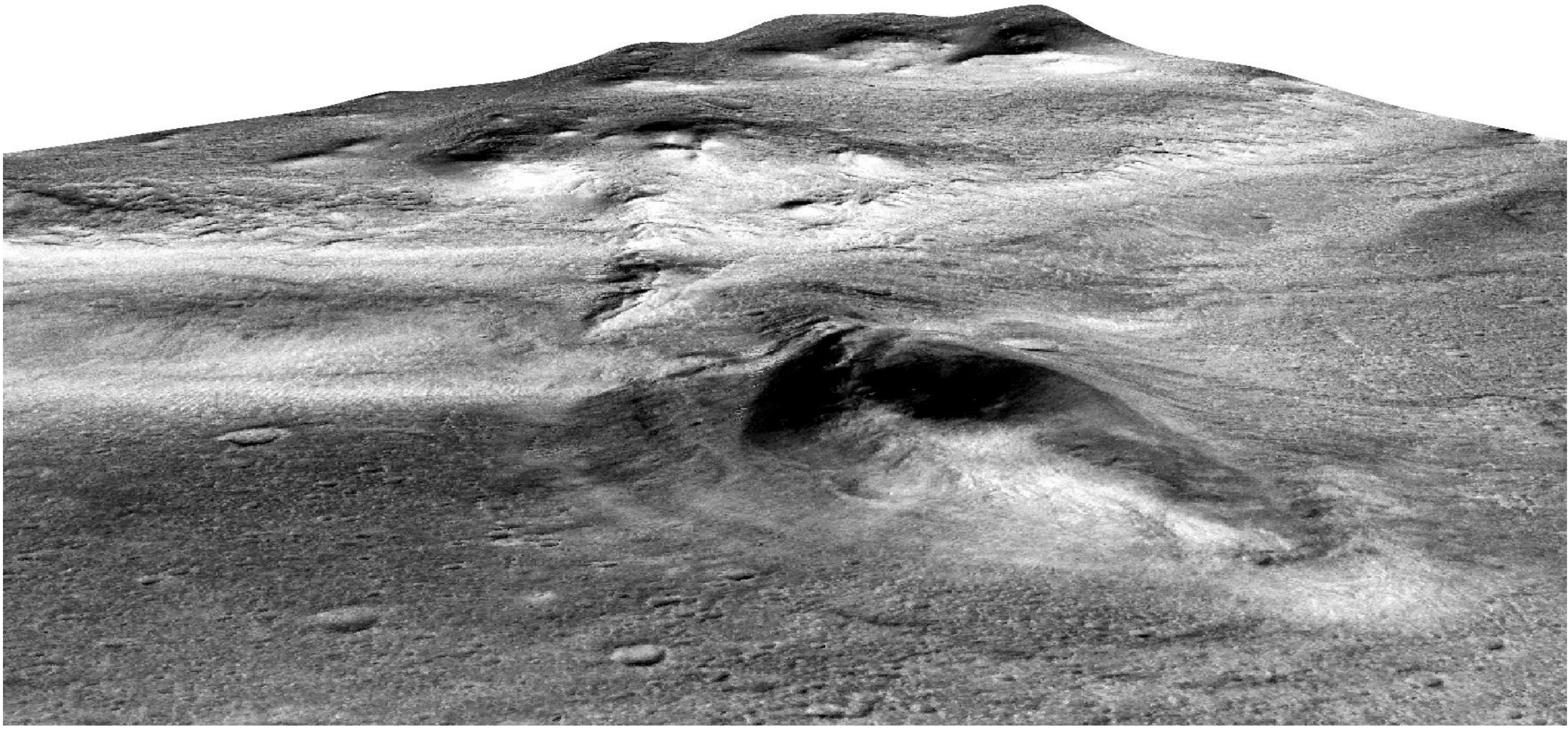

7.1 GEOLOGY ANG GEOMORPHOLOGY OF THE CNTZ

7.1.1 Geological and geomorphological summary

Here, we summarize the key findings presented in Chapter 4 on the different geologic units and geomorphic features mapped in the CNTZ. The geologic-geomorphic map distinguishes 19 geologic units that have been grouped according to their geographic distribution, and depicts the main landforms (see the 1:1.45M map in Annex). The highland province is composed of three units: The two well-differentiated members that comprise the Cimmeria dissected units ($Nhcd_a$ and $Nhcd_b$), and the Cimmeria basin unit (Nhc_b). The documented stratigraphic record of the CNTZ starts in the Early to Middle Noachian with the emplacement of the Cimmeria dissected units that represent the oldest exposed bedrock of this transitional zone. Both members are interpreted as moderately to heavily degraded undifferentiated highland materials related to impact, volcanic, basin-fill, and fluvial processes. These units are characterized by rugged and heavily cratered surfaces (e.g., Tanaka et al., 2005, 2014; Skinner and Tanaka, 2018) dissected by V-shaped valleys exhibiting an orthogonal pattern with a dominant NE-SW orientation and a secondary NW-SE trend near the dichotomy escarpment, most probably controlled by fractures. The widespread occurrence of NW-SE-striking lobate scarps related to thrust faults (e.g., Watters and Robinson, 1999) suggests that these units were affected by NE-SW-oriented tectonic shortening. Lobate scarps often disrupt crater floors and valleys leading to the formation of defeated and beheaded channels. Troughs probably related to extensional deformation occur in the vicinity of the dichotomy escarpment cutting into unit $Nhcd_b$ with a distinctive polygonal pattern with a dominant NW-SE orientation and a secondary NE-SW trend. The Cimmeria basin unit (Nhc_b) is a moderately cratered unit formed during the Late Noachian consisting of slightly to moderately degraded undifferentiated deposits probably related to fluvial, basin-fill and impact processes. This tectonically contracted unit, as suggested by the presence of NW-SE-oriented wrinkle ridges attributed to thrust faults (e.g., Andrews-Hanna, 2020), occurs in depressions inset into member $Nhcd_a$, exhibiting undulating surfaces and absence of channels.

Three units have been recognized in the transitional province north of the dichotomy escarpment, which are described in chronological order of formation: The Nepenthes knobby plateau unit (Ntn_{kp}), corresponding to the inter-crater plateaus with knobby topography of Nepenthes Mensae (e.g., Tanaka et al., 2005), is a moderately cratered unit formed during the Late Noachian. It consists of undifferentiated materials attributed to volcanic and impact products, and mass-wasted deposits forming aprons around residual reliefs (knobs and mesas) carved in materials of unit $Nhcd_b$. The occurrence of NW-SE-trending lobate scarps indicates that this unit has been tectonically contracted with a NE-SW shortening trend. The Nepenthes basin unit ($HNtn_b$) is spatially-linked to the low-lying plains associated with the NW-SE-trending closed depressions that used to host paleolakes (Rivera-Hernández and Palucis, 2019; García-Arnay and Gutiérrez, 2020), as well as with the floors of poorly-preserved impact basins. This unit, formed during the Late Noachian and Early Hesperian, is probably underlain by lacustrine, fluvial, and mass-wasted materials. It displays relatively smooth terrains locally interrupted by residual reliefs, wrinkle ridges, as well as volcano-like features associated with unit ANv_e, such as pitted cones and small tholi. The Nepenthes basin unit ($HNtn_b$) is locally contracted, as indicated by the presence of NW-SE-oriented wrinkle ridges. The youngest unit in the transitional province, formed during Early to Late Hesperian times, is the Nepenthes ridged plain unit (Htn_{rp}) consisting of tectonically contracted materials related to impact, mass-wasting, fluvio-lacustrine and volcanic processes. It occurs in the northeast sector of the mapped area exhibiting low-lying undulating plains with pervasive NW-SE-oriented wrinkle ridges and scattered knobs of unit $Nhcd_b$.

Six locally-distributed units have been identified in the CNTZ: The volcanic edifice and flow units (ANv_e and ANv_f, respectively) are two genetically-linked units emplaced from Late Noachian to Early Amazonian times ascribable to different types of volcanic edifices and high-TI lava fields, respectively. These units crop out in the deepest areas of the chain of closed depressions in Nepenthes Mensae, and locally in the highlands near the dichotomy. The volcanic edifice unit is characterized by pitted cones and small tholi, as well as isolated and coalesced raised fissure vents with sloping, and rugged to smooth surfaces, forming volcanic ridges with weak NE-SW and NW-SE prevalent orientations. The locally-contracted volcanic flow unit exhibits smooth to rugged, poorly-cratered surfaces, often with channels, overlapping lobes, NE-SW-striking wrinkle ridges, as well as NW-SE-aligned yardangs and sinkhole-like depressions with prevalent NW-SE orientation. The fluvial-related units comprise the valley and fan units (HNv and HNf, respectively) formed during the Late Noachian to Late Hesperian. The valley unit is carved into units $Nhcd_a$ and $Nhcd_b$, and rarely into unit Ntn_{kp}, displaying smooth deposits underlying the low-TI valley floors. The fan unit (HNf), which is laterally associated with unit HNv, is related to putative deltas and alluvial fans displaying smooth to corrugated surfaces affected by differential erosion and often with phyllosilicate-bearing outcrops. The landslide unit (ANl), which probably accumulated from the Late Noachian to the Middle Amazonian, consists of large landslides (e.g., rock spreads, slumps and falls) mostly associated with the dichotomy escarpment. This unit is characterized by rugged, rolling, and hummocky terrains. The eolian unit (Ae) consists of dark-tone, barchan and longitudinal dune fields of olivine-bearing sands formed throughout the Amazonian period. These deposits occur near the foot of the dichotomy escarpment indicating a dominant south-directed wind.

Impact craters with variable morphologies and sizes widely occur on the surface of the CNTZ. We have differentiated seven impact crater units depending on the size and preservation degree of the craters: Well-preserved craters with rim diameter between 5 and 13 km were mapped as the crater unit–undivided (AHc_u). In contrast, the preserved morpho-structural components of moderately- to well-preserved impact craters with rim diameter ≥13 km were distinguished as follows: The crater floor unit (AHc_f), the crater peak unit (AHc_p), the crater wall unit (AHc_w), the rim crater unit (AHc_r), and the crater ejecta units including two morpho-facies (units $AHce_a$ and $AHce_b$).

7.1.2 Origin and evolution of the closed depressions and the dichotomy escarpment

A sequence of endogenic and exogenic processes involved in the landscape evolution of the CNTZ focusing on the formation of the chain of closed depressions that used to host large paleolakes and in the evolution of the dichotomy escarpment is proposed here:

The disruption of fluvial valleys (Late Noachian to Late Hesperian in age) in the member a of the Cimmeria dissected unit ($Nhcd_a$) by lobate scarps unaffected by fluvial erosion, as well as the adaptation of some drainages to these compressional features (e.g., deflected fluvial valleys parallel to the toe of lobate scarps) suggest that the phase of NE-SW-oriented tectonic shortening may have started in the Late Noachian and probably ended sometime after the cessation of fluvial activity (Late Hesperian), which is roughly consistent with the global-scale compressional tectonic regime that occurred on Mars between the Late Noachian to Early Hesperian (e.g., Tanaka et al., 1991; Watters, 1993).

The topography of the Cimmeria region in the CNTZ is analogous to that of a large part of the highlands south the dichotomy, which shows a topographically higher sector that gradually descends from the highlands to the northern lowlands and frequently ends abruptly along a major escarpment that represents the dichotomy boundary (Watters and McGovern, 2006). The ca. 2 km high escarpment in the CNTZ defines the boundary between the highland and transitional provinces. The member b of the Cimmeria dissected units ($Nhcd_b$) associated with the dichotomy escarpment shows numerous troughs that control fretted valleys subparallel to the escarpment. The analyzed radargrams indicate that the escarpment and the troughs are related, respectively, to a master and secondary normal faults that dip consistently to the NE indicating a NE-SW extension direction with major geomorphic imprint on the landscape. The activity of these extensional faults probably generated: (1) the plateau situated south of the dichotomy escarpment with down-to-the-north topographic drops associated with secondary normal faults; and (2) the chain of interconnected NW-SE-trending closed depressions located at the foot of the dichotomy escarpment. These basins are probably downthrown blocks (i.e., keystone grabens) nested in the lower part of a larger half-graben morpho-structure (i.e., fault-angle depression), as inferred from the topography and the stratigraphic and structural relationships interpreted from the mapped units and radar reflections. The belt of depressions in Nepenthes Mensae was also attributed to extensional tectonics by Watters (2003a) and Watters and McGovern (2006), with the maximum lithospheric deflection located near the base of the dichotomy escarpment (Watters, 2003a).

Our observations suggest that, regardless of how and when the crustal dichotomy was originated, its current shape in the CNTZ is largely related to (1) dip-slip displacement along a down-to-the-northeast normal fault system that controlled the formation of half-graben basins within this extensional environment in Nepenthes Mensae; and (2) the development of different types of large landslides along the escarpment favored by the large local relief, and probably also by its continuous tectonic rejuvenation and the weakening of the materials by extensional deformation (i.e., faulting, fracturing). The Nepenthes basin unit ($HNtn_b$), which is generally confined to the lower part of the half-graben basins (nested keystone graben) and seems to reach its greatest thickness in the vicinity of the fault-controlled escarpment, was accumulated from the Late Noachian to Early Hesperian based on crater densities. The probable syntectonic deposition of the unit $HNtn_b$ by fluvio-lacustrine and mass-wasting processes suggests that extensional tectonics in the CNTZ was active at least during the Late Noachian to Early Hesperian.

The inferred compressional and extensional tectonic stress fields in the CNTZ, which exhibit the same direction (i.e., NE-SW), seem to have been active sometime from the Late Noachian to Late Hesperian, and probably until more recent epochs, but not simultaneously. Several lines of evidence suggest that the extensional phase postdate the compressional deformation: (1) the compressional structures do not affect to the most recent units; (2) the extensional structures have formed the most recent morpho-structures (e.g., the present-day dichotomy escarpment or the basins in Nepenthes Mensae), as well as the accommodation space in which the units $HNtn_b$ and ANv_f were deposited; and (3) the areas affected by extensional tectonics divide in half those that are tectonically contracted in the highland and transitional provinces. Other authors indicated that the compressional and extensional deformation occurred along the dichotomy boundary in the Eastern Hemisphere from the Late Noachian to Early Hesperian (e.g., McGill and Dimitriou, 1990; Watters and Robinson, 1999; Watters, 2003a, 2003b).

7.2 PALEOHYDROLOGY OF THE CNTZ

7.2.1 Main results of the paleohydrological reconstruction

Here, we summarize the main results presented in Chapters 4 and 5 concerning the paleohydrology in the CNTZ. The NW Terra Cimmeria and SE Nepenthes Mensae show numerous geomorphological and geochemical lines of evidence indicating the fundamental morphogenetic role that the liquid water has played in the configuration of this transitional zone. The watershed of Licus Vallis (NW Terra Cimmeria) occupies a total area of 156,377.80 km^2, representing the largest drainage basin in the study area, according to García-Arnay and Gutiérrez (2020).

The key results of the morphometric analysis carried out by García-Arnay et al. (2018) in the Licus Vallis watershed are the following: (1) The analyzed sector of the drainage basin of Licus Vallis presents a fourth order stream network of V-shaped valleys with a dominant dendritic pattern, suggesting that surface runoff was the main erosional process involved in the formation of the watershed. (2) The mapped streams have a total length of 2999.7 km, with a drainage density of 0.05 km^{-1}, which is a very low value in terms of terrestrial drainage density values (e.g., Carr and Chuang, 1997). (3) The mean bifurcation ratio is 5.2, which is larger than terrestrial values, typically ranging between 2 and 4 (Horton, 1945), suggesting a significant structural control partially related to tectonic activity during the development of the drainage network, as supported by the occurrence of defeated and beheaded channel sections disrupted by lobate scarps. (4) The observed paired terraces and knickpoints seem to support base-level variations in the mouth area of the watershed and/or rejuvenation by vertical tectonic movements (e.g., Goudge and Fassett, 2018). (5) The hypsometric curve indicates that the watershed was relatively young and poorly-developed when the fluvial activity ceased, as is also suggested by its immature topography and non-equilibrium profile. (6) Locally, some valley heads display theatre-like morphologies and lack any evidence of surface runoff, supporting that sapping erosional processes may have played a role in their headward expansion.

In general, the valley networks mapped in the NW Terra Cimmeria (unit HNv), including those of the Licus Vallis watershed, are largely formed by low-ranked V-shaped valleys with linear to sinuous trace and dendritic to trellis pattern, often exhibiting a pattern apparently controlled by lobate scarps, ridge crests and troughs. The channel network in the vicinity of the dichotomy tends to show a rectangular pattern, with channel sections following a dominant NE-SW trend and a secondary NW-SE orientation, probably controlled by fractures.

The majority of these valley networks exhibit moderately preserved fan-shaped deposits at their mouths, most of them interpreted as Gilbert-type deltas and alluvial fans (unit HNf) (e.g., Irwin et al., 2005; de Pablo and Pacifici, 2008; García-Arnay et al., 2018a, 2018b; Rivera-Hernández and Palucis, 2019; García-Arnay and Gutiérrez, 2020). We mapped a total of twentyfour fan-shaped features in the CNTZ (see Table 1 in Chapter 4), of which nine were analyzed in detail by García-Arnay and Gutiérrez (2020). The main results of the morphological and morphometric analyses are: (1) range from ~3.0 to ~85.4 km^2 in area, displaying two well-differentiated parts; low-gradient plains with mean slopes from ~2.3° to ~5.2°, and steep fronts with variable preservation conditions and average gradients from ~3.4° to ~15.8°; (2) in some cases the plains are dissected by small and rather subdued channels; (3) the delta-shape index (S_d) ranges between 0.56 (prolate geometry) and 1.02 (oblate geometry), with values comparable to those of deltas on Earth (e.g., Mikhailova, 2015); (4) most features display visible layering on their fronts, strongly suggesting that they are formed by stratified sediments; (5) the majority of the features have one lobe, whereas some of them exhibit two lobes; and (6) most of the deltas show a steep front with a continuous slope, but some exhibit stepped fronts with benches and slope breaks.

Furthermore, fifty-four coastal-like benches interpreted as paleoshore platforms were mapped along the margins of the depressions and encircling isolated residual reliefs within the depressions (García-Arnay and Gutiérrez, 2020). These landforms that probably developed by coastal erosion along paleoshorelines at different water-level elevations display smooth, subhorizontal or gently-sloping surfaces with lateral continuity, elevation consistency, and steep slopes associated with their lakeward edges. The relationship between the coastal-like benches and putative deltas is analyzed on the basis of their elevation values and relative spatial distribution. In particular, elevation values yield mean elevations of -1,946 m (standard deviation of 24 m) for putative deltas, and -1,986 m (standard deviation of 56 m) for benches related to the largest paleolake located in SE Nepenthes Mensae. These values permitted us to reconstruct the paleogeography of the paleolakes that used to host the chain of interconnected NW-SE-trending closed depressions. According to this paleohydrological reconstruction, the largest paleolake reached an area of ~12,787 km^2, with an estimated water volume of 3,648 km^3, and mean and maximum depths of ~290 m and ~1,000 m, respectively. The water level inferred from putative deltas of the largest depression in SE Nepenthes Mensae is ~500 m higher than the ones inferred for the “S” and Arabia levels from putative deltas located in open basins along the margins of the Martian lowlands (Clifford and Parker, 2001; Di Achille and Hynek, 2010b). This difference may be due to vertical movements related to tectonics and/or to deltas in the study area were probably associated with an endorheic basin occupied by an inner sea or large interconnected paleolakes.

The interpretation of fan-shaped features and benches as Gilbert-type deltas and paleoshore platforms, respectively, is largely based on their morphologic and morphometric characteristics, as well as their spatial distribution and terrestrial analogs. In addition, CRISM spectral analyses conducted in the deltas “D2” and “D11” in the CNTZ, as well as in the delta located at the southwestern part of the Robert Sharp Crater, east of study area (García-Arnay and Gutiérrez, 2020), have permitted us to infer (1) the occurrence of hydrated ferromagnesian phyllosilicates, which are the most common hydrated minerals on Mars (Carter et al., 2013), and (2) hydrated Al-rich smectites and/or hydrated silica, consistent with the presence of saponite (Mg-rich smectite) and nontronite (Fe-rich smectite) in the Fe/Mg-smectite-bearing unit, and montmorillonite (Al-rich smectite) and/or opal (hydrated silica) in the Al-smectite-/hydrated-silica-bearing unit. The detection of hydrated minerals together with the morpho-sedimentary environment supports the past presence of liquid water in the region (e.g., Poulet et al., 2005) and strengthens the interpretation whereby these deposits were accumulated in fan-delta environments.

7.2.2 Paleohydrological history

The following sequence of events based on ages estimated by crater counting and stratigraphic relationships has been proposed in order to constrain the history of water in the CNTZ, focusing on the development of fluvial valleys, putative deltas and paleolakes: (1) The belt of interconnected closed depressions that hosted the ancient lakes were probably formed during Late Noachian to Late Hesperian times as a result of extensional tectonics in the CNTZ. (2) From the Late Noachian, fluvial activity started with the presence of liquid water and runoff carving the Cimmeria dissected units $\mathrm{Nhcd_a}$ and $\mathrm{Nhcd_b}$ to form the valley networks (unit HNv) and fan-delta deposits (unit HNf). (3) These N-directed drainage systems fed the paleolakes developed in the endorheic depressions in SE Nepenthes Mensae. These long-standing water bodies with relatively long periods of lake-level stability allowed the development of the putative deltas at the mouth of the valleys, as well as coastal benches along the margins of the depressions and around residual reliefs. (4) The paleolakes probably experienced a long-term water-level decline punctuated by periods of stability, as supported by inset benches at different elevations. (5) Hydrological activity in the region probably lasted up to Late Hesperian times, with possible later reactivations as suggested by resurfacing ages indicated by crater size-frequency determinations, followed by the definitive desiccation of the paleolakes.

7.3 THE NATURE OF THE CLOSED DEPRESSIONS IN KOTIDO CRATER

7.3.1 Key results of the morphological, morphometric and spatial characterization

In this section, we summarize the main results presented in Chapter 6 related to the morphological, morphometric and spatial distribution analyses carried out on the 513 closed depressions mapped in the floor of Kotido Crater, providing a comprehensive characterization of these landforms associated with ELDs.

The closed depressions generally display continuous, well-defined scarped edges controlled by resistant light-toned caprocks, whereas some depressions exhibit prominent ridge-like edges or poorly defined boundaries. Their walls are underlain by more erodible material that is generally covered by debris slopes and rock-falls. The floor of the depressions tends to be mantled by dark-toned deposits, mostly dunes, which locally overlap the edges of the depressions. The depressions show a wide range of morphologies and dimensions: (1) A significant proportion of them have an elongated shape. (2) The NE-oriented elongated depressions frequently display sharper and steeper SW edges with often smaller nested depressions, whereas the NE edges show gentler slopes, seldom with vaguely-defined boundaries. (3) Some depressions show a tear-drop morphology, with a subcircular shape interrupted on the NE side by an outward projection. (4) Several depressions show wide-open arcuate fissures along the foot of the scarped edge, with the inner block apparently tilted towards the center of the basin. In addition, the depressions and depression alignments are frequently associated with fractures, which may have a variable expression: (1) low-relief ridges indicative of more resistant material; (2) darker tone lineaments without topographic expression; and (3) linear scarps attributable to differential erosion and/or dip-slip fault displacement.

The main results of the morphometric analysis of the 513 mapped depressions indicate that: (1) The major axis ranges from 8 m to 342 m (average 55 m) and the area from 44 m^2 to 29,371 m^2 (average 1,615 m^2). (2) The orientation of the major axis of the depressions show a broad NE prevalent trend. (3) They have an average elongation ratio of 0.7. (4) The perimeter of the depressions varies from 24 m to 1,248 m (average 149 m), and the mean circularity ratio is 0.71. (5) The depressions are rather shallow with maximum and average depths of 12 m and 2.8 m, respectively. (6) The volume of the depressions, roughly estimated with the DEM, reaches 124,515 m^3, with an average of 3,149 m^3. The volume of some of the smaller depressions was indirectly estimated with a regression that relates the area and the volume of the depressions. The whole set of inventoried depressions has an aggregate volume of 1,615,650 m^3. This value, together with the area of the mapped zone (21,725,412 m^2), yields an average lowering of the ground surface by depression-forming processes of 7.4 cm.

The key characteristics of the frequency-size distributions of the depressions are: (1) A higher correlation coefficient of logarithmic regression functions for the major axis and the area (R^2: 0.96) than for the volume (R^2: 0.94), which was measured with significantly lower accuracy, especially for the small depressions. (2) There is typically a deviation between the empirical major axis and area data and the regressions for extreme-size values, affecting to a larger size range for the volume data, particularly for the small-volume depressions.

The analysis of the relative spatial distribution of the depressions shows that: (1) A total of 513 depressions have been mapped in an area covering 21.7 km^2, yielding a density of 23.6 depressions/km^2. (2) A NNI of 0.82 has been calculated for the study area, with a z-score of -7.52 and a *p*-value of 0.0, indicating an overall random distribution with some local clustering. (3) The mapped depressions occupy a total area of 0.83 km^2, representing an areal density of 3.8%. (4) The spatially-distributed density models of depressions by number and area show an uneven distribution, with similar areas characterized by high density by number (>34 depressions/km^2) and area (>23%), and relatively large zones with very low density (<8 depressions/km^2 and < 2%). (5) The comparison of the density models of depressions and fractures indicates some spatial correlation in the NE half of the study area and the opposite in the SE quadrant, with high depression density and very low fracture density.

7.3.2 Formative processes and evolution

Several hypotheses have been proposed to explain the origin and evolution of the sinkhole-like depressions mapped in the evaporite-bearing ELDs of Kotido Crater:

The main morphogenetic mechanism to explain the formation of these depressions is likely related to evaporite-dissolution-induced subsidence, which involves subsurface dissolution by liquid water and subsidence of the overlying undermined sediments (Waltham et al., 2005; Gutiérrez and Cooper, 2013; Gutiérrez et al., 2014). Several lines of evidence support this hypothesis: (1) The study area is underlain by a suitable substratum for the development of karts features, as indicated by the occurrence of evaporitic sediments formed in a playa-lake environment fed by salt-rich groundwater rising from a confined aquifer, preferentially along fractures (Pondrelli et al., 2019). (2) The occurrence of open fissures along the foot of the scarped edges, with the downthrown side apparently toppled towards the center of the depression, providing evidence of ground deformation related to mass depletion in the subsurface, attributable to the development of dissolution cavities and the collapse of the roof material. (3) The inventoried depressions of Kotido Crater display morphologic and morphometric characteristics comparable to those reported for other enclosed depressions on Mars attributed to dissolution. (4) Some morphometric parameters of the depressions (e.g., major axis, area, volume, and depth) are comparable with the broad range of values documented for sinkholes on Earth. In the case of Kotido Crater, the best fit between different size parameters (major axis, area, and volume) and their cumulative frequency is obtained with logarithmic functions ($R^2 \geq 0.94$). Similarly, regressions generated with the major axis of sinkholes developed in different karst settings on Earth also show a high correlation ($R^2 \geq 0.92$) between the empirical data and logarithmic functions. In Kotido Crater and in the different areas on Earth indicated above, there is typically a deviation between the empirical data and the regressions for extreme-size values. The upper tail (small-size values) is generally attributed to the incompleteness of the inventories (it does not seem to be applicable to Kotido Crater) and to mechanical thresholds, whereas the lower tail (large-size values) can be attributed to the coalescence of depressions (e.g., Corral and González, 2019; Gutiérrez et al., 2019). (5) The depressions tend to occur spatially associated with fractures and the highest density of depressions concurs with the zone showing the highest density of fractures. These data support that the fracture system has played a significant role on the development and distribution of the depressions. In karst systems, fractures are major elements controlling the formation of subsurface cavities and the associated collapse sinkholes. These discontinuities provide preferential pathways for groundwater flow, which enlarge by dissolution through a self-accelerating process (e. g., Dreybrodt and Gabrovsek, 2004; Ford and Williams, 2007; Palmer, 2007). They also contribute to reduce the rock-mass strength, favoring the collapse of cavity roofs. (6) The layered deposits in which the depressions have been formed are perched around 120 m above the deepest point of the crater. These are adequate topographic conditions for the possible development of an epigene karst system, which could be affected by downward groundwater flows towards a topographic base level. In epigene systems karst is generally expressed through widely distributed features such as caves and sinkholes, whereas in hypogene environments those features tend to form dense clusters separated by regions of minimal karst development (Klimchouk, 2003; Frumkin and Fischhendler, 2005; Gutiérrez et al., 2019). The NNI of 0.82 calculated for the depressions of study area is consistent with an epigene environment characterized by karst landforms distributed over the entire investigated zone.

The liquid water responsible for the dissolution may have been derived from the melting of snow and/or ice, including permafrost, as it has been proposed to explain the karst-like landforms found in other regions of Mars (Baioni et al., 2009; Grindrod and Balme, 2010; Jackson et al., 2011; Baioni and Sgavetti, 2013; Flahaut et al., 2015; Baioni and Tramontana, 2016; Baioni, 2018). Episodic changes in Martian obliquity may explain the origin of the ice and/or snow that melted and generated these putative karst landforms in this equatorial region (Mustard et al., 2001; Laskar et al., 2004).

The resulting putative sinkholes display a number of features and spatial relationships strongly suggesting that they have been re-shaped and enlarged by eolian erosion, probably under the current wind regime, acting more intensively on their NE side, and rock-falls from the scarped margins, both causing enlargement of the depressions and eventually leading to their coalescence. Numerous depressions show a markedly asymmetric morphology, with more subdued and irregular edges on the downwind NE edge, where the wind has a higher erosional capability due to flow concentration and higher vorticity (Whitney, 1978). Moreover, some depressions show a stepped floor with smaller nested depressions typically associated with the SW sector. This type of geomorphic arrangement with nested surfaces is frequently observed in the floor of pans generated by eolian deflation (e.g., Goudie and Wells, 1995). Overall, the depressions of Kotido Crater show larger dimensions than those mapped in epigene evaporite karst terrains on Earth. Collapse sinkholes on Mars are expected to reach larger dimensions than on Earth under equivalent geometrical and mechanical conditions, given the lower gravitational acceleration in the former planet (3.7 ms^{-2} versus 9.8 ms^{-2}) (Smith et al., 2006).

Alternative hypotheses to explain the origin of these closed depressions have been also considered, such as wind erosion, impact craters, volcanic and hydrothermal processes, or thermokarst. Nevertheless, the available data tends to either refute them or strongly question their potential validity.

7.4 WAY FORWARD

One of the most striking landforms mapped in the CNTZ are the megalandslides that occur along the 2-km-high dichotomy escarpment. In particular, those probably related to lateral spreading processes (see an example in Fig. 7.1). However, despite of their significance, this Thesis lacks proper analyses addressing the formative processes and evolution of those remarkable mass movements occurring in the CNTZ.

We intend to complement the detailed mapping carried out in this Thesis with a comprehensive morphometric, spatial and subsurface analysis of the slope movements in order to: (1) unravel the mechanisms needed to trigger these giant deep-seated rock spreads, focusing on their possible interaction with the occurrence of paleolakes in the closed depressions, extensional tectonics and volcanic activity; (2) assess whether raft tectonics, an extreme type of extensional deformation (e.g., Duval et al., 1992; Mauduit et al., 1997), has played some role on their formation; and (3) compare these features with possible terrestrial analogs, such as the Hawaiian megalandslides known as “Nuuanu” and “Wailau”, with extraordinary runouts of around 200 km (e.g., Clague and Moore, 2002, Clague et al., 2002), representing some of the largest landslides known on Earth (e.g., Moore et al., 1994). The results of this study will be presented in a manuscript that will be submitted for a possible publication in a SCI international journal (e.g., Landslides).

***Fig. 7.1 (next page)**. 3D oblique view of giant rock spreads (ANl unit) occurring along the dichotomy escarpment in the center bottom of the image (CTX image mosaic).*

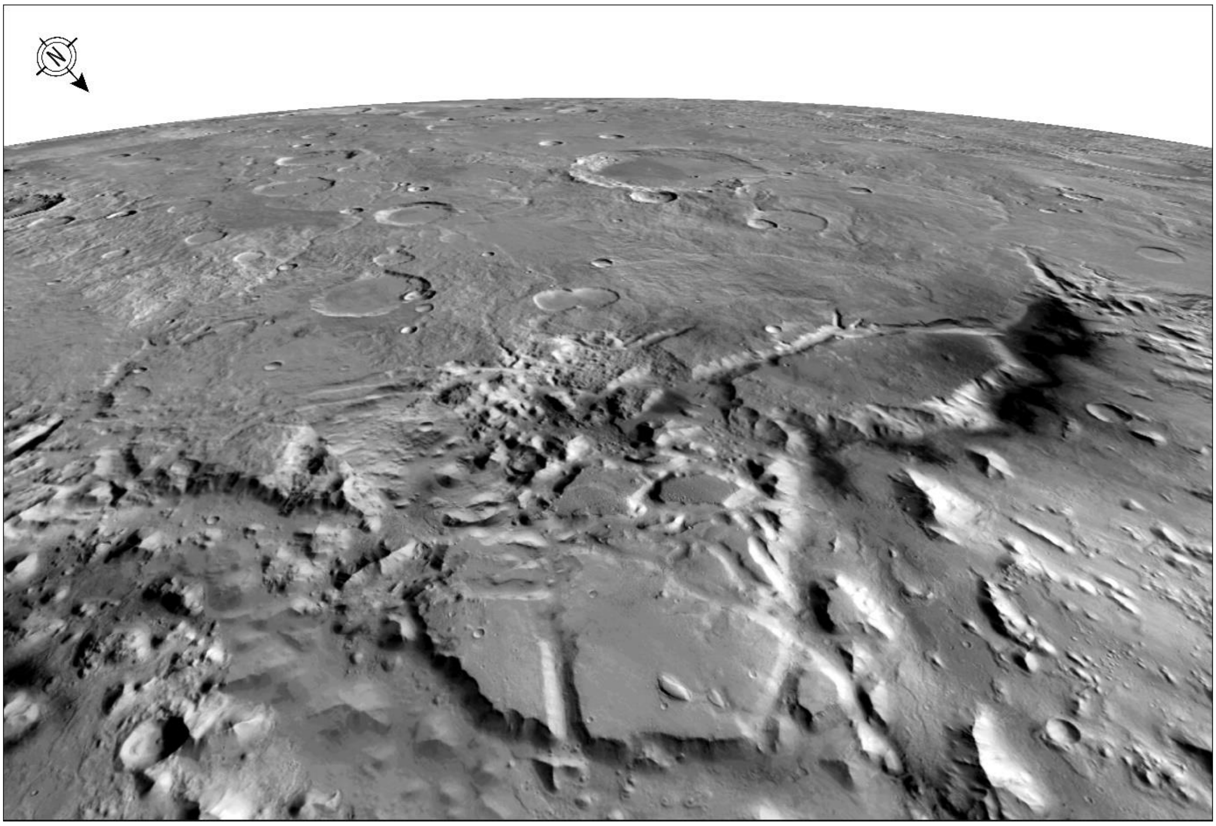
N

CHAPTER

8. Conclusions

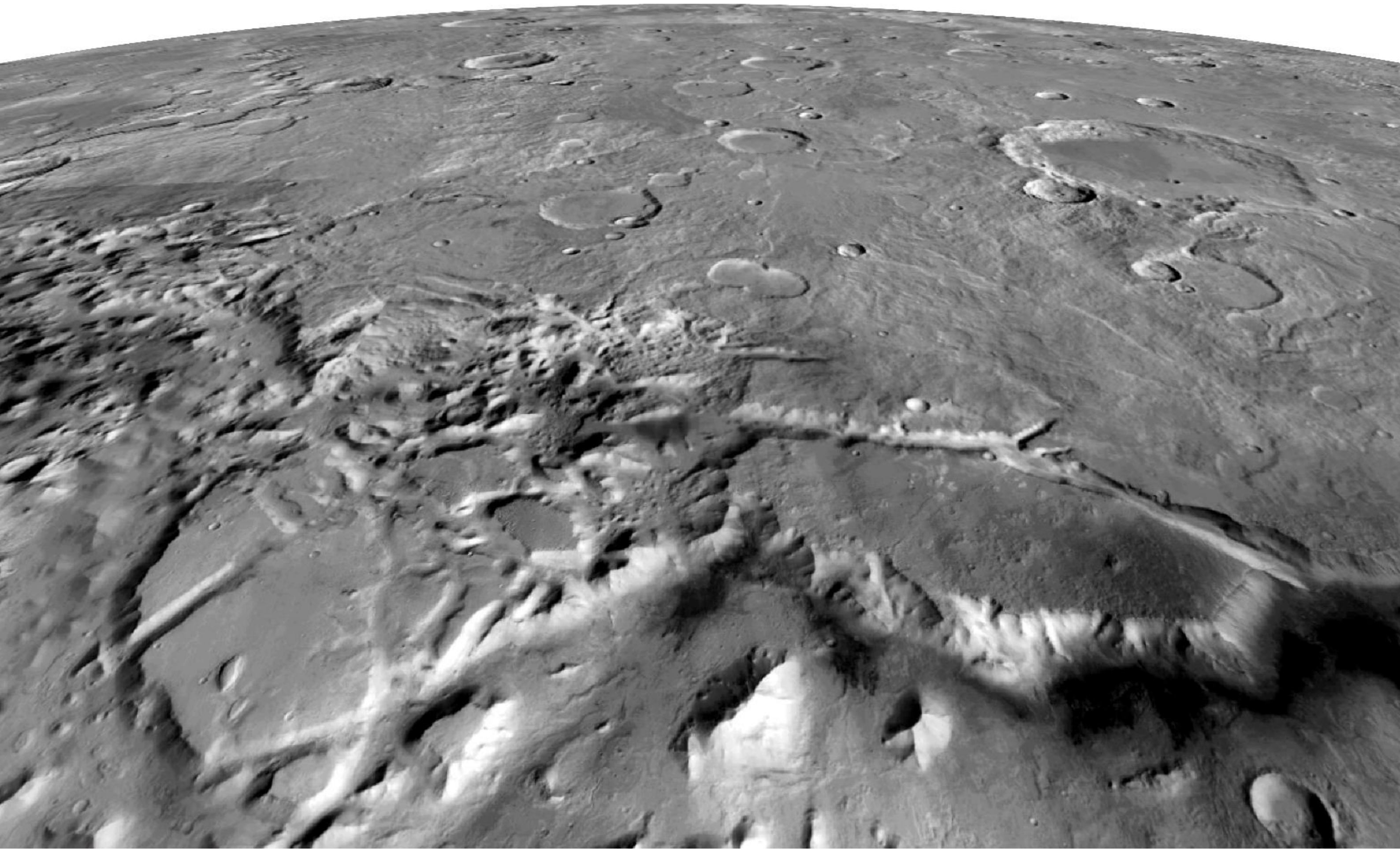

CONCLUSIONS

This PhD Thesis presents the findings derived from comprehensive studies based on the combination of geological-geomorphological mapping, and multiple morphological, morphometric, chronological, geochemical and subsurface analyses carried out on the transitional zone between the NW Terra Cimmeria and SE Nepenthes Mensae, as well as on the floor of Kotido Crater (SW Arabia Terra). The main contributions are:

1) The production of the 1:1.45M geologic-geomorphic map of the NW Terra Cimmeria and SE Nepenthes Mensae providing a detailed geologic-geomorphic framework for this area and other regions along the highland-lowland transitional zone, of special interest from the paleohydrological perspective and for understanding the evolution of early Mars. The mapping has permitted us to constrain:

    - The long-term geological history of this poorly explored transitional zone that ranges from the Early Noachian to recent times, differentiating nineteen geologic units that display a wide variety of geomorphic features.

    - The fundamental morphogenetic role played by the inferred compressional and extensional tectonics on the configuration of the landscape in the CNTZ at least from the Late Noachian to Late Hesperian. Extensional tectonics, which postdates the compressional phase, has contributed to the development of some of the most prominent geomorphic features of the region, including: (1) the plateau located to the south of the dichotomy in the highland province; (2) the 2-km-high dichotomy escarpment interpreted as a fault scarp; (3) the formation of a half-graben at the foot of the escarpment with keystone grabens nested in its lower part that used to host paleolakes in Nepenthes Mensae; (4) the fissure-type volcanic activity in the deepest areas of the basins; and (5) the megalandslides derived from the dichotomy escarpment.

2) The reconstruction of the paleohydrology in this transitional zone showing that fluvio-lacustrine activity has also played an important morphogenetic role in the area at least from Late Noachian to Late Hesperian times, as supported by:

    - The pervasive occurrence of tectonically-controlled valley networks carved into the Cimmeria region by runoff erosion, integrating young and poorly-developed watersheds. These fluvial systems experienced base level changes, as indicated by paired terraces and knickpoints. The presence of some valleys with theatre-like headcuts supports that sapping erosion processes may have played some role in their headward expansion.

    - The identification of 24 fan-shaped phyllosilicate-bearing deposits and 54 benches in SE Nepenthes Mensae, interpreted as likely relict Gilbert-type deltas and alluvial fans, as well as paleoshore platforms, respectively. Their elevations permitted us to approximately determine the mean water level at around −1,950 m of an ancient inner sea or a system of interconnected paleolakes that occupied the belt of NW-SE trending closed depressions. This past water level is consistent with the mean elevation reported for the putative Arabia shoreline. The possible interaction during the Late Noachian to Late Hesperian between the heat sources associated with the volcanic activity and the liquid water occupying the basins in Nepenthes Mensae makes this region a potential landing site for exploring past life signatures on Mars.

3) The nature of the closed depressions developed in the ELDs within Kotido Crater, which are most probably relict landforms related to subsurface dissolution of evaporites and collapse processes (i.e., collapse sinkholes). Several lines of evidence support this interpretation: (1) The presence of open fissures at the foot of the scarped margins of some depressions. (2) The dimensions of the depressions in Kotido Crater are comparable with those documented for sinkholes on Earth and Mars. (3) The cumulative frequency of the major axis of these depressions follow a logarithmic distribution, like in numerous evaporite and carbonate karst regions on Earth. (4) The spatial association and preferred orientation between elongated depressions and fractures suggest that both dissolution and subsidence processes were influenced by these latter features. (5) The topographic conditions, with the area perched around 120 m above the deepest zone of the crater floor, as well as the overall random distribution of the depressions (NNI: 0.82), are consistent with the occurrence of an epigene karst in the region. These putative sinkholes, probably enlarged and reshaped by long-sustained wind erosion, represent markers of past paleoclimatic and paleohydrological conditions suggesting the existence of underground circulation of liquid water. Their relatively fresh appearance, the lack of impact craters, and the comparison with depressions reported in other regions suggest a poorly-constrained Amazonian age.

CONCLUSIONES

Esta Tesis Doctoral presenta los hallazgos derivados de varios estudios exhaustivos basados en la combinación de cartografía geológica-geomorfológica, y de múltiples análisis morfológicos, morfométricos, cronológicos, geoquímicos y del subsuelo realizados en la zona de transición entre el noroeste de Terra Cimmeria y el sureste de Nepenthes Mensae, así como en el lecho del Cráter Kotido (suroeste de Arabia Terra). Las principales contribuciones son:

1) La elaboración del mapa geológico-geomorfológico, en escala 1:1.450.000, del noroeste de Terra Cimmeria y sureste de Nepenthes Mensae, que proporciona un marco geológico-geomorfológico detallado para esta área y otras regiones a lo largo de la zona de transición entre las tierras altas y bajas, de especial interés desde el punto de vista paleohidrológico, así como para entender la evolución del Marte primigenio. La cartografía nos ha permitido precisar:

    - La historia geológica, a largo plazo, de esta zona de transición, poco explorada, que abarca desde el Noéico temprano hasta tiempos recientes, diferenciando diecinueve unidades geológicas que muestran una amplia variedad de rasgos geomorfológicos.

    - El papel morfogenético fundamental que ha desempeñado la tectónica compresiva y extensiva en la configuración del relieve de esta zona, al menos desde el Noéico tardío hasta el Hespérico tardío. La tectónica extensiva, que postdata la fase compresiva, ha contribuido al desarrollo de algunos de los rasgos geomorfológicos más destacados de la región, entre ellos (1) la meseta situada al sur de la dicotomía en la provincia de tierras altas; (2) el escarpe de la dicotomía, de 2 km de altura, interpretado como un escarpe de falla; (3) la formación de un semigraben al pie de la dicotomía con *keystone grabens* anidados en su parte inferior que albergaron paleolagos en Nepenthes Mensae; (4) la actividad volcánica, de tipo fisural, en las zonas más profundas de las depresiones; y (5) los megadeslizamientos derivados del escarpe de la dicotomía.

2) La reconstrucción de la paleohidrología en la región, mostrando que la actividad fluvio-lacustre también ha jugado un importante papel morfogenético en el área, al menos desde el Noéico tardío hasta el Hespérico tardío, tal y como constatan:

    - Los sistemas de valle, controlados tectónicamente, en la región de Cimmeria formados por escorrentía superficial, dando lugar a cuencas hidrográficas jóvenes y poco desarrolladas. Estos sistemas fluviales experimentaron cambios en el nivel de base, como indican la presencia de terrazas simétricas y *knickpoints*. La presencia de algunos valles con cabeceras en forma de teatro sugiere que los procesos de erosión por *sapping* pueden haber desempeñado algún papel en la erosión remontante de estos valles.

    - La identificación de 24 depósitos, en forma de abanico, con superficies ricas en filosilicatos, así como 54 terrazas en el sureste de Nepenthes Mensae, interpretados como posibles deltas de tipo Gilbert y abanicos aluviales relictos, así como antiguas plataformas costeras, respectivamente. Sus elevaciones nos permitieron determinar, aproximadamente, el nivel medio del agua en torno a los -1.950 m, correspondiente a un antiguo mar interior o sistema de paleolagos interconectados que ocuparon el cinturón de depresiones cerradas con orientación noroeste-sureste. Este nivel del agua es coherente con la elevación media estimada para la línea de costa de Arabia en las tierras bajas. La posible interacción durante el Noéico tardío y el Hespérico tardío entre las fuentes de calor asociadas a la actividad volcánica y el agua líquida que ocupaba las depresiones en Nepenthes Mensae convierte a esta región en un lugar favorable para explorar posibles marcadores geoquímicos de vida pasada en Marte.

3) La naturaleza de las depresiones cerradas desarrolladas en los “ELDs” dentro del Cráter Kotido, que se formaron, probablemente, como resultado de la disolución de evaporitas y procesos de colapso (es decir, dolinas de colapso). Varias evidencias apoyan esta hipótesis: (1) La presencia de fisuras abiertas al pie de los márgenes escarpados de algunas depresiones. (2) Las dimensiones de las depresiones del Cráter Kotido son comparables a las documentadas para las dolinas de la Tierra y Marte. (3) La frecuencia acumulada del eje mayor de estas depresiones sigue una distribución logarítmica, como sucede en numerosas regiones kársticas evaporíticas y carbonatadas de la Tierra. (4) La asociación espacial y la orientación preferente entre las depresiones y las fracturas sugieren que, tanto los procesos de disolución, como de subsidencia, se vieron influenciados por la existencia de estas fracturas. (5) Las condiciones topográficas, con el área de estudio situada unos 120 m por encima de la zona más profunda del lecho del cráter, así como la distribución aleatoria de las depresiones (NNI: 0,82), son consistentes con la presencia de un karst epigénico en la región. Estas supuestas dolinas, probablemente ensanchadas y remodeladas por la acción de la erosión eólica durante un largo período de tiempo, constituyen potenciales marcadores de las condiciones paleoclimáticas y paleohidrológicas presentes en la región en el pasado, sugiriendo la circulación subterránea de agua líquida. El aspecto relativamente reciente de estas depresiones, junto con la ausencia de cráteres de impacto y su comparación con depresiones similares documentadas en otras regiones, sugieren una probable edad Amazónica.

CHAPTER

9. References

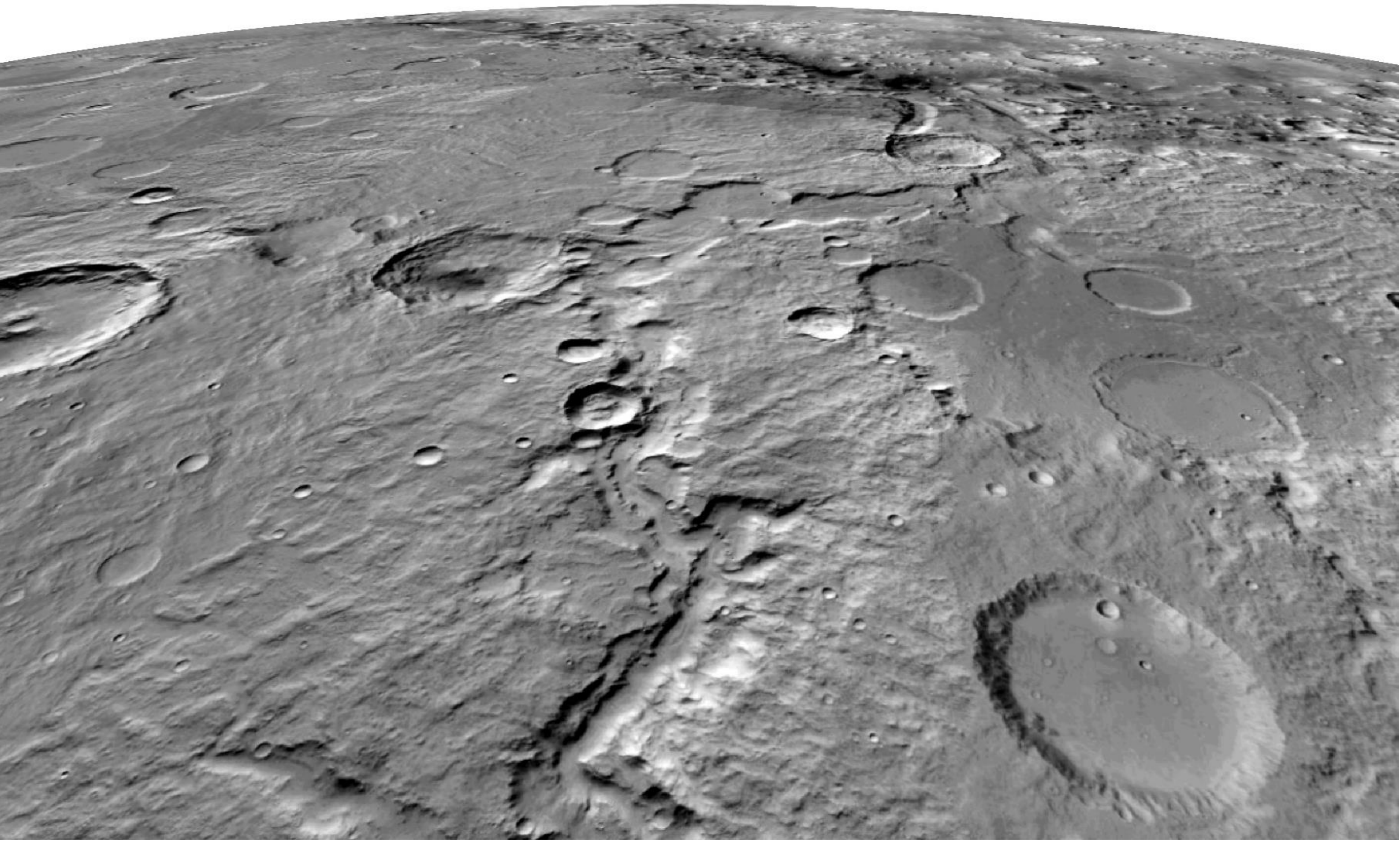

This Chapter compiles the references that have been used in Chapters 1-3 and 7, in the introductions of Chapters 4-6, and in figure captions of Annex.

Andrews-Hanna, J.C., 2020. The tectonic architecture of wrinkle ridges on Mars. Icarus 351, 113937. https://doi.org/10.1016/j.icarus.2020.113937.

Andrews-Hanna, J.C., Phillips, R.J., 2007. Hydrological modeling of outflow channels and chaos regions on Mars. J. Geophys. Res. Planets 112 (E8). https://doi.org/10.1029/2006JE002881.

Andrews-Hanna, J.C., Zuber, M.T., Banerdt, W.B., 2008. The Borealis basin and the origin of the martian crustal dichotomy. Nature 453(7199), 1212-1215. https://doi.org/10.1038/nature07011.

Andrews-Hanna, J.C., Zuber, M.T., Arvidson, R.E., Wiseman, S.M., 2010. Early Mars hydrology: Meridiani playa deposits and the sedimentary record of Arabia Terra. J. Geophys. Res. Planets 115 (E6). https://doi.org/10.1029/2009JE003485.

Baioni, D., 2013. Morphology and geology of an interior layered deposit in the western Tithonium Chasma, Mars. Planet. Space Sci. 89, 140–150. https://doi.org/10.1016/j.pss.2013.09.019.

Baioni, D., 2018. Karst Landforms as Markers of Recent Climate Change on Mars: An Example from a Late Amazonian Epoch Evaporate-Karst within a Trough in Western Noctis Labyrinthus. Recent and Current Landscape Evolution of the Red Planet. Elsevier, Amsterdam, Netherlands, Dynamic Mars, pp. 411–429. https://doi.org/10.1016/B978-0-12-813018-6.00014-5.

Baioni, D., 2019. Very recent karst landforms within Cagli crater, Sinus Meridiani, Mars. Ital. J. Geosci. 138, 262–273. https://doi.org/10.3301/IJG.2019.05.

Baioni, D., Sgavetti, M., 2013. Karst terrains as possible lithologic and stratigraphic markers in northern sinus Meridiani. Mars. Planetary and Space Science 75 (1), 173–181. https://doi.org/10.1016/j.pss.2012.08.011.

Baioni, D., Tramontana, M., 2016. Possible karst landforms in two unnamed craters in Tyrrhena Terra, Mars. Planet. Space Sci. 132, 57–65. https://doi.org/10.1016/j.pss.2016.08.011.

Baioni, D., Tramontana, M., 2017. Possible evaporite karst in an interior layered deposit in Juventae Chasma. Mars. International Journal of Speleology 46, 181–189. https://doi.org/10.5038/1827-806X.46.2.2085.

Baioni, D., Wezel, F.C., 2010. Morphology and origin of an evaporitic dome in Tithonium Chasma. Mars. Planetary and Space Science 58, 847–857. https://doi.org/10.1016/j.pss.2010.01.009.

Baioni, D., Zupan, Hajna N., Wezel, F.C., 2009. Karst landforms in a Martian evaporitic dome. Acta Carsologica 38 (1), 9–18. Retrieved from https://search.proquest.com/docview/869787639?accountid=14795.

Baioni, D., Zupan, H.N., Wezel, F.C., 2011. Karst landforms in an interior layered deposit within Coprates chasma, Mars. Acta Carsologica 40 (3), 473–481. Retrieved from https://search.proquest.com/docview/1668230512?accountid=14795.

Baker, V.R., 2001. Water and the Martian landscape. Nature 412 (6843), 228. https://doi.org/10.1038/35084172.

Beyer, R.A., Alexandrov, O., McMichael, S., 2018. The Ames stereo pipeline: NASA's open source software for deriving and processing terrain data. Earth and Space Science 5 (9), 537–548. https://doi.org/10.1029/2018EA000409.

Bibring, J.P., et al., 2006. Global mineralogical and aqueous Mars history derived from OMEGA/Mars Express data. Science 312 (5772), 400–404. https://doi.org/10.1126/science.1122659.

Caldwell, R.L., Edmonds, D.A., 2014. The effects of sediment properties on deltaic processes and morphologies: a numerical modeling study. J. Geophys. Res. Earth 119 (5), 961–982. https://doi.org/10.1002/2013JF002965.

Carr, M.H., 2012. The fluvial history of Mars. Phil. Trans. R. Soc. A. 370(1966), 2193-2215. https://doi.org/10.1098/rsta.2011.0500.

Carr, M.H., Chuang, F.C., 1997. Martian drainage densities. Journal of Geophysical Research: Planets, 102(E4), 9145-9152. https://doi.org/10.1029/97JE00113.

Carr, M.H., Head III, J.W., 2003. Oceans on Mars: an assessment of the observational evidence and possible fate. J. Geophys. Res. Planets 108 (E5). https://doi.org/10.1029/2002JE001963.

Carter, J., Poulet, F., Bibring, J.-P., Mangold, N., Murchie, S., 2013. Hydrous minerals on Mars as seen by the CRISM and OMEGA imaging spectrometers: updated global view. J. Geophys. Res. Planets 118, 831–858. https://doi.org/10.1029/2012JE004145.

Christensen, P.R., Jakosky, B.M., Kieffer, H.H., Malin, M.C., McSween, H.Y., Nealson, K., Mehall, G.L., Silverman, S.H., Ferry, S., Caplinger, M., Ravine, M., 2004. The thermal emission imaging system (THEMIS) for the Mars 2001 Odyssey Mission. Space Sci. Rev. 110 (1–2), 85–130. https://doi.org/10.1023/B:SPAC.0000021008.16305.94.

Christensen, P.R., Fergason, R.L., Edwards, C.S., Hill, J., 2013. THEMIS-derived thermal inertia mosaic of Mars: product description and science results. Lunar and Planetary Science Conference Abstracts vol. 44 (p. #2822).

Clague, D. A., Moore, J. G., 2002. The proximal part of the giant submarine Wailau landslide, Molokai, Hawaii. Journal of Volcanology and Geothermal Research, 113(1-2), 259-287. https://doi.org/10.1016/S0377-0273(01)00261-X.

Clague, D. A., Moore, J. G., Davis, A. S., 2002. Volcanic breccia and hyaloclastite in blocks from the Nuuanu and Wailau landslides, Hawaii. Washington DC American Geophysical Union Geophysical Monograph Series, 128, 279-296. https://doi.org/10.1029/GM128p0279.

Clifford, S.M., Parker, T.J., 2001. The evolution of the Martian hydrosphere: implications for the fate of a primordial ocean and the current state of the northern plains. Icarus 154 (1), 40–79. https://doi.org/10.1006/icar.2001.6671.

Corral, Á., González, Á., 2019. Power-law size distributions in geoscience revisited. Earth and Space Science 6. https://doi.org/10.1029/2018EA000479.

Davis, J. M., Aranos, L., Dickeson, Z. I., Fawdon, P., 2022. The Evolution of Ancient Fluvial Systems in Memnonia Sulci, Mars: Impact Crater Damming, Aggradation, and a Large Water Body on the Dichotomy? Journal of Geophysical Research: Planets, 127(2), e2021JE007021. https://doi.org/10.1029/2021JE007021.

De Carvalho-Junior O. A., Fontes-Guimaraes R., Montgomery D. R., Gillispie A. R., Trancoso-Gomes R. A., de Souza-Martins E., Correira-Silva N., 2014. Karst depression detection using ASTER, ALOS/PRISM and SRTM-derived digital elevation models in the Bambuí Group, Brazil. Remote Sensing, 6, 330–351. doi: https://doi.org/10.3390/rs6010330.

de Pablo, M.Á., Pacifici, A., 2008. Geomorphological evidence of water level changes in Nepenthes Mensae, Mars. Icarus 196 (2), 667–671. https://doi.org/10.1016/j.icarus.2008.04.005.

Di Achille, G., Hynek, B.M., 2010a. Deltas and valley networks on Mars: implications for a global hydrosphere. Lakes on Mars, pp. 223–248. https://doi.org/10.1016/C2009-0-06633-1.

Di Achille, G., Hynek, B.M., 2010b. Ancient ocean on Mars supported by global distribution of deltas and valleys. Nat. Geosci. 3 (7), 459–463. https://doi.org/10.1038/ngeo891.

Dickson, J.L., Kerber, L.A., Fassett, C.I., Ehlmann, B.L., 2018. A global, blended CTX mosaic of Mars with vectorized seam mapping: a new mosaicking pipeline using principles of non-destructive image editing. Lunar and Planetary Science Conference Abstracts vol. 49 (p. #2480).

Dreybrodt W., Gabrovsek F., 2004. Speleogenesis: computer models. In: Gunn, J. (Ed.). Encyclopedia of Caves and Karst Science. Fitzroy Dearborn, 677–681.

Doctor, D.H., Young, J.A., 2013. An evaluation of automated GIS tools for delineating karst sinkholes and closed depressions from 1-meter LIDAR-derived digital elevation data. In: Land, L., Doctor, D.H., Stephenson, J.B. (Eds.), Sinkholes and the Engineering and Environmental Impacts of Karst. National Cave and Karst Research Institute, Carlsbad, pp. 449–458. https://doi.org/10.5038/9780979542275.1156.

Duval, B., Cramez, C., Jackson, M. P. A., 1992. Raft tectonics in the Kwanza basin, Angola. Marine and Petroleum Geology, 9(4), 389-404. https://doi.org/10.1016/0264-8172(92)90050-O.

Elkins-Tanton, L.T., Hess, P.C., Parmentier, E.M., 2005. Possible formation of ancient crust on Mars through magma ocean processes. J. Geophys. Res. Planets 110(E12). https://doi.org/10.1029/2005JE002480.

Fassett, C.I., Head III, J.W., 2008. Valley network-fed, open-basin lakes on Mars: distribution and implications for Noachian surface and subsurface hydrology. Icarus 198 (1), 37–56. https://doi.org/10.1016/j.icarus.2008.06.016.

Fawdon, P., Gupta, S., Davis, J.M., Warner, N.H., Adler, J.B., Balme, M.R., Bell, J.F., Grindrod, P.M., Sefton-Nash, E., 2018. The Hypanis Valles delta: the last highstand of a sea on early Mars? Earth Planet. Sc. Lett. 500, 225–241. https://doi.org/10.1016/j.epsl.2018.07.040.

Fergason, R.L., Christensen, P.R., Kieffer, H.H., 2006. High-resolution thermal inertia derived from the Thermal Emission Imaging System (THEMIS): Thermal model and applications. J. Geophys. Res. Planets 111(E12). https://doi.org/10.1029/2006JE002735.

Fergason, R.L., Hare, T.M., Laura, J., 2018. HRSC and MOLA Blended Digital Elevation Model at 200m v2, Astrogeology PDS Annex. U.S. Geological Survey http://bit.ly/HRSC_MOLA_Blend_v0.

Figueiredo, P.M., Cabral, J., Rockwell, T.K., 2014. Recognition of Pleistocene marine terraces in the Southwest of Portugal (Iberian Peninsula): evidences of regional Quaternary uplift. Ann. Geophys. 56 (6). https://doi.org/10.4401/ag-6276.

Flahaut, J., Carter, J., Poulet, F., Bibring, J.P., van Westrenen, W., Davies, G.R., Murchie, S.L., 2015. Embedded clays and sulfates in Meridiani Planum. Mars. Icarus 248, 269–288. https://doi.org/10.1016/j.icarus.2014.10.046.

Ford D., Williams P., 2007. Karst Hydrogeology and Geomorphology. Wiley, 562. Forget, F., Haberle, R.M., Montmessin, F., Levrard, B., Head, J.W., 2006. Formation of glaciers on Mars by atmospheric precipitation at high obliquity. Science 311 (5759), 368–371. https://doi.org/10.1126/science.1120335.

Franchi, F., Rossi, A., Pondrelli, M., Cavalazzi, B., 2014. Geometry, stratigraphy and evidences for fluid expulsion within Crommelin crater deposits, Arabia Terra, Mars. Planet. Space Sci. 92, 34–48. https://doi.org/10.1016/j.pss.2013.12.013.

Frey, H., Shultz, R.A., 1988. Large impact basins and the mega-impact origin for the crustal dichotomy on Mars. Geophys. Res. Lett. 15, 229–232. https://doi.org/10.1029/GL015i003p00229.

Frey, H.V., Schultz, R.A., Maxwell, T.A., 1986. The Martian crustal dichotomy: Product of accretion and not a specific event? Lunar and Planetary Science Conference Abstracts vol. 17, pp. 241-242.

Frumkin, A., Fischhendler, I., 2005. Morphometry and distribution of isolated caves as a guide for phreatic and confined paleohydrological conditions. Geomorphology 67, 457–451. https://doi.org/10.1016/j.geomorph.2004.11.009.

García-Arnay, J.Á., 2016. Cartografía geomorfológica de la región de Nepenthes Mensae, Marte: evidencias de un antiguo mar. Universidad de Zaragoza, Zaragoza, Spain Master's thesis. Retrieved from. https://zaguan.unizar.es/record/58648/files/TAZ-TFM-2016-821.pdf.

García-Arnay, Á., Fernández, S., de Pablo, M.Á., Gutiérrez, F., 2018a. The dominant morphogenetic role of surface runoff in Licus Vallis, Mars: results from geomorphological and morphometric analyses. Geogaceta 63, 63–66 Retrieved from. http://www.sociedadgeologica.es/archivos/geogacetas/geo63/geo63_16.pdf.

García-Arnay, Á., Gutiérrez, F., de Pablo, M.Á., Fernández, S., 2018b. Characterization and interpretation of the fan-shaped and terrace-like features identified in Nepenthes Mensae, Mars. EGU General Assembly Conference Abstracts vol. 20 (p. # 808). Retrieved from https://figshare.com/articles/Characterization_and_interpretation_of_the_fanshaped_and_terrace-like_features_identified_in_Nepenthes_Mensae_Mars/9824609.

García-Arnay, Á., Gutiérrez, F., 2020. Reconstructing paleolakes in Nepenthes Mensae, Mars, using the distribution of putative deltas, coastal-like features, and terrestrial analogs. Geomorphology 359, 107129. https://doi.org/10.1016/j.geomorph.2020.107129.

Garvin, J.B., Sakimoto, S., Frawley, J.J., 2003. Craters on Mars: Global geomètric properties from gridded MOLA topography. In: Sixth international conference on Mars. In: Abstract #3277.

Gendrin, A., Mangold, N., Bibring, J.P., Langevin, Y., Gondet, B., Poulet, F., Bonello, G., Quantin, C., Mustard, J., Arvidson, R., 2005. Sulfates in martian layered terrains: the OMEGA/Mars express view. Science 307 (5715), 1587–1591. https://doi.org/10.1126/science.1109087.

Ghatan, G.J., Zimbelman, J.R., 2006. Paucity of candidate coastal constructional landforms along proposed shorelines on Mars: implications for a northern lowlands-filling ocean. Icarus 185 (1), 171–196. https://doi.org/10.1016/j.icarus.2006.06.007.

Golabek, G.J., Keller, T., Gerya, T.V., Zhu, G., Tackley, P.J., Connolly, J.A., 2011. Origin of the Martian dichotomy and Tharsis from a giant impact causing massive magmatism. Icarus 215(1), 346-357. http://dx.doi.org/10.1016/j.icarus.2011.06.012.

Goudge, T.A., Fassett, C.I., 2018. Incision of Licus Vallis, Mars, from multiple lake overflow floods. J. Geophys. Res. Planets 123 (2), 405–420. https://doi.org/10.1002/2017JE005438.

Goudge, T.A., Aureli, K.L., Head, J.W., Fassett, C.I., Mustard, J.F., 2015. Classification and analysis of candidate impact crater-hosted closed-basin lakes on Mars. Icarus 260, 346–367. https://doi.org/10.1016/j.icarus.2015.07.026.

Goudie, A.S., Wells, G.L., 1995. The nature, distribution and formation of pans in arid zones. Earth Sci. Rev. 38 (1), 1–69. https://doi.org/10.1016/0012-8252(94)00066-6.

Greeley, R., Guest, J., 1987. Geologic map of the eastern equatorial region of Mars. U.S. Geological Survey, IMAP 1802, Scale 1:5,000,000. https://doi.org/10.3133/i1802B.

Greeley, R., Batson, R.M., 1990. Planetary Mapping. Cambridge Univ. Press p. 296.

Grindrod P. M., Balme M. R., 2010. Groundwater processes in Hebes Chasma, Mars. Geophysical Research Letters 37(13), L13202. doi: https://doi.org/10.1029/2010GL044122.

Gutiérrez, F., Cooper, A., 2013. Surface morphology of gypsum karst. Treatise on geomorphology, karst. Geomorphology 6, 425–437. https://doi.org/10.1016/B978-0-12-374739-6.00114-7.

Gutiérrez, F., Parise, M., De Waele, J., Jourde, H., 2014. A review on natural and human-induced geohazards and impacts in karst. Earth Sci. Rev. 138, 61–88. https://doi.org/10.1016/j.earscirev.2014.08.002.

Gutiérrez, F., Fabregat, I., Roqué, C., Carbonel, D., Zarroca, M., Linares, R., Yechieli, Y., García-Arnay, Á., Sevil, J., 2019. Sinkholes in hypogene versus epigene karst systems, illustrated with the hypogene gypsum karst of the Sant Miquel de Campmajor Valley, NE Spain. Geomorphology 328, 57–78. https://doi.org/10.1016/j.geomorph.2018.12.003.

Hansen, V.L., 2000. Geologic mapping of tectonic planets. Earth Planet. Sc. Lett. 176(3–4), 527–542. https://doi.org/10.1016/S0012-821X(00)00017-0.

Harrison, K.P., Grimm, R.E., 2005. Groundwater-controlled valley networks and the decline of surface runoff on early Mars. J. Geophys. Res. Planets 110 (E12). https://doi.org/10.1029/2005JE002455.

Hartmann, W.K., 2005. Martian cratering 8: isochron refinement and the chronology of Mars. Icarus 174 (2), 294–320. https://doi.org/10.1016/j.icarus.2004.11.023.

Head III, J.W., Hiesinger, H., Ivanov, M.A., Kreslavsky, M.A., Pratt, S., Thomson, B.J., 1999. Possible ancient oceans on Mars: evidence from Mars Orbiter Laser Altimeter data. Science 286 (5447), 2134–2137. https://doi.org/10.1126/science.286.5447.2134.

Hearty, P.J., Hollin, J.T., Neumann, A.C., O'Leary, M.J., McCulloch, M., 2007. Global sea-level fluctuations during the Last Interglaciation (MIS 5e). Quat. Sci. Rev. 26 (17–18), 2090–2112. https://doi.org/10.1016/j.quascirev.2007.06.019.

Hiller, K.H., 1979. Geologic map of the Amenthes Quadrangle of Mars. U.S. Geological Survey, IMAP 1110, Scale 1:5,000,000. https://doi.org/10.3133/i1110.

Horton, R.E., 1945. Erosional development of streams and their drainage basins; hydrophysical approach to quantitative morphology. Geological society of America bulletin, 56(3), 275-370. https://doi.org/10.1130/0016-7606(1945)56[275:EDOSAT]2.0.CO;2.

Hynek, B.M., Di Achille, G., 2017. Geologic map of Meridiani Planum. Mars. US Geological Survey Scientific Investigations Map 3356.

Irwin, R.P., Howard, A.D., 2002. Drainage basin evolution in Noachian Terra Cimmeria, Mars. J. Geophys. Res. Planets 107 (E7). https://doi.org/10.1029/2001JE001818.

Irwin III, R.P., Watters, T.R., Howard, A.D., Zimbelman, J.R., 2004. Sedimentary resurfacing and fretted terrain development along the crustal dichotomy boundary, Aeolis Mensae, Mars. J. Geophys. Res. Planets 109(E9). https://doi.org/10.1029/2004JE002248.

Irwin, R.P., Howard, A.D., Craddock, R.A., Moore, J.M., 2005. An intense terminal epoch of widespread fluvial activity on early Mars: 2. Increased runoff and paleolake development. J. Geophys. Res. Planets 110 (E12). https://doi.org/10.1029/2005JE002460.

Irwin, R.P., Zimbelman, J.R., 2012. Morphometry of Great Basin pluvial shore landforms: implications for paleolake basins on Mars. J. Geophys. Res. Planets 117 (E7). https://doi.org/10.1029/2012JE004046.

Jackson, M.P.A., Adams, J.B., Dooley, A.R., Montgomery, D.R., 2011. Modelling the collapse of Hebes Chasma, Valles Marineris. Mars. Geological Society of America Bulletin 123 (7–8), 1596–1627. https://doi.org/10.1130/B30307.1.

Kargel, J.S., Dougherty, A., Feldman, W., Hogenboom, D., Marion, G., McCarthy, C., Prieto-Ballesteros, O., 2004. Hydrated Salts: Dehydration, dissolution, and incongruent melting in terrestrial evaporites and at Meridiani Planum, Mars. In AGU Fall Meeting Abstracts (Vol. 2004, pp. P21A-0205).

Ke, Y., Solomatov, V.S., 2006. Early transient superplumes and the origin of the Martian crustal dichotomy. J. Geophys. Res. Planets 111(E10). https://doi.org/10.1029/2005JE002631.

King, E.A., 1978. Geologic map of the Mare Tyrrhenum Quadrangle of Mars. US Geological Survey Report, IMAP 1073. https://doi.org/10.3133/i1073.

Kleinhans, M.G., 2005. Flow discharge and sediment transport models for estimating a minimum timescale of hydrological activity and channel and delta formation on Mars. J. Geophys. Res. Planets 110 (E12). https://doi.org/10.1029/2005JE002521.

Klimchouk, A.B., 2003. Conceptualization of speleogenesis in multi-story artesian systems: a model of transverse speleogenesis. Speleogenesis and Evolution of Karst Aquifers 1, 1–18.

Kneissl, T., van Gasselt, S., Neukum, G., 2011. Map-projection-independent crater size-frequency determination in GIS environments—new software tool for ArcGIS. Planet. Space Sci. 59 (11), 1243–1254. https://doi.org/10.1016/j.pss.2010.03.015.

Johnson, K.S., 2008. Evaporite-karst problems and studies in the USA. Environ. Geol. 53 (5), 937–943. https://doi.org/10.1007/s00254-007-0716-8.

Laskar, J., Correia, A.C.M., Gastineau, M., Joutel, F., Levrard, B., Robutel, P., 2004. Long term evolution and chaotic diffusion of the insolation quantities of Mars. Icarus 170 (2), 343–364. https://doi.org/10.1016/j.icarus.2004.04.005.

Levy, J.S., Head, J.W., Marchant, D.R., 2007. Lineated valley fill and lobate debris apron stratigraphy in Nilosyrtis Mensae, Mars: Evidence for phases of glacial modification of the dichotomy boundary. J. Geophys. Res. Planets 112(E8). https://doi.org/10.1029/2006JE002852.

Luzzi, E., Rossi, A.P., Pozzobon, R., Oehler, D.Z., Etiope, G., 2018. Becquerel crater radial faults: a possible target for methane seepage investigations. Lunar and Planetary Science Conference 49.

Malin, M.C., Carr, M.H., 1999. Groundwater formation of Martian valleys. Nature 397 (6720), 589. https://doi.org/10.1038/17551.

Malin, M.C., Edgett, K.S., 2000. Evidence for recent groundwater seepage and surface runoff on Mars. Science 288 (5475), 2330–2335. https://doi.org/10.1126/science.288.5475.2330.

Malin, M.C., Bell, J.F., Cantor, B.A., Caplinger, M.A., Calvin, W.M., Clancy, R.T., Lee, S.W., 2007. Context camera investigation on board the Mars Reconnaissance Orbiter. J. Geophys. Res. Planets 112 (E5). https://doi.org/10.1029/2006JE002808.

Mangold, N., Gendrin, A., Gondet, B., LeMouelic, S., Quantin, C., Ansan, V., Bibring, J.P., Langevin, Y., Masson, P., Neukum, G., 2008. Spectral and geological study of the sulfate-rich region of West Candor Chasma, Mars. Icarus 194 (2), 519–543. https://doi.org/10.1016/j.icarus.2007.10.021.

Mauduit, T., Guerin, G., Brun, J. P., Lecanu, H., 1997. Raft tectonics: the effects of basal slope angle and sedimentation rate on progressive extension. Journal of Structural Geology, 19(9), 1219-1230. https://doi.org/10.1016/S0191-8141(97)00037-0.

McCauley, J.F., Carr, M.H., Cutts, J.A., Hartmann, W.K., Masursky, H., Milton, D.J., Sharp, R.P., Wilhelms, D.E., 1972. Preliminary Mariner 9 report on the geology of Mars, Icarus 17, 289. https://doi.org/10.1016/0019-1035(72)90003-6.

McEwen, A.S., Eliason, E.M., Bergstrom, J.W., Bridges, N.T., Hansen, C.J., Delamere, W.A., Grant, J.A., Gulick, V.C., Herkenhoff, K.E., Keszthelyi, L., Kirk, R.L., Mellon, M.T., Squyres, S.W., Thomas, N., Weitz, C.M., 2007. Mars reconnaissance orbiter's high resolution imaging science experiment (HiRISE). J. Geophys. Res. Planets 112 (E5). https://doi.org/10.1029/2005JE002605.

McGill, G.E., 2000. Crustal history of north central Arabia Terra, Mars. J. Geophys. Res. Planets 105(E3), 6945-6959. https://doi.org/10.1029/1999JE001175.

McGill, G.E., Dimitriou, A.M., 1990. Origin of the Martian global dichotomy by crustal thinning in the late Noachian or early Hesperian, J. Geophys. Res. 95, 12,595–12,605. https://doi.org/10.1029/JB095iB08p12595.

McGill, G.E., Squyres, S.W., 1991. Origin of the Martian crustal dichotomy: Evaluating hypotheses. Icarus 93(2), 386-393. https://doi.org/10.1016/0019-1035(91)90221-E.

Michael, G.G., 2013. Planetary surface dating from crater size–frequency distribution measurements: multiple resurfacing episodes and differential isochron fitting. Icarus 226 (1), 885–890. https://doi.org/10.1016/j.icarus.2013.07.004.

Michael, G.G., Neukum, G., 2010. Planetary surface dating from crater size–frequency distribution measurements: partial resurfacing events and statistical age uncertainty. Earth Planet. Sci. Lett. 294 (3), 223–229. https://doi.org/10.1016/j.epsl.2009.12.041.

Mikhailova, M.V., 2015. Morphometry of river deltas. Water Res. 42 (1), 52–62. https://doi.org/10.1134/S009780781501008X.

Moore, J. G., Normark, W. R., Holcomb, R. T., 1994. Giant Hawaiian underwater landslides. Science, 264(5155), 46-47. https://doi.org/10.1126/science.264.5155.46.

Morgan, F., Seelos, F.P., Murchie, S.L., the CRISM Team, 2014. CRISM analysis toolkit (CAT). In: Gaddis, R.G., Hare, T., Beyer, R. (Eds.), Summary and Abstracts of the Planetary Data Workshop, June 2012: Open-File Report 2014-1056. U.S. Geological Survey, Reston, VA, USA, pp. 125–126.

Morgan, G.A., Head, J.W., Marchant, D.R., 2009. Lineated valley fill (LVF) and lobate debris aprons (LDA) in the Deuteronilus Mensae northern dichotomy boundary region, Mars: constraints on the extent, age and episodicity of Amazonian glacial events. Icarus 202(1), 22–38. https://doi.org/10.1016/j.icarus.2009.02.017.

Morgan, A.M., Wilson, S.A., Howard, A.D., 2022. The global distribution and morphologic characteristics of fan-shaped sedimentary landforms on Mars. Icarus, 385, 115137. https://doi.org/10.1016/j.icarus.2022.115137.

Murchie, S., et al., 2007. Compact reconnaissance imaging spectrometer for Mars (CRISM) on Mars reconnaissance orbiter (MRO). J. Geophys. Res. Planets 112 (E5). https://doi.org/10.1029/2006JE002682.

Mustard, J.F., Cooper, C.D., Rifkin, M.K., 2001. Evidence for recent climate change on Mars from the identification of youthful near-surface ground ice. Nature 412 (6845), 411–414. https://doi.org/10.1038/35086515.

Neukum, G., Jaumann, R., the HRSC Co-Investigator and Experiment Team, 2004. HRSC: the high resolution stereo camera ofMars Express. In:Wilson, A. (Ed.), Mars Express: The Scientific Payload. ESA, Noordwijk, The Netherlands, pp. 17–35 SP-1240.

Oehler D.Z., Allen C.C., 2008. Ancient hydrothermal springs in Arabia Terra, Mars. In: Lunar and Planetary Science Conference Abstracts, Vol. 39, p. #1391, DOI: https://doi.org/10.1109/IEMBS.2008.4650211.

Okubo, C.H., Schultz, R.A., Chan, M.A., Komatsu, G., 2009. Deformation band clusters on Mars and implications for subsurface fluid flow. Geol. Soc. Am. Bull. 121 (3–4), 474–482. https://doi.org/10.1130/B26421.1.

Ori G., Baliva A., 1999. Large bulges at the center of impact craters on Mars. In: Lunar and Planetary Science Conference Abstracts, Vol. 30, DOI: https://doi.org/10.1248/yakushi1947.119.11_868.

Palmer, A.N., 2007. Cave geology. Cave Books, Daytom 454.

Parenti, C., Gutiérrez, F., Baioni, D., García-Arnay, Á., Sevil, J., Luzzi, E., 2020. Closed depressions in Kotido crater, Arabia Terra, Mars. Possible evidence of evaporite dissolution-induced subsidence. Icarus 341, 113680. https://doi.org/10.1016/j.icarus.2020.113680.

Parker, T.J., Gorsline, D.S., Saunders, R.S., Pieri, D.C., Schneeberger, D.M., 1993. Coastal geomorphology of the Martian northern plains. J. Geophys. Res. Planets 98 (E6), 11061–11078. https://doi.org/10.1029/93JE00618.

Pondrelli M., Baliva A., Di Lorenzo S., Marinangeli L., Rossi A. P., 2005. Complex evolution of paleolacustrine systems on Mars: an example from the Holden crater. J. Geophys. Res. Planets, 110(E4). doi: https://doi.org/10.1029/2004JE002335.

Pondrelli, M., Rossi, A.P., Marinangeli, L., Hauber, E., Gwinner, K., Baliva, A., Di Lorenzo, S., 2008. Evolution and depositional environments of the Eberswalde fan delta,Mars. Icarus 197 (2), 429–451. https://doi.org/10.1016/j.icarus.2008.05.018.

Pondrelli, M., Rossi, A.P., Ori, G., van Gasselt, S., Praeg, D., Ceramicola, S., 2011. Mud volcanoes in the geologic record of Mars: the case of Firsoff crater. Earth Planet. Sci. Lett. 304 (3–4), 511–519. https://doi.org/10.1016/j.epsl.2011.02.027.

Pondrelli, M., Rossi, A.P., Le Deit, L., Fueten, F., van Gasselt, S., Glamoclija, M., Cavalazzi, B., Hauber, E., Franchi, F., Pozzobon, R., 2015. Equatorial layered deposits in Arabia Terra, Mars: Facies and process variability. Geol. Soc. Am. Bull. 127 (7–8), 1064–1089. https://doi.org/10.1130/B31225.1.

Pondrelli M., Rossi A. P., Le Deit L., Schmidt G. W., Pozzobon R., Hauber E. and Salese F., 2019. Groundwater control and process variability on the equatorial layered deposits of Kotido crater, Mars. J. Geophys. Res. Planets, 124(E3), 779–800. doi: https://doi.org/10.1029/2018JE005656.

Poulet, F., Bibring, J.P., Mustard, J.F., Gendrin, A., Mangold, N., Langevin, Y., Arvidson, R.E., Gondet, B., Gomez, C., the Omega Team, 2005. Phyllosilicates on Mars and implications for early Martian climate. Nature 438 (7068), 623–627. https://doi.org/10.1038/nature04274.

Preuschmann S., Benkkert D., Wagner R., Neukum, G., the HRSC Co-Investigator Team, 2006. Karst-like topography within the Ganges Chasma region. Geophys. Res. Abstr., 8: 09383.

Reese, C.C., Orth, C.P., Solomatov, V.S., 2010. Impact origin for the Martian crustal dichotomy: Half emptied or half filled? J. Geophys. Res. Planets 115(E5). https://doi.org/10.1029/2009JE003506.

Reese, C.C., Orth, C.P., Solomatov, V.S., 2011. Impact megadomes and the origin of the martian crustal dichotomy. Icarus 213(2), 433-442. https://doi.org/10.1016/j.icarus.2011.03.028.

Rivera-Hernández, F., Palucis, M.C., 2019. Do deltas along the crustal dichotomy boundary of Mars in the Gale crater region record a northern ocean? Geophys. Res. Lett. 46, 8689–8699. https://doi.org/10.1029/2019GL083046.

Robbins, S., Hynek, B., 2013. Utility of laser altimeter and stereoscopic terrain models: application to Martian craters. Planet. Space Sci. 86, 57–65. https://doi.org/10.1016/j.pss.2013.06.019.

Roberts, J.H., Zhong, S., 2006. Degree-1 convection in the Martian mantle and the origin of the hemispheric dichotomy. J. Geophys. Res. Planets 111(E6). https://doi.org/10.1029/2005JE002668.

Rossi, A., Neukum, G., Pondrelli, M., Gasselt, S.V., Zegers, T., Hauber, E., Chicarro, A., Foing, B., 2008. Large-scale spring deposits on Mars? J. Geophys. Res. Planets 113 (E8). https://doi.org/10.1029/2007JE003062.

Schaeffer, M., 1990. Geochemical evolution of the northern plains of Mars: early hydrosphere, carbonate development and present morphology. J. Geophys. Res. Solid Earth 95 (B9), 14291–14300. https://doi.org/10.1029/JB095iB09p14291.

Schon, S.C., Head, J.W., Fassett, C.I., 2012. An overfilled lacustrine system and progradational delta in Jezero crater,Mars: implications for Noachian climate. Planet. Space Sci. 67 (1), 28–45. https://doi.org/10.1016/j.pss.2012.02.003.

Scott, D.H., Carr, M.H., 1978. Geologic Map of Mars: U.S. Geological Survey Investigations Series, I-1083, Scale 1:25,000,000. http://pubs.er.usgs.gov/publication/i1083.

Seu, R., Phillips, R. J., Biccari, D., Orosei, R., Masdea, A., Picardi, G., Safaeinili, A., Campbell, B.A., Plaut, J.J., Marinangeli, L., Smrekar, S.E., Nunes, D.C., 2007. SHARAD sounding radar on the Mars Reconnaissance Orbiter. J. Geophys. Res. Planets 112(E5). https://doi.org/10.1029/2006JE002745.

Skinner Jr, J.A., Tanaka, K.L., 2003. How should planetary map units be defined? Lunar and Planetary Science Conference Abstracts vol. 34 (p. #2100). Retrieved from: https://www.lpi.usra.edu/meetings/lpsc2003/pdf/2100.pdf.

Skinner Jr, J.A., Tanaka, K.L., 2018. Geological Map of the Nepenthes Planum Region, Mars. US Geological Survey Scientific Investigations Map 3389, Scale 1:1,506,000. https://doi.org/10.3133/sim3389.

Silverman, B.W., 2018. Density estimation for statistics and data analysis. Routledge. https://doi.org/10.1201/9781315140919.

Sleep, N.H., 1994. Martian plate tectonics. J. Geophys. Res. Planets 99(E3), 5639-5655. https://doi.org/10.1029/94JE00216.

Smith, Z.E., Tullis, J.A., Steele, K.F., Malfavon, L., 2006. Martian sinkholes: Implications for large scale evaporite deposits. 37th Annual Lunar and Planetary Science Conference.

Solomon, S.C., Aharonson, O., Aurnou, J.M., Banerdt, W.B., Carr, M.H., Dombard, A.J., Frey, H.V., Golombek, M.P., Hauck, S.A. II, Head, J.W. III, Jakosky, B.M., Johnson, C.L., McGovern, P.J., Neumann, G.A., Phillips, R.J., Smith, D.E., Zuber, M.T., 2005. New perspectives on ancient Mars. Science 307, 1214–1220, https://doi.org/10.1126/science.1101812.

Strahler, A.N., 1952. Hypsometric (area-altitude) analysis of erosional topography. Geol. Soc. Am. Bull. 63(11), 1117-1142. https://doi.org/10.1130/0016-7606(1952)63[1117:HAAOET]2.0.CO;2.

Sunamura, T., 1992. Shore platforms. Geomorphology of Rocky Coasts. vol. 302. Wiley, Chichester, pp. 139–183.

Tanaka, K.L., Golombek, M.P., Banerdt, W.B., 1991. Reconciliation of stress and structural histories of the Tharsis region of Mars. J. Geophys. Res. Planets 96(E1), 15617-15633. https://doi.org/10.1029/91JE01194.

Tanaka, K.L., Scott, D.H., Greeley, R., 1992a. Global stratigraphy. In: Kieffer HH, Jakosky BM, Snyder CW, Matthews MS (eds) Mars. University Arizona Press, Tucson, pp 345–382.

Tanaka, K.L., Chapman, M.G., Scott, D.H., 1992b. Geologic map of the Elysium region of Mars. US Geological Survey Report, IMAP 2147. https://doi.org/10.3133/i2147.

Tanaka, K.L., Skinner, J.A., Hare, T.M., 2005. Geologic map of the northern plains of Mars. US Geological Survey Scientific Investigations Map 2888, Scale 1:15,000,000. https://doi.org/10.3133/sim2888.

Tanaka, K.L., Skinner Jr., J.A., Dohm, J.M., Irwin III, R.P., Kolb, E.J., Fortezzo, C.M., Platz, T., Michael, G.G., Hare, T.M., 2014. Geologic Map of Mars. US Geological Survey Scientific Investigations Map 3292, Scale 1:20,000,000. pamphlet 43 p. https://doi.org/10.3133/sim3292.

Trenhaile, A.S., 1987. Shore platforms. The Geomorphology of Rock Coasts. Oxford University Press, USA, pp. 192–239.

Viviano, C.E., Seelos, F.P., Murchie, S.L., Kahn, E.G., Seelos, K.D., Taylor, H.W., Taylor, K., Ehlmann, B.L., Wiseman, S.M., Mustard, J.F., Morgan, M.F., 2014. Revised CRISM spectral parameters and summary products based on the currently detected mineral diversity on Mars. J. Geophys. Res. Planets 119(6), 1403–1431. https://doi.org/10.1002/2014JE004627.

Viviano-Beck, C.E., et al., 2015.MRO CRISM type spectra library. NASA Planetary Data System. Retrieved from. http://crismtypespectra.rsl.wustl.edu.

Waltham, A.C., 1989. Ground Subsidence. Blackie, Glasgow and London (202 p).

Waltham, T., Bell, F.G., Culshaw, M.G., Knez, M., Slabe, T., 2005. Sinkholes and subsidence: karst and cavernous rocks in engineering and construction (Vol. 382). Berlin: Springer.

Warner, N.H., Gupta, S., Calef, F., Grindrod, P., Boll, N., Goddard, K., 2015. Minimum effective area for high resolution crater counting of Martian terrains. Icarus 245, 198–240. https://doi.org/10.1016/j.icarus.2014.09.024.

Watters, T.R., 1993. Compressional tectonism on Mars. J. Geophys. Res. Planets 98(E9), 17049-17060. https://doi.org/10.1029/93JE01138.

Watters, T.R., 2003a. Lithospheric flexure and the origin of the dichotomy boundary on Mars, Geology 31, 271–274. https://doi.org/10.1130/0091-7613(2003)031%3C0271:LFATOO%3E2.0.CO;2.

Watters, T.R., 2003b. Thrust faults along the dichotomy boundary in the eastern hemisphere of Mars, J. Geophys. Res. Planets 108(E6), 5054. https://doi.org/10.1029/2002JE001934.

Watters, T.R., Robinson, M.S., 1999. Lobate scarps and the Martian crustal dichotomy. J. Geophys. Res. Planets 104(E8), 18981-18990. https://doi.org/10.1029/1998JE001007.

Watters, T.R., McGovern, P.J., 2006. Lithospheric flexure and the evolution of the dichotomy boundary on Mars. Geophys. Res. Lett. 33(8). https://doi.org/10.1029/2005GL024325.

Watters, W.A., Geiger, L.M., Fendrock, M., Gibson, R., Hundal, C.B., 2017. The role of strength defects in shaping impact crater planforms. Icarus 286, 15–34. https://doi.org/10.1016/j.icarus.2016.12.024.

Whitney, M.I., 1978. The role of vorticity in developing lineation by wind erosion. Geol. Soc. Am. Bull. 89 (1), 1–18. https://doi.org/10.1130/0016-7606(1978)89<1:TROVID>2.0.CO;2.

Wilhelms, D.E., 1990. Geologic mapping. In: Greeley, R., Batson, R.M. (Eds.), Planetary Mapping. Cambridge University Press, NY, pp. 208-260.

Wilhelms, D.E., Squyres, S.W., 1984. The Martian hemispheric dichotomy may be due to a giant impact. Nature 309(5964), 138-140. https://doi.org/10.1038/309138a0.

Wood, L.J., 2006. Quantitative geomorphology of the Mars Eberswalde delta. Geol. Soc. Am. Bull. 118 (5–6), 557–566. https://doi.org/10.1130/B25822.1.

Wyrick, D., Ferrill, D.A., Morris, A.P., Colton, S.L., Sims, D.W., 2004. Distribution, morphology, and origins of Martian pit crater chains. Journal of Geophysical Research: Planets, 109(E6). https://doi.org/10.1029/2004JE002240.

Zazo, C., Goy, J.L., Dabrio, C.J., Lario, J., González-Delgado, J.A., Bardají, T., Hillaire-Marcel, C., Cabero, A., Ghaleb, B., Borja, F., Silva, P.G., Roquero, E., Soler, V., 2013. Retracing the Quaternary history of sea-level changes in the Spanish Mediterranean–Atlantic coasts: geomorphological and sedimentological approach. Geomorphology 196, 36–49. https://doi.org/10.1016/j.geomorph.2012.10.020.

Zhong, S., Zuber, M.T., 2001. Degree-1 mantle convection and the crustal dichotomy on Mars. Earth Planet. Sc. Lett. 189(1-2), 75-84. https://doi.org/10.1016/S0012-821X(01)00345-4.

Zuber, M.T., Smith, D.E., Solomon, S.C., Muhleman, D.O., Head, J.W., Garvin, J.B., 1992. The Mars Observer laser altimeter investigation. J. Geophys. Res. Planets 97 (E5), 7781–7797. https://doi.org/10.1029/92JE00341.

Annex. 1:1.45M Geologic-geomorphic map of NW Terra Cimmeria and SE Nepenthes Mensae

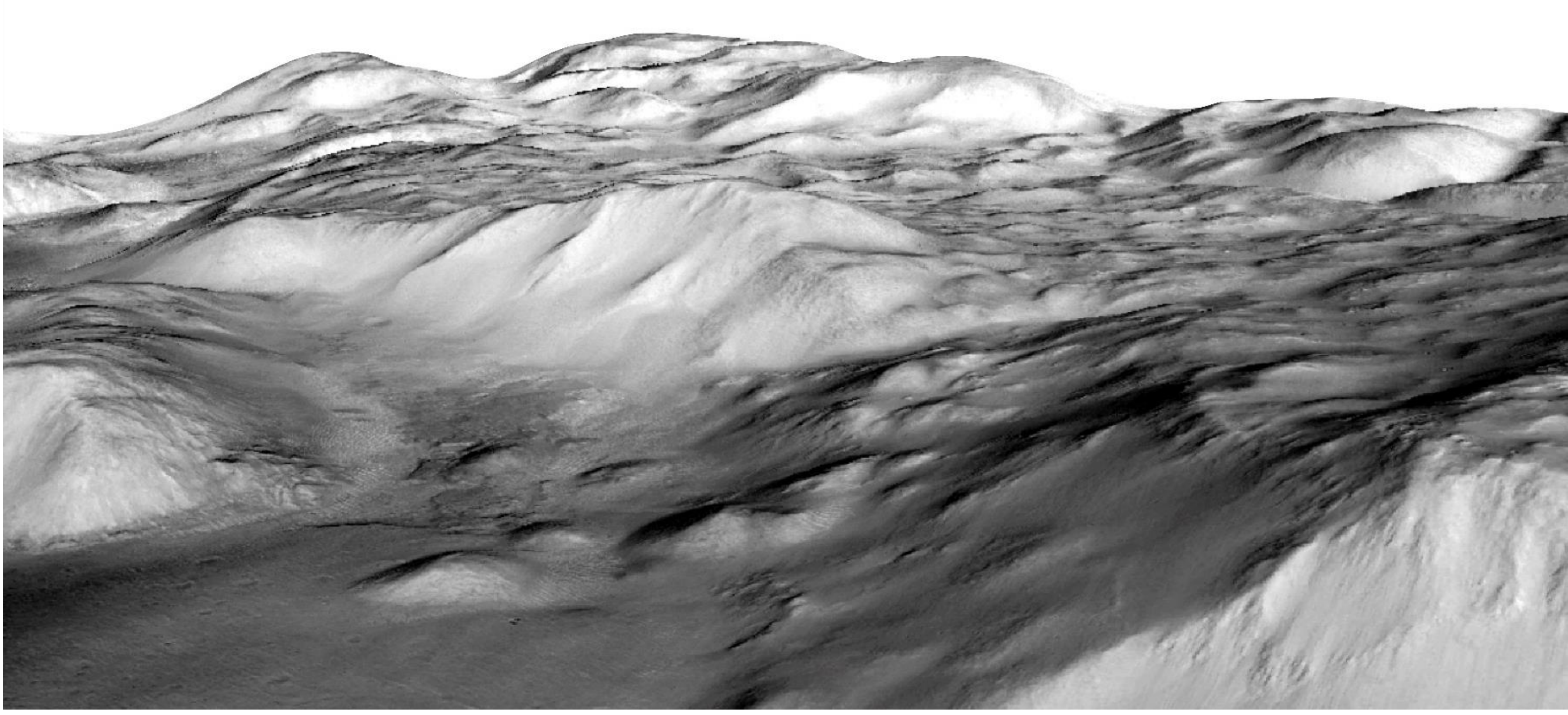

Geologic-geomorphic map of the Terra Cimmeria-Nepenthes Mensae transitional zone, Mars - 1:1.45Million

Departamento de
Ciencias de la Tierra
Universidad Zaragoza

Á. García-Arnay[a]

[a] Grupo Procesos Geoambientales y Cambio Global, IUCA, Departamento de Ciencias de la Tierra, Universidad de Zaragoza, 50009 Zaragoza, Spain (arnay@unizar.es)

Instituto Universitario de Investigación
en Ciencias Ambientales
de Aragón
Universidad Zaragoza

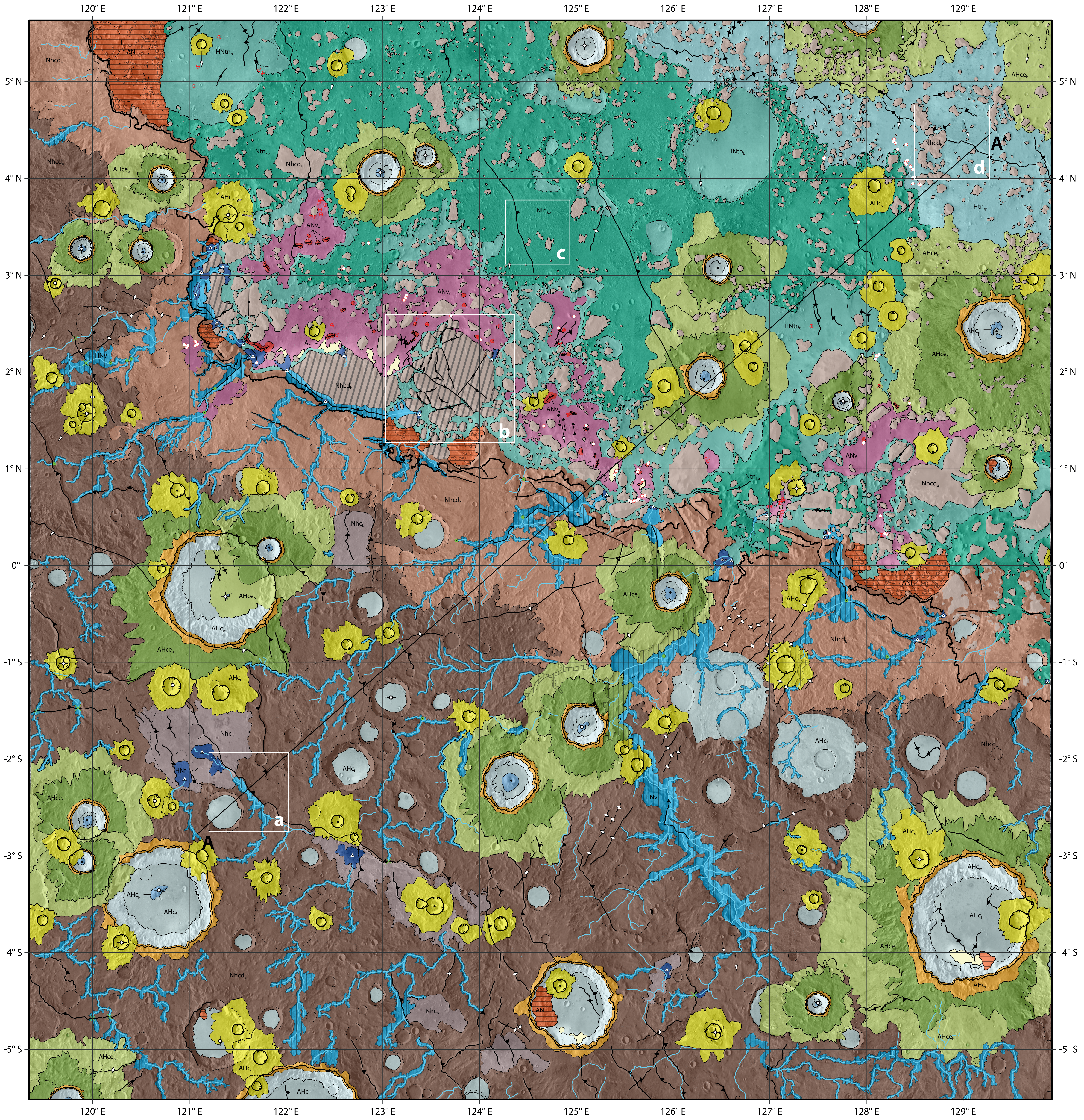

Scale 1 : 1,450,000 (at publication scale)

0 50 100 Kilometers 150 200 250

N

Geographic Coordinate System: GCS_Mars_2000_Sphere

Projection System: Equidistant Cylindrical (central meridian: 125º)

Datum: D_Mars_2000_Sphere

Spheroid: Mars_2000_Sphere_IAU_IAG

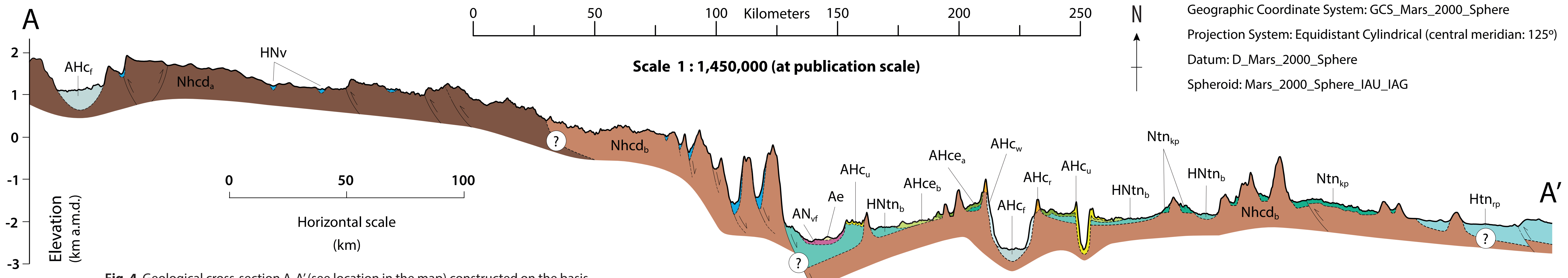

Fig. 4. Geological cross-section A-A' (see location in the map) constructed on the basis of cartographic relationships and crater-counting-based ages (Fig. 3a, b).

DESCRIPTION OF MAP UNITS

Unit label	Unit name	Unit description
	HIGHLAND PROVINCE - Cimmeria region units	
Nhcd$_a$	**Cimmeria dissected unit - Mb a**	Rugged and heavily cratered surfaces dissected by V-shaped valleys. It occurs in the topographically higher sector (Fig. 2a). NW-SE-striking lobate scarps, and rarely ridge crests.
Nhcd$_b$	**Cimmeria dissected unit - Mb b**	Rugged and less cratered surfaces than Mb a, and heavily dissected by V-shaped valleys. It crops out in the plateau situated south of the dichotomy, forming residual reliefs in the transitional province (Fig. 2b). Localized NE-SW-oriented ridge crests, and scarce occurrence of lobate scarps with NW-SE orientation. Mb b grades into the older Mb a.
Nhc$_b$	**Cimmeria basin unit**	Moderately cratered unit occurring in depressions inset into member Nhcd$_a$, exhibiting smooth surfaces, wrinkle ridges, and absence of channels (Fig. 2a).
	TRANSITIONAL PROVINCE - Nepenthes region units	
Ntn$_{kp}$	**Nepenthes knobby plateau unit**	Inter-crater plateaus of Nepenthes Mensae characterized by knobby terrains (Fig. 2c) with NW-SE-trending lobate scarps. It grades into the older unit Nhcd$_b$ and younger unit HNtn$_b$.
HNtn$_b$	**Nepenthes basin unit**	Smooth terrains locally interrupted by residual reliefs, wrinkle ridges, pitted cones and small tholi. It occurs in closed depressions and old impact basins, and overlies unit Nhcd$_b$.
Htn$_{rp}$	**Nepenthes ridged plain unit**	Undulating, low-lying plains with pervasive NW-SE-oriented wrinkle ridges and scattered knobs of unit Nhcd$_b$ (Fig. 2d). It overlies unit Nhcd$_b$ and grades into the older unit Ntn$_{kp}$.
	WIDELY OCCURRING - Impact crater units	
AHc$_u$	**Crater unit - undivided**	Well-preserved craters with rim diameter between 5 and 13 km. It is characterized by hummocky crater floors with rare occurrence of central peak or pit, and lobate ejecta.
AHce$_a$	**Crater ejecta unit - facies a**	Inner unit characterized by rugged lobes with flowbands around moderately to well-preserved impact craters with rim diameter ≥13 km.
AHce$_b$	**Crater ejecta unit - facies b**	Outer unit formed by distal deposits characterized by smooth flow-oriented lobes around moderately to well-preserved impact craters with rim diameter ≥13 km.
AHc$_r$	**Crater rim unit**	Inward-facing scarps frequently dissected by gullies of moderately to well-preserved impact craters with rim diameter ≥13 km.
AHc$_w$	**Crater wall unit**	Scarps, discontinuous terraces, blocks, and rockfalls with locally rugged surfaces of moderately to well-preserved impact craters with rim diameter ≥13 km.
AHc$_f$	**Crater floor unit**	Smooth, near-planar surfaces, frequently displaying a central peak and/or pit in the center of moderately to well-preserved impact craters with rim diameter ≥13 km (Fig. 2a).
AHc$_p$	**Crater peak unit**	Hills with irregular and grooved surfaces, and frequent occurrence of central pits of moderately to well-preserved impact craters with rim diameter ≥13 km.
	LOCALLY DISTRIBUTED - Volcanic, fluvial, eolian, and mass-wasting units	
ANv$_e$	**Volcanic edifice unit**	Isolated and coalesced raised fissures with sloping, and rugged to smooth surfaces, as well as small cone- and mound-shaped features. Locally grades into the coeval unit ANv$_f$.
ANv$_f$	**Volcanic flow unit**	Smooth to rugged, poorly-cratered surfaces, often with channels, overlapping lobes, and NE-SW-striking wrinkle ridges. Locally overlies units HNtn$_b$ and Nhcd$_b$, and underlies HNf.
HNv	**Valley unit**	Smooth deposits underlying the low-TI valley floors. It is carved in units Nhcd$_a$ and Nhcd$_b$, and rarely in unit Ntn$_{kp}$.
HNf	**Fan unit**	Fan-shaped deposits with smooth to corrugated surfaces due to differential erosion. This unit is laterally associated with unit HNv (Fig. 2a, b).
AHl	**Landslide unit**	Rugged, rolling, and hummocky terrains mostly occurring associated with the dichotomy escarpment. Locally overlies units Nhcd$_b$ and HNtn$_b$.
Ae	**Eolian unit**	Dark-tone, barchan and longitudinal dune fields occurring near the foot of the dichotomy escarpment, and locally overlying units ANv$_f$, HNtn$_b$ and Nhcd$_b$.

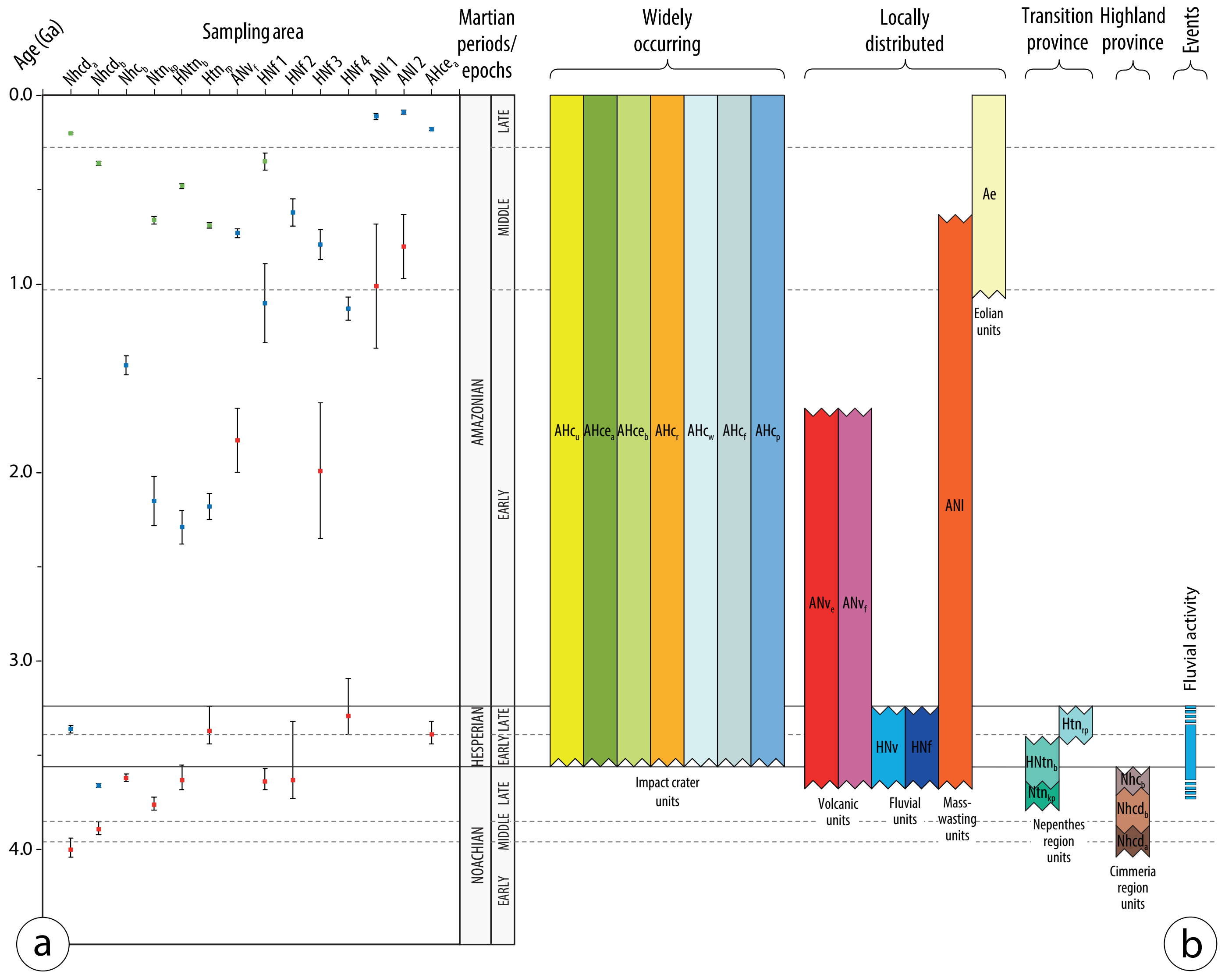

Fig. 3. (a) Diagram showing age estimations (boxes), and their error bars (vertical black lines) for the main mapped units. (b) Correlation of map units based on ages estimated by crater counting and geometrical relationships between units. Hachured polygon borders indicate possible, extended durations. Horizontal continuous and dashed lines indicate the boundaries between the Martian geological periods and epochs, respectively (Michael, 2013).

MAP SYMBOLS

Contacts

- Accurate
- Approximate
- Inferred

Ridges

- Wrinkle ridge
- Ridge crest
- Volcanic ridge
- Inverted channel

Depressions

- Trough
- Channel
- Sinkhole
- Valley

Scarps

- Dichotomy escarpment
- Lobate scarp

Craters (Mapped all crater rims >5 km in diameter)

- Crater rim - raised
- Crater rim - subdued
- Central peak
- Central pit

Fluvial features

- Flow direction
- Knickpoint
- Beheaded channel
- Alluvial fan/delta

Residual reliefs

- Knob or Mesa

Volcanic features

- Pitted cone
- Small tholi

Mass-wasting features

- Rock slumps
- Rock spreads

Eolian features

- Yardang
- Wind streaks

SURFACE FEATURES

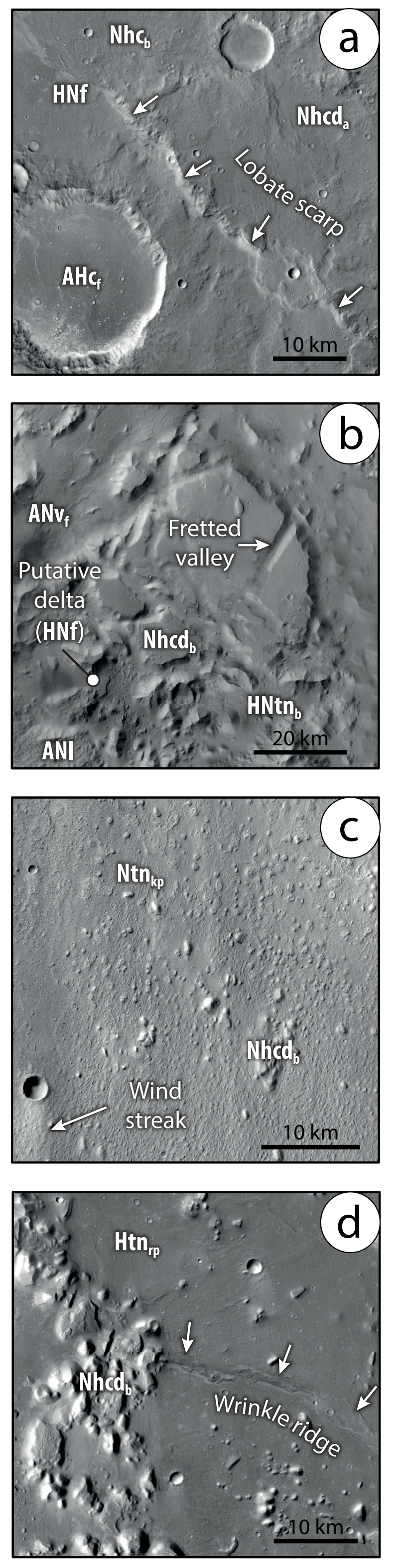

Fig. 2. CTX images (locations showed in the map). (a) SW-facing lobate scarp in unit Nhcd$_a$. (b) Mesa-like landform in a megalandslide dissected by troughs. (c) Knobby terrain of the unit Ntn$_{kp}$. (d) Tectonically-contracted plains of the unit Htn$_{rp}$ exhibiting wrinkle ridges and knobs. North is up in all images.

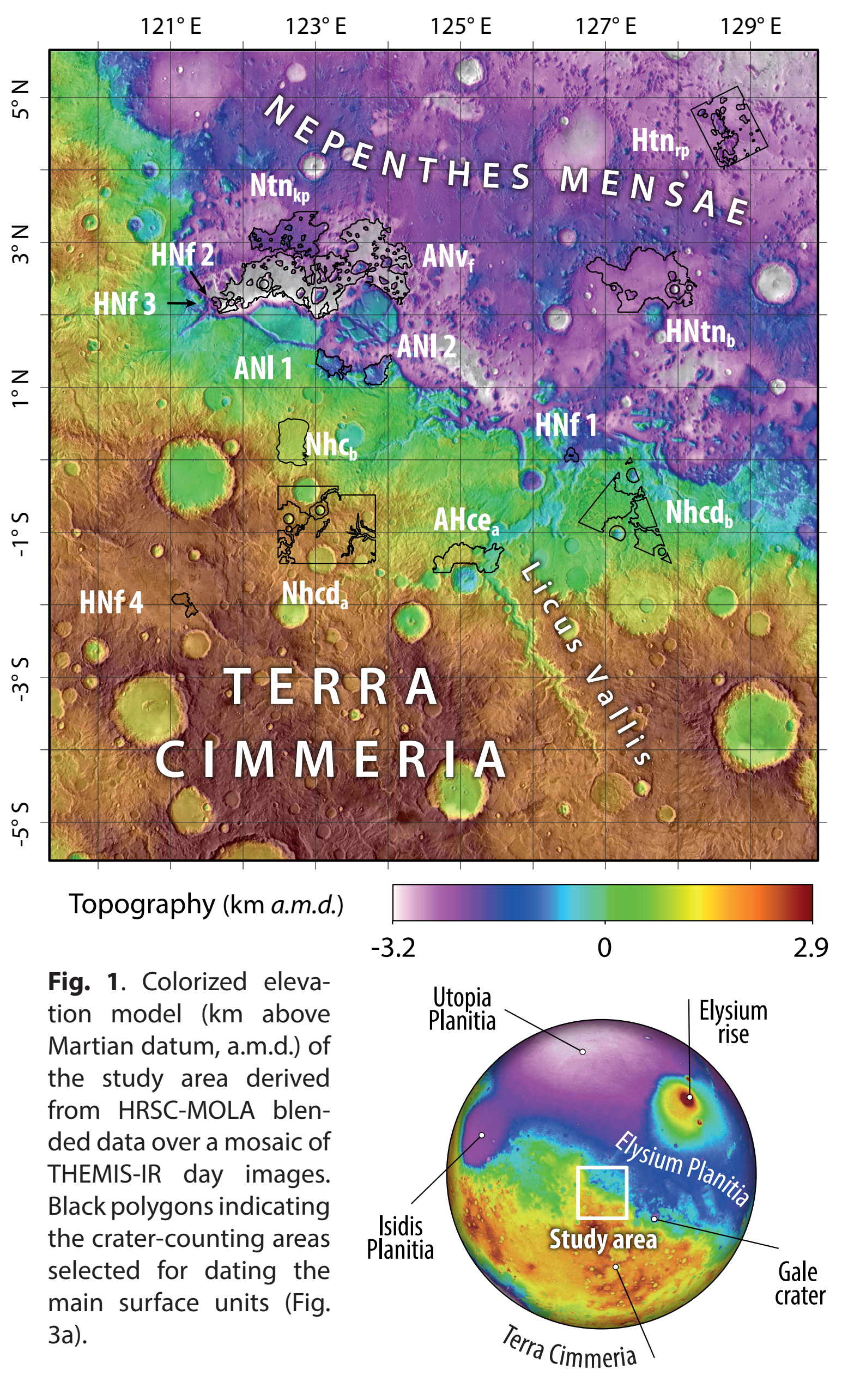

Fig. 1. Colorized elevation model (km above Martian datum, a.m.d.) of the study area derived from HRSC-MOLA blended data over a mosaic of THEMIS-IR day images. Black polygons indicating the crater-counting areas selected for dating the main surface units (Fig. 3a).

Back cover image credit: ESA/DLR/FU Berlin (G. Neukum), CC BY-SA 3.0 IGO

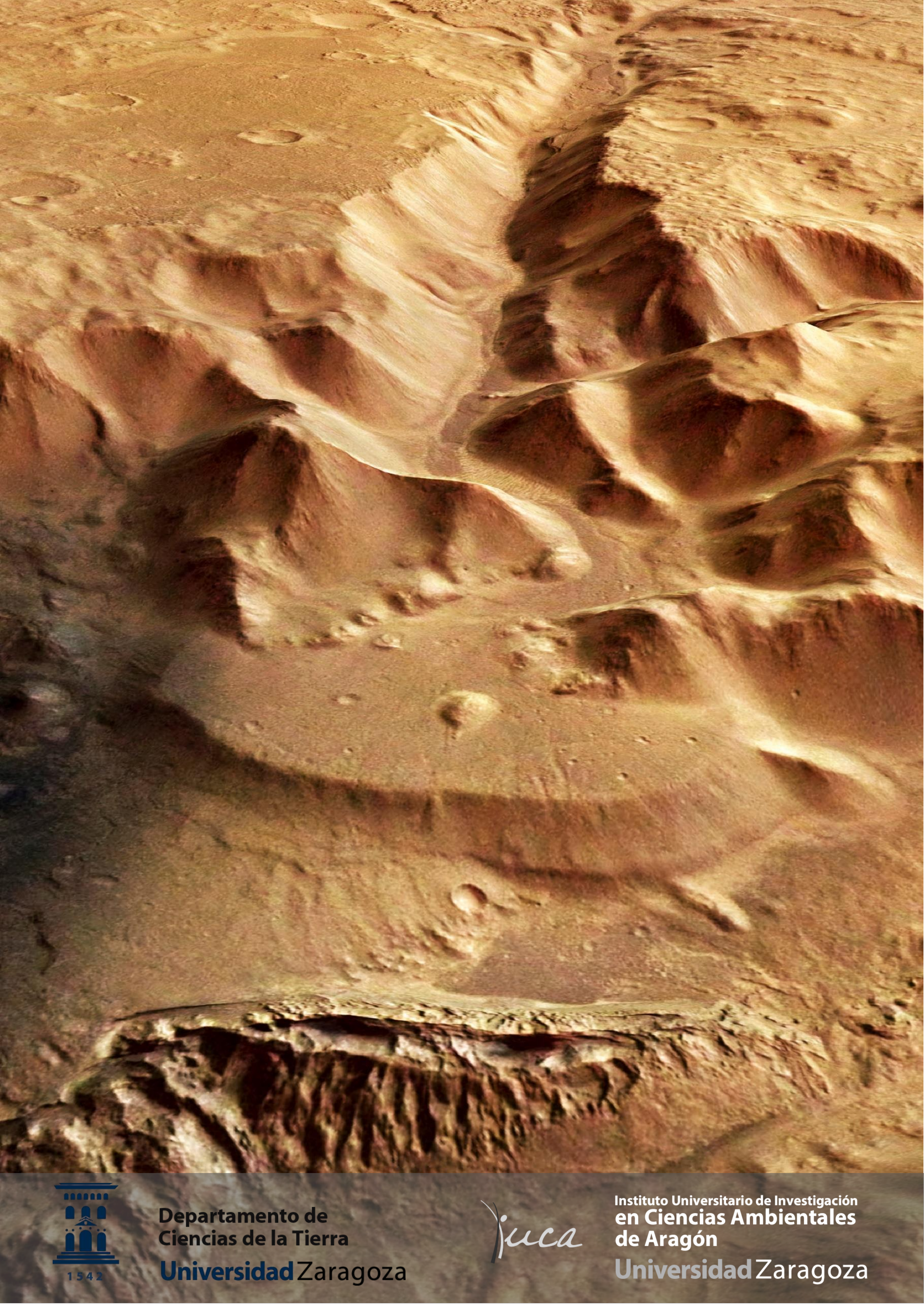

Departamento de
Ciencias de la Tierra
Universidad Zaragoza

Instituto Universitario de Investigación
en Ciencias Ambientales
de Aragón
Universidad Zaragoza